Imperial College
London

A Novel Flexible and Steerable Probe for Minimally Invasive Soft Tissue Intervention

by
Luca Frasson

Submitted in part fulfilment of the requirements
for the degree of Doctor of Philosophy
and the Diploma of Imperial College

London, November 2010

Imperial College of Science, Technology and Medicine
Department of Mechanical Engineering

Declaration of Originality

I, Luca Frasson declare that this thesis is my own work and that, to the best of my knowledge, it contains no material previously published, or substantially overlapping with material submitted for the award of any other degree at any institution. Information derived from the published and unpublished work of others has been acknowledged in the text and a list of references is given in the bibliography.

Abstract

Current trends in surgical intervention favour a minimally invasive (MI) approach, in which complex procedures are performed through increasingly small incisions. Specifically, in neurosurgery, there is a need for minimally invasive keyhole access, which conflicts with the lack of maneuverability of conventional rigid instruments. In an attempt to address this fundamental shortcoming, this thesis describes the concept design, implementation and experimental validation of a novel flexible and steerable probe, named "STING" (Soft Tissue Intervention and Neurosurgical Guide), which is able to steer along curvilinear trajectories within a compliant medium.

The underlying mechanism of motion of the flexible probe, based on the reciprocal movement of interlocked probe segments, is biologically inspired and was designed around the unique features of the ovipositor of certain parasitic wasps. Such insects are able to lay eggs by penetrating different kinds of "host" (e.g. wood, larva) with a very thin and flexible multi-part channel, thanks to a micro-toothed surface topography, coupled with a reciprocating "push and pull" motion of each segment. This thesis starts by exploring these foundations, where the "microtexturing" of the surface of a rigid probe prototype is shown to facilitate probe insertion into soft tissue (porcine brain), while gaining tissue purchase when the probe is tensioned outwards. Based on these findings, forward motion into soft tissue via a reciprocating mechanism is then demonstrated through a focused set of experimental trials in gelatine and agar gel. A flexible probe prototype (10 mm diameter), composed of four interconnected segments, is then presented and shown to be able to steer in a brain-like material along multiple curvilinear trajectories on a plane. The geometry and certain key features of the probe are optimised through finite element models, and a suitable actuation strategy is proposed, where the approach vector of the tip is found to be a function of the offset between interlocked segments. This concept of a "programmable bevel", which enables the steering angle to be chosen with virtually infinite resolution, represents a world-first in percutaneous soft tissue surgery.

The thesis concludes with a description of the integration and validation of a fully functional prototype within a larger neurosurgical robotic suite (EU FP7 ROBOCAST), which is followed by a summary of the corresponding implications for future work.

Dedication

To my dear Livia

Acknowledgements

There is a vast amount of people who contributed to make the research presented in this thesis possible, directly or indirectly, and I would really like to try to thank all of them in this couple of pages. Since I am not going to write another PhD dissertation in the future, this is also my last chance to say all the thanks I may have never said!

An additional thesis would be required to properly thank my supervisor, **Dr. Ferdinando Rodriguez y Baena**. Ferdinando is the boss I wish everybody could have; he is brilliant and patient, he discreetly led my research work, pushing me to express my creativity and guiding me through difficult times during my PhD. With the same discretion, as a friend rather than as a teacher, he tried to pass me his technical (but not only!) expertise with, I believe, successful results.

Another big thank is due to my second supervisor, **Prof. Brian Davies**: I was really lucky to be able to discuss my work, at any point during my research, with a pioneer of medical robotics. Support from a professor with such a worldwide reputation and long experience gave me the confidence to believe in what I was doing and in the decisions I was taking.

A lot of the work presented in this thesis would not have been possible without the technical help and suggestions of **Mr. Phil Wilson**.

The success of the research I am describing in this thesis cannot result but from strong teamwork which was carried out with my friends and colleagues at MIM Lab.

Starting from the people I have worked with on the flexible probe project, first of all I would like to thank **Tassanai**. We arrived almost together in London and with him I have shared most of my time in the Lab, but also outside (and at the beginning, in a new country, things are not that easy!). Tassanai is for me a strong example of generosity and creativity...(generosity and creativity often very difficult, almost impossible, to hold back!). I thank **Seong-Young** for his extreme patience in helping me on many aspects; a man of peace and determination. **Matthew** has always been available for me, always willing to listen, to spend his time to discuss my technical (and not just!) issues and very modestly providing me with extremely useful suggestions. Not from the MIM Lab, but almost adopted by the MIM Lab, thanks to **Saverio**, "the" example of commitment and hard work, and

thanks to **Cristian**, my "wife in London" before we both actually got married; Saverio and Cristian really helped me in addressing research fields about which I was not confident at all. All these colleagues are clear in my mind as examples of "respect". I'd then like to thank **Gorkem** for sharing with me difficulties and, above all, satisfaction when looking at the flexible probe successfully curving inside gelatine. Thanks to **Elnaz** for bringing a new and fresh "women's" prospective in an otherwise male dominated lab (and for bringing very nice pistachios).

Many thanks to **Yaroslav** for his ability to be a "mould-breaker" and for infecting me and everybody else with his enthusiasm and creativity; **Abbi**, who taught me how to be calm and relaxed in every situation (and for safely driving Tassanai and Seong-Young to Sicily); **Andy**, for showing me what being rigorous means, particularly in research. Thanks to **Ryo**: the word "no" is not in his vocabulary, the most gentle person I have ever met. Going a bit further back in the past, thanks to **Zion**, an example of hard work and high research ambition, thanks to **Haytham**, my "godfather" at the beginning of my experience in London and thanks to fun-loving **Marc**.

Thanks also to the students who helped out with my research: **Julia**, **Saurabh**, **Danial**, **Julius** and **Francesco**.

Special thanks to **Dr. Andreas Schneider**, with whom I collaborated during the first year of my research, to **Dr. Daniele Dini** and **Dr. Patrick Degeenar**, for sharing their expertise, and **Dr. Esther Rodriguez y Villegas**, for convincing me to finish writing my thesis, and because "behind a great man there is always a great woman".

I wish to take a moment to express my gratitude to all my friends, particularly those at "Our Lady of Victories". My housemates, **Ian** and **Saverio**, always ready to listen to me and to cheer me up. I have already thanked **Cristian**, but not his wife **Elisa** (and their baby **Agnese**). And then **Marina**, **Matthieu** and **Paulina**, **Silvia** and **Andrea**, **Tiziano**, **Miguel**, **Andy**, **John**, **Francesco**, **Christian**, **George**, **Tammy** (and **Simeon**). I cannot forget my first housemates, **Sachin** and **Andrea**, and **Maryann**, who taught me a proper british accent. My oldest friends, who were waiting for my return to Italy, **Fuskio**, **Cuono**, **Palma**, **Sergio** and **Vegio** (with corresponding families and girlfriends). And all the friends from the "**Casa di Tobia**" and **don Severino**.

Finally, I wish to express my deepest gratitude to my parents, **Marinella** and **Carlo**, who have always been very supportive of all my choices and have always trusted me, often even more than I trusted myself. Thanks to my sister **Stefania**, who substituted me in the family and took care of my wife for 3 years, and thanks to my little cool brother **Gabriele**; I have really missed both of them during my stay abroad (and I guess and hope, vice versa). A special thank you also to **nonno**

Gigi, **nonna Adriana** and **nonna Marisa**, who passed away too early to see me become a grown-up.

The reason why I can now thank so many good friends, with whom I have shared my three years in London, lies only in one person, who first believed in me and convinced me to have the courage for life-changing decisions: thanks to my girlfriend (2007), fiancee (2008) and finally wife (2009) **Livia**, for her patient wait and loving support.

Contents

Acknowledgements **4**

Contents **7**

List of Figures **11**

List of Tables **22**

1 Introduction **26**
1.1 Introduction 26
1.2 Medical motivation 27
1.3 Aim and objectives 28
1.4 Outline of the thesis 29
1.5 Publication output 31

2 Literature Review **35**
2.1 Medical background 35
2.1.1 Brain anatomy, function and pathology 35
2.1.2 Brain interventions: diagnosis and treatment 37
2.1.3 Instrumentation for MI keyhole neurosurgery 38
2.2 Percutaneous interventions: accessing curvilinear trajectories 40
2.2.1 Steering via bevel-tip flexible needle 41
2.2.2 Steering via needle bending 45
2.2.3 Steering via active cannulas 46
2.3 Biological inspiration from ovipositing wasps 47
2.3.1 Oviposition strategy 48
2.3.2 Basic anatomy of the ovipositor 49
2.3.3 The ovipositor tip 50
2.3.4 Ovipositor penetration mechanism 53
2.3.5 Ovipositor steering mechanisms 55
2.3.6 Discussion of biological inspiration 58
2.4 Literature review conclusions 60

3 Biological Foundations **61**
3.1 Biological inspiration for a flexible and steerable probe 61
3.2 Achieving forward penetration with "zero net force" on the tissue . . . 63
3.2.1 Rationale 63
3.2.2 Probe-tissue interaction: effect of anisotropic surface texture . 64
3.2.2.1 Surface topography - Size and shape range 64
3.2.2.2 Protocol definition 65
3.2.2.3 Results and discussion 66
3.2.2.4 Conclusions 70
3.2.3 Reciprocal motion 71
3.2.3.1 Materials and methods 72
3.2.3.2 Results 76
3.2.3.3 Discussion 79
3.2.3.4 Conclusions 82
3.3 Conclusions: towards a concept demonstrator for a flexible steerable probe 82

4 STING - a Soft Tissue Intervention and Neurosurgical Guide **85**
4.1 Introduction 85
4.2 Concept evolution 86
4.3 Concept analysis 87
4.4 The alpha prototype system 90
4.4.1 Manufacturing methods and materials for probe prototype development 90
4.4.2 The alpha prototype 91
4.4.3 Experimental setup 94
4.5 The "programmable bevel" concept 95
4.5.1 Testing protocol 97
4.5.2 Results and discussion 97
4.6 Reciprocal motion for reduced buckling 99
4.6.1 Testing protocol 100
4.6.2 Results and discussion 103
4.7 Achieving complex trajectories in a 2D space 106
4.7.1 Testing protocol 106
4.7.2 Results and discussion 107
4.8 Discussion of Failures 107
4.9 Conclusions 109

5 Modelling for Design Optimisation **112**
5.1 Introduction . . . 112
5.2 Methodology . . . 113
5.2.1 Parametric probe-interlock model . . . 113
5.2.2 Model definition and assessment . . . 116
5.2.3 Cross-section optimisation procedure . . . 119
5.2.4 Experimental validation of the optimum geometry . . . 123
5.3 Results and discussion . . . 125
5.4 Conclusions . . . 129

6 Towards the development of a 3D model **131**
6.1 Introduction . . . 131
6.2 Materials and methods . . . 132
6.2.1 Beam resting on elastic foundations . . . 132
6.2.2 Non-linear elastic foundation modulus . . . 135
6.2.3 Boundary value problem solved with a relaxation method . . . 138
6.2.4 Numerical algorithm for the identification of the critical buckling load . . . 141
6.3 Results and Discussion . . . 143
6.4 Conclusions . . . 147

7 New Probe Prototype and System Integration **148**
7.1 Introduction . . . 148
7.2 Materials and methods . . . 149
7.2.1 Beta prototype design . . . 149
7.2.2 Beta prototype manufacturing . . . 152
7.2.3 Experimental setup and protocol . . . 152
7.3 Results and discussion . . . 154
7.4 ROBOCAST: flexible probe system integration . . . 159
7.5 Conclusions . . . 164

8 Conclusions and Future Work **166**
8.1 Overview . . . 166
8.2 Summary of salient contributions . . . 169
8.3 Clinical contributions . . . 170
8.4 Future work . . . 170
8.4.1 Computational modelling . . . 170
8.4.2 Medical mechatronics . . . 171
8.4.3 Medical image computing . . . 171
8.4.4 Histological analysis . . . 172

8.5 Conclusions 172

Bibliography **173**

Appendix A Flexible Probe Design Process **184**

Appendix B Medical-Grade Silicone Extrusion **191**

Appendix C Reciprocal Motion **194**

Appendix D The ROBOCAST Project **198**

List of Figures

2.1 Regions of the human brain 36
2.2 a) Stereotactic frame for brain biopsy (Leksell Sterotactic System); b) Brain biopsy needle, the inner cannula is partially inserted in the outer cannula; c) Detail of the window in the outer cannula 39
2.3 a) Definition of the bevel tip angle; b) The final needle locations, extracted from difference images, with different bevel angles illustrate the steering effect of the bevel tip. A 5^o bevel exhibits the most bending while an 80^o bevel the least [Webster et al., 2005]. 41
2.4 a) CAD model of the friction-drive needle-insertion mechanism proposed for flexible needle steering, in yellow, the rubber wheels; b) Needle rotation mechanism; c) Close view of the telescoping support sheath, shown in a compressed view to expose the needle (on the right) [Webster, 2007]. 42
2.5 An example path of a flexible steerable needle. The needle is rotated 180^oat its base in order to flip the bevel orientation thus reversing the concavity of the curvature. The needle avoids the obstacles and reaches the target [Reed et al., 2008a] 43
2.6 By "duty-cycling" the rotation of the needle base, different curved trajectories are achieved inside the tissue phantom [Engh et al., 2006a] 44
2.7 a) Virtual spring model and needle bending; b) 6-DOF parallel robot inserting a flexible needle in soft tissue following a curved trajectory[Glozman and Shoham, 2007] 45
2.8 A prototype active cannula made of super-elastic Nitinol tubes. The inset line drawing indicated degrees of freedom. External diameter dimensions of the two tubes comprising the cannula are also shown.[Webster et al., 2009] 47
2.9 Giant ichneumon wasp *Rhyssa persuasoria*. Adult boring the surface of trunk infested with wood wasp larvae. Image courtesy of Boris Hrasovec, Faculty of Forestry, Bugwood.org 48

2.10 Diagrammatic representation of oblique view of transversely cut ovipositor with lower valves protruding [Quicke et al., 1995] 49
2.11 Diagrams of transverse sections through ovipositors of: a) *Xyelida* (Xyelidae); b) *Megalyra* (Megalyridae); c) *Monomachus* (Monomachidae); d) *Stethantyx* (Tersilochinae), section as seen in expanded state [Quicke et al., 1994] 49
2.12 Diagrammatic figures of hymenopteran ovipositor. a) lateral view of tenthredinid ovipositor; b) lateral view of braconid ovipositor divided in the middle [Quicke et al., 1994] 50
2.13 *Encarsia*: Scanning electron micrographs of external morphology. a) Ventral view showing left and right lower ovipositor valves (LV1 and LV2), ovipositor sheath (S). b) Apex of upper valve (UV) showing serrations (A-E), the distal pair are positioned medially (A,B) while posterior ones alternate on right (C,E) and left (D) side. Scale bars: a)=10μm; b)=1μm [Gerling et al., 1998] 51
2.14 *Eritmocerus*: Scanning electron micrographs of external morphology. a) General view showing depth and upwards curvature of ovipositor; b) Angular crease (arrow) of lower valve and blunt apex of upper valve. Scale bars: a)=10μm; b)=5μm [Gerling et al., 1998] 51
2.15 *Orussus abietinus* ovipositor tip; 1vv first valvula, 2vv second valvula [Vilhelmsen et al., 2001]. 52
2.16 Tip of the ovipositor of *Sirex noctilio*. Teeth 1 to 4 (P) point proximal and are "pull teeth"; teeth 6 and 7 and higher (D) point distally and are "push teeth" [Vincent and King, 1995]. 52
2.17 Tip of the ovipositor of M. n. nortoni. Teeth are numbered, all pointing proximally. Dark spots (arrows) are probably chemosensors, strain sensors occur in the area marked by the asterisks [Vincent and King, 1995]. 53
2.18 *Orussus* spp. female targeting a larva in the wood. The red arrow (right) shows the location of the ovipositor muscular system in the metasoma. The long and flexible ovipositor is concealed in the body and coiled in an S-shaped twist as indicated by the blue arrow (left). The black heavy line represents the section in the *Orussus* body and in the wood [Quicke et al., 1999, Vilhelmsen et al., 2001]. 54
2.19 Strut of length L being loaded from above (P). The critical buckling load, P_{crit}, is affected by the end conditions and by the length L. . . . 54

2.20 Two parts of ovipositor cutting into a wood cell. The left valve is pulling on a piece of wood cell with force T. The right valve can add this to the compressive force, limited by the critical Euler buckling load, giving a total force of penetration of $T+P_{crit}$ [Vincent and King, 1995] 56
2.21 a) Intact ovipositor of *Zaglyptogastra levisulcata* at rest, b) ventrally flexed. c) Isolated upper valve of the ovipositor of *Zaglyptogastra equitator*, d) isolated lower valve [Quicke, 1991] 57
2.22 Generalised diagram of *Zaglyptogastra* ovipositor apex showing relative position of upper and lower (shaded) valves: a), at rest; b), when flexed ventrally [Quicke, 1991] 57
2.23 Diagrammatic example of the steering mechanism [Quicke et al., 1995] 57
2.24 Scanning electron micrographs of intact ovipositor apices of *Gasteruption assectator*. Arrows indicate bosses on lower valves; stars indicate corresponding protuberances on upper valve [Quicke and Fitton, 1995] 58
2.25 a,b) Scanning electron micrographs of isolated upper ovipositor apices of *Pristaulacus*; c,d) isolated lower valves. Stars indicate corresponding abrupt interruption of upper valve sub-lateral groove; arrows indicate bosses at end of lower valve ridge. "r" and "a" indicate rhachis and aulax respectively [Quicke and Fitton, 1995] 59

3.1 Diagrammatic representation of the forces involved during one step of the reciprocal motion; the lower probe part is stationary, while the upper part is pushed inside the tissue. The extraction friction force exerted by the stationary part avoids the tissue from moving to the left, together with the upper moving part, on the very low friction bearing. 64
3.2 a) Optical microscope pictures of micro-structured strips made from SU-8 photoresist: fin-like and triangular teeth, tooth dimensions ranging from 500 to 10 µm; b) Detailed SEM pictures of the micro-structured strips [Schneider et al., 2008a]. 65
3.3 *Left:* a SEM picture of the needle core, with the grooves for the insertion of the strips; *Right:* SU-8 strips with $500\mu m$ fin-like structures inserted and glued to the MSTL core needle – for size comparison, tip of a ball pen on the right side 65
3.4 Experimental set-up with smooth needle. 66

3.5 Force Profile: different phases for a typical experiment with three cycles (50 µm Triangular Teeth). D: Tissue Deformation; I: Insertion; R: Reversing; E: Extraction. Black Arrow points to the instant when the surface is pierced. 67
3.6 Force profile: first cycle for 5 different needles - smooth needle (Smooth), 10 µm topography (10TF), 50 µm triangular teeth (50T), 50 µm fin-like teeth (50F) and 100 µm fin-like teeth (100F) 68
3.7 250 µm fin-like teeth needle. Evident brain tissue lodged between the teeth (black arrow). 69
3.8 Force profile: 2nd and 3rd cycle average for 5 different needles. 69
3.9 A selection of the microtextured samples with (from left to right): 500 µm, 100 µm and 50 µm teeth and the Smooth sample, including both triangular ("T") and fin-like ("F") geometries. 73
3.10 Experimental rig setup including two stepper motors (a) and corresponding electronics (b), a CompactRIO controller (c), reciprocating mechanism (d), low-friction air bearing with optical encoder (e) and control laptop running LabView v. 8.5 (f). 75
3.11 Charts illustrating the traversing capabilities of the different microtextured samples in 6 wt.% gelatine (top) and 0.5 wt.% agarose. Limitations of the experimental setup can justify the anomalies shown in the displacement profile for the 500 and 100 µm samples, where no clear difference in the behaviour of the fin-like teeth and the triangular teeth was found. 78
3.12 Tissue damage measurements via optical profilometry. a) 3D topography of a 0.5 wt. % agar gel, note that the profile left by the 500F sample may not be exactly orthogonal to the agar gel surface, and this may have caused a bias of the localised forces towards the left; b) corresponding depth map, c) topography of a 6 wt. % gelatine sample. 80

4.1 a) Flexible probe prototype cross-section (Ø= 12 mm, length = 200 mm) composed of four interlocked segments. Two functional channels are included: one for medical procedures (e.g. localised drug delivery), the other houses an electro-magnetic tracking sensor required to control probe position and orientation [Frasson et al., 2010a]. b) An example of a planar curvilinear trajectory in gelatine. 88
4.2 Diagram of the flexible multi-part probe in three different bending configurations. The inset shows an example of probe cross-section, in order to illustrate how the probe segments are interlocked together. . 89
4.3 Alpha prototype. a) 3D view with material labels; b) Cross-section . 92

4.4 Alpha prototype attached to the actuation box 94
4.5 Experimental setup for prototype testing 95
4.6 Diagram of the resistive forces acting on the flexible multi-part probe when one probe segment (black) is protruded in respect of others (grey). 96
4.7 Flexible probe trajectories for different steering offset values. Each picture corresponds to the last frame of the video records 98
4.8 Fitted trajectories. a) Best fit circles for each tested steering offset; b) Enlarged view of the trajectories achieved for offsets between -30 mm and 30 mm. (Only a selection of results is shown) 98
4.9 Relationship between offset and curvature with linear fit. 100
4.10 Probe buckling inside a compliant medium. At a certain instant t_0 the flexible probe has achieved a particular trajectory inside the medium; at the next instant t_1, because of the tissue resistive forces acting on the probe's body, the inserting force causes the middle of the probe to buckle, while the tip does not move forward. A "reciprocal motion" insertion strategy is believed to reduce the buckling effect. 101
4.11 Modified experimental setup for the second testing protocol of "reciprocal motion". 103
4.12 Image analysis method for the second testing protocol of "reciprocal motion". 103
4.13 Probe contours during the "reciprocal motion" test (left) and "direct push" test (right). The probe contour is captured every 30 secs. The probe contours at the very beginning of the tests (first minute) are not shown. 104
4.14 Probe contours of the "direct push" and "reciprocal motion" new tests; the contours are overlaid onto the initial (start) and final (end) original frame images. 105
4.15 Example of a double curve trajectory achieved in gelatine. The probe prototype used for this experiment has a more rigid tip (VeroWhite, Section 4.4.2), but this is not affecting the results. 107
4.16 Example of failure: one segment separates from the others during an experiment performed in gelatine 109

5.1 Schematic of the simplified model 114
5.2 Local instabilities that the probe may experience 115
5.3 Diagrammatic of the numerical model devised for the FE simulations 115

5.4 a) Simplified probe cross-section. b) The part of the cross-section which constitutes the FE model of the interlocking mechanism (dotted square). The geometrical parameters used to define the cross-section are *N*, *R1*, *R2* and *W*; the clearance between the segments is 0.05 mm. c) Diagrammatic of the numerical model devised for the FE simulations. 117
5.5 Horizontal and vertical limits for possible parameter combinations. Upper limit from Equation 5.1: *H*=2.50 mm; minimum horizontal distance from sidewalls *dH*=0.10 mm. Upper limit from Equation 5.2: *V*=1.50 mm; minimum distance from working channel *dV*=0.22 mm. . 118
5.6 Extraction force versus vertical displacement profiles for simulations with different friction coefficients between contact surfaces (from 0 to 1.2, typical of polymer-polymer contact). The geometrical parameters of the model used for this simulation are: *N*=0.7, *R1*=0.3, *R2*=0.25, *W*=0.2 mm. 119
5.7 Optimum search procedure. A Latin hypercube Sampling algorithm is followed by a Simulated Annealing algorithm. *N*, *R1*, *R2*, *W* are considered as inputs, extraction force as the output. 120
5.8 Example of CLHS algorithm for a two-parameter space (variables *R1* and *R2*, range 0.1-0.45). In blue the starting LHS combinations, in green the permuted LHS combinations, the red line represents the inequality constraint $R1 + R2 \leq 0.75$. 121
5.9 Experimental test of the interlocking mechanism. The male and female samples are firmly glued to steel plates. The top plate, attached to a 100 N load cell (2525-807 Series Drop-through), is moved vertically at a constant speed (0.5 mm/s). 124
5.10 a) RP molds for the male (left) and female (right) samples; b) the silicone-rubber samples extracted from the molds (paper grid dimensions of 5x5 mm). 124
5.11 Undeformed and deformed cross-sectional optimal geometry 126
5.12 Undeformed and deformed cross-sectional geometry of the alpha prototype 126
5.13 Vertical extraction force profile versus vertical displacement for the optimal interlock geometry and the interlock geometry of the alpha probe prototype as obtained from the 2D simulations (force expressed per unit length due to plane strain assumption). 127
5.14 Vertical extraction force profile versus vertical displacement of the 3D FE simulation and of an experimental test. The dotted line represents possible quality deterioration of numerical results due to computational limitations. 128

6.1 Schematic of the model devised for the analysis of probe axial behaviour under a load P, which is resting on elastic foundations (which represents the cross-sectional interlock stiffness). 133
6.2 Linear interpolation of the average interlock stiffness of the optimal geometry ("Optimum geom") and the geometry of the alpha prototype ("Current geom"), for the full cross-section (extraction force values are double those in Figure 5.13). The intercept is set to 0-0. The coefficient of the linear interpolation represents the foundation modulus k_f. 136
6.3 Beam deflection for the three scenarios envisioned in Table 6.1. Hinged ends are assumed as boundary conditions. 137
6.4 Non-linear elastic foundation function $f_{nl}(y(x))$ (red dotted line). Interlock stiffness, as calculated from the 2D cross-sectional model (blue line). Diagrammatics of the 4 interlock configurations in correspondence of the main sections of the non-linear elastic foundation function are shown at the bottom. The original interlock stiffness when male and female parts are in contact is approximated with a 4^{th}order polynomial. 138
6.5 Interior and exterior nodes of a beam of length l, used for the central finite difference scheme. A deflected beam is shown in red as an example, to illustrate how two different boundary conditions (hinged end to the left, fixed end to the right) are implemented in the finite difference scheme (see Table 6.2). 140
6.6 Beam deflection in four different cases. *Top-left:* Euler's buckling of a hinged beam; *top-right:* Euler's buckling of a fixed beam; *bottom-left:* buckling of a beam on linear elastic foundations characterised by a $k_f = 0.079$ (corresponding to the linearised interlock stiffness of the cross-sectional geometry of the alpha prototype); *bottom-right:* buckling of a beam on linear elastic foundations characterised by a $k_f = 0.123$ (corresponding to the linearised interlock stiffness of the optimal cross-sectional geometry). 144
6.7 Beam deflection in correspondence of the critical buckling load for the optimal interlock geometry (top) and the geometry of the alpha prototype (bottom). Both hinged and fixed end conditions are illustrated. The green lines represent the interlock clearance (second "interlock configuration" in Figure 6.4): ± 0.05 mm for the optimal interlock and ± 0.073 mm for the interlock of the alpha prototype. The red line represents the interlock disengagement limit. 146

7.1 Beta probe prototype. a) 3D view with material labels. b) Cross-section at sections AA and BB, with relevant quotes (in mm). c) Transparent 3D view of the probe's back: note the bent shape of the channel for the EM sensor (or Drug Delivery). 150
7.2 Pre-bent probe segment: projected views. 152
7.3 New RP flexible probe prototype. a) Four segments, two of which are pre-bent and have a more rigid tip. b) Segment assembly, all segments are aligned and the probe is straight; tip's probe in the inset, where the more rigid tip of one of the segments is visible. c) Segment assembly, one of the pre-bent segments is projected forward to show its tendency to bend. 153
7.4 Flexible probe trajectory achieved through a "direct push" insertion strategy, with an offset of 10 mm 154
7.5 "Direct push" and "reciprocal motion" trajectories (thick lines) projected onto the best-fit plane and corresponding circles of best fit. Note that each trajectory is plotted with respect to its central position, thus the x-y axes do not correspond to the original EM reference system. 155
7.6 "Direct push" and "reciprocal motion" trajectories (thick lines) projected onto the best-fit plane and corresponding circles of best fit, zoomed view 155
7.7 Relationship between offset and curvature for "direct push" and "reciprocal motion" experiments. A linear fit for the two sets of experiments is also identified. 157
7.8 Mean off-plane absolute error and error standard deviation for "direct push" (blue) and "reciprocal motion" experiments (red). 158
7.9 Examples of off-plane error for a "direct push" (+12 mm steering offset) experiment (top) and for a "reciprocal motion" (+5 mm steering offset) experiment (bottom). Note that, in this case, the "reciprocal motion" experiment was shorter than the "direct push" experiment. . 159
7.10 ROBOCAST system view. The GP robot is holding the FP robot, which is holding the trocar where the flexible probe is inserted. The actuator box, which is sitting on GP Axis-4, transmits the actuation via the "Flexible Transmission Link" to the flexible probe. 161
7.11 ROBOCAST system, zoomed view. The EM tracking system is used to provide position and orientation (5DOF) of the EM sensor inserted at the tip of the flexible probe 162

7.12 a) FP robot and trocar assembly. b) Trocar with 4 optical markers. c) Detail of the trocar cap, the teflon tubes, the inner cables and the EM sensor. 163
7.13 Flexible probe segment provided with a liquid delivery system. 163
7.14 Interface between actuator box and GP axis-4 side plate. 1) Interface dismounted. 2) Interface mounted. 163

A.1 First rigid probe prototype (material used: "Accura 60", [3DSystems-Inc., 2009]). a) single segment cross section; b) 4-part probe cross-section, the clearance between segments is 0.2 mm; c) assembly of non-aligned probe segments; c) picture of the prototype 185
A.2 Pictures of the actuation RIG: the multi-part probe is held by the four rubber wheels, each pressed against the core of one segment. 4 lead-screws (see black handles) are used to independently adjust the later forces pressing against the probe segments. 186
A.3 First flexible probe prototype. a) Cross-section with relevant measurements (in mm). b) Sketch of the inner tube (yellow) used to interlocked the segments (black). c) RP inner tube. d) RP single segment. e) RP assembled probe (please note that the probe is 80 mm long and 12 mm in OD). 188
A.4 a) Cross-section of an intermediate prototype, characterised by a central inner core, with circular symmetry and a clearance gap of 0.1 mm; b) Picture of rigid RP sample; c) Picture of flexible RP sample (TangoBlack). This prototype, even though overall unsatisfactory, demonstrated that an arrow-shape interlock between the lateral segments and the inner core was indeed effective, and therefore maintained in following prototypes. However, the 0.1 mm clearance was found to be too tight for the flexible prototype. 189
A.5 Precursor of the alpha flexible probe prototype. a) Cross-section with relevant measurements (in mm); b) Picture of the flexible probe (the white handles, glued to the probe surface, were used for manual probe insertion into gelatine). 190
A.6 Single probe segment inserted into gelatine. The high flexibility of the material is confirmed by the small radius of curvature assumed by the segment. 190

B.1 a) Proposed 4-segment cross-section with relevant dimensions in mm. b)Real segment cross-section with relevant dimensions in mm. This design takes into account material shrinking which happens after extrusion; the central channel, for example, it is not circular but elliptical. c) Picture of the cross-section of an assembled probe. 192
B.2 a) Silicone probe segments with rigid coupling and custom made trocar. b) Assembled silicone probe segments. Each segment is connected to a transmission cable. c) Silicone probe assembly partially inserted into the trocar. Inset: trocar cross-section to house the rigid couplings. d) Actuation system for silicone probe prototype. 192
B.3 a) Silicone probe curvilinear shape achieved in gelatine. b) Silicone probe segment irreversible separation during insertion process. c) Picture of the failed probe. 193
C.1 "Reciprocal motion" actuation strategy for a simplified two-part probe. The grey line corresponds to the displacement of Segment I (top graph) and its Velocity profile (bottom graph). The black line corresponds to Segment III. V is the maximum stroke velocity, A the stroke amplitude and O the desired steering offset. 195
C.2 Three possible probe configurations. a) Probe at rest. b) Probe in unacceptable configuration; Segment I and III are both separately protruding further than any other segment. c) Probe in acceptable configuration. 196
C.3 "Reciprocal motion" actuation strategy for a four-part probe. The grey line corresponds to the displacement of Segment I (top graph) and its Velocity profile (bottom graph). The black line, the dot-dashed line and the dashed line correspond to Segment III, II and IV respectively. Black arrows point at instants when passive segments do not need to be actuated. 197
D.1 ROBOCAST System at a glance. A 6-axis serial gross positioning robot (1) is used to support a miniature parallel robot (2) holding the biomimetic steerable probe (3) to be introduced through a keyhole opening in the skull of the patient; an electromagnetic tracking system (4) is used to control position and orientation of the steerable probe tip, while an optical tracking system (5) monitors robot and patient positions; operative images are visualised on a screen (6) and a central station (7) is in charge of the supervision of the system [Robocast-Project, 2010]. 199

D.2 Block diagram of the system architecture. The high level controller takes into consideration pre-operative images (e.g. MRI, CT) and probe constraints (e.g. maximum radius of curvature) to define a minimum risk path inside the brain, which will then be used by the low level controller to generate appropriate motion signals to drive the probe towards the target. A position sensor (e.g. electromagnetic tracker) will provide tip position feedback. 200
D.3 Overall software configuration for feedback control 201

List of Tables

2.1 Biological features in ovipositing wasp and corresponding performance achievements 59

3.1 Biological features in ovipositing wasp and corresponding features for a flexible and steerable probe. 62
3.2 Peak force values (gf: gram force); maximum standard deviation not greater than ±2.16 gf (Insertion Peak Force of the 10TF needle, 2nd and 3rd cycle). 70
3.3 Binary results summary, including the type of sample/tissue interaction observed ("S" for sliding, "ED" for elastic deformation, "H" for hooking and "PD" for plastic deformation and/or cutting. An "x" in column 5 represents complete failure, while Young's modulus estimates were obtained from [Samur et al., 2005, Woo et al., 1980, Miller and Chinzei, 1997, Jamani et al., 1989, Craig and Peyton, 1960]. . . . 77
3.4 Distance traveled (mm) and gripping ratio (Distance Traveled/Stroke) with a stroke of 8.84 mm for 0.5 wt.% Agarose. 79

4.1 Steering Offset vs. Curvature and Steering Radius 99
4.2 Ratio of Expansion Area: "direct push" vs. "reciprocal motion" . . . 105

5.1 Maximum and minimum values of the geometrical parameters 122
5.2 Maximum and minimum values of the geometrical parameters for the SA algorithm, and initial parameter combination (best LHS solution) 123
5.3 Geometrical parameters of the optimum solution, peak extraction force values of optimum and current geometry. 127
5.4 Mean and standard deviation of peak extraction force from experiments; peak force from FE simulation and corresponding percent difference. 128

6.1 Beam buckling: effect of elastic foundation (beam with hinged ends) 136
6.2 Finite difference boundary conditions for a beam with hinged or fixed ends 140

6.3 Theoretical critical buckling load compared to the critical buckling load as obtained from the proposed algorithm. 143
6.4 Critical buckling load for a beam resting on non-linear foundations, as derived from the stiffness of the alpha prototype interlock geometry and from the stiffness of the optimised interlock geometry. 145

7.1 Steering Offset vs. Curvature and Steering Radius 156

D.1 Original Specifications and Deviations 202

Abbreviations

MI	Minimally Invasive
CAS	Computer Assisted Surgery
MRI	Magnetic Resonance Imaging
DBS	Deep Brain Stimulation
CT	Computer Tomography
CSF	Cerebrospinal Fluid
DOF	Degree of Freedom
OD	Outer Diameter
3D	Three Dimensional
STFC	Science and Technology Facility Council
RAL	Rutherford Appleton Laboratory
UV	Ultraviolet
MSTL	Microstereolithography
RP	Rapid Prototyping
CAD	Computer Aided Design
SMA	Shape Memory Alloy
EM	Electro-Magnetic
GUI	Graphical User Interface
2D	Two Dimensional
FE	Finite Element

LHS	Latin Hypercube Sampling
SA	Simulated Annealing
CLHS	constrained LHS
GP	Gross Positioning
FG	Fine Positioning
ID	Inner Diameter
ICT	Information and Communication Technologies
RMS	Root Mean Square

Chapter 1

Introduction

"What is now proved was once imagined" - W. Blake

1.1 Introduction

The brain is one of the most delicate, probably the most important and the most mysterious organ in the body. Despite the homogeneous appearance of cerebral tissue, brain functions are highly organised in an extremely complex network which controls all physical and cognitive human behaviour. And while imaging technology and our understanding of brain pathology, physiology and function have improved dramatically in recent years, few technological breakthroughs have affected the intra-operative instrumentation used in minimally invasive (MI) neurosurgery on a broad scale. Conventional rigid instruments limit entry paths to follow a straight line trajectory. This drastically reduces the planning choices that a surgeon is able to make to maximise safety during the medical procedure when, for example, the insertion path of a needle or a rigid instrument intersects neural tracts, blood vessels or critical brain areas. The introduction of Computer Assisted Surgery (CAS) systems in neurosurgical procedures represents a clear effort to improve safety and accuracy of MI techniques. "Shared control" and "telesurgical" robotic systems [Nathoo et al., 2005], for example, address safety and accuracy of MI neurosurgical procedures by coupling image guidance with the scaling and dexterity-enhancing properties of surgical robotics. However, their effectiveness is limited by the predominantly passive nature of their function and by limitations inherent in conventional instruments.

Nature suggests a very elegant solution to the problem of accessing deep targets in soft tissue, through curved trajectories, with thin and flexible probes and while reducing tissue damage. Indeed the ovipositor structure and function of certain parasitic wasps [Quicke et al., 1994, 1999] has inspired a novel device - a flexible and steerable probe, called STING (Soft Tissue Intervention and Neurosurgical Guide)

- coupled with a novel strategy for accurately accessing curvilinear trajectories in soft tissue using minimally invasive methods.

This chapter introduces the motivation and objectives of the research presented in this thesis, followed by an outline of the overall structure of the thesis.

1.2 Medical motivation

The current trend in medical intervention favours less invasive approaches with a tendency towards localized therapies. Percutaneous insertion of needles and probes are common procedures employed in modern clinical practice for a vast amount of applications: blood/fluid sampling, tissue biopsy, catheter insertion, cryogenic ablation, electrolytic ablation, brachytherapy, localized chemotherapy, localized drug delivery, deep brain stimulation (DBS) electrode implantation, confocal laser scanning microscopy and a number of other MI surgical procedures. Two main kinds of instruments are used in percutaneous intervention: thick rigid probes and thin flexible needles. Thick and rigid probes can be pointed to the target with the aid of a visualization system (e.g. ultrasound), but their manipulation causes significant pressure on the tissue. Conversely, thin and flexible needles tend to be less damaging to the surrounding tissue, but deflect and buckle against tissue resistance. Additionally, both thick and thin probes are generally unsuitable for following curved paths, for instance if obstacle avoidance is required.

Brain biopsy is the most significant example for illustrating the main challenges in MI brain interventions. Brain biopsy is a diagnostic procedure that involves the collection of a small quantity of "undefined" (benign or malign) tissue from a specified region (usually a lesion) of the brain. In the conventional technique a thin straight metal cannula is inserted through a small hole in the skull of the patient. Once the target area has been identified on pre-operative image data (e.g. Computer Tomography or Magnetic Resonance Imaging), the entry point, the position and the orientation of the cannula are defined through the use of a stereotactic frame or of a neuronavigation system (e.g. VectorVision™, [Brainlab-Gmbh, 2010]). Three major risks of this MI technique are: non-diagnosis, hemorrhage and infection.

- Non-diagnosis can occur if the target area is missed or if the lesion cannot be adequately pinpointed.
- Hemorrhage is usually the result of erroneous planning (e.g. the straight path intersects a major blood supply) or poor technique (e.g. excessively fast or uneven insertion).
- Infection is a standard risk in any procedure that involves cutting of the skin.

The complexity and time requirements of brain biopsy can also escalate in those instances where the surgeon is forced to alter the entry point to give a straight-line trajectory due to the presence of obstacles (or "no-go areas") obstructing the ideal path. This limitation often results in a greater distance between entry and target points, with an increase in deflection amplitude and risk of tissue damage. Rigid biopsy needles also limit tissue sampling to the straight-line insertion path, requiring multiple insertions if suspicious adjacent locations need to be analysed.

The medical and technical challenges involved in brain biopsy can be extended to any diagnostic or therapeutic procedure which requires the insertion of an instrument into soft tissue. Therefore, there is a clear need for the development of novel, active, "smart instrumentation" that will:

- enable surgeons to target lesions deep within the body both safely and accurately, by allowing them to chose a desired curvilinear trajectory and a desired entry point
- improve patients' care, through technology that may facilitate the treatment of previously inoperable conditions
- benefit healthcare providers by reducing surgical complications, hospitalisation time and costs.

In addition to improvements to current medical procedures involving percutaneous interventions (i.e. penetration of a soft tissue), research upon a novel "smart instrumentation" could potentially lead to the introduction of new medical procedures, both for diagnosis and interventions, which currently do not exist due to limitations in instrumentation.

1.3 Aim and objectives

The aim of the study presented in this thesis is:

to prove the viability of a novel, biologically-inspired, probe steering mechanism as demonstrated by a fully functional prototype capable of curvilinear motion on a plane within a compliant medium of brain-like tissue consistency.

Research presented herein has resulted in the following objectives being met:

- understand the medical need and the technical challenges in soft tissue surgery
- understand and conceptualise the key features of the principle of ovipositing wasps. These constitute the inspiration for the development of a novel steerable instrument for percutaneous interventions

- establish the foundations for a biologically inspired flexible and steerable probe
- provide a concept-demonstrator for the flexible steerable probe, based on the key assumptions identified
- design a flexible and steerable probe prototype and actuation system
- analyse and optimise the prototype design and performance using numerical and mathematical models, experimentally validated
- develop and test probe prototype and actuation system
- integrate flexible probe prototype system into a robotic system for next-generation neurosurgical procedures

Although previous research has been conducted on the topic of flexible needle steering into soft tissue (refer to chapter 2), the research described in this thesis presents a novel method of achieving curvilinear trajectories into soft tissue with an innovative, probe design and actuation mechanism.

The research presented in this thesis was conducted by the author in the Mechatronics in Medicine Laboratory, at Imperial College, London, between June 2007 and August 2010. It should be made clear here that a proportion of the work presented in Chapter 4 was done in conjunction with my fellow researcher S.Y. Ko, who was responsible for the manufacturing of the final flexible probe actuator. The work presented in Chapter 3 was done in collaboration with my fellow researcher T. Parittotokkaporn, who has mainly focused on testing sample preparation and experiment implementation. The integration of the flexible probe prototype into a robotic neurosurgical suite, described in Chapter 7, was done in conjunction with my fellow researcher S.Y Ko and in collaboration with other project partners. A detailed breakdown of the work done by the author, as opposed to other researchers in the group, is included in the introduction of, respectively, Chapter 3, Chapter 4 and Chapter 7.

1.4 Outline of the thesis

The remainder of this thesis is organised as specified hereafter:

Chapter 2 reviews three aspects relevant to the research topic. Firstly the medical background is reported: brain anatomy, function and pathology are introduced. A brief description of common surgical procedures for brain interventions and the state of the art of neurosurgical instrumentation used in clinics, with a focus on brain biopsy, will follow. Secondly a review of the main research around flexible

needle steering for percutaneous interventions is provided, pointing out current solutions and corresponding limitations. Finally, a detailed analysis of the biological source of inspiration for the development of the novel flexible and steerable probe will follow. The most interesting aspects related to oviposition by Hymenoptera wasps will be described: the ovipositor structure, the ovipositing mechanism and the steering strategy for targeting specific areas in the substrate.

Chapter 3 covers the foundations of the research on a biologically inspired flexible and steerable probe for soft tissue penetration. The advantageous mechanism of tissue penetration as shown by ovipositing wasps is replicated in a simplified fashion, in two different sets of experiments, with the aim of demonstrating the feasibility of forward tissue penetration with "zero net force". On the basis of the results presented and discussed, conclusions and suggestions for the development of a fully-working, functional, steerable probe prototype are provided.

Chapter 4 describes the evolution of the concept for the biologically inspired flexible and steerable probe into a concept demonstrator able to prove multiple planar curvilinear trajectories with varying radii in a compliant medium (STING). Three main hypotheses underlying the proposed concept are identified:

- probe steerability along curvilinear trajectories with different radii
- probe steerability along curvilinear trajectories with reduced risk of buckling
- probe steerability along multiple curve trajectories.

The hypotheses are demonstrated through the use of a probe prototype built in a flexible rubber-like material and composed of interlocked segments able to slide with respect to each other. Discussion of the technical problems encountered are presented, and conclusions of the concept viability drawn.

Chapter 5 centres upon the optimisation of the probe design, with a focus on one of the most critical features: the interlocking mechanism between the segments. The interlocking mechanism is indeed a crucial feature in ensuring that the probe segments slide reciprocally, but at the same time do not separate. A model of the probe's cross-section is devised, and an optimisation procedure is applied to identify the best interlock geometry, in terms of resistance to failure (i.e. irreversible segment separation). The model is also validated experimentally. Finally, conclusions concerning the development of an optimised prototype are drawn.

Chapter 6 describes the preliminary approach towards the development of a 3D model of the flexible probe, with a focus on how the interlocking mechanism affects probe segment irreversible separation when the segment is driven by an axial push. While limited in scope, this study forms the basis for the extension of an initial simplified analytical and numerical approach to probe behaviour modelling towards

the understanding and modelling of all the complex interactions which occur during the actuation of a multi-part flexible and steerable probe. Starting from the buckling analysis of a beam resting on non-linear elastic foundations, a method to formulate a link between probe failure conditions (i.e. probe segment buckling) and actuation strategies is proposed and discussed.

Chapter 7 presents the design of a new flexible probe prototype, the cross-sectional geometry of which was modified having taken into account the results from the optimisation procedure described in Chapter 5. Results about the steerability performance of the new prototype in a compliant medium are then discussed. Finally this chapter concludes with a description of the integration of the flexible probe prototype within a neurosurgical robotic suite (EU FP7 ROBOCAST).

Chapter 8 concludes with an overview of the research presented in this thesis on the topic of flexible probe steering for percutaneous intervention. A summary of the salient contributions of this research is presented and suggestions for future research on several aspects regarding flexible probe steering are proposed.

1.5 Publication output

Parts of this research work have been accepted and published in journal papers or conference proceedings, and a patent has been filed. Publication details and main content are listed hereafter:

Journal Publications

- L. Frasson, S. Y. Ko, A. Turner, T. Parittotokkaporn, B. L. Davies, J. F. Vincent, and F. Rodriguezy Baena, "STING: a soft-tissue intervention and neurosurgical guide to access deep brain lesions through curved trajectories", Proceedings of the Institution of Mechanical Engineers. Part H, Journal of engineering in medicine, 224(6):775-788, 2010.
  Overview of the STING project. The author led on the analysis of the biomimetic foundations for the development of a novel method of soft tissue penetration along curvilinear trajectories by means of a flexible probe and on providing a system overview concerning also the integration of the flexible probe in a robotic neurosurgical suite (Chapters 3, 4, 7). In addition, preliminary approaches to control and path planning strategies are described.

- L. Frasson, T. Parittotokkaporn, B. L. Davies, and F. Rodriguez y Baena, "Early Developments of a Novel Smart Actuator Inspired by Nature", Int. J. Intelligent Systems Technologies and Applications, vol. 8, pp. 409-422, 2010.
  This article, led by the author in collaboration with a colleague, summarises

the work done on demonstrating the feasibility of a biologically-inspired penetration mechanism for a multi-part probe, which does not require a "push from the back" actuation (Chapter 3).

- A. Schneider, L. Frasson, T. Parittotokkaporn, F. M. Rodriguez y Baena, B. L. Davies, and S. E. Huq, "Biomimetic microtexturing for neurosurgical probe surfaces to influence tribological characteristics during tissue penetration", Microelectronic Engineering, vol. 86, pp. 1515-1517, 2009.
  This article, led by collaborators expert in micro-manufacturing methods, focuses on the micro-manufacturing techniques deployed to create anisotropic surface textures to be added to novel neurosurgical probes. Such surface textures are inspired by the ovipositor tip features as shown by ovipositing wasp, and influence probe-tissue interaction during tissue penetration. As described in Chapter 3 the author was involved with providing design specifications and performing experimental tests of probe insertion in biological tissues.

- S. Y. Ko, L. Frasson and F. Rodriguezy Baena, " Closed-loop planar motion control of a steerable probe with a programmable bevel inspired by nature.", Submitted to IEEE Transactions on Robotics (T-RO), 2010.
  This paper describes the flexible and steerable probe prototype, its steering strategy and mechanism, the closed-loop control required to maintain such novel steerable probe on a predefined curvilinear path and the experimental results concerning control performance. As evident from Chapter 4, the author was involved with the prototype development and with the definition and experimental test of the steering strategy, but not with the definition and implementation of the control strategy.

Conference Contributions

- L. Frasson, J. Neubert, S. Reina, M. Oldfield, B. L. Davies, F. Rodriguez y Baena, "Development and Validation of a Numerical Model for Cross-section Optimization of a Multi-Part Probe for Soft Tissue Intervention", in 32nd Annual International Conference of the IEEE Engineering in Medicine and Biology Society, pp. 3202-3205, 2010.
  This article, entirely led by the author, consists of the description of the finite element model and the optimisation algorithm used to optimise the cross-sectional design of the interlocking mechanism of the flexible probe prototype (Chapter 5).

- L. Frasson, S. Reina, B. L. Davies, and F. M. Rodriguez y Baena, "Design Optimization of a Biologically Inspired Multi-Part Probe for Soft Tissue Surgery",

in 11th International Congress of the IUPESM, Medical Physics and Biomedical Engineering Munich, Germany, pp. 307–310, 2009.
This article, entirely led by the author, introduces a parametric method for modeling the design of the flexible probe prototype and aimed at performing design optimisations (Chapter 5).

- L. Frasson, T. Parittotokkaporn, B. L. Davies, and F. Rodriguez y Baena, "Early Developments of a Novel Smart Actuator Inspired by Nature", in 15th International Conference on Mechatronics and Machine Vision in Practice, pp. 163-168, 2008.
  This article resulted in the journal publication already described above (Chapter 3).

- L. Frasson, T. Parittotokkaporn, A. Schneider, B. L. Davies, J. F. V. Vincent, S. E. Huq, P. Degenaar, and F. M. R. Baena, "Biologically inspired microtexturing: Investigation into the surface topography of next-generation neurosurgical probes", in 30th Annual International Conference of the IEEE Engineering in Medicine and Biology Society, pp. 5611-5614, 2008.
  This article, led by the author in collaboration with a fellow colleague, focuses on the characterisation of the interaction between a rigid probe with various kinds of anisotropic surface textures and porcine brain tissue, with regard to insertion and extraction forces (Chapter 3).

- T. Parittotokkaporn, L. Frasson, A. Schneider, S. E. Huq, B. L. Davies, P. Degenaar, J. Biesenack, and F. M. Rodriguez y Baena, "Soft tissue traversal with zero net force: Feasibility study of a biologically inspired design based on reciprocal motion", in ROBIO 2008, IEEE International Conference on Robotics and Biomimetics, pp. 80-85, 2009.
  This article, written in collaboration with a fellow colleague, proves the viability of soft tissue traversal with zero net force, as demonstrated by a biologically inspired reciprocal motion of toothed samples (Chapter 3).

- T. Parittotokkaporn, L. Frasson, A. Schneider, B. L. Davies, P. Degenaar, and F. M. R. Baena, "Insertion Experiments of a Biologically Inspired Microtextured and Multi-Part Probe Based on Reciprocal Motion", in 32nd Annual International Conference of the IEEE Engineering in Medicine and Biology Society, pp. 3190-3193, 2010.
  Based on the preliminary results published in the previous two articles and presented in Chapter 3, this article demonstrates a zero-net force soft-tissue penetration mechanism for a multi-part probe provided with anisotropic surface textures. The author was involved with the design and development of

the multi-part probe and of the experimental setup.

- S.Y. Ko, L. Frasson, B.L. Davies, F. Rodriguez y Baena, "Software & Hardware Integration of a Biomimetic Flexible Probe within the ROBOCAST Neurosurgical Robotic Suite", The Hamlyn Symposium on Medical Robotics, pp. 5-6, 25 May 2010, London, UK.
  This article describes the flexible probe integration within a neurosurgical robotic suite. The author was mainly concerned with the design of the mechanical interfaces between the flexible probe system and the other robots, as described in Chapter 7.

Patent

- F. M. Rodriguez y Baena, L. Frasson, and J. F. Vincent. Steerable probes, Patent filed on 30 November 2009, Application Number 0920938.8.
  The patent covers the design and functioning of the flexible multi-part probe, taking into account various possible modifications to both design and functioning. Various applications, not solely medical, are suggested.

Chapter 2

Literature Review

This chapter focuses on three aspects relevant to the research topic. Firstly, the medical background is reported: brain anatomy, function and pathology are introduced. A brief description of common surgical procedures for brain interventions and the state of the art of neurosurgical instrumentation used in clinics, with a focus on brain biopsy, will follow. Secondly, a review of the main research around flexible needle steering for percutaneous interventions is provided, pointing out current solutions and corresponding limitations. Finally, a detailed analysis of the biological source of inspiration for the development of the novel flexible and steerable probe will follow. The most interesting aspects related to oviposition by Hymenoptera wasps will be described: the ovipositor structure, the ovipositing mechanism and the steering strategy for targeting specific areas in the substrate.

2.1 Medical background

2.1.1 Brain anatomy, function and pathology

The human brain controls the *central nervous system*, by way of the cranial nerves and spinal cord, the *peripheral nervous system* and it regulates virtually all human activities, both involuntary and voluntary. Anatomically, the brain is located inside the skull. The human skull is a complex flat bone (thickness varies from 4 to 12 mm) which protects the brain; it is completely covered by the scalp, a skin layer of 5 to 7 mm. The base of the skull is irregular and contains a ridge, a large window for the spinal cord (magnum) and small holes for arteries, veins and nerves. The brain is then covered by the meninges, which are composed of three layers: the outer layer is a tough and thick fibrous tissue called the *dura mater*, the middle layer is the *arachnoid mater* which allows the attachment of the dura mater with the delicate innermost membrane, the *pia mater*, in touch with the brain and the spinal cord. The space between the arachnoid mater and the pia mater is occupied by the

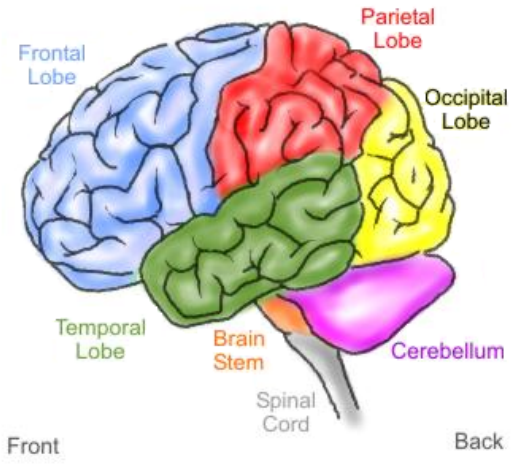


Figure 2.1: Regions of the human brain

cerebrospinal fluid (CSF), which acts as a buffer for the cortex providing mechanical and immunological protection to the brain inside the skull. The brain parenchyma is composed of white and grey matter, blood vessels, and ventricles (cavity filled with the cerebrospinal fluid). The grey matter (the outer layer of the cerebral cortex) mainly consists of neuronal cells and neuroglia cells. The white matter (subcortical regions) consists of myelinated neurons and it is surrounded by supporting cells.

It is possible to physically distinguish several regions in the cerebral cortex (see Figure 2.1); some cerebral regions are more directly responsible for certain functions, for example, the *prefrontal cortex*, in the frontal lobe, is responsible for planning, emotion and judgment, the *visual cortex*, in the occipital lobe, is responsible for primary visual perception and the *primary somatosensory cortex*, in the parietal lobe, for processing sensory information.

Although all brain areas are extremely important for human health and life, it is possible to differentiate them in terms of the corresponding neural function in healthy subjects and the severity of dysfunctions related to the potential local damage. For example, while a trauma to the brainstem can easily trigger a coma condition, a trauma to the memory area in the temporal lobe will most probably cause a transient memory deficit.

There is a vast variety of pathological conditions related to the brain: trauma, tumors, infections, congenital diseases (e.g. Down syndrome), functional diseases (e.g. epilepsy), neurodegenerative diseases (e.g. Parkinson's disease), mental disorders. These brain disorders can be addressed through either surgical or pharmacological treatments.

2.1.2 Brain interventions: diagnosis and treatment

A detailed description of all medical conditions and interventions related to the brain is outside the scope of this thesis, nevertheless, a brief description of brain tumors will follow. This pathology is selected as the most relevant and representative example for the research herein presented, because both its diagnosis and treatment could benefit from the use of a flexible and steerable probe.

Brain tumor is an abnormal growth of cells within the brain. Brain tumors can be benign or malign (cancer) and can be located anywhere in the brain, causing generally an increase of intracranial pressure and consequently headaches, nausea and altered state of consciousness. Depending on the tumor location and the damage caused to the surrounding brain structures, different types of neurologic symptoms may arise (e.g. cognitive and behavioural impairment, personality changes, hemiparesis, visual field impairment, tremor, etc).

Given the large variety of brain tumors, diagnosis is not easy. Non invasive medical imaging methods such as computer tomography (CT) and especially magnetic resonance imaging (MRI) are used to obtain initial information about the tumor (location, size, appearance, boundaries, etc). However, the definitive diagnosis can only be confirmed by histological examination of tumor tissue samples obtained either by means of brain biopsy or open skull surgery. Brain biopsy is preferred to open skull surgery because of its limited invasiveness. A long and thin instrument is used to access the suspicious brain region through a small cylindrical aperture in the skull (usually < 1 cm in diameter) [Hall, 1998]. This technique is defined as "keyhole neurosurgery" [Perneczky, 1999].

The principal treatment for single brain tumors is surgical removal, generally performed during open skull interventions. In the case of multiple metastatic tumors, radiotherapy and chemotherapy treatments are selected. Drug delivery is often used to treat brain cancers with the aim of reducing tumor proliferation, in different ways [Blakeley, 2008]: systemic delivery (intravenous or oral), intra-arterial delivery, implanted therapies (drug-capsulated wafers that diffuse chemotherapy agent over time are implanted in the tumor resection cavity, [Guerin, 2004]), infusion into CSF cavities and convection-enhanced delivery (infusional catheters implanted through keyhole neurosurgery in the tumor site, [Raghavan et al., 2006]).

Within all current clinical diagnostic methods and treatments for brain tumors, MI keyhole neurosurgery for brain biopsy (diagnosis) and convection-enhanced delivery (treatment) are the ones which could, at present, benefit from the introduction of the flexible and steerable probe presented in this thesis. However, the capability of safely reaching any brain area with a MI approach exploiting a steerable probe, could potentially boost further clinical developments, allowing the use of MI tech-

niques for already existing but invasive techniques or for novel techniques.

2.1.3 Instrumentation for MI keyhole neurosurgery

Stereotactic brain biopsy is chosen as an example for illustrating a typical keyhole neurosurgical procedure and the instrumentation required.

Stereotactic surgery involves mapping the brain in the stereotactic space (3D coordinate system) with the aid of MRI and/or Computer Tomography (CT) scans, in order to accurately localise the target area (e.g. the suspicious brain area in case of tumor biopsy). An external frame, attached to the patient's skull (see Figure 2.2a), allows accurate positioning and orientation of the needle used to perform the medical procedures (i.e. biopsy, DBS electrode implantation, drug delivery). The stereotactic frame uses guide bars fitted with high precision vernier scales, orientated according to a set of three coordinates (Cartesian or polar) to position the needle along the linear trajectory of insertion. In correspondence of the entry point, the surgeon opens a hole in the skull (keyhole) and exposes the brain by removing the external membrane (dura mater). The surgeon manually inserts the needle into the brain, along the predefined trajectory to a depth corresponding to the the location of the target.

A standard needle for brain biopsy is shown in Figure 2.2b. It is a disposable, single use, stainless steel needle, 2.11 mm in diameter, composed of an outer and an inner cannula. The outer cannula is provided with a window which faces brain tissue (Figure 2.2c). When the window is open, the tissue penetrates into the outer cannula aperture and can be sampled thanks to the inner cannula. This operation is generally performed more than once by turning the aperture towards different sides of the brain tissue, but without modifying the needle position. It should be noted that the tip of the needle is blunt, in order to avoid vessel puncture and therefore preventing internal hemorrhage.

Neuronavigation systems are an alternative to stereotactic frames. Neuronavigator arms are passive intraoperative position-sensing systems. The six-dimensional coordinates (three components of translation, three components of rotation) of a surgical tool attached to the neuronavigation arm, are obtained from position sensors (e.g. encoders, potentiometers, etc) and can be registered with some preoperative three-dimensional medical images using anatomic landmarks or fiducials, with the aim of displaying in real time and with high accuracy the location of the surgical tool on preoperative images [Schiffbauer, 1999]. Armless neuronavigation systems based on optical tracking of the surgical tool (e.g. VectorVision™ [Brainlab-Gmbh, 2010]) are currently more used for their ease of use.

In an attempt to improve the safety and accuracy of MI neurosurgical proce-

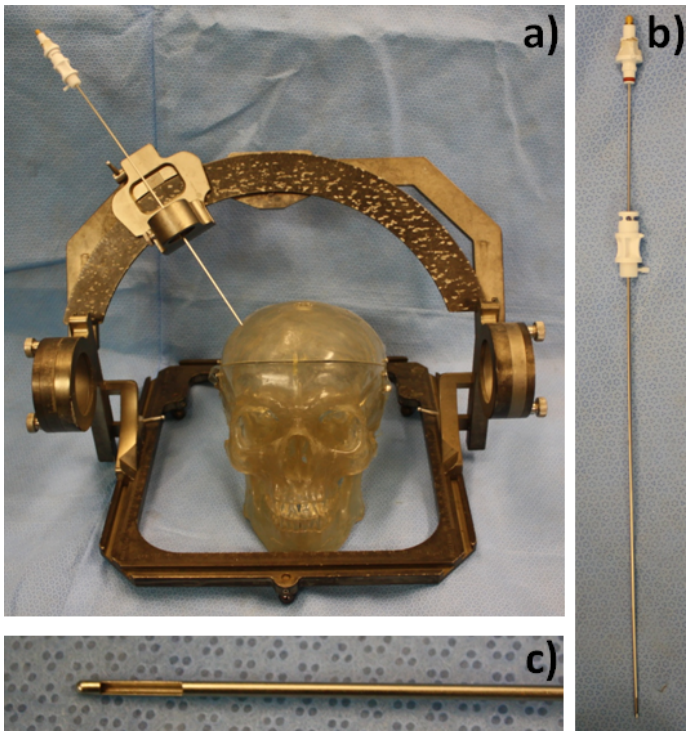


Figure 2.2: a) Stereotactic frame for brain biopsy (Leksell Sterotactic System); b) Brain biopsy needle, the inner cannula is partially inserted in the outer cannula; c) Detail of the window in the outer cannula

dures, "shared control" systems and "telesurgical systems" also exist [Nathoo et al., 2005]. Shared control robotic systems are used to place instrument holders according to a plan, allowing the surgeon to direct conventional instrumentation along the path defined by the robot. Shared control systems have been used successfully in stereotactic procedures, but also in pedicle screw insertion (e.g., the bone mounted mini-robot in Shoham et al. [2003]) and in servo-assisted insertion of conventional endoscopic instrumentation (e.g. Evolution 1 [Zimmermann et al., 2004]). Telesurgical robotic manipulators are used to perform microsurgery and stereotaxy procedures benefiting from intraoperative image-guided computer-assisted systems. The most advanced and complete example of a telesurgical robotic systems for neurosurgery is NeuroArm [NeuroArm, 2010]. NeuroArm is a MRI-compatible image-guided computer-assisted systems, equipped with a high-definition microscope and a force sensor system to provide haptic feedback to the surgeon sitting at the control-workstation [Louw et al., 2004]. NeuroArm has been proved to perform as well and as accurately as conventional microsurgical techniques for tumor resections, with demonstrated safety technology [Pandya et al., 2009]. Another robotic system, NeuroMate, was used to perform stereotactic procedures in a frameless mode, specifically for deep brain stimulator implantation in keyhole interventions [Varma and Eldridge, 2006] and it is currently commercialised and worldwide distributed by Renishaw [NeuroMate, 2010].

However, stereotactic frames, neuronavigation systems and more recent "shared control systems", are mainly used to orient and position conventional straight and rigid instruments (i.e. biopsy needle) before their insertion into the brain.

Our understanding of brain is continuously deepening; imaging technologies are allowing more accurate diagnosis of brain pathologies or dysfunctions; more effective chemotherapy agents are being synthesised; new localised radiotherapy procedures are being coupled with systemic drug delivery; keyhole neurosurgical procedures are put on trial for previously intractable pathologies, such as DBS electrode implantation for epilepsy or severe depression. However, few technological breakthroughs have affected the intra-operative instrumentation used in MI neurosurgery. The majority of the instruments which actually penetrate brain tissue are rigid stainless steel needles. As such they limit the entry paths to straight line trajectories and they limit the number of locations accessible through a single insertion.

These limitations are driving different streams of research on the development of flexible needles able to be actively steered into soft tissue, along curvilinear trajectories. A literature review of these research streams will follow in the next section.

2.2 Percutaneous interventions: accessing curvilinear trajectories

The ability to steer the tip of a flexible tool (a catheter, a needle or a probe), following a curvilinear trajectory of insertion, constitutes a great advantage in MI interventions. Surgical probes for MI access can be broadly categorised into two main groups: endoluminal vs. percutaneous probes. Endoluminal probes (such as endoscopes and endovascular catheters) exploit natural orifices and accessible vessels within the body to direct a tool (e.g. optical fiber, tissue sampler, etc.) to the target. Their use has proved very successful in a few key specialities, such as gastrointestinal surgery, endovascular aneurysm repair and, in the case of brain tumor diagnosis, endoscopy through the nostrils.

Percutaneous (i.e. through the skin) instruments are widely used across the full spectrum of "invasive intervention" as they are highly versatile with regard to the entry point and access route to a chosen soft tissue target. Current procedures which involve percutaneous insertion of needles and catheters range from blood/fluid sampling, tissue biopsy, catheter insertion, tissue ablation and brachytherapy to deep brain stimulation and diagnostic imaging, with new approaches appearing in the literature at an ever increasing rate.

Current percutaneous instruments can be classified into two main groups: thick and rigid probes (e.g. laparoscopes) vs. thin and flexible needles (e.g. biopsy or

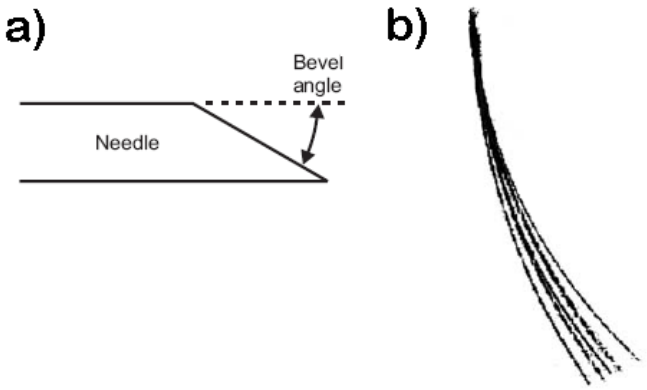


Figure 2.3: a) Definition of the bevel tip angle; b) The final needle locations, extracted from difference images, with different bevel angles illustrate the steering effect of the bevel tip. A 5^o bevel exhibits the most bending while an 80^o bevel the least [Webster et al., 2005].

brachytherapy needles). Thick and rigid probes have the advantage that they can be pointed to the target with the aid of a visualization system (e.g. ultrasound) and will not deform under load. Their manipulation, however, causes significant pressure on the tissue, which limits the surgeon's degree of freedom. Conversely, thin and flexible probes tend to be less damaging to the surrounding tissue, but deflect and buckle against tissue resistance, resulting in loss of placement accuracy, which is inversely proportional to the depth of the target. Additionally, both groups suffer from the same underlying technological and functional limitation: they cannot be guided along curvilinear trajectories. This is a fundamental drawback of percutaneous probes, which limits their application to surgical procedures where a straight line approach is viable.

The problem of deflection of a thin needle during soft tissue penetration [Kataoka et al., 2001] can be advantageously utilised if the deflection could be monitored and controlled, in order to drive the needle along a predefined curvilinear "deflection" trajectory. This concept is at the basis of the approach identified by two research groups which aim to solve the needle steering challenge. Their work, together with a third different approach will be outlined in the next sections.

2.2.1 Steering via bevel-tip flexible needle

Webster et al. [2005] have shown that, as a flexible needle with a bevel tip is pushed through soft tissue, the asymmetry of the tip itself causes the needle to bend along a curved trajectory with a single radius, depending on the bevel angle (Figure 2.3a) [Webster, 2007, Alterovitz et al., 2005].

The needle used by Webster et al. [2005] is a 0.83 mm diameter solid Nitinol cylinder (simulating a 21 gauge needle) with a smooth surface and a hand machined

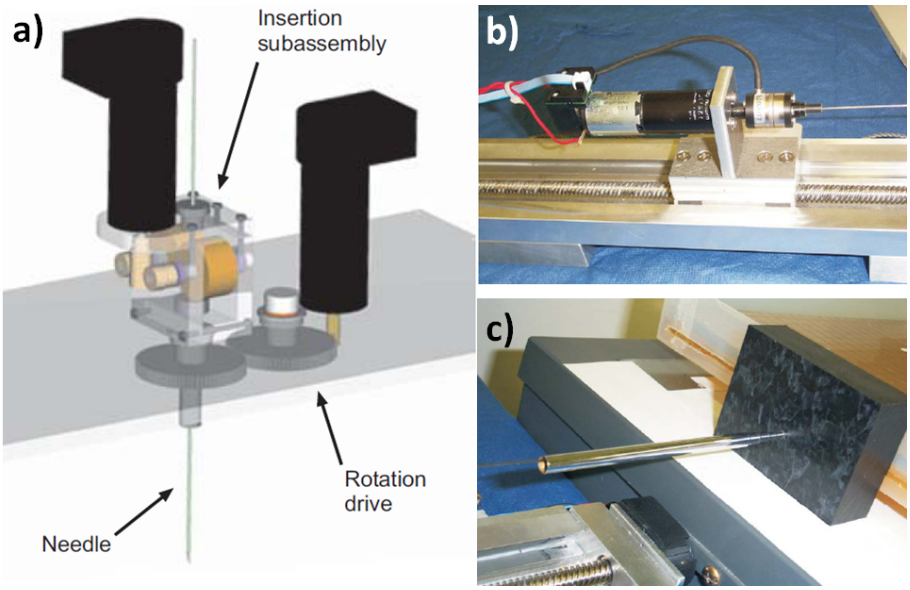


Figure 2.4: a) CAD model of the friction-drive needle-insertion mechanism proposed for flexible needle steering, in yellow, the rubber wheels; b) Needle rotation mechanism; c) Close view of the telescoping support sheath, shown in a compressed view to expose the needle (on the right) [Webster, 2007].

bevel tip. In order to insert the flexible needle into a soft tissue, avoiding **buckling**, two different solutions are tested: in the first device the flexible needle is grasped by two opposing rubber wheels in a position close to the tissue entry point, with the aim of reducing the unsupported needle length outside the tissue and then pushed exploiting a friction drive mechanism (Figure 2.4a); the second solution concerns the use of a telescoping support device as a support sheath (Figure 2.4c). Different needle curvatures depending on different bevel angles are shown in Figure 2.3b.

However, for a given needle-tissue pair, only a single curvature is achievable. The needle tip geometry, the needle stiffness and the tissue stiffness univocally determine the radius of curvature of the path of flexible needle insertion [Wedlick and Okamura, 2009].

A multiple curve planar trajectory can be obtained by orienting the bevel tip at different angles during insertion. Orienting the bevel tip is achieved by rotating by 180° the base of the needle (Figure 2.4b). This needle base rotation is inverting the concavity of the curvilinear trajectory. An algorithm is used to compensate the torsion effect on the needle shaft when the base of the needle is rotated [Reed et al., 2008b].

Wedlick and Okamura [2009] demonstrated that flexible needles, pre-bent or pre-curved near the tip, possess greater dexterity than simple bevel tip needles and can therefore achieve smaller radii of curvature. However, reorientation of the bevel tip by a 180° rotation could result in severe tissue disruption, limiting the complexity of curved trajectories achievable, as well as the range of target tissues for which this

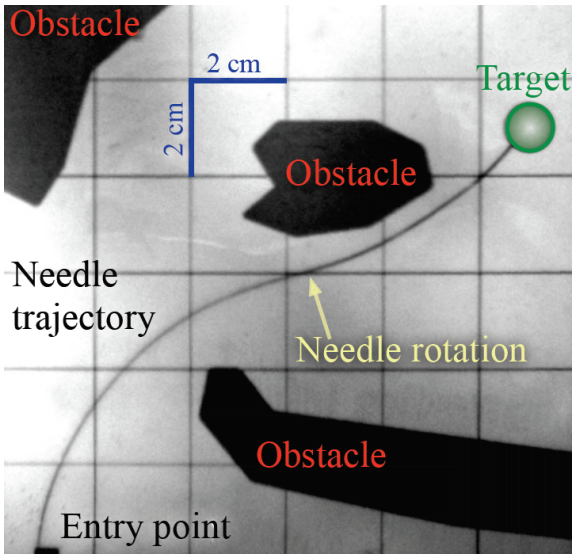


Figure 2.5: An example path of a flexible steerable needle. The needle is rotated 180^oat its base in order to flip the bevel orientation thus reversing the concavity of the curvature. The needle avoids the obstacles and reaches the target [Reed et al., 2008a]

approach would be viable.

Bevel-tip needle steering relies on open-loop trajectory controls, based on a kinematic model of the needle, coupled with a needle-tissue interaction model. Needle-tissue interaction is indeed studied and modeled, with the aim of understanding how the forces acting at the needle-tissue interface determine needle deflection [Misra et al., 2008, 2009]. A nonhonolomic kinematic model based on steering due to bevel tip asymmetry is used to predict the needle path [Webster et al., 2006] and several trajectory planning algorithms are proposed accordingly [Alterovitz et al., 2005, Duindam et al., 2008, Jijie et al., 2008, Reed et al., 2008a]. A closed-loop control, developed to take into account uncertainty during curvilinear planar insertion, is presented by Reed et al. [2008a]. The control strategy relies on a position estimator based on stereo camera images: an "on-off" controller switches between "bevel-right" and "bevel-left" in order to reorient the bevel tip respectively from left to right and viceversa.

An example path of a double curve trajectory for the flexible needle is shown in Figure 2.5, where obstacles are avoided in order to reach the desired target.

Majewicz et al. [2010] performed flexible needle steering in *ex vivo* tissue (goat liver). In contrast to studies in artificial tissue, different bevel tip angles did not produce different insertion curvatures, due to inhomogeneity and viscoelasticity of the biological tissue. Majewicz et al. [2010] also demonstrated three potential clinical applications of needle steering in *ex vivo* tissue simulations: ablation, biopsy and brachytherapy. Because of the small flexible needle diameter (from 0.38 to

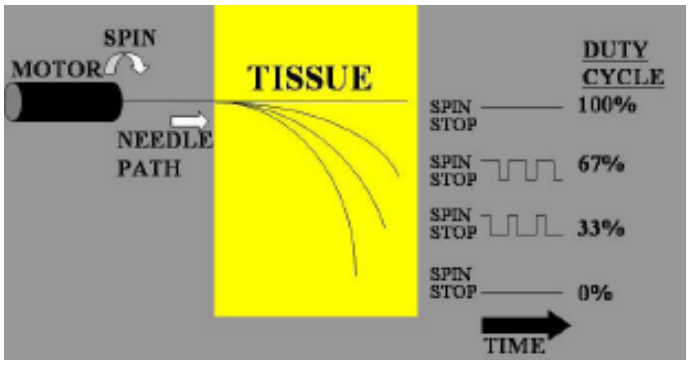


Figure 2.6: By "duty-cycling" the rotation of the needle base, different curved trajectories are achieved inside the tissue phantom [Engh et al., 2006a]

0.74 mm outer diameter OD), however, the flexible needle is simply used as a guide wire. In the ablation technique, a catheter ablator is passed over the flexible needle. Alternatively, a teflon sheath is passed over the needle and, after needle removal, used to introduce standard biopsy and brachytherapy needles along the trajectory previously identified by the flexible needle.

Building on the bevel-tip concept, it was shown that a control strategy to alter the trajectory of the bevel tip during insertion is possible [Minhas et al., 2007, Engh et al., 2006b]. Proportional control of the curvature of the trajectory was achieved via duty-cycled spinning the base of the needle itself, where the approach angle of the needle can be controlled through a cyclical rotation along the longitudinal axis (Figure 2.6). A 100% base-rotation duty cycle produces a straight trajectory, while a 0% base-rotation duty cycle produces the trajectory with maximum curvature.

The needle used for the experiments was a custom built prototype, consisting of a 1.27 mm diameter stainless steel needle tip attached to a 0.28 mm diameter nitinol wire. The tip had a bevel tip angle of 10° and was bent an additional 15° at a distance of 6.3 mm from the end of the tip [Minhas et al., 2007]. In order to test needle steering by means of duty-cycled rotation in human cadaver brain tissue (softer than artificial tissue), the cross-sectional area of the tip was increased, with respect to the needle shaft (nitinol wire), by using a needle tip with bigger diameter (2.1 mm) [Minhas et al., 2009]. The experiments were performed under C-arm fluoroscopy in order to identify and correct the position of the needle tip. A nonlinear control law was developed to drive the needle to track a predetermined curvilinear planar path [Wood et al., 2010].

The main shortcoming of the bevel-tip approach to needle steering pertains to limitations in the cross-sectional diameter of the needle, which is inherent to the steering mechanism itself. Since trajectory control is achieved through duty cycling or 180° tip flipping, the material which the needle is made of needs to be sufficiently stiff to enable the transmission of a torque along the entire length of the needle

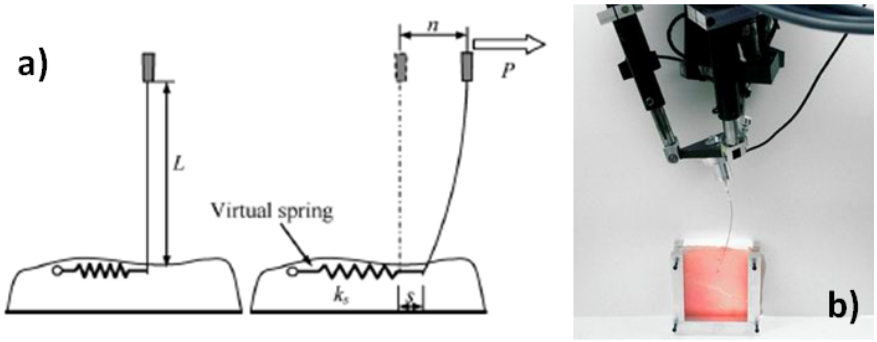


Figure 2.7: a) Virtual spring model and needle bending; b) 6-DOF parallel robot inserting a flexible needle in soft tissue following a curved trajectory[Glozman and Shoham, 2007]

(which explains the choice of a nitinol stranded wire), while the diameter should be small enough for the needle to be flexible and thus able to bend. Given the contrasting requirements of a stiff structure coupled with the need for a highly flexible needle, such limitation on the maximum outer diameter cannot be exceeded under any circumstance, and it restricts the number of possible clinical applications.

Furthermore, considering the relatively large size of the needle tip used in the duty-cycled rotation technique, a drilling effect is expected, with possible severe tissue damage.

2.2.2 Steering via needle bending

Needle steering and motion planning based on needle-base manipulation was first developed for haptic needle insertion simulations [DiMaio and Salcudean, 2002, 2005a]. The same authors DiMaio and Salcudean [2005b] defined a "needle manipulation Jacobian", using numerical needle insertion models that include needle deflection and soft tissue deformation, to demonstrate needle tip placement and obstacle avoidance.

A similar approach to needle steering was proposed by Glozman and Shoham [2007], where a standard rigid needle (0.711 mm in diameter) is steered along a curved trajectory inside soft tissue (turkey breast muscle) by applying a moment at its base (Figure 2.7a), thanks to a 6 DOF parallel robot equipped with a 6 DOF force sensor holding the needle (Figure 2.6b). The needle is stiff relative to the tissue and steering is accomplished by the deformation of the tissue itself. The insertion trajectory is planned by modelling tissue and needle interaction and deformation using a simplified spring approach [Glozman and Shoham, 2007, 2004].

The targeting performance for this approach relies upon tissue stiffness and resistance, and therefore the range of applicable soft materials where such control strategy can be used is limited. The application of this approach on soft and delicate tissues such as brain would result in severe tissue tear. In addition, steering

capabilities deteriorate with needle insertion depth.

2.2.3 Steering via active cannulas

The third and final approach to needle steering is based on "Active Cannulas". They are combined, pre-curved, concentric tubes, which can be axially extended and rotated with respect to each other to control the tip position and orientation thanks to the elastic interaction between the tubes themselves. The main difference with regard to the previous two approaches is that active cannulas do not require a tissue medium in order to steer, but this does not preclude their use as steerable needles, if a suitable cannula-tissue interaction model is applied [Webster, 2007].

Active cannulas can be classified as continuum robots (infinite degree-of-freedom robots characterised by flexible backbones, as opposed to hyperredundant robots, where the backbone consists of a finite number of short rigid links). According to Webster [2007], active cannulas show greater dexterity with respect to size, if compared to other snake-like robot architectures and, because bending forces are created within the backbone structure itself, and not via external mechanisms (i.e. wires, or pneumatic actuators), their miniaturisation is more viable.

Okazawa et al. [2005] firstly developed the Hand-Held Steerable Needle Device, which exploits the bending behaviour of a preloaded cannula (a slightly modified off-the-shelf biopsy needle) sliding in a more rigid stylet, thus controlling the curvature of the bending by changing the length of the cannula projecting from the stylet.

Currently, three different research groups have been working on concentric tube robots with very similar outcomes: Osaka University [Terayama et al., 2007, Furusho et al., 2008], Boston University [Dupont et al., 2010, Sears and Dupont, 2006] and The John Hopkins University [Webster et al., 2009, Lyons et al., 2010, Webster, 2007].

The active cannula of Webster et al. [2009], composed of concentric, precurved, elastic tubes is shown in Figure 2.8. By modelling the kinematic and dynamic properties of these nested segments, accurate tip motion control in three-dimensions has been demonstrated [Lyons et al., 2010]. Burdette et al. [2010] have integrated a two segment active cannula with an Ultrasonic Interstitial Thermal Therapy probe, performing multiple thermal ablation in *ex-vivo* bovine liver. With a single penetration, by retracting and pushing only one of the nested tubes, three tissue locations were ablated, while being monitored by 3D ultrasound.

While this approach poses a relatively simpler control problem, as the tube segments and their interaction can be modeled using beam theory, the range of available trajectories achievable with any one needle embodiment is highly limited. Since each pre-curved tube has a "fixed" geometry and radius of curvature, a trajectory with

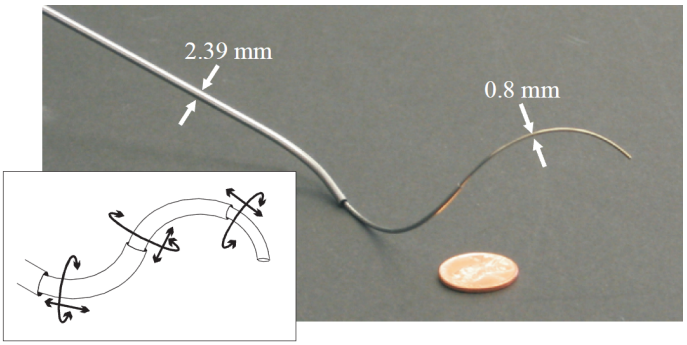


Figure 2.8: A prototype active cannula made of super-elastic Nitinol tubes. The inset line drawing indicated degrees of freedom. External diameter dimensions of the two tubes comprising the cannula are also shown.[Webster et al., 2009]

variable curvature is impossible by design. In addition, the number of curves in the path is irreversibly tied to the number of segments (e.g. 3 concentric tubes can only produce a curved path with 2 constant radius curves), which limits the range of applications for which the probe would be suitable.

Furthermore, each tube configuration is a function of the relative position and orientation of the various nested tubes and, because of the tube segment interaction, the intermediate tube configurations may be significantly different from the final multiple-curve configuration. This may result in excessive tissue deformation when the active cannula is steered into a very soft medium. In summary while it is possible to direct the tip along a predefined curvilinear trajectory, with the concentric tube concept, the body of the cannula will not comply to the surrounding tissue and thus it may cause tearing during a complex curved insertion.

When we look at Nature through the example of ovipositing wasps, a novel approach to needle steering, which could address the limitations herein described, is suggested. Therefore a detailed overview of the biological inspiration is presented in the following section.

2.3 Biological inspiration from ovipositing wasps

Nature is often a good inspiration for demanding engineering tasks and the structure and function of biological systems can become the model for the design and the engineering of effective solutions to real-life problems. The aim of biomimetic engineering is finding biological examples which can be someway useful, taking the desirable features and abstracting them according to the required task.

The idea to develop a next-generation probe for soft tissue surgery, which is flexible, and can be safely steered inside the brain with minimum tissue damage, targeting precisely deep brain zones, originates from the biological example of ovipositing



Figure 2.9: Giant ichneumon wasp *Rhyssa persuasoria*. Adult boring the surface of trunk infested with wood wasp larvae. Image courtesy of Boris Hrasovec, Faculty of Forestry, Bugwood.org

wasps (Figure 2.9). Ovipositing wasps, and particularly the wood-boring wasp Sirex noctilio, have already constituted an useful inspiration for the development of a drill and sampler system for planetary subsurface sampling in low gravity environments, where standard penetration strategies have been proved ineffective [Gao et al., 2005, Menon et al., 2006].

A review about the ovipositor structure and function will follow, pointing out all the features which gave inspiration for the current research on flexible probe steering.

2.3.1 Oviposition strategy

Inside the Hymenoptera order, females typically have a special ovipositor for inserting eggs into hosts or otherwise inaccessible places. In case of parasitic families, the ovipositor is able to penetrate the host (generally larvae). Some parasitic wasps can paralyse the host injecting venom through the ovipositor, others can also hold the host thanks to particular sharp clips [Van Lenteren et al., 1998]. The ovipositor structure mostly depends on the location of the host: hosts concealed in wood require a longer ovipositor with efficient wood drilling capabilities, while for exposed hosts, a shorter ovipositor is sufficient. Other wasps reach weakly concealed or concealed hosts by threading their ovipositors through cracks in the substrate. Sometimes the whole wasp enters the substrate during oviposition [Quicke et al., 1999].

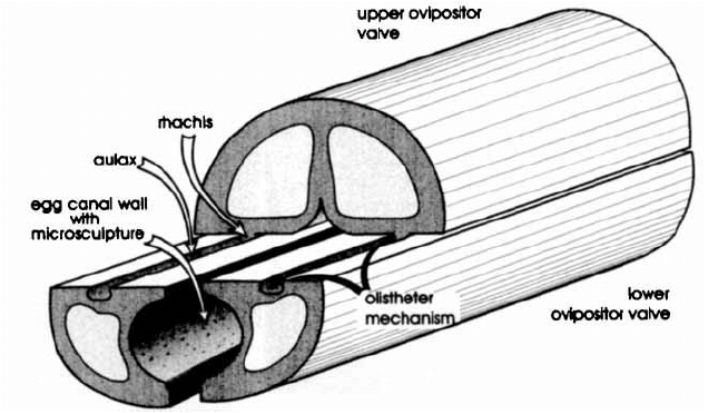


Figure 2.10: Diagrammatic representation of oblique view of transversely cut ovipositor with lower valves protruding [Quicke et al., 1995]

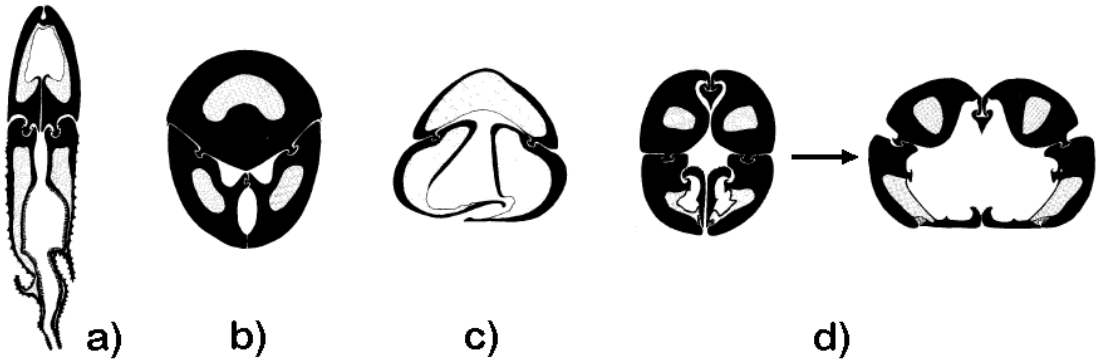


Figure 2.11: Diagrams of transverse sections through ovipositors of: a) *Xyelida* (Xyelidae); b) *Megalyra* (Megalyridae); c) *Monomachus* (Monomachidae); d) *Stethantyx* (Tersilochinae), section as seen in expanded state [Quicke et al., 1994]

2.3.2 Basic anatomy of the ovipositor

The ovipositor comprises of three parts: a single upper valve and a pair of lower valves which together form a hollow tube along the lumen through which eggs and/or venom can pass. The upper valve is interlocked with both of the lower valves by means of a dovetail joint; a longitudinal ridge (rachis) on the upper valve runs within a corresponding groove (aulax) on the lower valve. The combination of rachis and aulax is known as olistheter (Figure 2.10) [Quicke et al., 1999].

There are hundreds of different species of ovipositing wasp and all of them have a different ovipositor section: in Figure 2.11, a selection of 4 of them is chosen.

The ovipositor of *Xyelida* (Figure 2.11a) is laterally compressed (this is an adaptation for the placement of eggs in superficial plant tissue); this ovipositor also presents internal and external microsculpture whose function is probably to avoid the egg from moving backwards, during oviposition. In *Megalyra,* the interlocking mechanism between the lower valves creates an extra pair of channels which reduces

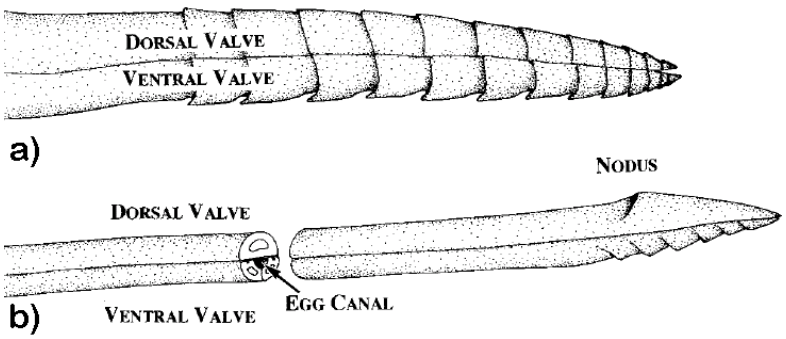


Figure 2.12: Diagrammatic figures of hymenopteran ovipositor. a) lateral view of tenthredinid ovipositor; b) lateral view of braconid ovipositor divided in the middle [Quicke et al., 1994]

the area of contact between the segments; this may results in reducing the friction between the sliding valves (Figure 2.11b). In *Monomachus,* the lower valves overlap widely ventrally, so that the ovipositor can partially unfold in order to allow the egg canal to enlarge during oviposition (Figure 2.11c). The complex interlocking mechanism of *Stethantyx*, shown in Figure 2.11d, seems to facilitate the expansion of the egg canal during oviposition [Quicke et al., 1994].

2.3.3 The ovipositor tip

In some Hymenopteras (Symphyta), the tip of both the upper (dorsal) and the lower (ventral) valve have a tooth-like surface involved in tearing the substrate or providing purchase during drilling (Figure 2.12a). However, in ichneumoids, only the lower valves have teeth; in most other groups, it is the upper valve which is serrated. Frequently, the apex of the ovipositor valve(s) without serrations is furnished with a single protuberance (nodus) or occasionally with a notch (Figure 2.12b). The notch seems to be a sort of articulation, as if the tip might be able to bend upwards, to facilitate the exit of the egg [Quicke et al., 1999].

Different tips reflect different ovipositing behaviours: a clear example refers to the two genera, *Encarsia* and *Eretmocerus*, both of which attack white-flies. *Encarsia* females use their ovipositor to penetrate the dorsal cuticle (the epidermis) of the white-fly nymph, while standing on it. Therefore, the tip of their ovipositor is sharp, spiky, and sturdy enough to cut through the host's cuticle. *Eretmocerus* females, instead, oviposit while standing beside their host and inserting their ovipositor between the abdomen of the host nymph and the leaf surface [Gerling et al., 1998].

The upper valve of the ovipositor of *Encarsia* (Figure 2.13) is furnished, at the apex, with a number of serrations; the distal teeth are disposed medially, while the proximal teeth alternate on the left and right sides, like the offset teeth of a saw.

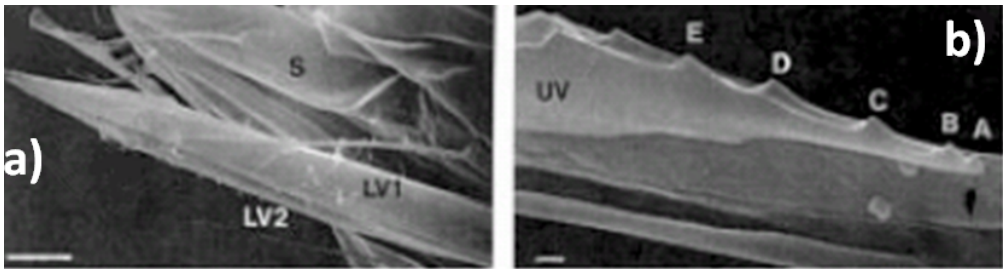


Figure 2.13: *Encarsia*: Scanning electron micrographs of external morphology. a) Ventral view showing left and right lower ovipositor valves (LV1 and LV2), ovipositor sheath (S). b) Apex of upper valve (UV) showing serrations (A-E), the distal pair are positioned medially (A,B) while posterior ones alternate on right (C,E) and left (D) side. Scale bars: a)=10μm; b)=1μm [Gerling et al., 1998]

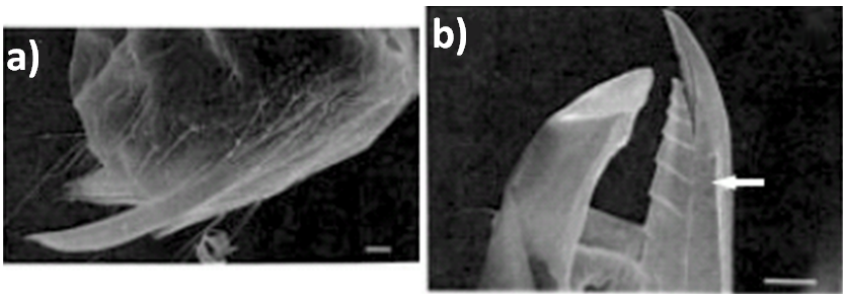


Figure 2.14: *Eritmocerus*: Scanning electron micrographs of external morphology. a) General view showing depth and upwards curvature of ovipositor; b) Angular crease (arrow) of lower valve and blunt apex of upper valve. Scale bars: a)=10μm; b)=5μm [Gerling et al., 1998]

The ovipositor of the *Eritmocerus* is more robust and up-curved (Figure 2.14) and the serrations do not appear to be offset and are much less pointed and sharp. This shape is adapted for sliding the ovipositor between the leaf surface and the host, while avoiding penetration or wounding of the latter [Gerling et al., 1998].

The *Orussus* spp. is a parasitic wasp which finds its host by tapping with the antennae on the surface of the wood. Once it targets the host, it penetrates the wood with the ovipositor shown in Figure 2.15. Formation of sawdust is not observed during oviposition of *Orussus* spp. This is probably due to the fact that the ovipositor penetrates the wood by displacing the fibers rather than shredding them. Like in other Hymenoptera wasps ovipositing in dense substrates, the ovipositor is circular in cross-section, probably in order to minimise surface area and therefore friction [Vilhelmsen et al., 2001].

The last two examples worth mentioning refer to the horn-tail sawfly *Sirex noctilio* and its ichneumonoid parasitoid *Megarhyssa nortoni nortoni*. The ovipositor of *S. noctilio* is relatively short and robust (**0.2-0.3 mm diameter, 10mm length**), that of *M. n. nortoni* is long and thin (**0.1-0.2 mm diameter, 50 mm length**), and flexible to a radius of 0.5 mm before breaking. Both of them drill holes in pine

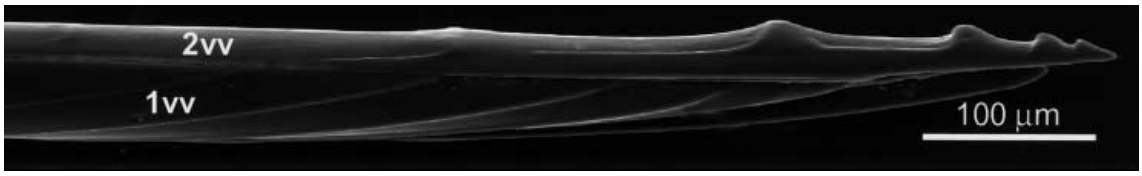


Figure 2.15: *Orussus abietinus* ovipositor tip; 1vv first valvula, 2vv second valvula [Vilhelmsen et al., 2001].

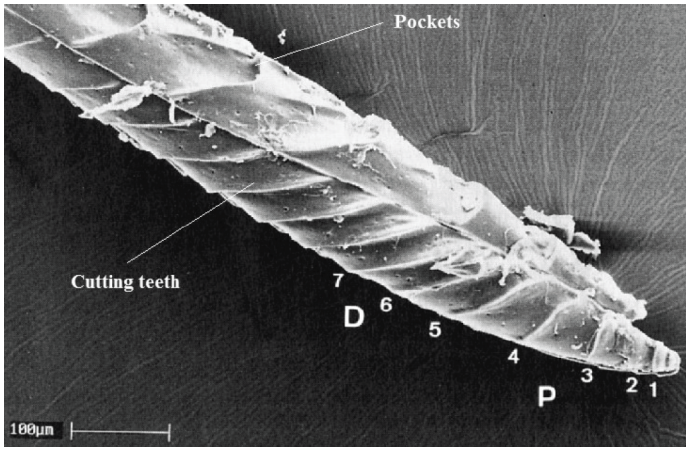


Figure 2.16: Tip of the ovipositor of *Sirex noctilio*. Teeth 1 to 4 (P) point proximal and are "pull teeth"; teeth 6 and 7 and higher (D) point distally and are "push teeth" [Vincent and King, 1995].

trees [Vincent and King, 1995].

In both these ovipositors, the teeth at the tip are disposed in such a way to facilitate tissue penetration. In *M. n. nortoni* all the teeth point proximally (Figure 2.17), to purchase grip during substrate penetration. In *S. noctilio* the first four teeth point proximally and are called pull-teeth (Figure 2.16, P), teeth 5 and 6 go through a short transition and then the other teeth (Figure 2.16, D) point distally (cutting or push-teeth). The pull-teeth are used to gain purchase during substrate penetration, and they cut only during the upstroke, while the cutting teeth are used to penetrate further into the tissue (the penetration strategy will be described in detail in Section 2.3.4).

Interestingly, the spacing between the teeth is quite similar to the diameter of the wood cells, and this may suggest that it would be possible for each tooth to "hit" a cell wall at the same time, increasing the effectiveness of substrate penetration.

In both ovipositors the teeth have significant amounts of Manganese and Zinc: the distribution of metals is closely allied to those regions which are subjected to the greatest abrasive wear and/or the highest loads; metal particles can increase the hardness of the flexible ovipositor teeth, improving the efficiency of hard tissue (wood) penetration.

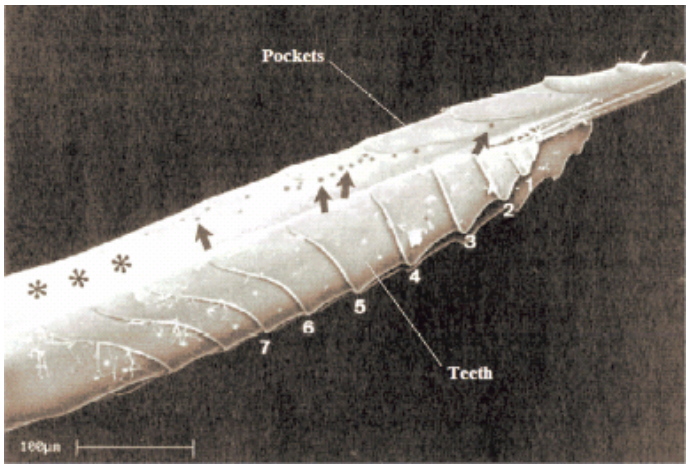


Figure 2.17: Tip of the ovipositor of M. n. nortoni. Teeth are numbered, all pointing proximally. Dark spots (arrows) are probably chemosensors, strain sensors occur in the area marked by the asterisks [Vincent and King, 1995].

2.3.4 Ovipositor penetration mechanism

The ovipositor valves are devoid of intrinsic musculature, and the mechanism of movement relies on musculature within the metasoma (the posterior part of the body) moving the valves relative to each other (Figure 2.18).

Vincent and King [1995] made interesting calculations and observations to give insight into the reasons underlying the capability of ovipositing wasps to make holes in substrates as demanding as wood, with a very thin and flexible ovipositor.

The long and thin ovipositor tends to buckle when the tip is pressed against the substrate by a force applied at its base. This is technically known as Euler buckling. The critical load (P_{crit}) at which the ovipositor will buckle elastically can be calculated from Euler's formula:

$$P_{crit} = \frac{\beta \pi^2 EI}{L^2} \tag{2.1}$$

where β is a constant related to the end condition (β=1 for a freely moving pin joint; $\beta = 2$ for a totally restricted joint at one end only; $\beta = 4$ for constraints at both ends, Figure 2.19), E is the Young's modulus, I is the second moment of cross-section and L is the unsupported length of the ovipositor.

A long and thin ovipositor will tend to deflect sideways, as any slightly off-centre loading causes it to buckle elastically. If the elastic limit is not exceeded no permanent damage will be caused. However, the forces available for penetrating the wood cells will be limited and the control of the penetration direction will also be significantly affected. Wasps face this problem in different ways: the ovipositor is inserted into the abdomen at the proximal end, and sometimes it is slided inside a grove with clips which lock the ovipositor straight into place, and this doubles the

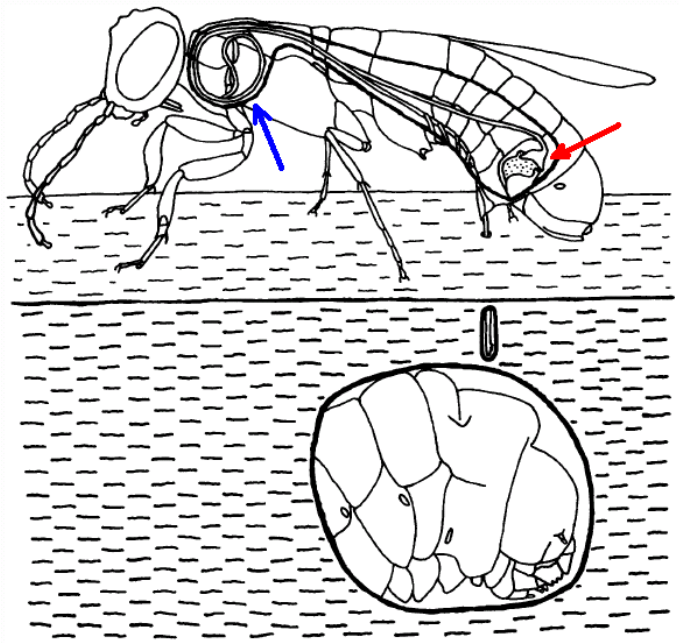


Figure 2.18: *Orussus* spp. female targeting a larva in the wood. The red arrow (right) shows the location of the ovipositor muscular system in the metasoma. The long and flexible ovipositor is concealed in the body and coiled in an S-shaped twist as indicated by the blue arrow (left). The black heavy line represents the section in the *Orussus* body and in the wood [Quicke et al., 1999, Vilhelmsen et al., 2001].

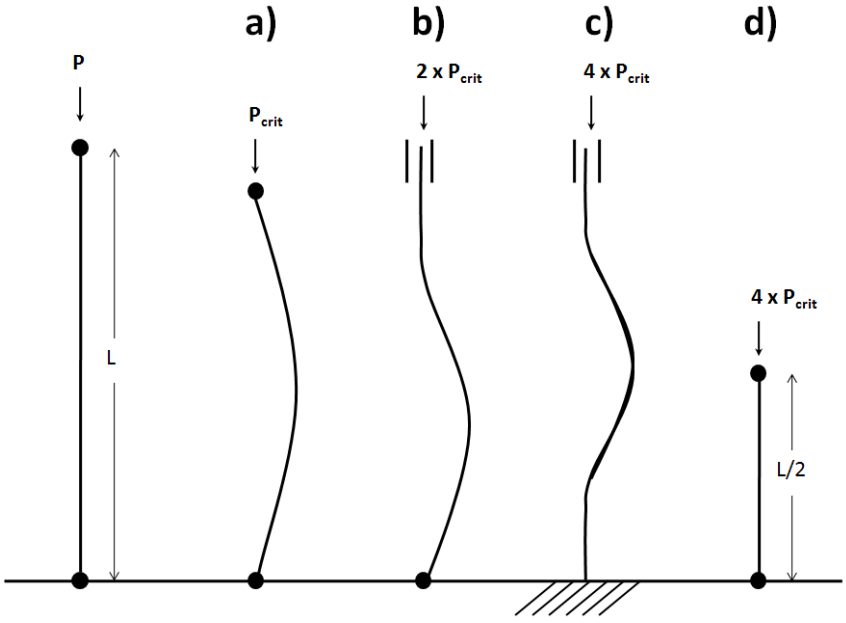


Figure 2.19: Strut of length L being loaded from above (P). The critical buckling load, P_{crit}, is affected by the end conditions and by the length L.

critical load (Figure 2.19b). In this way, the unsupported length of the ovipositor that it is under compression is also reduced, giving a four-times increase in critical load (Figure 2.19d). When the ovipositor penetrates the substrate, the distal end also becomes stabilised, which further doubles the critical load (Figure2.19c). The advantage of stabilising the tip of the ovipositor by drilling a narrow hole in the initial few millimeters gives an explanation to the particular ovipositor topography seen in Figure 2.16, where the first pull-teeth are anchored in the wood. The increase in the rate of drilling, for *Sirex noctilio*, from **1mm/min** to **1.5mm/min** after the initial stage suggests that the insect can exert a greater force when drilling in a deeper hole.

Vincent and King [1995] calculated the theoretical buckling load for the ovipositor structure of two different species, *S. noctilio* and *M. n. nortoni* and compared it to the experimental load required to buckle a dissected ovipositor structure with the same boundary conditions. The calculated loads were found to be 50% higher than those observed, and this was attributed to the structure being composed of two valves left free to slide against each other, thus reducing the bending resistance.

However, examining the mode of "drilling" for the *M. n. nortoni*, it was concluded that the force required to break the wood fibers is still 10 times in excess of the theoretical critical buckling load. This has been explained by the effect exerted by the alternate movements of the lower valves during drilling: the valve being retracted, being in tension, stabilising the opposite lower valve and upper valve being under compression (Figure 2.20). The tensile force can stabilise buckling and allow the development of greater end loads, though the extent to which this is significant is difficult to determine [Vincent and King, 1995]. Therefore, the reciprocal tension and compression of the two separate lower valves stabilises the ovipositor sufficiently for a significant end force to be generated without the ovipositor buckling.

2.3.5 Ovipositor steering mechanisms

Hymenopteran ovipositors have no intrinsic musculature and all of their movements have to result from the actions of muscles inside the abdomen, but in many species the tip can be guided independently, allowing it to play a more active part in host location. Some wasps can even locate particular structures within the prey, for example a ganglion [Quicke et al., 1999]. In other instances some species of wasps need to lay eggs in a number of separate, but adjacent locations and the ability to bend the ovipositor is a considerable advantage, because there is no need to withdraw the ovipositor and penetrate the substrate afresh.

The females of the braconid genus *Zaglyptogastra* are able to bend their ovipositor tips more than 180^o. The upper valve of the ovipositor is associated with the

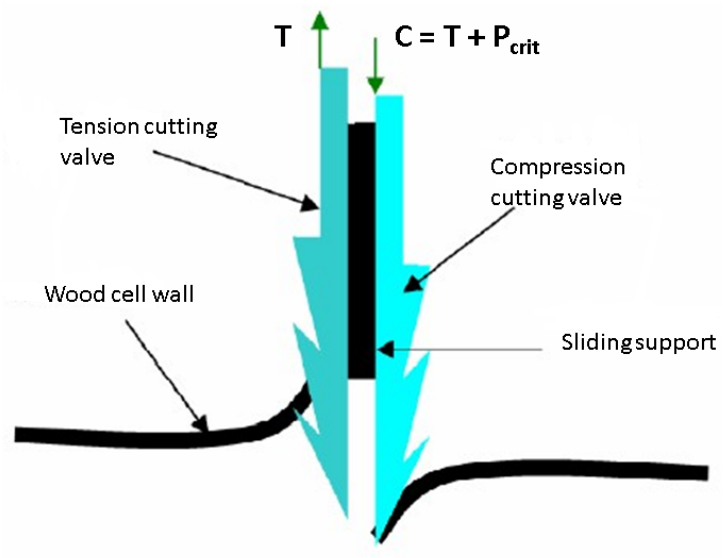


Figure 2.20: Two parts of ovipositor cutting into a wood cell. The left valve is pulling on a piece of wood cell with force T. The right valve can add this to the compressive force, limited by the critical Euler buckling load, giving a total force of penetration of $T + P_{crit}$ [Vincent and King, 1995]

ovipositor steering mechanism, it is multiply arched and its tip is blunt, whereas the lower valves are sharp and capable of penetrating human skin [Rahman et al., 1998, Quicke, 1991]. Both upper and lower valves present a series of thickened strongly sclerotised sections (Figure 2.21, c and d respectively) alternate to nodal narrowings.

In its normal, resting posture, the nodal regions of both the upper and the lower valves of the the ovipositor of *Zaglyptogastra* species are aligned and therefore the ovipositor is more or less straight (Figure 2.21a). When the lower valves are protruded relative to the upper valve, their internodal swellings are aligned opposite the nodal narrowings of the upper valve, and this causes a ventral bending (Figure 2.21b) [Quicke, 1991]. Figure 2.22 shows a generalised diagram of this concept.

A different mechanism for ovipositor bending is shown in Figure 2.23 where a boss on the upper valve, projecting in the lower valve forces the tip to bend either ventrally or dorsally, according to the valve which is tensioned.

In the Gasteruptidae, the lateral edges of both lower valves project laterally close to the ovipositor tip (Figure 2.24a, b, d; arrowed), and there is a corresponding boss on the outer side of the upper valve (Figure 2.24a, b, c; starred). In the resting position, when the valves are equally extended, the projections are aligned and just in contact, and the ovipositor is straight. The bosses in the upper valve stop the lower valves from being protruded beyond the resting position. Attempts to push the lower valve beyond this position (or to retract the upper valve), because of the presence of the interlocking mechanism (olistheter) between the valves, force the ovipositor to curve upwards in a manner analogous to the bending of a bi-metal

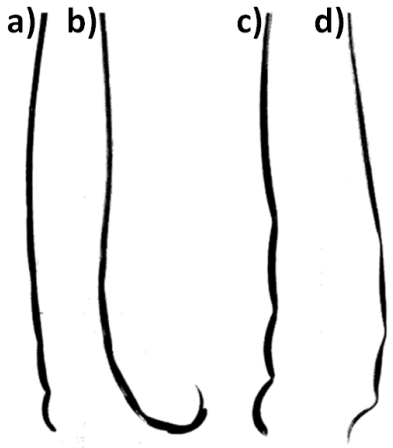


Figure 2.21: a) Intact ovipositor of *Zaglyptogastra levisulcata* at rest, b) ventrally flexed. c) Isolated upper valve of the ovipositor of *Zaglyptogastra equitator*, d) isolated lower valve [Quicke, 1991]

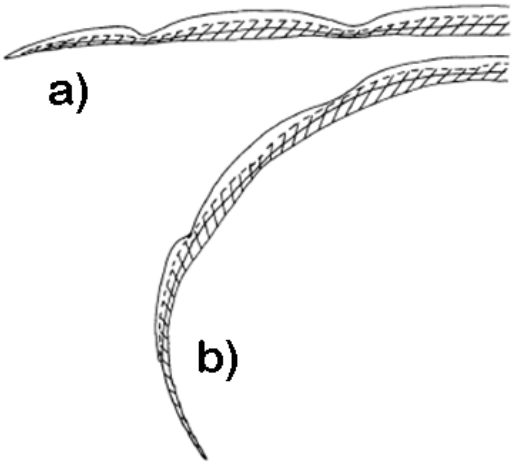


Figure 2.22: Generalised diagram of *Zaglyptogastra* ovipositor apex showing relative position of upper and lower (shaded) valves: a), at rest; b), when flexed ventrally [Quicke, 1991]

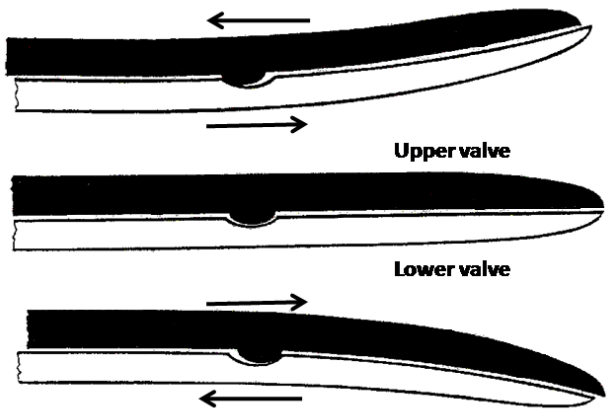


Figure 2.23: Diagrammatic example of the steering mechanism [Quicke et al., 1995]

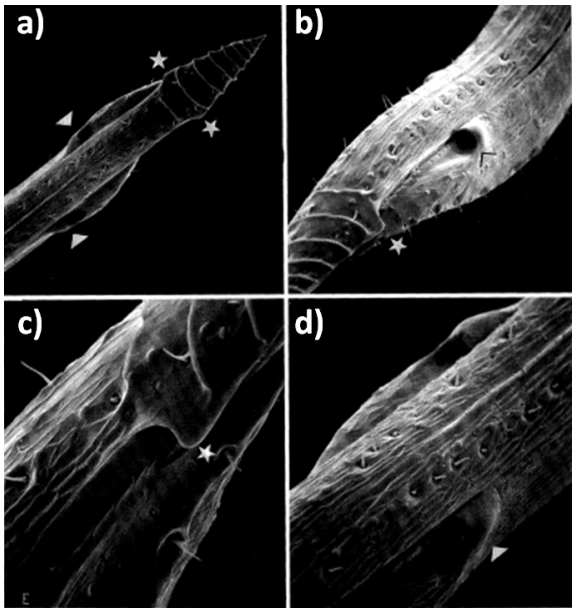


Figure 2.24: Scanning electron micrographs of intact ovipositor apices of *Gasteruption assectator*. Arrows indicate bosses on lower valves; stars indicate corresponding protuberances on upper valve [Quicke and Fitton, 1995]

strip in a thermostat [Quicke and Fitton, 1995].

A similar concept but a different shape is shown by the Aulacidae: they have no bosses, and no steering mechanism is obvious in intact ovipositors. However, the upper valve presents and additional longitudinal groove virtually all along the entire length (Figure 2.25a, b; starred) and parallel to the rhachis. Corresponding to the upper valve groove, each lower valve has a longitudinal rounded ridge running lateral to the aulax (Figure 2.25c, d; arrows). The grooves and the ridges both terminate abruptly near to the ovipositor apex. When at rest with the valves equally extended, their ends are virtually abutting, but attempts to push the lower valve posteriorly will force the ovipositor to curve dorsally.

Finally, it is worth mentioning that *Gasteruption* females are capable of rotating the distal metasomal segments (from which the ovipositor is protruded) along the axis of the metasoma itself, and, by combining this rotation with the bending of the ovipositor in just one plane, they can position their ovipositor tip anywhere within roughly half of a hemisphere.

2.3.6 Discussion of biological inspiration

Table 2.1 summarises the main biological features which allow ovipositing wasps to be so effective in penetrating different kinds of substrates, targeting suitable locations for egg-laying. Three main achievements of the ovipositing strategy can explain the extreme efficiency demonstrated by these insects: reduced buckling,

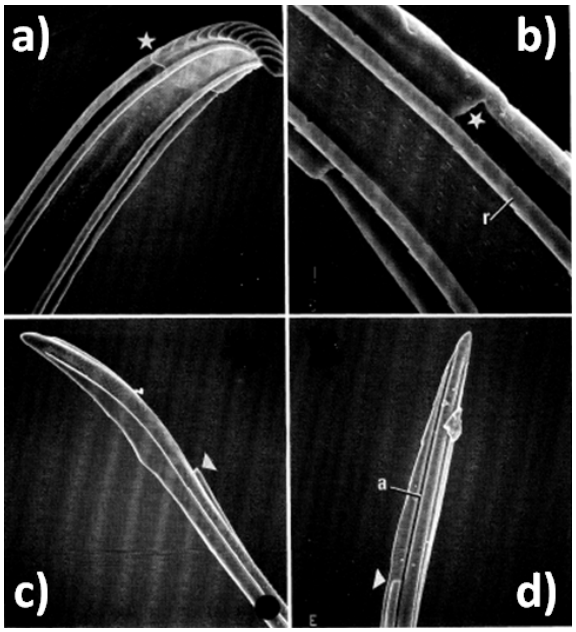


Figure 2.25: a,b) Scanning electron micrographs of isolated upper ovipositor apices of *Pristaulacus*; c,d) isolated lower valves. Stars indicate corresponding abrupt interruption of upper valve sub-lateral groove; arrows indicate bosses at end of lower valve ridge. "r" and "a" indicate rhachis and aulax respectively [Quicke and Fitton, 1995]

steerability and reduced tissue damage.

Ovipositors are generally very long, thin and flexible; however, an ovipositor 0.1-0.2 mm in diameter and 50 mm in length is used to penetrate a tissue as hard as wood avoiding critical **buckling**, thanks to a reciprocating mechanism of three different ovipositor parts. The valves, able to slide with respect to each other, but interlocked together by the olistheter mechanism, can be reciprocally pulled (tension) and pushed (compression). This mechanism, coupled with the anisotropic external morphology of the ovipositor tip, allows the valve in tension to grip the

Ovipositing Wasp Features		
Ovipositor Anatomy composed of Upper Valve and Lower Valves		
Olistheter Mechanism		
Tension/Compression Penetration Mechanism		
Anisotropic External Morphology of Ovipositor Tip		
Absence of Intrinsic Musculature		
Orientable Ovipositor Tip		
Functional Advantages		
Reduced Buckling	Steerability	Reduced Tissue Damage

Table 2.1: Biological features in ovipositing wasp and corresponding performance achievements

tissue, while the valve in compression is pushed further, following the "rail" provided by the opposite valve.

This penetration mechanism, where one valve is the "rail" for the opposite, coupled with the capability of orienting the ovipositor tip, allows the wasp to **steer** the ovipositor, when targeting a particular location inside the soft tissue of the host, and this is achieved without any intrinsic musculature in the ovipositor itself; the force required to actuate the ovipositor valves resides in the abdomen of the insect, at the very base of the ovipositor structure. By nature of the ovipositor, an hollow working channel exists throughout the valves and, as a result of the actuation mechanism, the egg-laying channel can be positioned at different locations in the host.

Considering that the parasitic species lay their eggs in living hosts, which are supposed to feed the eggs till hatching, it can be assumed that **minimum damage** is caused in the host. Furthermore, while eggs are pushed along the egg canal, the wasp holds firmly the host thanks to particular features in the external morphology of the ovipositor.

2.4 Literature review conclusions

The medical need for the development of novel "smart instrumentation", particularly in the neurosurgical field was described, with a focus on the medical procedures currently applied for the diagnosis and treatment of brain tumors (i.e. brain tumor biopsy, localised drug delivery). Current research on flexible needle steering was described, pointing out the main limitations to the approaches identified so far: limitations in the dimensions of the instruments, in the range of the curvilinear trajectories available and problems due to excessive tissue tearing. Finally, a detailed review of the biological inspiration was provided, covering the most interesting aspects of wasp oviposition.

The biological example can indeed help to address the challenges of designing flexible and steerable instruments for percutaneous intervention, equipped with functional inner channels. Ovipositing wasps provide useful inspirations on how to tackle the problem of buckling of a flexible instrument and on how to identify a strategy for achieving curvilinear trajectories in soft tissue, causing minimal tissue disruption.

The biological features listed in Table 2.1 will be considered in the next chapters, particularly in Chapters 3 and 4, where a study on the foundations and a concept demonstrator of a biologically inspired flexible probe will be analysed and described.

Chapter 3

Biological Foundations

This chapter covers the foundations of the research on a biologically inspired flexible and steerable probe for soft tissue penetration. The advantageous mechanism of tissue penetration, as shown by ovipositing wasps, is replicated in a simplified fashion, in two different sets of experiments, with the aim of demonstrating the feasibility of forward tissue penetration with "zero net force". On the basis of the results presented and discussed, conclusions and suggestions for the development of a fully working functional steerable probe prototype are provided.

Some of the work presented in this chapter has been published in journal articles [Frasson et al., 2010c,a, Schneider et al., 2009] and conference articles [Frasson et al., 2008b,a, Schneider et al., 2008a,b, Parittotokkaporn et al., 2009].

3.1 Biological inspiration for a flexible and steerable probe

While Section 2.2 provided an overview of the research on flexible needle steering and described the main limitations in the techniques currently adopted, Section 2.3 shows how ovipositing wasps elegantly solve the challenge of accurate tissue penetration with a long, thin and flexible structure.

Buckling of a flexible tool inside or outside soft tissue is very critical in clinical applications for neurosurgery, where any unexpected deviation from the pre-planned trajectory can result in damage of important brain parts (e.g. blood vessels, neural tracts). On the other hand, achieving curvilinear trajectories in soft tissue, while limiting tissue damage, is of vital importance for the improvement of current MI, keyhole, neurosurgical interventions and for the possibility of designing novel interventional strategies.

Table 3.1 illustrates how the features which make the oviposition strategy so effective could be matched to the features of a novel flexible probe for soft tissue

Ovipositing Wasp Features	**Flexible and Steerable Probe Features**
Ovipositor Anatomy composed of Upper Valve and Lower Valves	Multi-Part
Olistheter Mechanism	Interlocking Mechanism
Absence of Intrinsic Musculature	Absence of "active" components on the probe itself
Anisotropic External Morphology of Ovipositor Tip	Anisotropic Surface Texture
Tension/Compression Penetration Mechanism	Reciprocal Motion
Orientable Ovipositor Tip	Programmable Bevel Tip
Functional Advantages	
Reduced Buckling Steerability Reduced Tissue Damage	

Table 3.1: Biological features in ovipositing wasp and corresponding features for a flexible and steerable probe.

surgery that is able to steer in a compliant medium, while avoiding critical buckling and excessive tissue damage.

The hypothesis for the research upon a biologically-inspired, flexible and steerable probe can be summarised in the following statement:

A multi-part probe composed of interlocked segments with anisotropic surface texture, could penetrate soft tissue thanks to a strategy of reciprocal actuation of the probe segments. Curvilinear trajectories could be achieved without the use of "active components", by relying upon the tissue-probe interaction and upon the interaction between the different parts of the probe (programmable bevel tip).

Section 3.2 will describe the preliminary studies on attempting to replicate the penetration strategy as experienced by ovipositing wasps. On the basis of these studies, conclusions will be drawn (Section 3.3), which will simplify and guide the design and development of a concept demonstrator for percutaneous interventions with a flexible steerable probe (Chapter 4).

With regard to the work presented in this chapter, the author was responsible for the definition of the experimental protocols, for the implementation of the experimental setup, and for the analysis of the results, while a colleague, Mr Tassanai Parittotokkaporn, was responsible for the sample choice, preparation, and for running the experiments.

3.2 Achieving forward penetration with "zero net force" on the tissue

3.2.1 Rationale

As detailed in Section 2.3, the wasp ovipositor is composed of two (or more) interlocked segments which are characterised by a "toothed" outer surface to improve grip at the ovipositor-substrate interface and are able to slide reciprocally with respect to each other (Figures 2.15, 2.16, 2.17). After initial purchase into the target material, the two segments are sequentially pushed and pulled to produce forward motion. The backward pointing teeth of the "pulled segment" grip the tissue, thus facilitating and stabilising the insertion of the "pushed segment". Virtually no net force is generated on the tissue by the ovipositor assembly and, consequently, the risk of buckling is greatly reduced and there is no theoretical limit on the ovipositor length.

Figure 3.1 illustrates the testing setup which was proposed to prove the concept of "forward motion through a reciprocating mechanism", as demonstrated by ovipositing wasps. A two-part probe, provided with an anisotropic surface texture, can achieve forward penetration into soft tissue by reciprocally actuating the two parts comprising the probe, with the result of exerting an overall net force on the tissue equal to zero and therefore reducing the risk of buckling.

A simplified equation describing this behaviour is proposed:

$$F_c + F_i < F_d < F_e \tag{3.1}$$

where F_c is the force required at the tip of the probe to cut and displace the tissue, F_i is the force caused by the probe surface sliding against the tissue during insertion, F_e is the force caused by the probe surface "gripping" the tissue when attempting to remove the probe from the tissue, and F_d is the force used to drive the moving part of the probe inwards.

Two main steps have been identified in order to prove the concept of reciprocal motion: probe-tissue interaction, and forward motion through a reciprocating mechanism. These two topics will be the focus respectively of Sections 3.2.2 and 3.2.3.

The main simplification at this stage of the research is that only straight motion is performed and considered: no steering mechanism is applied, and a rigid probe will be used.

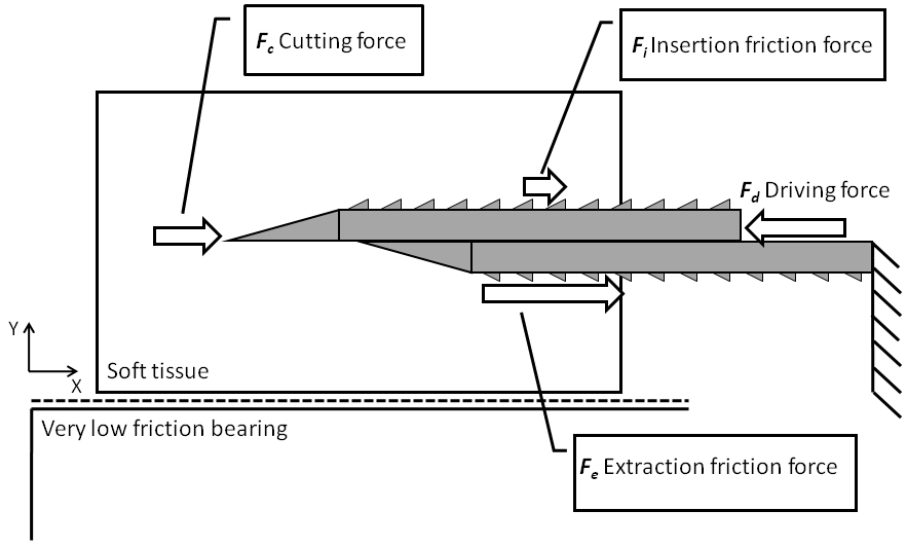


Figure 3.1: Diagrammatic representation of the forces involved during one step of the reciprocal motion; the lower probe part is stationary, while the upper part is pushed inside the tissue. The extraction friction force exerted by the stationary part avoids the tissue from moving to the left, together with the upper moving part, on the very low friction bearing.

3.2.2 Probe-tissue interaction: effect of anisotropic surface texture

The main objective of this study is to identify a suitable anisotropic probe surface texture which can satisfy Equation 6.9 (i.e. where the force required to insert the moving segment of a two-part probe is less than the force experienced by the stationary segment in the opposite direction). However tissue damage experienced during the insertion and the extraction of the probe into soft tissue needs to be taken into account.

The preliminary study of the novel probe requires the selection of a suitable probe surface geometry, in terms of both dimension and shape. Then, a method is defined in order to characterise the insertion and the extraction of a needle with the bio-inspired surface into biological tissue (pig brain). In this study the forces measured during both insertion and extraction, and tissue damage, are taken into account.

3.2.2.1 Surface topography - Size and shape range

In the preliminary study, microstructures with simple geometries are considered. Test strips 75 mm long and 0.9 mm to 1.4 mm wide, with high-aspect-ratio microstructures of SU-8 (photoresist material) are fabricated using UV-lithography, in collaboration with the Science and Technology Facilities Council (STFC) at the Rutherford Appleton Laboratory (RAL). Along the lateral wall, triangular and fin-

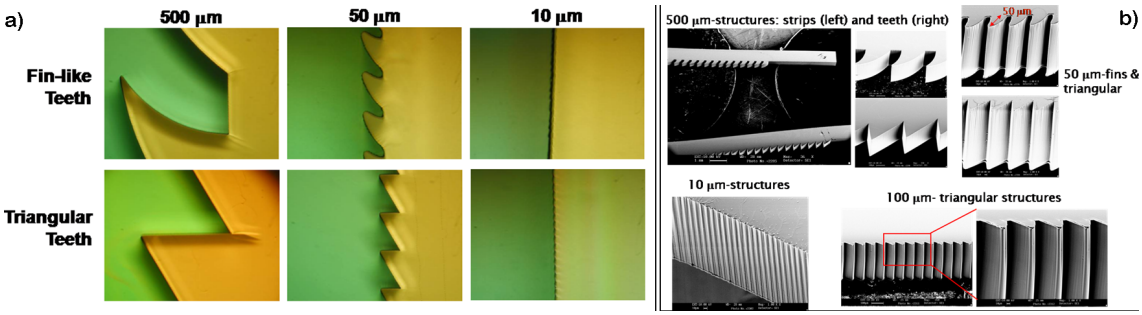


Figure 3.2: a) Optical microscope pictures of micro-structured strips made from SU-8 photoresist: fin-like and triangular teeth, tooth dimensions ranging from 500 to 10 µm; b) Detailed SEM pictures of the micro-structured strips [Schneider et al., 2008a].

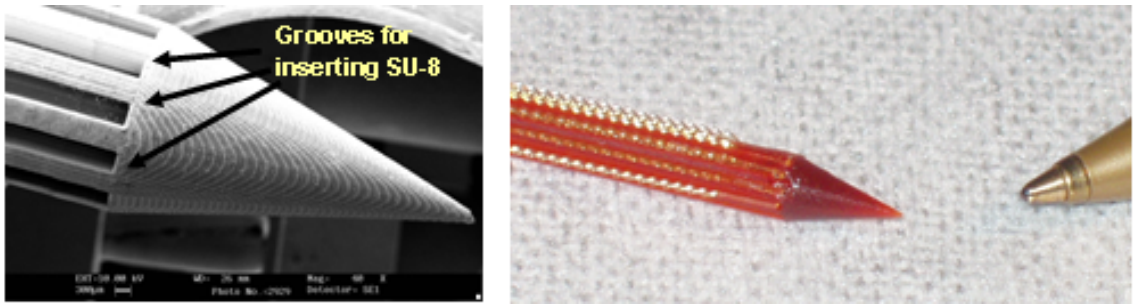


Figure 3.3: *Left:* a SEM picture of the needle core, with the grooves for the insertion of the strips; *Right:* SU-8 strips with 500μm fin-like structures inserted and glued to the MSTL core needle – for size comparison, tip of a ball pen on the right side

like teeth (Figure 3.2) are developed, emulating the typical microtexturing of the ovipositor. The dimension of interest is the lateral width of the tooth (protruding outwards from the axis of the probe) and the chosen sizes are 500 µm, 250 µm, 100 µm, 50 µm and 10 µm. For all these dimensions, both triangular teeth and fin-like teeth strips are manufactured by RAL. The exception was for the 10 µm strips, where the distinction between fin and tooth microstructures is small, owing to manufacturing limitations (compare Figure 3.2) [Schneider et al., 2008a].

Twelve strips are then inserted and glued into the grooves of a rigid needle frame (Figure 3.3), produced by microstereolithography (MSTL), with a diameter of 4.4 mm, and an overall length of 80 mm, ending with a conical tip. The final needle can be seen in Figure 3.3 (right). An additional smooth needle (4.4 mm diameter), made by MSTL, is used as a reference for benchmarking purposes.

3.2.2.2 Protocol definition

Needle insertion and extraction is tested with a Testing Instron machine (Instron Dual Column Model 5565 Series, [Instron, 2010]) equipped with a 100 N load cell (2525-807 Series Drop-through Load Cell 100 N, 0.25% of the indicated load accu-

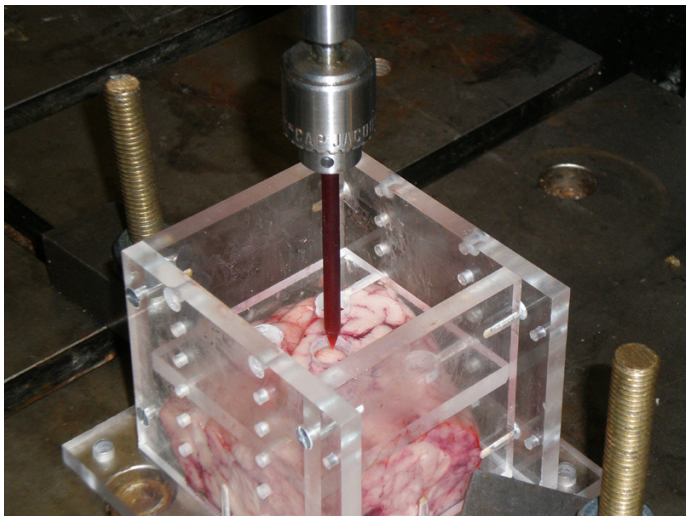


Figure 3.4: Experimental set-up with smooth needle.

racy). The target tissue is pig brain and it is extracted from the skull and deprived of the dura by a neurosurgeon. The brain is then positioned in a transparent plastic box with 5 holes at the top and at the bottom (inner space 50 mm x 50 mm x 50 mm) as in Figure 3.4. The test is carried out within 24 hours of death, and lasts 1 hour.

The needle is inserted into and retracted from the soft tissue down to a depth of 30 mm three times. Cutting forces are experienced during the first cycle, while the second and third cycles should be similar, including the effect of frictional forces at the probe/tissue interface only. All the experiments are run at an insertion and extraction velocity of 1 mm/s, to minimise the effect of rate dependent behaviours. The location of the needle insertion is identified and recorded by a neurosurgeon to ensure that the brainstem, which would bias the results due to its unique material properties, is avoided.

The experiments are recorded with a video camera (Sanyo VCC-6975P) in order to identify the different phases of the needle insertion and extraction process. To synchronise the force profile and the video recording, a software for screen capture is used. Bluehill.2 software [Instron, 2010], used to drive the Instron machine, shows the real time force profile, while the live camera feed is displayed on the same screen.

3.2.2.3 Results and discussion

The graph in Figure 3.5 shows the typical Force-Time profile of a test in pig brain with the 50 µm triangular teeth needle. According to the video recordings, it is possible to divide the experiment into 4 different phases.

1. The first phase (**D, Tissue Deformation**) corresponds to the deformation of the brain by the needle, prior to the outer membrane being pierced for the first time. In the first cycle it is often possible to distinguish the breaking

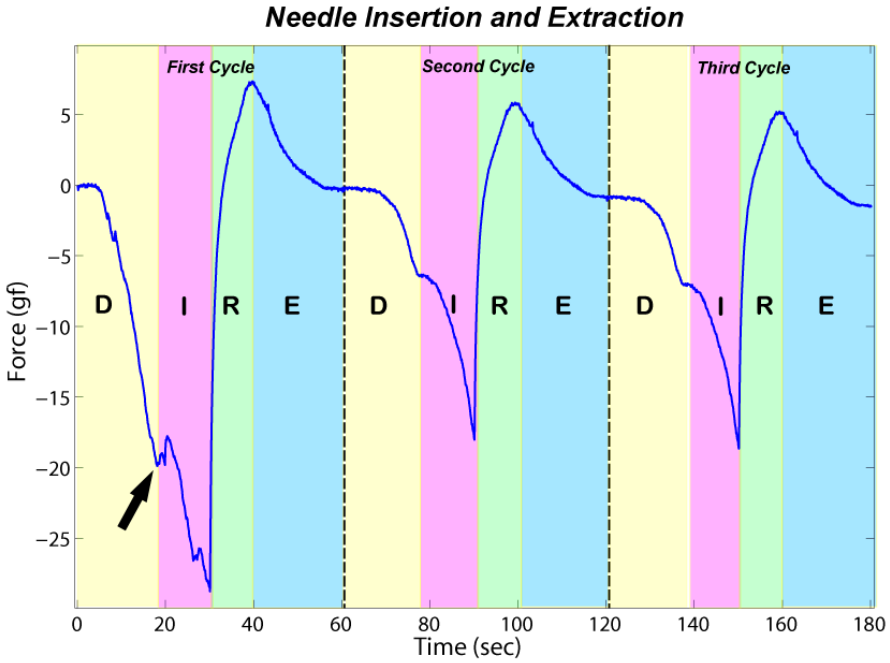


Figure 3.5: Force Profile: different phases for a typical experiment with three cycles (50 µm Triangular Teeth). D: Tissue Deformation; I: Insertion; R: Reversing; E: Extraction. Black Arrow points to the instant when the surface is pierced.

of the outer surface of the tissue by a sudden drop in the force value (black arrow in Figure 3.5). Even if the dura membrane has been removed, the pia membrane is still covering the whole brain surface. Because of the viscoelastic properties of brain, the brain tissue collapsing into the needle track and the needle adhering to the tissue itself, this deformation phase is also seen during the second and the third cycles but the force recorded is smaller.

2. The second phase (**I, Insertion**) corresponds to needle insertion inside the tissue, while the tissue remains virtually stationary. Again, in the first cycle the forces experienced during the insertion phase are larger because the tissue has to be cut by the conical tip.

3. Reversal of the movement corresponds to a sudden reversal of the force value. During the third phase (**R, reversing the motion**) the tissue is deformed according to the retraction of the needle, and, for some time, there is no relative motion between the tissue and the needle.

4. Immediately after the upper peak in the force value, the fourth phase (**E, Extraction**) starts. The needle is sliding out from the brain tissue and the force values decrease as the needle surface area in contact with the tissue decreases.

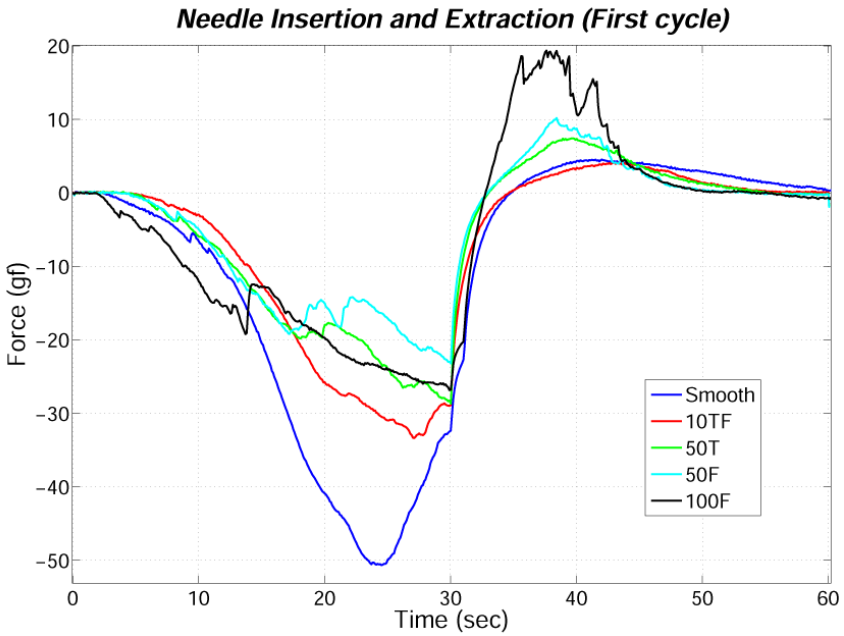


Figure 3.6: Force profile: first cycle for 5 different needles - smooth needle (Smooth), 10 µm topography (10TF), 50 µm triangular teeth (50T), 50 µm fin-like teeth (50F) and 100 µm fin-like teeth (100F)

In Figure 3.6 the results obtained during the first cycle of insertion and extraction for 5 different needles are shown. In these tests, the bigger toothed needles (500 µm and 250 µm, both triangular and fin-like teeth) were discarded due to the evident tissue damage caused (Figure 3.7).

The overall insertion profile is in good agreement with previous literature on needle insertion [Hing et al., 2007, Kataoka et al., 2002]. Qualitatively, the profile indicates that, during the first insertion, where both cutting force and friction force (related to the clamping force [Simone and Okamura, 2002, Kataoka et al., 2002]) are present, the strips of teeth seem to prevent adherence between the needle and the tissue, thus the forces experienced are smaller. The force measured during the first insertion appears to be related to the needle surface geometry: in particular, the smooth needle requires the greatest insertion force. It is also possible to distinguish the behaviour of the 50 µm triangular teeth (Figure 3.6, green line) from the 50 µm fin-like teeth needles (Figure 3.6, cyan line), where the fin-like teeth are less invasive (i.e. insertion requires less force). The behaviour of the 100 µm fin-like teeth needle (Figure 3.6, black line) is slightly different, but this may be due to the fact that the needle was tested in a different brain sample.

During phases R and E (reversing and extraction), the surface geometry of the needles visibly affects the force profile; bigger geometries require bigger extraction forces. This behaviour is made clear by averaging the force profile of the second and the third cycles (Figure 3.8).

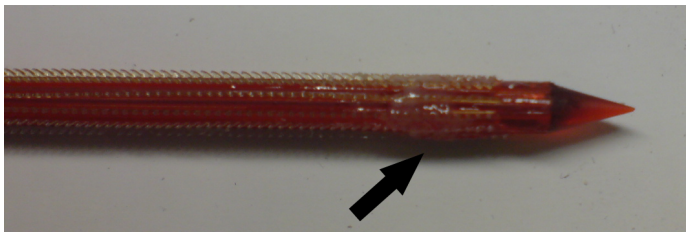


Figure 3.7: 250 µm fin-like teeth needle. Evident brain tissue lodged between the teeth (black arrow).

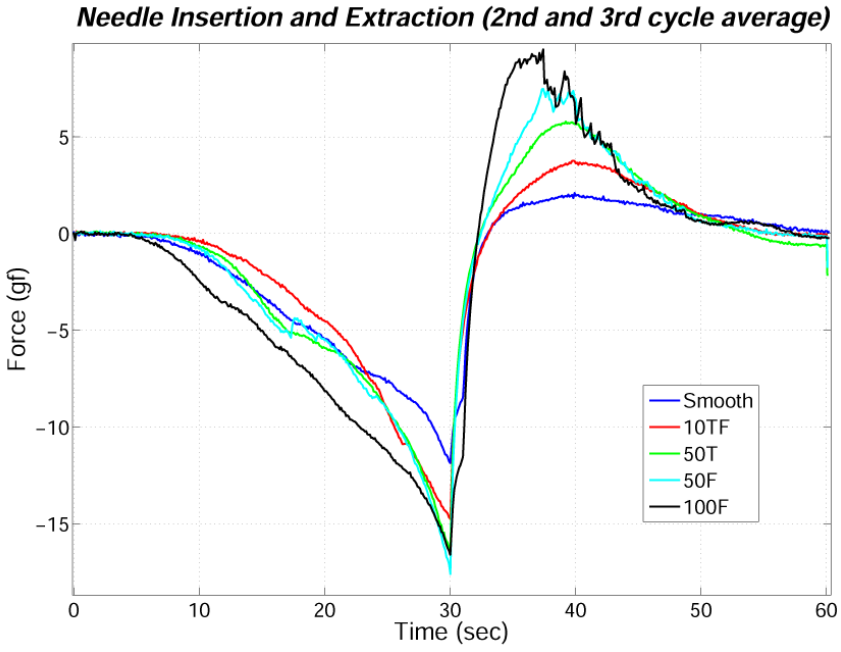


Figure 3.8: Force profile: 2nd and 3rd cycle average for 5 different needles.

Cycle	1st		2nd - 3rd	
Needle	*Insertion Peak Force (gf)*	*Extraction Peak Force (gf)*	*Insertion Peak Force (gf)*	*Extraction Peak Force (gf)*
Smooth	50.65	4.54	11.86	2.09
10TF	33.37	4.10	14.75	3.76
50T	28.68	7.43	16.39	5.79
50F	23.20	10.19	17.60	7.48
100F	26.83	19.36	16.60	9.52

Table 3.2: Peak force values (gf: gram force); maximum standard deviation not greater than ± 2.16 gf (Insertion Peak Force of the 10TF needle, 2^{nd} and 3^{rd} cycle).

Differences in the needle insertion force profiles of the second and third cycle (phases D and I) are not observable. Once the tissue has been cut, the surface geometries make no a real difference to the forces measured - although the peak forces are almost ordered according to the surface geometry (Table 3.2). During needle extraction (phases R and E), the force profile is affected by the tooth dimension. The smooth needle requires the smallest amount of force, the 100 µm fin-like teeth needle the greatest. Again, it is clearly possible to distinguish the performance of teeth with the same dimension (50 µm), but different geometry (fin-like and triangular): during extraction, the fin-like teeth needle requires a larger force. Peak forces during insertion and extraction are listed in Table 3.2.

3.2.2.4 Conclusions

This preliminary study shows that even very fine anisotropic textures affect the force measured during penetration and retraction of a textured needle into animal brain tissue. The results obtained are promising, but still limited in scope. Very small surface topographies affect the forces experienced in the two directions of motion, facilitating the insertion and increasing the gripping force when the needle is pulled. However, insertion still requires greater force than extraction. This phenomenon is more clear considering Equation 3.1: the force required by the tip of a needle to move forward into the tissue ($F_c + F_i$), is up to an order of magnitude larger than the forces measured along the lateral contact surface between the needle and the tissue itself during extraction *(F_e)*. The reason for this is the large force required to cut through the tissue *(F_c)* during first insertion. Increasing the size of the teeth could help to reduce the difference between insertion and extraction forces. However this option is discarded for the severe damage caused to the target soft tissue.

Implications of this study with respect to the initial hypothesis presented in Section 3.1 will be outlined in the final section of this chapter (Section 3.3).

These results suggest further interesting conclusions, which are beyond the scope

of this thesis, but which are worth mentioning here. New surface topographies for instruments used in neurosurgery can be designed in order to facilitate the insertion and avoid the slipping of certain instruments which are currently manufactured with a smooth surface. For instance, in Deep Brain Stimulation (DBS) for Parkinson's disease, one of the complications is electrode migration [Blomstedt and Hariz, 2005], and similarly, even if quite rare, a Hydrocephalus Shunt complication is the proximal migration of the ventriculoperitoneal shunt [Acharya et al., 2002]. By designing a more advanced surface topography, which is able to grip the tissue without causing damage, it may be possible to reduce the occurrence of such complications in these interventions. A similar technique could also be applied to enhance the effectiveness of conventional surgical tools, such as brain retractors.

One aspect not addressed here, which is the focus of parallel research carried out by the research group, is "tissue damage". The relationship between needle force and tissue damage could be explained by the amount of physical damage measured on the needle track generated into biological tissue after insertion and extraction. Quantitative measures in this context would include, for instance, the hole dimension, the track surface topography (e.g. depth map) and the length of any cracking lines. However, a more interesting tissue damage study could be performed by considering the number of dead neurons around the needle tract, for example by using cell-counting assays. This test should be done *in vivo* with pigs in order to obtain accurate results.

3.2.3 Reciprocal motion

The second step of the study consisted of actuating two parts of a simplified probe assembly, which included a suitable anisotropic surface at the probe-tissue interface. If the probe could be inserted into a tissue sample positioned on a very low friction bearing, to minimise all other external forces, without the need for an overall axial push, the concept of forward motion with "zero net force" would be validated (Figure 3.1). It is worth restating that forward motion with "zero net force" (i.e. the probe is pulling itself inside the tissue) is the underlying reason for the hypothesis of avoiding critical probe buckling during insertion. However, considering the results from the previous study which demonstrated the high impact of the cutting force *(F_c)* experienced by the tip of the probe during insertion and partially nullified the effect of anisotropic surface texture, a simplification was made. Two textured samples with geometrical and dimensional tooth features identical to those used in the previous study (Section 3.2.2) are **reciprocated onto the surface** of soft tissue samples positioned on a very low friction bearing. The aim of this approach is to isolate the sliding/gripping behaviour of an anisotropic surface when moved in two

different directions, in the absence of cutting forces due to tissue penetration. If the concept of reciprocal motion onto the surface of soft tissue samples (i.e. tissue traversal) is proved viable, a possible final embodiment of a fully working functional probe prototype could include a standard actuation drive ("push from the back"). A standard actuation drive could indeed be coupled with the reciprocal motion of anisotropic surfaces. This will allow the probe to overcome the force required by the tip to cut through the tissue, while keeping the advantages of reciprocal motion of anisotropic surfaces.

A number of microtextured samples, with features including every combination of two teeth geometries (triangular and fin-like) and three sizes (500 µm, 100 µm and 50 µm tooth width), were manufactured and mounted onto a custom-built reciprocating mechanism. Two stepper motors with relevant control hardware provided actuation and a crank-shaft was employed to convert rotary to linear harmonic motion. A custom-built, low friction, air bearing was also manufactured in order to reduce the effect of any external forces to a minimum. Trials on a variety of soft tissues were carried out to qualitatively evaluate the concept on a broad selection of material properties, including elastic and plastic deformation behaviour and the presence or absence of fibers within the substrate. A trial was considered successful if the corresponding sample was able to travel on to the surface of the tested tissue, while a trial was considered to fail if forward motion was not detected. Then, detailed experiments on agar gel and gelatine, including a comparative tissue damage study based on optical profilometry, was carried out to investigate the degree of indentation caused by the reciprocating mechanism during tissue traversal. On the basis of this evidence, possible reasons behind successful and failed trials are proposed and recommendations are made upon the conditions (blade geometry and size for specific material properties) which are necessary for soft tissue traversal via reciprocal motion, while causing minimum tissue damage in the process.

3.2.3.1 Materials and methods

The microtextured samples used for the experiments and fabricated with the same technique explained in Section 3.2.2 are shown in Figure 3.9. The dimension of interest (i.e. the depth of the protruding feature of the tooth) was set to 500 µm, 100 µm and 50 µm with an additional smooth sample for reference. Because of the broader selection of testing materials with respect to the experiment outlined in Section 3.2.2, where only brain tissue was used, samples with tooth dimensions of 500 µm were taken into account. All samples were rounded at both corners to minimise any edge loading which could occur while the sample is dragged along the tissue.

A variety of tissue specimens were preliminarily tested, which included inorganic

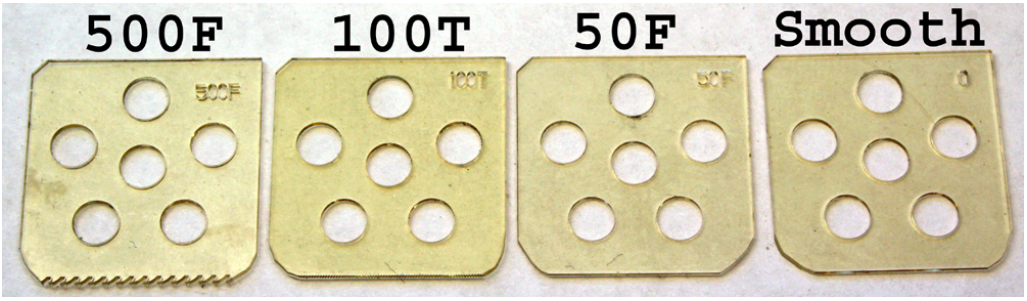


Figure 3.9: A selection of the microtextured samples with (from left to right): 500 µm, 100 µm and 50 µm teeth and the Smooth sample, including both triangular ("T") and fin-like ("F") geometries.

materials (aluminum, glass, rubber and synthetic fabric), organic materials (paper, wax, silicone, gelatine and agar gel) and a selection of biological soft tissues (porcine muscle, liver and brain). In order to test muscle fiber, sliced pork meat was used and the specimen was positioned such that the reciprocating motion direction was perpendicular to the exposed fibers.

On the basis of these trials, a more thorough analysis of agar gel, a gelatinous substance derived from seaweed, and gelatine was performed. Both materials have often been used to simulate brain tissue because their material properties can be tuned by varying the water concentration in the solution prior to solidification. Two different agar gel concentrations, 0.5 and 1.6 wt.%, were tested. The first value was selected on the basis of the study by Varkey [2006], which determined that 0.5 wt.% agar gel most accurately represented living human brain tissue for microelectrode implantation studies. The second, higher concentration, was chosen to investigate the effect of increased elastic modulus and brittleness on mechanism performance. Similarly, 6 wt.% gelatine, the material properties of which have been compared to canine brain [Ritter et al., 1998], was tested and the results between agar and gelatine compared. Each solution was stained with 0.2 cc of Trypan blue to facilitate viewing under a microscope, then poured into plastic Petri-dishes (diameter 89 mm, 14 mm high, 50 cc of mixture) for testing and analysis. The solid state was obtained after 30 minutes at room temperature and each sample was tested and analyzed within one day of preparation.

As per the study hypothesis, the reciprocating motion of the samples, which possess different frictional characteristics in the two directions of motion, enables a tissue specimen to be moved forward in a chosen direction, either towards or away from the reciprocating mechanism. In order to eliminate any bias introduced by external forces on the tissue specimen, the specimen (and mounting plate) should be free to move. Therefore, it is mandatory to minimise the frictional force of the moving plate. To this end, a linear air bearing prototype was developed and incorporated into the rig assembly (Figure 3.10). An aerostatic bearing was chosen,

since a very low friction coefficient (around 0.0001), more than one order of magnitude smaller than grease lubrication bearings (0.001-0.005) [Powell, 1970], can be achieved. The bearing size is 200 mm x 150 mm x 23 mm. The air bearing platform is suspended within an air film with air pressure of 7 bar from the upper cover, 2 bar form the side wall and 1.5 bar from the base.

The developed experimental rig, which is able to move each microtextured sample backwards and forward, is shown in Figure 3.10. However, while the synchronised motion of two samples is possible with this setup (thanks to the two motors), it was chosen to reciprocate only one of the two samples while maintaining the second stationary. This protocol achieves the same overall function, while minimising mechanism induced oscillations of the test piece. The rotating movement of the stepper motor (stepper motor w/rear shaft, 12 V 500 mNm, step angle 1.8°) was converted into a reciprocating action by means of a crank-shaft mechanism, as illustrated in Figure 3.10. This enables the microtextured sample to achieve simple harmonic motion over the tissue specimen, which is positioned onto the air linear bearing. Two light aluminium rods (with a weight of 2 g) are used to secure the samples to the actuation system. The electrical pulse sequence is applied to the motor via a drive board (4-phase unipolar stepper motor drive board) so that the number of steps and the speed of rotation are determined by the number of pulses and by the frequency of the input signal (1.8° step angle of rotation of the spindle, 400 steps/revolution in Half Step configuration). The air bearing was placed next to the reciprocating actuator and an optical encoder (Agilent AEDR-8000 series reflective surface mount optical encoder) was mounted onto the frame (linear code strip 2.95 lines/mm, encoder resolution 0.083 mm) to record the instantaneous position of the moving plate. A CompactRIO real time controller (NI cRio-9014, [National-Instruments-Inc., 2010]), programmed via a graphical user interface implemented in LabView v.8.5 [National-Instruments-Inc., 2010], was used to drive the stepper motor via the driver board and to record the data from the positional encoder. The direction and position of the sliding plate where the tissue specimen is fixed was monitored and data stored by the LabView real time interface for post-processing. Both the normal force applied to microtextured samples in the direction of the tissue specimen and the speed of the stepper motor were maintained at a low and constant value throughout the experiments to reduce the number of parameters affecting the results.

In order to obtain information about tissue damage, each specimen was first observed under a light microscope (Carl Zeiss Axioskop 40). Then, an optical profilometer (Confocal laser scanner Xyris 4000, TaiCaan Technologies Ltd.; resolution up to 0.01 μm) was chosen to obtain the three-dimensional surface profile of the tissue surface after indentation. Direct scanning of the semi-transparent materials

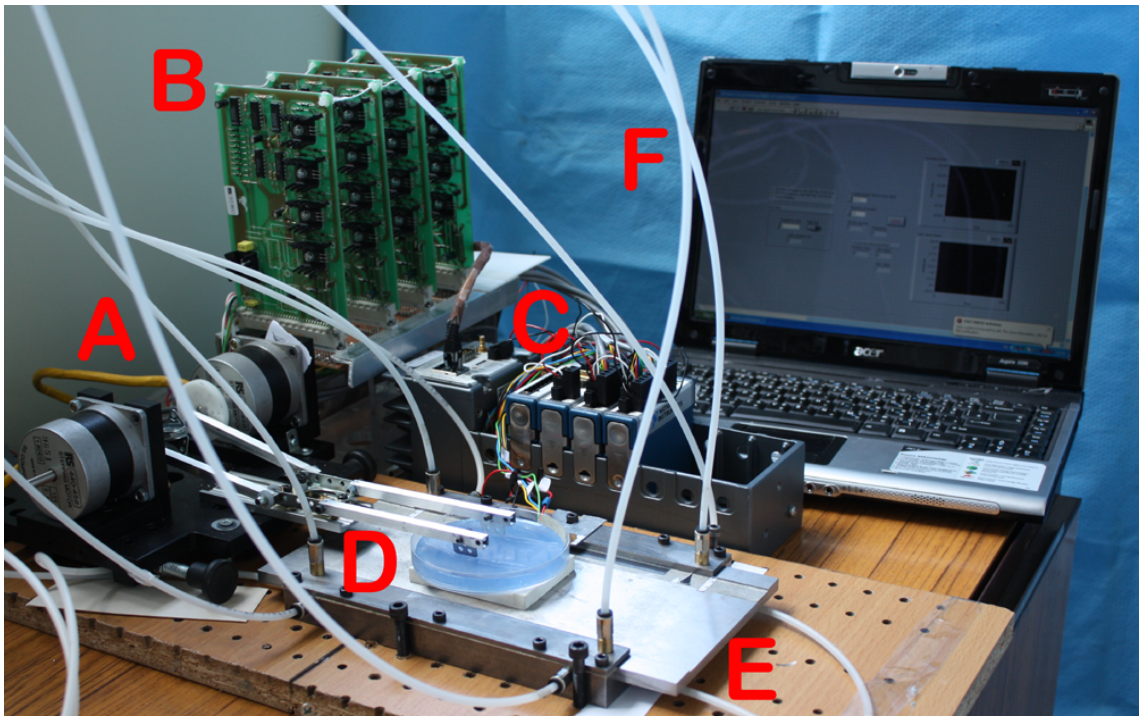


Figure 3.10: Experimental rig setup including two stepper motors (a) and corresponding electronics (b), a CompactRIO controller (c), reciprocating mechanism (d), low-friction air bearing with optical encoder (e) and control laptop running LabView v. 8.5 (f).

was not possible due to laser beam scattering. Microscopic replicas of the damaged surfaces were therefore produced with special fast-setting molding rubber (Microset 101RF, Synthetic rubber replicating compound, resolution 0.1 µm), which was subsequently measured via optical profilometry. The TaiCaan "Boddies 2D" software package, which provides a large selection of surface analysis and 3D imaging tools, was used to process the profiler-generated data (Figure 3.12).

The testing protocol applied to characterise the interaction between the samples and the different tissues was as follows: at first, an SU-8 serrated sample was mounted into the reciprocating mechanism with the teeth directed in such a way as to push the agar sample away from the actuator mechanism. A second sample, with equal tooth geometry and size as the first one, was placed parallel to it, with the teeth pointing in the same direction. The reciprocating mechanism was then used to provide the "pushing and pulling" of the first sample at a constant stroke of 8.84 mm. Two complete revolutions were performed for each test, starting with a complete pull and followed by a complete push, twice in sequence. The experiments were also recorded with a video camera (Sony Handycam HDR-SR10E) in order to identify the different phases of sample and tissue motion. Furthermore, a real time interface controller implemented in LabView was used to run the stepper motors and to display the position vs. time profile of the sliding plate on a laptop screen.

Position vs. time data were also saved for post-processing. The tissue specimens were placed centrally onto the sliding plate and the two samples (one moving and one stationary) were rested on the tissue specimen with the toothed side facing the tissue and parallel to it. Two tests were run for each tissue sample and the position-time profile was averaged. Finally, the surface damage of a selection of representative specimens was observed and recorded via optical profilometry.

3.2.3.2 Results

At first, hardware calibration was conducted. The clearance of the air bearing was measured to be approximately 0.05 mm above and 0.25 mm below the sliding plate. By inclining the bearing with fine shims of increasing size until motion of the plate was detected, and by knowing the mass of the sliding plate, the friction coefficient between the sliding plate and air film was calculated to be approximately 0.00037. It was shown experimentally that, by adding the weight of a Petri-dish containing the tissue specimen, the sliding plate maintains its frictionless features. An accurate estimate of the stroke obtained with this setup was computed by setting the input signal for the motor (frequency 75 Hz, Half Step configuration) and recording the displacement of the air bearing (via the optical encoder) after securing the sample holder (mounted at the end of the crank-shaft) to the sliding plate itself. Highly repeatable results were achieved, with a harmonic stroke of 8.84 mm amplitude. The position vs. time function for the stroke is shown in black in Figure 3.11. By holding both the speed of the motor (11.25 rpm) and applied normal force in the direction of the tissue (2 g) constant, simple harmonic motion of the samples with 5.22 mm/sec maximum speed and 6.15 mm/sec^2 maximum acceleration was achieved. These values were shown empirically not to produce unwanted inertial forces of the sliding plate, while allowing sufficient time for the tissue to deform (elastically or plastically) under load.

A summary of the materials tested, including a binary result (a list of sample geometries and sizes for tests which succeeded or an "x" to represent complete failure) pertaining to the ability of *any* microtextured sample pair to traverse the tissue surface, is included in Table 3.3. As can be seen, most of the materials failed to work as expected with any of the microtextured samples tested. Most of the inorganic materials and the biological soft tissue specimens did not provide sufficient "grip", resulting in periodic oscillations about the original starting point. It is also apparent from these preliminary results that the Young's modulus of the material is not correlated to the success of a trial.

Agar gel and gelatine are chosen as representative specimen samples for further investigation, as they have previously been used in brain-related comparative studies with good results [Varkey, 2006, Ritter et al., 1998]. A graphical representation of

Material Category	Specimens	Young's Modulus (MPa)	Sample/Tissue Interaction Type	Reciprocating Motion with Samples (µm)
Inorganic Materials	Aluminum	6.9×10^4	S	x
	Glass	$5\text{-}9 \times 10^4$	S	x
	Rubber	10-100	ED	x
	Synthetic fabric	-	H	500 F-T
Organic Materials	Tissue paper	-	H	500 F-T, 100 F-T
	Candle wax	0.63	S	x
	Silicone pad	8.8×10^{-2}	ED	x
	Gelatin (80%wt)	-	S	x
	Gelatin (60%wt)	0.21×10^{-2}	ED	500 F
	Agar gel (1.6%wt)	0.72	S	500 F
	Agar gel (0.5%wt)	-	PD	500 F-T, 100 F-T, 50 F
Biological Soft Tissues	Porcine muscle	0.8	H	500 F-T, 100 F-T
	Porcine liver	1.5×10^{-2}	C	x
	Porcine brain	0.74×10^{-2}	C	x

Table 3.3: Binary results summary, including the type of sample/tissue interaction observed ("S" for sliding, "ED" for elastic deformation, "H" for hooking and "PD" for plastic deformation and/or cutting. An "x" in column 5 represents complete failure, while Young's modulus estimates were obtained from [Samur et al., 2005, Woo et al., 1980, Miller and Chinzei, 1997, Jamani et al., 1989, Craig and Peyton, 1960].

the results obtained for all combinations of blade geometry and size for 0.5 wt.% agar gel and 6 wt.% gelatine is illustrated in Figure 3.11.

While there are some subtle differences between samples, the performance of all specimens can be broadly subdivided into combinations where forward motion was achieved and those where it was not. Specifically, it is apparent that, while most agar gel combinations worked as expected (i.e. caused forward motion of the specimen), virtually all gelatine trials failed to produce the desired motion. This suggests that the material properties of the soft tissue specimen play a dominant role relative to the microtexture geometry, but further work will be needed to identify the key parameters which affect this behaviour.

Additionally, among the successful trials, good correlation between microtexture size and any slip between the "gripping" sample and the tissue was found. The y-axis displacement between the two "sliding plateaux" in Figure 3.11 was compared to one complete stroke of the stepper motor, converted into a linear range by means of the crank-shaft arrangement (8.84 mm). Results have been summarised in Table 3.4, where a "Gripping Ratio" of "1" represents perfect grip.

A selection of representative samples, including four microtextured geometries and two materials, is illustrated in Figure 3.12. Specifically, Figure 3.12a shows the three-dimensional surface of the 500T (left) and 500F (right) on 0.5 wt.% agar

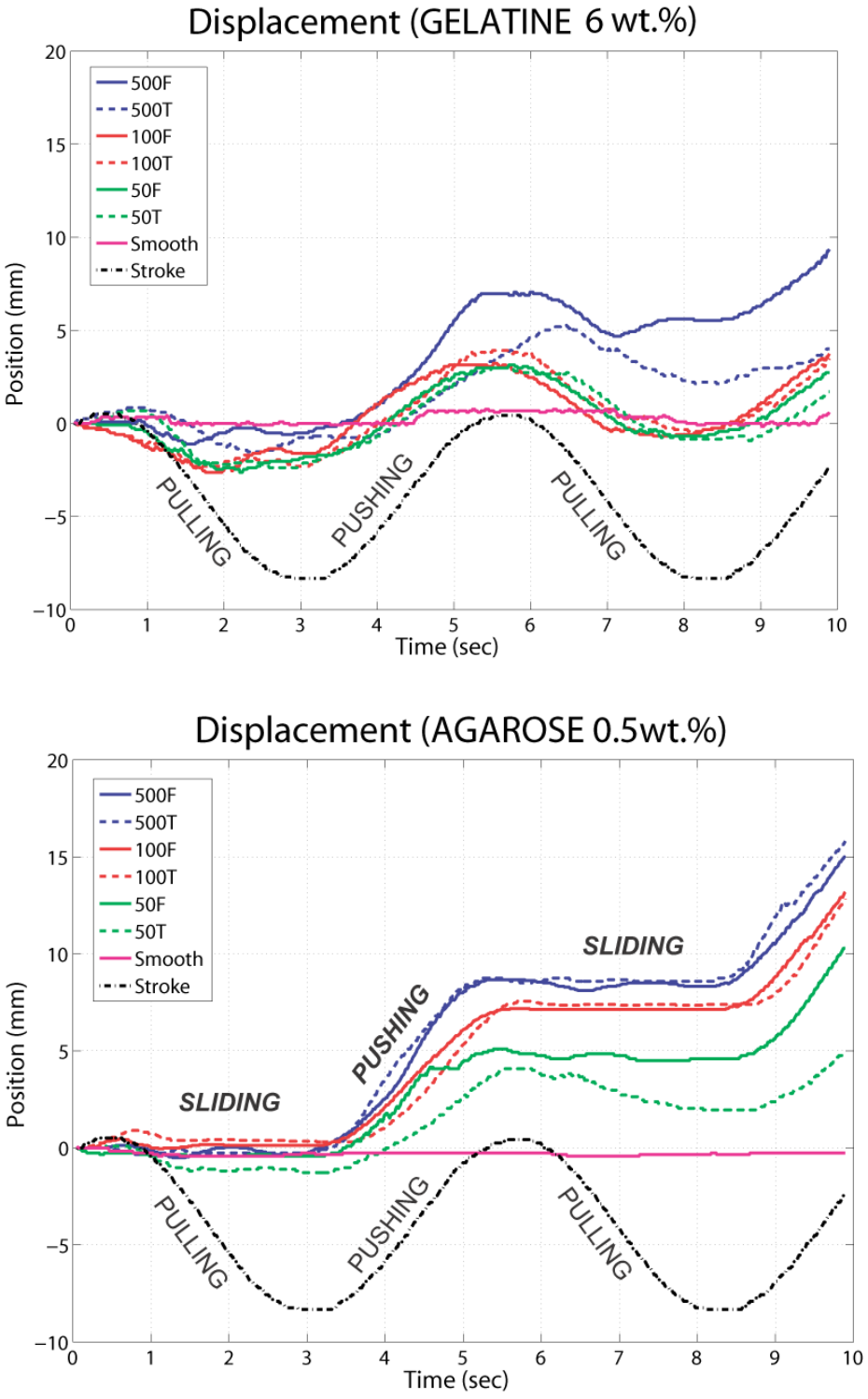


Figure 3.11: Charts illustrating the traversing capabilities of the different micro-textured samples in 6 wt.% gelatine (top) and 0.5 wt.% agarose. Limitations of the experimental setup can justify the anomalies shown in the displacement profile for the 500 and 100 µm samples, where no clear difference in the behaviour of the fin-like teeth and the triangular teeth was found.

Sample (μm)	**Distance Traveled (mm)**	**Gripping Ratio**
500F	8.55	0.97
500T	8.86	1.00
100F	7.00	0.79
100T	6.91	0.78
50F	5.03	0.57
50T	3.74	0.42
Smooth	0.005	∼0

Table 3.4: Distance traveled (mm) and gripping ratio (Distance Traveled/Stroke) with a stroke of 8.84 mm for 0.5 wt.% Agarose.

gel, where the cross-sectional depth profile of each is illustrated in Figure 3.12b. Similarly, Figure 3.12c depicts the 3D topography of a damaged 6 wt.% gelatine specimen, after reciprocal motion testing with 100F (left) and 500T (right) microtextured samples.

3.2.3.3 Discussion

From the results of preliminary experiments on a broad selection of tissue specimens, it is clear that the concept of tissue traversal based on reciprocal motion is indeed valid, but only works on a small subset of the materials tested. Based on experimental observations, it is suggested that the sample/tissue interaction can be categorised into five distinct behaviours.

- If the tissue is unaffected by the reciprocal motion of the sample ("S" for Sliding), there is virtually no interaction between the microtextured surfaces of the sample and the underlying tissue.
- If the material is highly elastic, such is the case for gelatine, the surface deflects away from the teeth ("ED" for Elastic Deformation) and thus there is no real gripping of the tissue during motion.
- For very fine, "razor blade-like" surface textures, or when the tissue specimen is very soft, the material is simply cut and thus no forward motion occurs ("C" for cutting). The last two categories embody successful behaviour.
- If the specimen includes fibers within the substrate, the microtextured teeth simply act as hooks ("H"), in which case there is no real elastic or plastic deformation in the process.
- The final category is typical of the trials on agar gel, although similar results on liver and brain may have been possible with a more advanced protocol

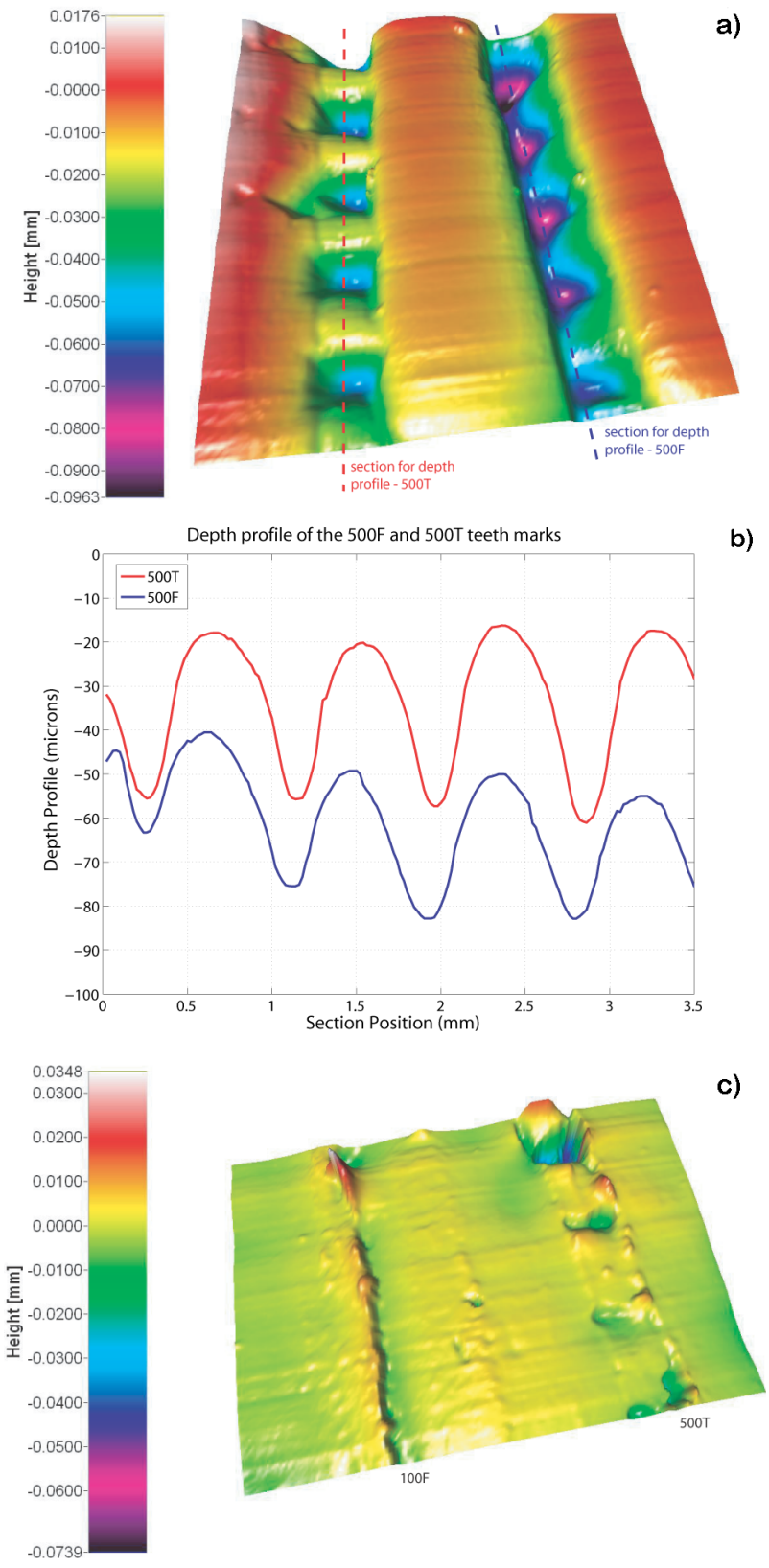


Figure 3.12: Tissue damage measurements via optical profilometry. a) 3D topography of a 0.5 wt. % agar gel, note that the profile left by the 500F sample may not be exactly orthogonal to the agar gel surface, and this may have caused a bias of the localised forces towards the left; b) corresponding depth map, c) topography of a 6 wt. % gelatine sample.

to test organic materials (it proved impossible to produce organic specimens which were absolutely flat, thus causing uneven sample/tissue interaction). In this case, it is believed that a mixture of cutting and plastic behaviour ("PD" for Plastic Deformation) occurs, which improves gripping of the teeth, thus enabling forward motion.

Figure 3.11b illustrates how very fine surface textures, such as those included in the 50T and 50F samples, are able to successfully grip agar gel in one direction, while sliding in the other. Further evidence for the mixture of cutting and plastic deformation occurring with agar gels is provided by the tissue damage results illustrated in Figure 3.12. As can be seen, the tracks produced by the samples on agar gel are substantially different from those of gelatine. While only a small selection of results is shown here, a similar pattern of damage, independent of concentration and sample geometry/size, was observed on all the specimens where forward motion was achieved. As illustrated in Figure 3.12c, gelatine specimens showed random tearing of the tissue, mixed with regions with virtually no detectable tissue damage. Conversely, Figure 3.12a illustrates a more consistent pattern of tissue damage, with clear indentations which approximately mirror the geometry of the sample used in the relative experiment. Specifically, both lines in Figure 3.12b describe a clear indentation pattern, with an average width of 864 µm per gap, which correlates well with the distance between the teeth ($500\mu m/tan(30^o) = 866.5\mu m$, where 30^o is the slope of each tooth), coupled with a negligible amount of plastic deformation. The average depth of each indent is 37 µm, which, however, is substantially less than the 500 µm depth of each tooth. This suggests that each sample only partially penetrates the surface to provide grip.

While there is insufficient evidence to draw definitive conclusions about this behaviour, a qualitative interpretation of the results suggests that successful tissue traversal is highly dependent on the material properties of a chosen sample tissue. Gelatine exhibits a well known hyperelastic behaviour [Pavan et al., 2009], which seems to prevent the samples from cutting into the tissue surface (i.e. the surface elastically deforms under load). Conversely, the more brittle characteristics of agar gel seem to be ideal for this type of actuation mechanism, as very fine surface textures can be used to achieve forward motion. It is unclear to what extent each sample is cutting rather than plastically deforming the agar specimen in order to produce the even track illustrated in Figure 3.12a, but it is believed that a combination of both is necessary for a successful forward motion along the tissue surface.

3.2.3.4 Conclusions

While limited in scope, these results clearly demonstrate that effective tissue traversal can be achieved through a reciprocating mechanism without causing excessive tissue damage. Fine surface topographies, such as the 50 µm triangular and fin-like teeth, have been shown to work repeatably with the right choice of material. However, no combination of geometry and size was found to satisfy the requirements for certain gelatine concentrations and biological soft tissues, such as liver and brain. Soft tissue traversal via reciprocating motion may thus be limited in application to certain soft materials, possibly fibrous or brittle materials, such as muscle and agar gel.

In addition, the results can be broadly subdivided into tests which succeeded and tests which did not. Thus, by disregarding the increasing amount of slip between the texture and the tissue for decreasing tooth size (Table 3.4), since it does not impair forward motion, a valid recommendation would be to select the smallest working topography for a chosen soft material. This would achieve the desired motion with minimum tissue damage.

Additional implications of this study, with regard to the original hypothesis presented in Section 3.1 will be outlined in the following section.

3.3 Conclusions: towards a concept demonstrator for a flexible steerable probe

As explained in Section 2.3, the ovipositing wasp capability of inserting their ovipositor in different substrates by increasing the critical buckling load of the ovipositor structure is supposedly due to the particular mechanism of tissue penetration. This involves, according to Table 3.1, the following features:

- the ovipositor anatomy is composed of upper valve and lower valve (often split into two segments) able to slide with respect to each other
- the ovipositor tip presents an anisotropic external morphology to ease substrate penetration
- an actuation mechanism where the valves are reciprocally pushed and pulled, stabilises ovipositor penetration against buckling

These features are a subset of all the ovipositing wasp features listed in Table 3.1. Table 3.1 also suggests how these and other features could potentially be implemented to design a flexible steering probe and suitable actuation strategy.

The preliminary studies described so far have focused on the concept of a multi-part probe insertion strategy, where inward tissue penetration is caused by the reciprocal movement of toothed segments rather than by a direct push from the back of the probe.

Two specific studies have been conducted: the first was aimed at identifying a surface topography for a rigid needle which could make needle insertion easier than needle extraction; the second was aimed at identifying the right combination of tooth dimension and material type which could enable an effective tissue surface traversal. These two studies were considered as the basis for the development of a multi-part probe which could insinuate itself inside soft tissue without the need for pushing, with the aim of eliminating buckling. Indeed, because no net force is acting on the probe assembly in ideal conditions, it cannot buckle. In addition a multi-part probe, where the segments are inserted one at a time, is believed to reduce tissue deformation during penetration, thanks to the stabilisation provided by the stationary segments. It is believed that, if the number of segments composing the multi-part probe is increased (i.e. four interlocked segments instead of two) and only one segment is moved at a time, probe insertion can be stabilised even further. Three stationary segments can indeed hold the surrounding tissue with respect to the moving segment, with the positive effect of reducing tissue deformation.

The conclusion of this work is that a reciprocal motion of a segmented probe provided with anisotropic texture could be implemented to penetrate a specific tissue with virtually no net axial push on the probe assembly from the back.

However these studies have also shown that there are several practical and theoretical limitations to the development of a fully-working, flexible, probe prototype capable of demonstrating curvilinear steerability in a compliant medium. The main limitations are as follows:

- in order to prove the feasibility of a "zero net force" insertion strategy (which is considered as the sufficient condition for reducing buckling) for a multi-part probe with anisotropic external surface, a very low friction bearing is deemed necessary. It is required to eliminate all external forces acting either on the target tissue or the actuation system. However there are several practical problems arising when a low friction bearing is used. The insertion depth achievable is directly dependent on the low friction bearing range of motion, which is quite limited. Moreover, the inertia of the target tissue and of the bearing plate can affect the insertion performance depending on the speed and acceleration of the moving segments.

- according to the results presented in Section 3.2.2, the force required by the tip of the probe to cut through the tissue can be almost one order of magni-

tude larger than the force experienced when the toothed probe is tensioned outwards. Furthermore, the limit in the maximum available tooth dimension is dependent on the amount of tissue damage. These aspects are limiting the effectiveness of the anisotropic surface texture required to achieve a "zero net force" insertion when two different probe's segments are reciprocally pushed and pulled.

- the amount of tissue damage introduced by the toothed surfaces was not quantitatively assessed in the two preliminary studies described in Sections 3.2.2 and 3.2.3. The effect of the probe toothed surfaces on living tissue is of paramount importance in order to establish the feasibility of "forward penetration with zero net force".

- the two studies presented in this chapter were conducted assuming the simplification of a straight line insertion path achieved with a rigid probe. The conclusions cannot be directly extended to the case of a curvilinear path achieved with a flexible probe.

- the outcome of the reciprocal motion penetration mechanism is highly dependent on the tissue material properties.

These limitations led the author to propose a simplified concept demonstrator (described in the following chapter) as a more viable and practical way to show that a flexible probe, inspired by ovipositing wasps can indeed be steered into a compliant medium along a curvilinear trajectory.

The "zero net force" insertion strategy will be discarded (i.e. low friction bearing and anisotropic probe surface are not required) and flexible material options will be explored for the probe prototype.

It should be stated that parallel research on "zero net force" reciprocal motion of a microtextured rigid four-part probe, where three probe segments are stationary and only one is pushed at a time, is currently being conducted by another member of the author's research group, Mr. Tassanai Parittotokkaporn. This strategy is believed to decrease the cutting force experienced by the probe segment tip while increasing the "gripping" force provided by 3 out of the 4 stationary probe segments; a publication by Parittotokkaporn et al. [2010] provides further details on this study.

Chapter 4

STING - a Soft Tissue Intervention and Neurosurgical Guide

This chapter describes the evolution of the concept for the biologically inspired flexible and steerable probe into a concept demonstrator able to prove multiple curvilinear trajectories with varying radii in a compliant medium. Three main hypotheses underlying the proposed concept are identified and demonstrated. The three hypotheses are: probe steerability along curvilinear trajectories with different radii, probe steerability with reduced risk of buckling and probe steerability along multiple curve trajectories. Discussion of the technical problems encountered will be presented, and conclusions of the concept viability drawn.

The work presented in this chapter was at the basis for the development of a patent on "Steerable Probes" [Rodriguez y Baena et al., 2009]. Part of this work was also submitted for a journal publication [Ko et al., 2010b].

4.1 Introduction

In Chapter 3 a preliminary study on the insertion strategy as shown by ovipositing wasps was carried out, focusing on a few of the inspirational key aspects that can be potentially considered for the development of a fully working steerable probe, such as "reciprocal motion" by means of "anisotropic surface textures" (see Table 3.1). According to the conclusions of this study, a reciprocal insertion motion of a probe composed of different segments and provided with anisotropic surface textures can be implemented to penetrate soft tissue with virtually no net axial push from the back and therefore significantly reduced risk of buckling. However, although viable, the study on the described insertion strategy has shown practical and theoretical limitations which advise against the implementation of this approach to demonstrate steering of a flexible multi-part probe.

Therefore, building on the conclusions drawn in Chapter 3 and referring again to the elegant example of ovipositing wasps (Section 2.3), and to the previous research on flexible needle steering (Section 2.2), the aim of this chapter is to describe the development of a new approach to percutaneous insertion of flexible probes along curvilinear trajectories, by means of a reciprocating motion, coupled with a novel steering mechanism.

The information contained in the following sections has far reaching implications with regard to the development of new minimally invasive tools for surgery, however the specific methods developed are only taken to proof-of-concept stage through laboratory testing. Clearly, the work presented in this chapter was the result of a complex and time consuming iterative process, the outcome of which is described here. Further details of the key breakthroughs in the design process, outlined in chronological order, can be found in Appendix A.

Based on the biological inspiration, a novel design for a flexible probe is proposed, which allows the implementation of a novel probe motion (i.e. soft tissue penetration) and steering strategy. The bio-inspired flexible and steerable probe is code-named STING, Soft Tissue Intervention and Neurosurgical Guide.

With regard to the work presented in this chapter, the author was solely not responsible for the development of the actuation system and the graphical user interface.

4.2 Concept evolution

Section 2.2 described the main limitations of the research on flexible needle steering (limitations in the maximum dimensions of the instruments, in the range of the curvilinear trajectories available and problems due to excessive tissue tearing). In Chapter 3, a first approach towards the development of a novel probe insertion mechanism inspired by ovipositing wasps was discussed, with regard to a two-part rigid probe inserted along straight line trajectories. The main advantage of the described mechanism consisted in the elimination of the need for a "push from the back", resulting in a significantly reduced risk of buckling. However, because of the force required by the probe's tip to cut through the tissue, the study also highlighted the need for a small, but finite forward push to aid the insertion into soft tissue.

Based on this limitation, and on further considerations regarding steerability issues, which will be described shortly, an evolution of the original concept of a two-part probe into a four-part probe was proposed.

Concerning the implementation of a "zero net force" insertion strategy, it was clear from the beginning how the disparity between the number of stationary parts (or segments) and the moving parts could improve the reciprocal motion insertion

strategy, both by increasing the "toothed" stationary probe surface (thus increasing the "extraction force", F_e in Figure 3.1) and by reducing the cutting force (F_c in Figure 3.1), because of the reduced dimensions of the tip cutting through the tissue at each "reciprocal motion" stroke (one quarter of the tip rather than half).

Furthermore, a four-part probe shows additional conceptual advantages with regard to the aim of demonstrating the steering capabilities of a flexible probe. A flexible probe steered into soft tissue along curvilinear trajectories tends to deflect and buckle inside the tissue. However, cyclic actuation of one single segment in turn (i.e. with three stationary segments at any one time) can stabilise the penetration process, minimising the undesired buckling effect. In a way, the three stationary segments constitute the rail for the motion of the fourth one, regardless of the actual curvilinear shape assumed by the probe in the soft tissue.

In addition, a flexible four-part probe can be potentially guided independently by each segment along a curvilinear trajectory in a 3D space: the interaction between the tip of each probe segment and the tissue can determine a specific steering direction and, by coupling this effect for the various probe segments, a complex 3D trajectory can theoretically be followed.

A cross-section of the preliminary flexible probe prototype, herein called "alpha" prototype, used to perform the experiments described in this chapter is shown in Figure 4.1a. This 4-part prototype, which is further described in the following sections, is used to prove the concept of probe steering along multiple curvilinear trajectories in a compliant medium, as qualitatively shown in Figure 4.1b. While a complete description of the evolution of the design into the alpha prototype is beyond the scope of this chapter, details of the iterative design process are provided in Appendix A.

4.3 Concept analysis

The research strategy adopted to demonstrate flexible probe steering in a compliant medium was to aim for a complete proof of concept, which is the particular focus of the study presented in this chapter. Qualitative conclusions about the concept viability and considerations about the technical issues encountered were then used as the basis of a quantitative study of some of the key features of the concept (Chapters 5 and 6). These results were then used to build an improved prototype, or "beta" prototype, which fulfills the specifications of a European funded project in neurosurgical robotics. A study of the improved performance achieved with the beta prototype and its integration within FP7 ROBOCAST [Robocast-Project, 2010] is included in Chapter 7.

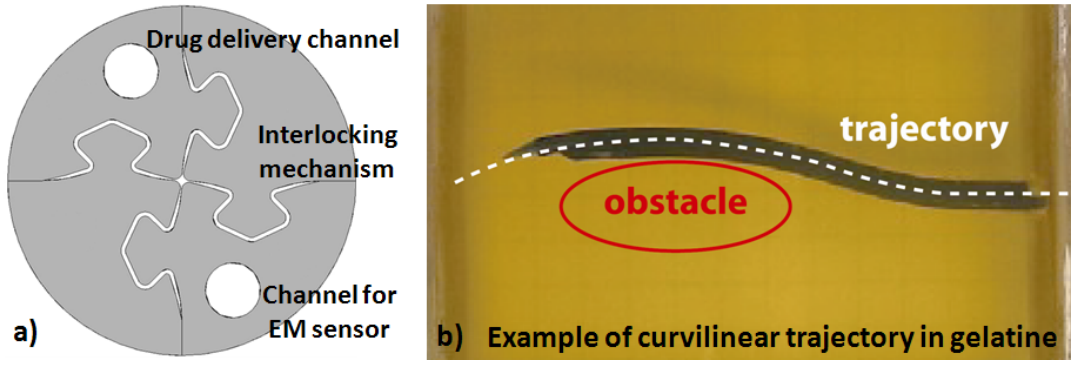


Figure 4.1: a) Flexible probe prototype cross-section (Ø= 12 mm, length = 200 mm) composed of four interlocked segments. Two functional channels are included: one for medical procedures (e.g. localised drug delivery), the other houses an electromagnetic tracking sensor required to control probe position and orientation [Frasson et al., 2010a]. b) An example of a planar curvilinear trajectory in gelatine.

This chapter focuses on the simple proof of concept of some of the key advantages of the flexible probe steering approach. Therefore, arbitrary choices and simplifications dictated by contingency (i.e. limitations in time and budget resources) and by previous successful or unsuccessful attempts will be taken into account and underlined where necessary.

The list of functional specifications aimed for in the research presented hereafter can be summarised as follows:

- probe able to steer in 2D
- probe design able to cater for a possible future extension to 3D
- probe able to steer along arbitrary curvilinear trajectories (i.e. with varying radius of curvature)
- probe able to achieve multiple curvilinear trajectories
- probe able to perform with reduced risk of buckling within tissue

These functional specifications result into two main design specifications, which are also the key features distinguishing this work from the previous work on flexible needle steering (Section 2.2):

- probe made out of a flexible material (i.e. which can comply to the surrounding tissue)
- probe composed of several interlocked segments, where each segment is able to independently guide the probe in a different direction and where the cyclical actuation of each segment in turn is expected to substantially reduce the risk of buckling within tissue.

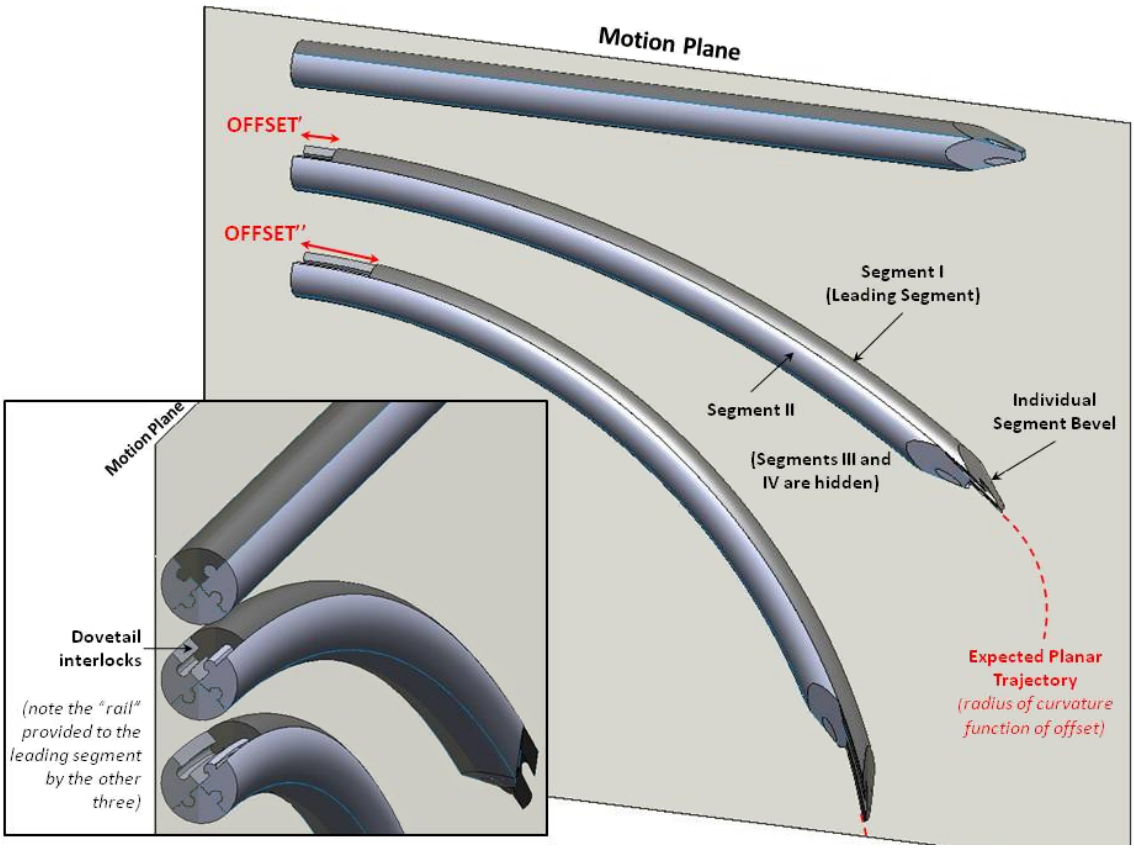


Figure 4.2: Diagram of the flexible multi-part probe in three different bending configurations. The inset shows an example of probe cross-section, in order to illustrate how the probe segments are interlocked together.

By successfully addressing both the functional and design specifications summarised above, the research presented in this chapter has resulted in a probe which can steer in a compliant medium along curvilinear trajectories with **different radii**, with **reduced buckling** inside tissue.

Figure 4.2, which shows a diagrammatic of the multi-part flexible probe, illustrates the main conceptual features of the steerable flexible probe. The probe is composed of four segments (named as segment I, II, III, IV in Figure 4.2) interlocked together thanks to a dovetail mechanism (see inset in Figure 4.2). Each probe segment features a bevel tip. The interlocking mechanism allows the different probe segments to slide one with respect to the others along the longitudinal direction of the probe. Thanks to this relative motion between segments, the probe can steer along curvilinear trajectories with different radii, as illustrated by the different configurations assumed by the probe in Figure 4.2. This unique approach to probe steering takes the name of "programmable bevel steering", details of which are included in Section 4.5, where a relationship between the offset between segments and the radius of curvature is proposed. Furthermore, because each segment is “con-

strained" by the other three, a reciprocal motion actuation, where each segment is pushed in turn, limits the risk of buckling during penetration into a compliant medium.

This work is described in Sections 4.5, 4.6 and 4.7. The flexible probe prototype system briefly described in Section 4.2 (alpha prototype) is described in detail in the following section.

4.4 The alpha prototype system

To address the functional and design specifications for the development of a flexible probe prototype system suitable for proof of concept studies (i.e. a fully functional prototype capable of curvilinear motion within a compliant tissue of brain-like consistency), two main rigs and several probe prototypes were designed, developed and manufactured (see Appendix A). Particularly, four main challenges appeared clearly since the first steps were taken towards the implementation of a successful proof-of-concept:

- the identification of a suitable multi-part probe design, where different segments are interlocked together but able to slide reciprocally
- the identification of a suitable soft material, flexible enough to bend when inserted into a compliant medium of brain-like consistency and at the same time stiff enough to be actuated and driven from the back of the probe (i.e. stiff in tension and compression)
- the identification of a suitable, "iterative", flexible-probe manufacturing method, which could permit modifications and improvements of new prototype designs according to prototype performances, with limited budget and time
- the identification of a suitable actuation strategy for the flexible multi-part probe

Several simplifications and arbitrary choices were made, in order to successfully address the challenges mentioned above. These have been highlighted, where necessary, in the following sections.

4.4.1 Manufacturing methods and materials for probe prototype development

The manufacturing method which was identified as the most suitable, in terms of costs and prototype production times, was Rapid Prototyping (RP).

RP is an "additive manufacturing technology" which allows the manufacturing of Computer Aided Design (CAD) models. Layers of materials (liquid or powder) are laid down in such a way that the model is built up from a series of cross-sections. The different layers are then "joined" together with different techniques (e.g. melting, sintering, curing). The drawbacks of RP relate to the limited manufacturing spatial resolution and the limited choice of materials available.

The RP method was compared to two main alternative methods: injection molding and extrusion (see Appendix B). Both alternative methods allow the use of a wider range of flexible materials. Technical manufacturing difficulties also exist in these methods, but they can be addressed through finer refinements of the manufacturing tools at increasingly higher costs, while, in the case of RP, the spatial resolution is physically limited by the printing machines available (42 μm in the X and Y direction and 16 μm in the Z direction, [Objet-Geometries-Ltd., 2010a]). The dimension of the smallest feasible feature of a model is limited by the RP spatial resolution and by the material chosen: it is suggested that RP prototypes in flexible materials should not have "weak" features smaller than 1 mm. However, considering the initial requirements for a manufacturing method which is affordable and results in a short lead time, RP was chosen as the most suitable manufacturing method for this early phase of work.

In parallel to the development and testing of different probe prototypes, which took several months, RP techniques also improved, and a new RP machine was launched by Objet [Objet-Geometries-Ltd., 2010a]. The RP machine, "Connex500^{TM}", was the first multi-material 3D printing system. This printing machine is able to jet two different model materials simultaneously, allowing to print different parts of a model in materials with different mechanical or physical properties. In addition, composite materials (so called "Digital Materials^{TM}", [Objet-Geometries-Ltd., 2010b]) can be obtained by mixing two different materials during the printing process; with this method, materials with a range of different Shore A hardness values can be obtained.

4.4.2 The alpha prototype

The Connex500^{TM} machine was used for the development of the alpha prototype, which will be shortly described, together with the novel actuation mechanism.

The prototype is composed of 4 interlocked segments made of different materials. The key geometrical features (length = 200 mm, outer diameter (OD) = 12 mm) are illustrated in Figure 4.3, where a 3D view and the cross-section of the prototype are shown. The OD dimension of 12 mm derives from the limited manufacturing resolution of the RP method. The prototype length of 200 mm was arbitrarily defined

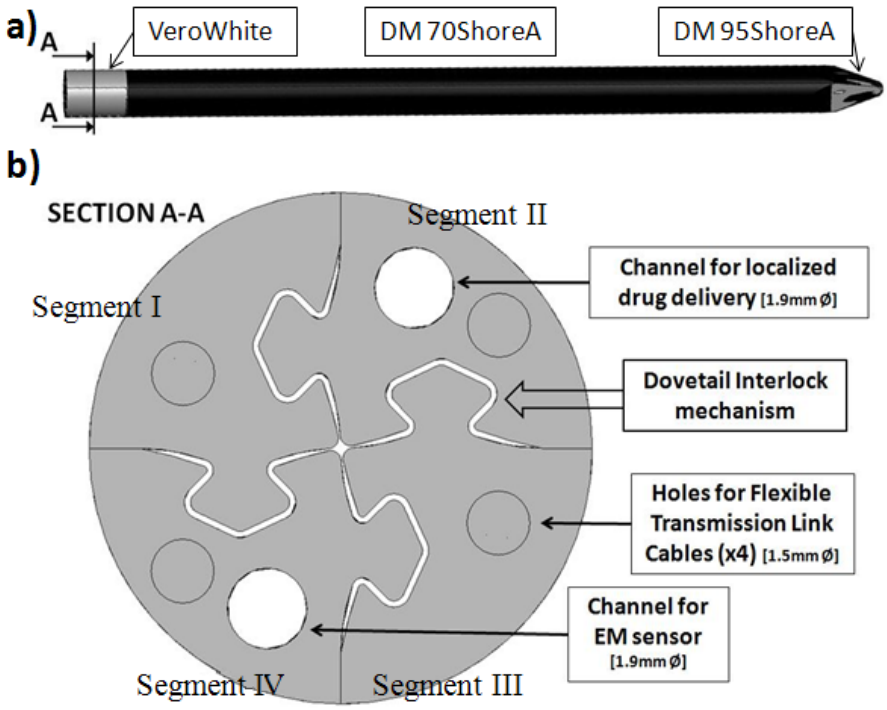


Figure 4.3: Alpha prototype. a) 3D view with material labels; b) Cross-section

by taking into account the typical working volume of an adult skull.

Two of the segments are equipped with 1.9 mm diameter hollow channels, which run along the full length of the probe: one houses an Electro-Magnetic (EM) tracking sensor [Norhter-Digital-Inc., 2010a] required to estimate the probe's tip position and orientation, the other acts as a general purpose working channel which can, for instance, be used for suction or drug delivery.

Each segment is composed of three parts with different material properties:

- the core is composed of a rubber-like material with high elasticity; specifically a Digital Material^{TM} was chosen (DM_9870, hardness of 70 Shore A, tensile strength of 3 MPa, elongation at break of 60% and tensile tear resistance of 13 N/mm, [Objet-Geometries-Ltd., 2010b]). The DM_9870 material is a mixture of TangoBlackPlus material (27 Shore Scale A and elongation at break of 218%) and VeroWhite Material (VeroWhite – FullCure 830; tensile strength of 50 MPa, hardness of 83 Shore Scale D, elongation at break of 20%).

- the leftmost extremities of each probe segment (Figure 4.3a) are made out of a rigid plastic material (VeroWhite – FullCure 830; tensile strength of 50 MPa; hardness of 83 Shore Scale D; elongation at break of 20%) to improve the probe material toughness at stress points. The leftmost part of each segment also features a 1.5 mm OD hole, which is used to secure the probe to a mechanical transmission cable, as shown in Figure 4.4.

- the rightmost part (the tip) of 2 out of the 4 segments (segment I and segment III) is made out of a Digital Material^{TM} more rigid than the segment core. A DM_9895 material was selected (hardness of 95 Shore A, tensile strength of 20 MPa, elongation at break of 30% and tensile tear resistance of 46 N/mm, [Objet-Geometries-Ltd., 2010b]). Since the aim of the research herein presented is to achieve a planar curvilinear trajectory, only two opposing segments are required to steer "left and right". This explains the choice of hardening the tip of these two leading segments in order to ensure that a fixed bevel tip angle is maintained. The choice of hardening the tip of the two steering segments derives from the fact that, as observed during manual tests of an early prototype (with flexible material tips) in gelatine, the very tip of the steering segments bent against tissue resistance and therefore lead the probe to curve during tissue penetration along the direction of the deformed tip rather than according to the bevel tip angle. The bevel tip angle of the alpha prototype was set to 20^{o}.

As stated in Section 4.2, a "push from the back" actuation strategy was identified as the most suitable for a concept demonstrator (Appendix A includes further details about how a push from the back was found to be the ideal choice for probe insertion). The actuation box developed to drive the alpha prototype is shown in Figure 4.4. Each segment of the probe is controlled via a linear actuator assembly connected to a transmission link cable (defined as "mechanical transmission cable" in Figure 4.4) with a diameter of 1.5 mm. The transmission link is formed by a shape memory alloy (SMA) wire (NiTi SE 508, nickel titanium, [EUROFLEX-GmbH, 2010]); the material is chosen for its superelastic properties at room temperature (elastic ductility 10 times greater than steel) and for its high buckling resistance ([EUROFLEX-GmbH, 2010]). The four linear actuators are packaged into a free-standing actuation box to improve handling and integration into the experimental setup (shown in Figure 4.4).

Each linear actuator is composed of:

- a DC motor with embedded encoder (Maxon Amax22, Model # 300679, 4.4 gear ratio, Maxon Motors Inc.)
- a lead screw (4mm pitch, Automation Ltd.) - screw and nut
- a rigid shaft coupling to connect the motor shaft with the screw
- a linear bearing (Igus Ltd.) attached to the nut, to ensure only axial motion
- a mechanism for fixing the "mechanical transmission cables" to the moving nut

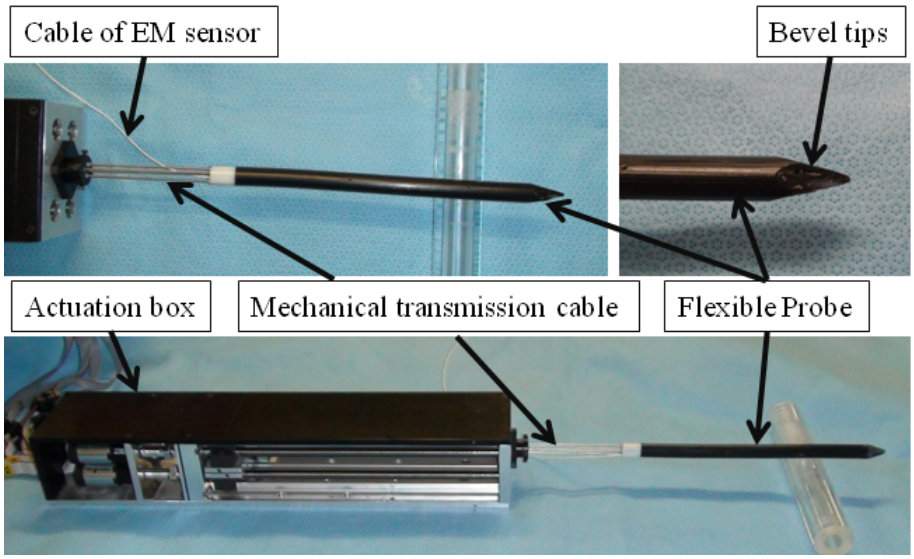


Figure 4.4: Alpha prototype attached to the actuation box

The three potential main advantages of the new proposed biologically inspired approach to flexible probe steering, hypothesised in Section 4.3 and here repeated, will be demonstrated in the next sections through the alpha prototype system just described:

1. the probe can steer in a compliant medium along curvilinear trajectories with different radii
2. the probe can steer in a compliant medium along curvilinear trajectories with reduced risk of buckling
3. the probe can steer in a compliant medium along multiple curved trajectories

Three sets of experiments were performed to prove the three hypotheses. A common experimental setup, shown in Figure 4.5 and described in Section 4.4.3 was used to perform the different experiments, which are outlined in the following sections.

4.4.3 Experimental setup

Figure 4.5 shows the experimental setup used to test the steering capabilities of the alpha probe prototype in a gelatine sample. The linear actuators are controlled via a compactRIO embedded controller programmed in Labview [National-Instruments-Inc., 2010]. A Labview-based graphical user interface (GUI) was developed and integrated into the setup in order to log key control parameters. An electro-magnetic (EM) tracking sensor (Aurora 5DOF Flex Cord sensor with 1.8 mm diameter, [Norhter-Digital-Inc., 2010a]) was employed to estimate the probe's tip position. A 6 wt.% gelatine phantom was prepared, as the gelatine at 20˜21ºC is

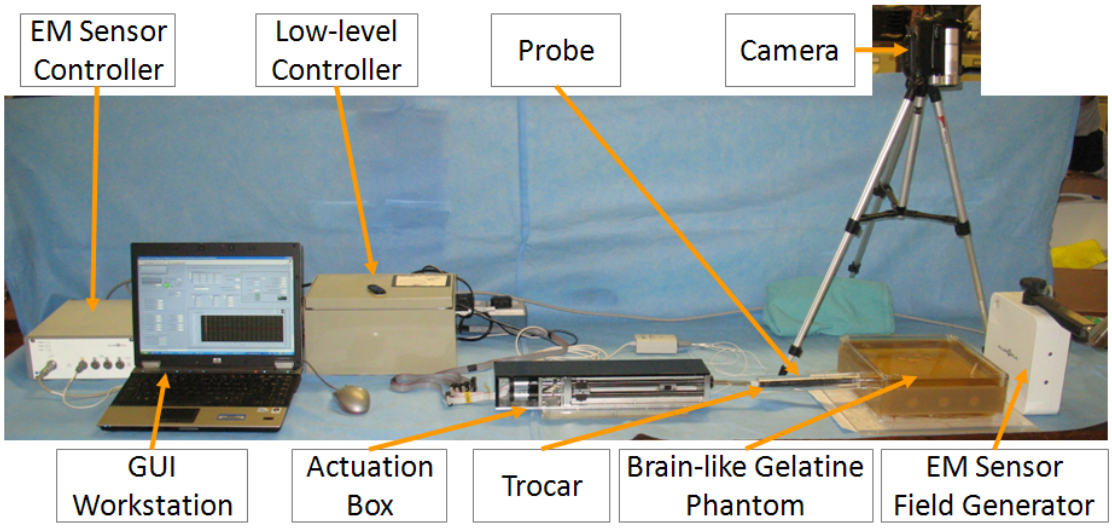


Figure 4.5: Experimental setup for prototype testing

reported to nearly replicate the resistance of in vitro canine brain at 38^{o}C [Minhas et al., 2007]. Gelatine, instead of agar gel (see Section 3.2.2), was selected for its ready availability and for practicality, since it is easier to handle and solidifies homogenously when large volumes are required. A custom-made trocar, with 12.5 mm inner diameter, was also added to the setup to eliminate the possibility of probe buckling outside of the gelatine phantom. As a complement to the EM tracking data, all trajectories were also captured using a video camera (Sony Handycam HDR-SR10E) mounted on a static tripod in a top-down view arrangement. The probe segments were lubricated with a silicone compatible lubricant.

4.5 The "programmable bevel" concept

Hypothesis: *"The probe can steer in a compliant medium along curvilinear trajectories with different radii"*

Previous research on flexible needle steering (Section 2.2.1) has shown that the asymmetric resistive forces acting on a bevel needle tip inserted into soft tissue force the needle to bend along a curved circular trajectory [Webster et al., 2005, Alterovitz et al., 2005]. However, for a given set of needle and tissue properties (i.e. needle tip geometry, needle stiffness and tissue stiffness), only one single radius of curvature is achievable, as demonstrated experimentally by Wedlick and Okamura [2009].

The concept proposed in this thesis, named "*programmable bevel tip*" states that, thanks to the multi-part design of the flexible probe, the radius of curvature obtained during probe insertion into a compliant medium can vary according to the relative position of the various probe segments. Figure 4.6 illustrates the effect of the resistive forces acting on the bevel tips of two non-aligned probe segments.

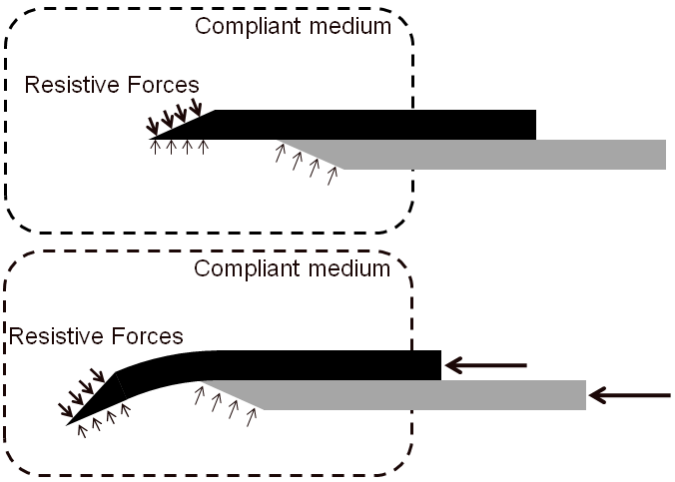


Figure 4.6: Diagram of the resistive forces acting on the flexible multi-part probe when one probe segment (black) is protruded in respect of others (grey).

When the assembly is pushed forward into the compliant medium, the unsupported part of the protruding segment tends to bend under the effect of the resistive forces, thus leading the whole probe to follow the trajectory imposed by the very tip of the probe.

Thanks to the sliding capability of the interlocked segments, when one segment is pushed forward, it becomes the "leading" segment (segment I in Figure 4.2 or the black segment in Figure 4.6). It is then this offset segment which determines the plane and the concavity of the curvilinear trajectory when the probe is pushed forward. As shown in Figure 4.2, the radius of curvature obtained during the insertion process (or "steering angle") is believed to be a function of the offset between the leading segment and the other segments. The bigger the offset, the smaller the radius of curvature (compare, in Figure 4.2, the probe in the resting position, the probe in the OFFSET-I configuration and the probe in the OFFSET-II configuration).

Each probe segment has a fixed bevel tip angle. Therefore, for a given probe segment stiffness and medium, there is only one single radius of curvature which can be generated [Wedlick and Okamura, 2009]. However, since the leading segment is protruding at the probe's tip according to the offset imposed at the base, it is believed that the amount of unsupported length associated to the leading segment affects the deflection magnitude experienced by the segment as a result of tissue reaction forces during insertion. Therefore, by modifying the offset of the leading segment, it is possible to re-orient the segment's tip (*programmable bevel tip*) and thus to control the trajectory followed by the probe assembly.

The testing protocol used to empirically demonstrate the viability of the "programmable bevel tip" concept is described in the next section.

4.5.1 Testing protocol

Ten simple flexible probe insertions into gelatine were performed varying the steering offset between the leading segment and the other three segments, using the experimental setup shown in Figure 4.5.

The offsets considered are: -30, -25, -20, -15, -10, -5, 0, 10, 20 and 30 mm (note that offset sign relates to steering direction: segment I is associated to a negative offset, segment III to a positive one). Preliminary trials demonstrated that larger offsets caused the leading segment to be more likely to buckle. The probe was oriented in such a way that the segments I and III bend in a plane approximately horizontal, to ensure that the probe does not approach too closely either the bottom of the gelatine box, or the surface of the gelatine. The trajectories of the tip of the segment containing the EM sensor were recorded using EM tracking measurements. Each test started at rest, with all four segments aligned and embedded 10 mm into the gelatine sample. The leading steering segment (segment III for a positive offset and segment I for a negative offset) was then driven further into the tissue by the required offset amount. Finally, all four segments were pushed together into the sample at a constant speed of 1 mm/s to a depth of approximately 150 mm. The 1 mm/s speed was set according to the time required by an experienced neurosurgeon to insert a DBS probe during a neurosurgical intervention (as calculated from video footage). This speed setting also broadly agrees with the recommendation by Binder et al. [2005] of advancing and withdrawing microelectrodes or other instruments at a rate not greater than 0.5 mm/s, in order to avoid hemorrhage complications.

After each test, trajectory data measured by the EM tracking system were first projected onto the plane of best fit. A "principal component analysis", executed with a function available in MATLAB, was used to calculate the coefficients of the first two principal components defining the normal vector to the plane of regression which minimises the perpendicular distances between the data and the fitted model. The projected data were then fitted to a circle to find the average radius of curvature for each trajectory. On the basis of these measurements, curvature values (i.e. the inverse of the radii of curvature) for each offset were computed.

4.5.2 Results and discussion

Figure 4.7 shows the pictures captured by the camera at the end of each of the 10 experiments of the "programmable bevel tip" test. From a qualitative observation of the pictures, it appears that there is a proportional relationship between the offset and the degree of curvature achieved in gelatine by the flexible probe.

Most of the trajectories and corresponding circles are plotted in Figure 4.8a, while Figure 4.8b shows an enlarged view of the same.

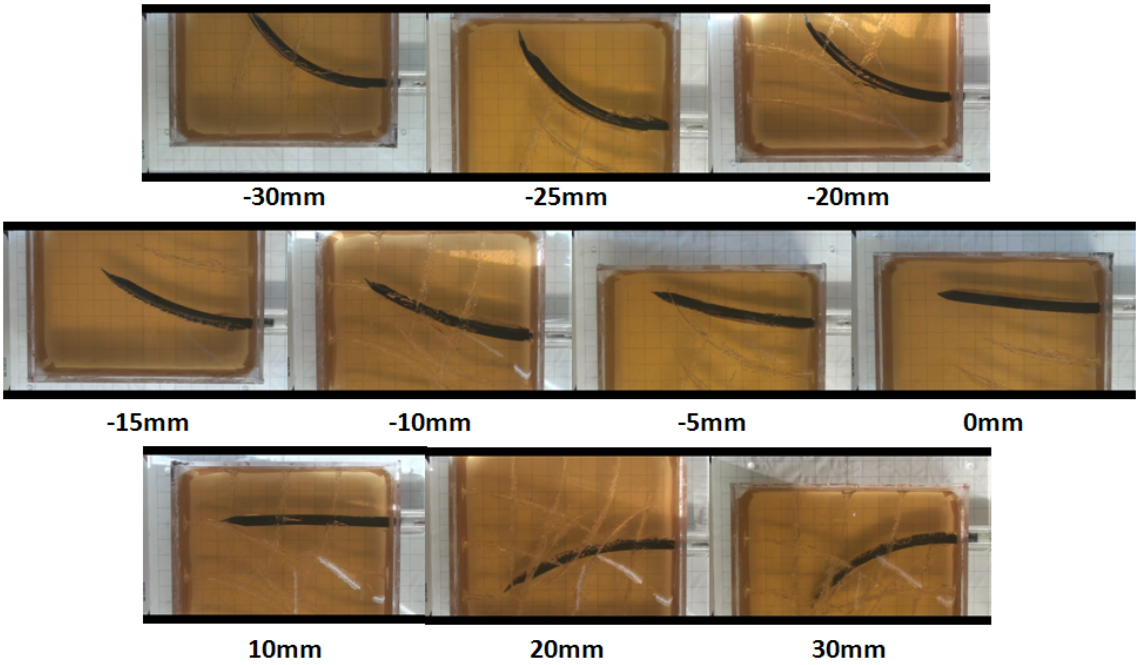


Figure 4.7: Flexible probe trajectories for different steering offset values. Each picture corresponds to the last frame of the video records

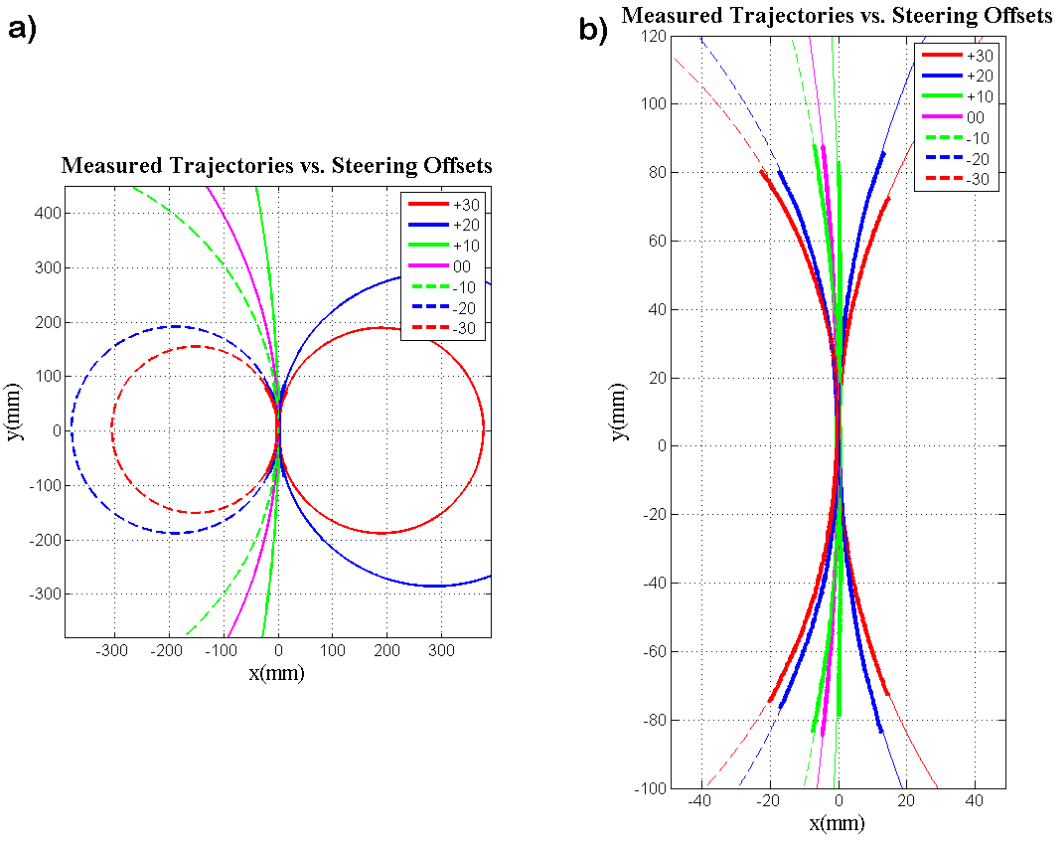


Figure 4.8: Fitted trajectories. a) Best fit circles for each tested steering offset; b) Enlarged view of the trajectories achieved for offsets between -30 mm and 30 mm. (Only a selection of results is shown)

Offset (mm)	**Curvature** ($mm^{-1} \cdot 10^{-3}$)	**Steering Radius** (mm)
-30	-6.5	-153
-25	-5.6	-180
-20	-5.3	-190
-15	-3.6	-274
-10	-2.0	-504
-5	-1.7	-578
0	-1.2	-829
10	0.4	2472
20	3.5	287
30	5.3	189

Table 4.1: Steering Offset vs. Curvature and Steering Radius

Computed radii of curvature and curvature values for each offset are listed in Table 4.1 and plotted in Figure 4.9, where a linear trend of the offset-curvature relationship is also shown.

According to Figure 4.9, the curvature is approximately proportional to the steering offset, with a coefficient of $1.96 \times 10^{-4}\,\text{mm}^{-2}$. The slight asymmetry in curvature values between positive and negative offsets could stem from manufacturing inaccuracies, trocar alignment errors, probe deformation, etc. This, however, is accounted for by the small but finite x-axis intercept of 4.04 mm, as illustrated in Figure 4.9. While the linear approximation adopted here represents a substantial simplification and will require further work, it is sufficiently accurate to demonstrate that a relationship does exist between offset and curvature and that this relationship is approximately linear.

4.6 Reciprocal motion for reduced buckling

Hypothesis: *"The probe can steer in a compliant medium along curvilinear trajectories with reduced risk of buckling"*

The capability of sliding the interlocked segments with respect to each other not only allows the reorientation of the probe's bevel tip by offsetting one of the four segments, but it also allows the implementation of a "reciprocal motion" insertion strategy which takes inspiration from the reciprocating mechanisms described in Chapter 3 ("zero net force" reciprocal motion of probe segments achieved by means of anisotropic surface textures). "Reciprocal motion" is herein intended as the insertion of each probe segment one at a time, while the other three remain stationary.

The hypothesis states that, when "reciprocal motion" is applied to the various probe segments, the insertion process is stabilised and buckling of the flexible probe

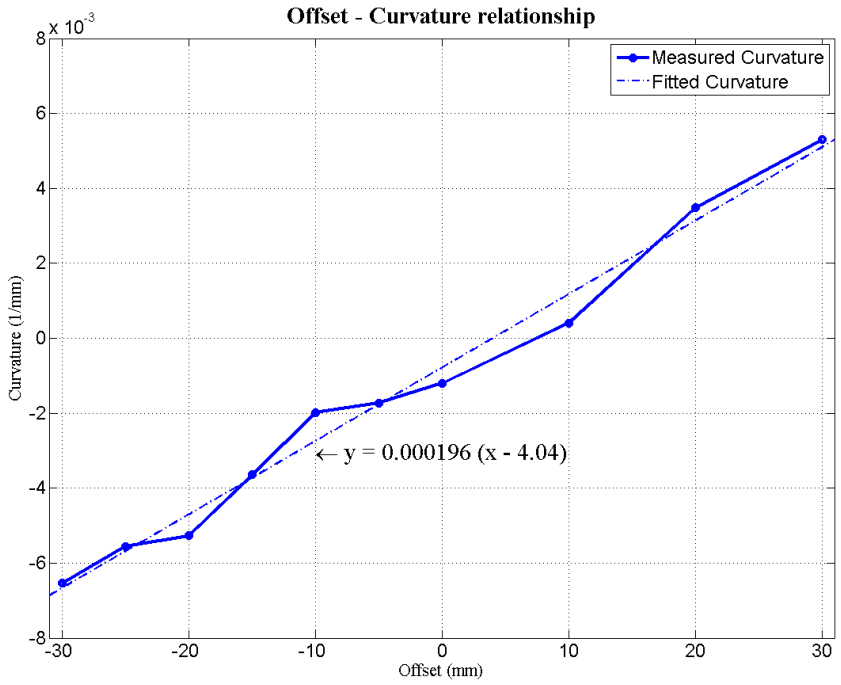


Figure 4.9: Relationship between offset and curvature with linear fit.

in the compliant medium is reduced (see Figure 4.10 for the definition of "buckling" in this context). From an intuitive point of view, when each probe segment is inserted one at a time, the remaining stationary segments act as "rails", helping to transfer the forward push from the back of the probe, along the axis of the probe, to the tip. It is believed that, thanks to this approach to probe insertion, each segment will follow the "rail" provided by the other segment, guiding the probe's body to follow the tip. This strategy will prevent the probe's body from deviating from the track laid out by the tip (i.e. buckling), therefore avoiding tissue tear. Ideally, whatever curvilinear configurations are taken by three segments, the fourth can be slid forward without affecting the existing configuration of the probe as a whole. This strategy is also believed to minimise the amount of tissue deformation at the probe-tissue interface, with a consequent reduction in tissue damage, because only one quarter of the whole probe's volume is moved at each instant.

4.6.1 Testing protocol

The aim of this test was to compare the behaviour of the different insertion strategies, "direct push" and "reciprocal motion", when the probe is inserted along a curvilinear trajectory.

Two preliminary probe insertions were performed, according to the following protocol:

1. *Direct Push*: the probe was inserted 10 mm inside the gelatine, with all probe

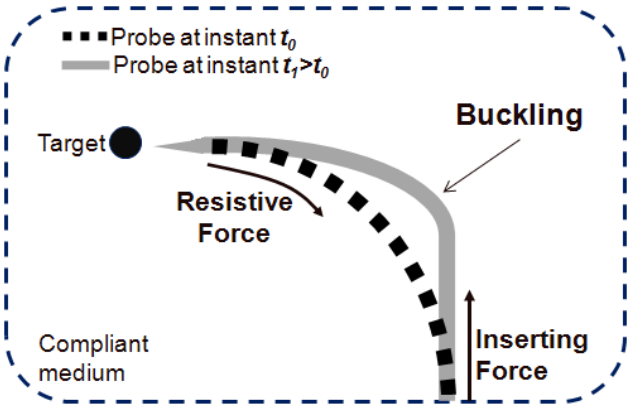


Figure 4.10: Probe buckling inside a compliant medium. At a certain instant t_0 the flexible probe has achieved a particular trajectory inside the medium; at the next instant t_1, because of the tissue resistive forces acting on the probe's body, the inserting force causes the middle of the probe to buckle, while the tip does not move forward. A "reciprocal motion" insertion strategy is believed to reduce the buckling effect.

segments aligned; the speed parameter was set to 1 mm/s. The four segments were then actuated together, but, until the desired offset was reached (+30 mm), the speed of segment III (leading segment) was increased by a predefined amount, compared to the global velocity of 1 mm/s. At the same time the speed of the other segments was reduced by the same amount . Once the offset was reached, all probe segments were pushed together inside the gelatine at a speed of 1 mm/s, down to a depth of 190 mm.

2. *Reciprocal Motion*: the probe was inserted 10 mm inside the gelatine, with all probe segments aligned; the amplitude of the stroke used to reciprocally push each probe segment was set to 8 mm. All segments were then reciprocally actuated with an average speed of 4 mm/s (overall probe motion of 1 mm/s, peak speed of 8 mm/s, see Appendix C), but, until the desired offset was reached (+30 mm), the amplitude of the stroke of segment III (i.e. the leading segment) was increased by a predefined amount, bigger than the intended amplitude of 8 mm. At the same time, the amplitude of the other segments was reduced by the same amount. Once the offset was reached, the cycle of segment strokes was repeated until the whole probe was pushed inside the gelatine, down to a depth of 190 mm. A detailed and in depth explanation of the "reciprocal motion" insertion strategy devised for these experiments is available in Appendix C.

The stroke amplitude of 8 mm was set based on considerations about the results of preliminary "reciprocal motion" tests. This value, coupled with a stroke speed of

4 mm/s, was found to ensure that the deformation of the probe segments (i.e. the compression of the moving segment with respect to the tension of the stationary segments) is overcome. An imposed stroke amplitude of 8 mm at the base of one probe segment is therefore almost completely transmitted up to the tip (Section 4.8 provides further information about segment deformation).

A suitable offset rate of change for both experiments (i.e. one which would result in the desired offset for both the protocols to be reached at similar penetration depths) was manually tuned and a suitable speed was identified by trial and error.

In both cases, being interested in assessing buckling (i.e. any deviation of the probe's body from the trajectory traveled by the tip, Figure 4.10), a large penetration depth (190 mm) was reached, which was coupled with a large offset (+30 mm). In order to assess buckling, the overall shape of the curved probe at different time frames was captured using the video camera system and processed through a manual segmentation process implemented in MATLAB.

A second protocol was also implemented to illustrate more clearly the potential benefits of a "reciprocal motion" insertion strategy as opposed to a "direct push" strategy. In this protocol, the experimental setup shown in Figure 4.5 was slightly modified (Figure 4.11). The gelatine box was removed and substituted with a second trocar ("Tip Trocar" in Figure 4.11), positioned at an angle of 30° with respect to the trocar at the base of the probe. The probe was free to slide inside both trocars, which were also lubricated using a standard silicone grease. The probe was inserted in both trocars (see "Camera View" in Figure 4.11). The part of the probe exposed between the two trocars was 125 mm long. In this way, the central part of the probe's body between the two trocars was left free to bend (buckle) because no tissue resistive forces were acting around it.

Three tests were performed for each insertion strategy: "direct push" was performed by pushing the probe 50 mm forward at 1 mm/s; "reciprocal motion" was performed by reciprocally actuating each probe segment with an average speed of 4 mm/s (overall probe motion of 1 mm/s) and an amplitude of 8 mm for each stroke, until the whole probe was pushed 50 mm forward.

An automatic segmentation process was then implemented in MATLAB to calculate the area of "expansion" of the probe (i.e. the bending/buckling of probe's body) during the experiment. Figure 4.12 shows a typical original image of the probe's body at rest. A binary image is then obtained and the probe's edges are extracted. The probe edge extraction is performed for all the frames of interest; the area of the probe contour in the first frame is calculated and used as a reference (red contours in Figure 4.12). The total area (or "area of expansion") is calculated as the area enclosed between the contours of the probe in the first frame and the contours of the probe in the frame when probe buckling is greatest. The ratio between the

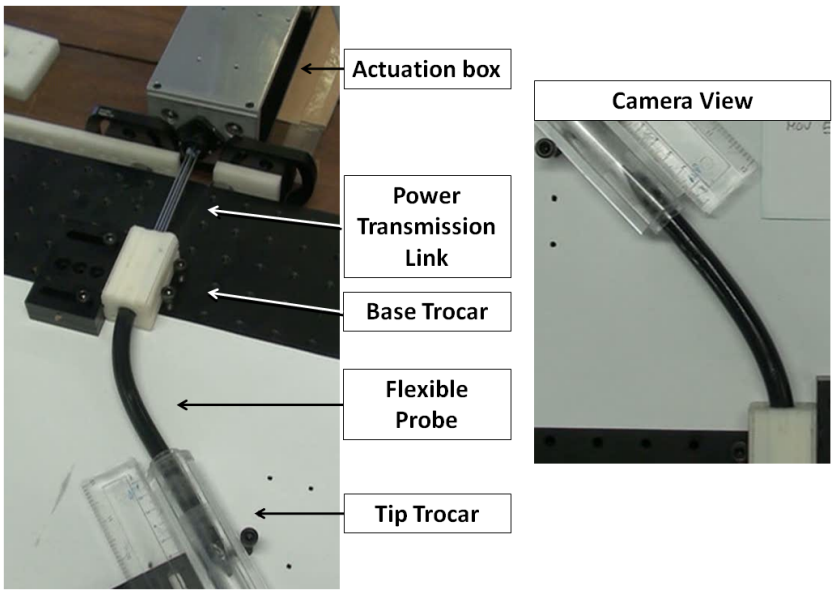


Figure 4.11: Modified experimental setup for the second testing protocol of "reciprocal motion".

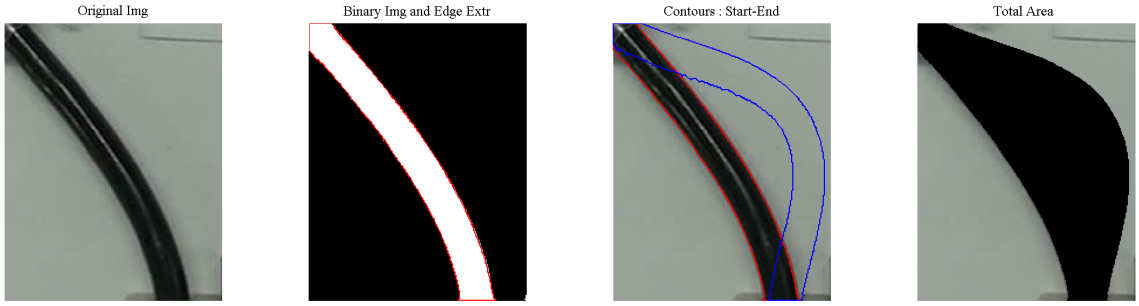


Figure 4.12: Image analysis method for the second testing protocol of "reciprocal motion".

total area and the initial area is finally calculated and used as a measure of the extent of buckling experienced by the probe after final insertion.

4.6.2 Results and discussion

The "reciprocal motion" tests were aimed at identifying possible differences in probe behaviour during two different types of insertion strategies: "reciprocal motion" and "direct push". The experiments relative to the first "reciprocal motion" protocol, which was performed in gelatine, were recorded with the video camera (Figure 4.5). Image frames were captured every 30 seconds and the corresponding images were manually processed in order to select the probe contours. The results are shown in Figure 4.13.

Results in Figure 4.13 show that both insertion strategies produced a small amount of buckling. The contour of the probe's body captured in the last frame shows that the probe is slightly more bent than at previous instants (Figure 4.10).

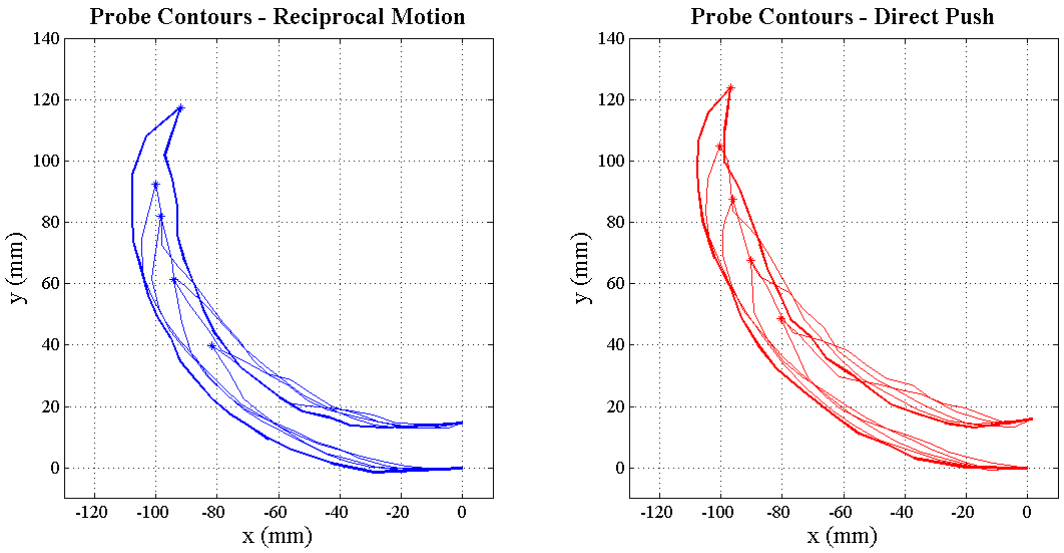


Figure 4.13: Probe contours during the "reciprocal motion" test (left) and "direct push" test (right). The probe contour is captured every 30 secs. The probe contours at the very beginning of the tests (first minute) are not shown.

Qualitatively, it could appear that there is a small difference in buckling between the "reciprocal motion" insertion strategy and the "direct push" strategy, whereas buckling in the "direct push" test seem slightly more pronounced. However, considering the limited accuracy of the video recordings and of the manual method for the identification of the probe contours, quantitative evaluations of the buckling behaviour were not proposed. Limitations in the measurement accuracy are mainly due to the probe deviating from the initial original horizontal plane of curvature, loosing its parallelism with the camera plane and to the operator-dependent manual method of selecting the probe contours from the recorded images.

Furthermore, even though the largest viable steering offset was chosen (+30 mm) in order to produce a highly curved trajectory (i.e. small radius) and the full insertion length was used in the experiments (i.e. 190 mm out of 200 mm probe length), these conditions are apparently not extreme enough to trigger evident buckling in a gelatine sample with brain-like consistency. Although these results do not demonstrate that "reciprocal motion" can reduce buckling, they definitely confirm that the material chosen for the probe prototype (section 4.4.2) represents a good compromise between the need for a soft material (i.e. able to produce large curvatures) and the need for a material stiff in tension and compression (able to transmit the driving axial force along the full length of the probe). It should be stated here that a probe prototype with reduced diameter and increased bending capabilities is expected to be more evidently affected by the buckling problem, although such investigation will be carried out in the scope of future work.

Therefore a second "reciprocal motion" testing protocol was devised. This pro-

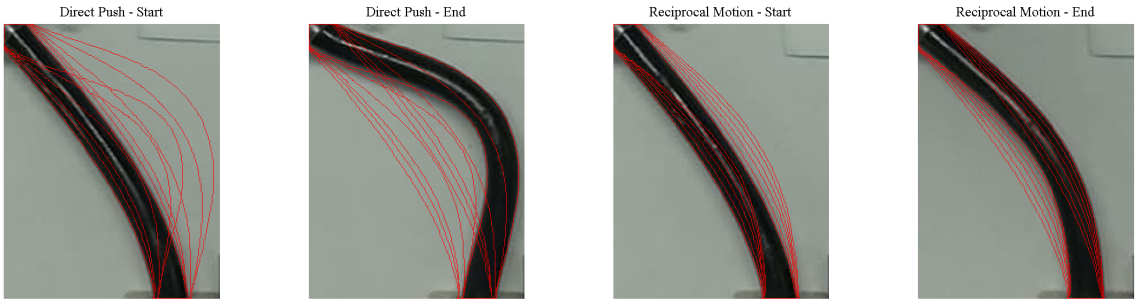


Figure 4.14: Probe contours of the "direct push" and "reciprocal motion" new tests; the contours are overlaid onto the initial (start) and final (end) original frame images.

Test	**Method**	**"Area of Expansion" Ratio**	**Average ±STD**
1	Direct Push	2.59	2.37±0.20
2		2.33	
3		2.19	
4	Reciprocal Motion	1.51	1.54±0.06
5		1.51	
6		1.61	

Table 4.2: Ratio of Expansion Area: "direct push" vs. "reciprocal motion"

tocol does not represent a realistic probe insertion into a compliant medium, but it directly shows the main benefit of a "reciprocal motion" insertion strategy: the capability of the flexible probe to follow a trajectory of insertion, with reduced buckling, despite a set of adverse boundary conditions.

Figure 4.14 shows the probe contours automatically extracted from the segmented images from the video recordings (every 10 seconds) of a "direct push" test and a "reciprocal motion" test. Table 4.2 summarises the "area of expansion" ratio for all 6 tests, and the average area of expansion for the "direct push" and the "reciprocal motion" tests.

Although limited in scope because of the artificial experimental setup devised for these tests, the results demonstrate that a "reciprocal motion" actuation strategy is significantly beneficial in reducing excessive probe deflection (i.e. buckling). It should be noted that in these experiments, buckling is triggered by the contact conditions of the trocar used at the probe's tip (Figure 4.11a). The driving axial force presents a component which is normal to the direction of the tip trocar. Therefore, a friction force tangential to the trocar direction is generated, which prevents the probe from sliding through the trocar. This happen during both "direct push" and "reciprocal motion" strategies, but in the latter case, the motion is less affected by the contact conditions. In addition, from qualitative observations of the video recordings of "reciprocal motion" tests, it appears that an additional factor determines the

probe's deformation (i.e. the "area of expansion"): friction between the sliding segments. Even though the probe segments are lubricated, the friction between the sliding segments causes the probe to partially twist and swing at each stroke, and this can justify the fact that the "area of expansion" ratio during reciprocal motion experiments is significantly bigger than 1.

4.7 Achieving complex trajectories in a 2D space

Hypothesis: *"The probe can steer in a compliant medium along multiple curved trajectories"*

A combination of the "programmable bevel" concept and "reciprocal motion" actuation strategy is believed to allow a multi-part, flexible probe to achieve complex curvilinear trajectories in a compliant medium, with reduced probe buckling during tissue penetration. To achieve multiple curves (i.e. to change the concavity of the probe path part way through the insertion process), the offset between the two steering segments is gradually changed, with the first leading segment giving way to the opposite segment at the point where "left motion" becomes "right motion".

4.7.1 Testing protocol

The aim of this test was to demonstrate that multiple curve planar trajectories can be achieved through a combination of the "programmable bevel tip" and "reciprocal motion" strategy.

The experimental setup shown in Figure 4.5 was employed. The probe was actuated according to the "reciprocal motion" protocol explained beforehand and detailed in Appendix C, but a new steering command was manually sent to the actuators, via the GUI, in order to steer the probe in the opposite direction when required by the operator. The probe was inserted 10 mm inside the gelatine, with all probe segments aligned. The stroke amplitude was set to 8 mm. All segments were reciprocally actuated with an average speed of 4 mm/s (overall probe motion of 1 mm/s), but until the desired offset (+25 mm) was reached, the amplitude of the stroke of segment III (leading segment) was increased with respect to the others. Once the desired offset was reached, the cycle of segment strokes was repeated until a new steering command was sent. When the probe was approximately inserted 70 or 80 mm into tissue, the operator issued the new steering command: the desired offset was set to -25 mm. This command forces the segment opposite the leading one (i.e. segment I) to increase the stroke amplitude with respect to the others. Over a few stroke cycles, segment III aligns with the other segments (II and IV) while segment I becomes the new leading segment. The probe will then curve in the



Figure 4.15: Example of a double curve trajectory achieved in gelatine. The probe prototype used for this experiment has a more rigid tip (VeroWhite, Section 4.4.2), but this is not affecting the results.

opposite direction.

4.7.2 Results and discussion

Figure 4.15 shows the picture captured by the camera at the end of one "multiple curve trajectory" test. A double-curve trajectory was achieved through a "reciprocal motion" insertion strategy where the steering offset was inverted (i.e. approximately half way into the insertion process). These results, even though qualitative, confirm that achieving curvilinear trajectories with multiple curvatures, through reciprocal motion, is indeed viable. However, the number and variety of possible curvilinear trajectories depend on the relationship between probe length and maximum curvature achievable, and ultimately on probe material flexibility and cross-sectional dimensions. For this reason, the number of possible curve trajectories was found to be quite limited in the tests performed with the current probe prototype, which justify the focus on the optimisation of a number of key design parameters of the probe, which will follow in subsequent chapters.

4.8 Discussion of Failures

This short section lists the main technical problems encountered during the various experiments described in this chapter, which could lead or were proven to lead to failure in achieving the desired curvilinear trajectory.

- *Buckling:* even though the presence of the external trocar prevents the flexible probe from buckling outside the tissue, the probe can still buckle inside the

tissue (Figure 4.10). This problem has been tackled by opting for a "reciprocal motion" insertion strategy (Section 4.6.2), but a clear demonstration of the efficacy of this strategy inside a compliant tissue has not been proved yet. In addition a more fundamental understanding of the mechanical reasons underlying the potential benefits of the "reciprocal motion" insertion strategy should be addressed in future work.

- *Segment deformation:* when a single segment is moved with respect to the others (at each stroke in the case of "reciprocal motion" or when the steering offset is modified in the case of "direct push"), each segment undergoes more or less marked deformations, and therefore there may be discrepancies between the offset imposed at the base and the offset actually measured at the tip. For example, one segment tends to compress when it is pushed with respect to the others, and then tends to release the accumulated compression and stretch when the neighbours are moved forward.

- *Probe twisting:* whenever one segment is moved with respect to the others (at each stroke in the case of "reciprocal motion" or when the steering offset is modified in the case of "direct push"), the probe tends to twist along its long axis. Consequently, the tip orientation changes with respect to the planned trajectory, with the consequent introduction of an unwanted off-plane error, which cannot be corrected in the current 2D probe configuration.

- *Segment separation:* it may occur (Figure 4.16) that, at a certain point along the probe length, or at the probe's tip, one segment (most likely the segment which is being pushed) disengages from the remaining segments (interlocking mechanism failure). From this point on, the segments are likely to come apart, because one ore more segments are no longer fully restricted by the others.

The last three problems are supposedly caused, ultimately, by the frictional forces between the segments which, however, depend on many other factors: probe material and frictional properties, the lubrication regime between the segments, the geometrical design of the interlocking mechanism, the configuration assumed by the probe in the medium, the medium's material and frictional properties and the actuation strategy (e.g. insertion speed, stroke amplitude and stroke speed for "reciprocal motion" and offset generation method).

The problem of segment separation is considered to be the most critical, because it represents ultimate and irreversible failure. Indeed, probe buckling, probe twisting and probe segment deformation can be partially corrected through a close-loop control strategy, by modifying the actuation inputs (stroke amplitude, speed and steering offset at the base [Ko et al., 2010b]). On the contrary, segment separation

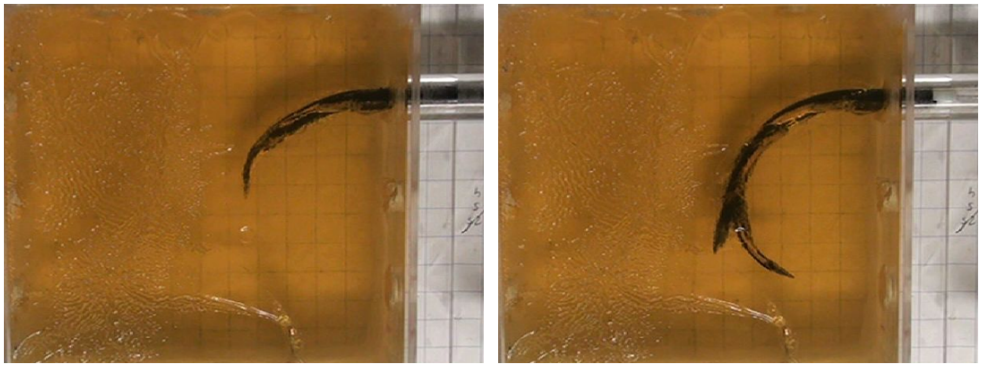


Figure 4.16: Example of failure: one segment separates from the others during an experiment performed in gelatine

is irreversible and cannot be corrected by any means. For this reason, irreversible segment separation will be addressed in the next chapter, where an optimisation procedure for the interlocking mechanism of the prototype is proposed. Future research will focus on addressing and minimising the effect of the outstanding issues.

4.9 Conclusions

This chapter describes the author's successful attempt to address, with limited resources and at a proof-of-concept level, the aim of the research discussed in this thesis and defined, in Chapter 1, as follows:

"to prove the viability of a novel, biologically-inspired, probe steering mechanism as demonstrated by a fully functional prototype capable of curvilinear motion on a plane within a compliant tissue of brain-like consistency"

Inspired by the biological example of ovipositing wasps and by previous research on needle steering, and strong of the foundations outlined in Chapter 3, a fully functional prototype is proposed, in the form of a flexible multi-part probe composed of four interlocked segments.

This prototype, developed alongside a suitable actuation rig, is used to prove the three main hypotheses underlying the novel flexible probe's ability to achieve curvilinear planar motion within a compliant tissue of brain-like consistency:

1. the probe can steer along planar curvilinear trajectories with different radii
2. the probe can steer along planar curvilinear trajectories with reduced buckling
3. the probe can steer along planar multiple curve trajectories

Three different sets of experiments are performed to prove the three hypotheses:

1. the first experiment demonstrates that the flexible multi-part probe can follow curvilinear trajectories with different radii, and that the curvature is a function

of the offset between the two steering segments, which can be controlled - a programmable bevel tip.

2. the second experiment addresses the topic of flexible probe buckling during insertion into a compliant medium. A "reciprocal motion" strategy was devised to reduce the possibility of buckling of the multi-part probe. Because of practical limitations, it was not possible to demonstrate significant differences in buckling when a "direct push" strategy is adopted instead of a "reciprocal motion" strategy. However, the experiment demonstrates that under different conditions (in air, rather than in a compliant medium), a "reciprocal motion" strategy is significantly less affected by buckling than "direct push" actuation.

3. the third experiment qualitatively demonstrates that multiple curves can be achieved during one insertion of the flexible multi-part probe. Specifically a double curve trajectory was achieved by modifying the steering offsets of some of the probe segments.

To conclude, a flexible multi-part probe prototype, composed of interlock segments able to slide with respect to each other, was used to prove the viability of a novel, biologically-inspired, probe steering mechanism. This was demonstrated by showing that the probe is able to steer along an arbitrary planar trajectory, thanks to a "programmable bevel tip" and with reduced risk of buckling, thanks to a "reciprocal motion" insertion strategy.

Because of the proof-of-concept aim, the scope of the experiments performed is limited and many issues, limitations and questions remain unsolved.

For instance, with regard to the flexible probe prototype, specifications about the mechanical and frictional properties of the material, also with respect to the properties of the compliant medium, should be taken into account for the design and development of an optimised prototype. The actuation strategies here described are empirically shown to provide positive results, in the specific embodiment considered. However, different combinations of stroke amplitude and speed could result in changes to probe behaviours.

It is clear that this study has laid the basis for a more detailed and quantitative research effort which spans across many topics, which can be taken to a much deeper level and thus impact related fields more significantly (see Chapter 8). However, based on preliminary considerations regarding the flexible probe's behaviour and failure, the research presented in this thesis focuses on a key probe design feature, the interlocking mechanism between probe segments, which is the topic of Chapter 5, where an optimisation procedure for the interlock design is proposed. Furthermore, Chapter 6 tackles the basis of an analytical approach towards the parametrisation

of a complete model of the flexible probe, aimed at describing and understanding its behaviour, with a particular focus on irreversible failure scenarios.

It should be stated that parallel research on modeling probe-tissue interaction at the bevel tip interface, with the aim of simulating flexible probe bending during soft tissue penetration, is currently being conducted by another member of the author's research group [Oldfield et al., 2011].

Chapter 5

Modelling for Design Optimisation

This chapter centres upon the optimisation of the probe design, with a focus on one of the most critical features: the interlocking mechanism between the segments. The interlocking mechanism is indeed a crucial feature in ensuring that the probe segments slide reciprocally, but at the same time do not separate. A model of the probe's cross-section is devised and an optimisation procedure is applied to identify the best interlock geometry in terms of resistance to failure (i.e. irreversible segment separation). The model is also validated experimentally. Finally, conclusions with regard to the development of an optimised prototype are drawn.

Part of this work has been published in conference publications [Frasson et al., 2009, 2010b].

5.1 Introduction

The previous chapter has shown that steering of a flexible multi-part probe in a compliant medium is viable and that the "programmable bevel tip" can be controlled to achieve different curvilinear trajectories. The programmable bevel tip can be modified by adjusting the offset between the segments and this requires the segments to slide smoothly with respect to each other and without separating. In addition, smooth and steady sliding between the probe segments is of paramount importance to ensure an effective "reciprocal motion" insertion strategy (Section 4.6), which is important to reduce the risk of probe buckling when complex trajectories are followed.

However, in Section 4.8 it was shown that complications may arise, which affect the probe's performance (e.g. probe buckling and twisting, irreversible segment separation and deformation). From experimental observations, it appeared clearly that irreversible separation of the probe segments should be the critical problem to be tackled. The geometry of the interlocking mechanism, together with the probe material, is a key element on which this kind of failure depends.

The aim of this chapter is thus to identify critical operative conditions which may result in the failure of the probe, where particular relevance is given to irreversible segment separation, and therefore to define an optimisation procedure for the design of the interlocking mechanism. This is aimed at understanding which geometrical features have the greatest influence on resistance to failure.

This chapter describes the numerical model developed for the optimisation of the interlocking mechanism geometry, the implementation of the optimisation procedure to identify the best interlock geometry and the experimental validation of the model of the best interlock. Conclusions about the models developed and future developments for the design of an optimised probe prototype will be presented (Section 5.4).

5.2 Methodology

In order to address probe failure, a general model of the probe is devised (Section 5.2.1); the model provides the foundations for a systematic parametric analysis of the probe cross-section. A finite element (FE) analysis of the most relevant parameter combinations is proposed using Abaqus v6.8 [Simulia-Corp, 2010] (Section 5.2.2), and an optimisation procedure of the probe cross-section (particularly the geometry of the interlocking mechanism) is applied through numerical models (Section 5.2.3). The results are then validated through experiments (Section 5.2.4).

5.2.1 Parametric probe-interlock model

A simplified 2D model of the probe is shown in Figure 5.1.

The model consists of a moving part, *b*, connected via an interlocking mechanism to a fixed part, *a*. The moving part is to be driven by a constant force, *N*, which, in the real implementation, is provided by a suitable actuator assembly (Section 4.4.2). The interlocking mechanism adopted and shown in Figure 5.1 is similar to the "dovetail interlock mechanism" presented in the previous chapter (see Figure 4.3). A reference system aligned with the axis of the probe is centred in correspondence of the end point of the trocar. In this model, the effect of the unsupported length between the trocar and the soft tissue is considered to be negligible with respect to the length of the probe when inserted into the tissue. In addition, the tissue is modelled as isotropic and considered soft enough not to trigger instabilities.

The interfacial friction coefficient, *f*, between the moving parts, and its variations along the probe's length, are believed to be the main cause of instability (Section 4.8). The friction coefficient depends on the level of lubrication chosen to reduce the tangential force originating from the relative movement between the parts consti-

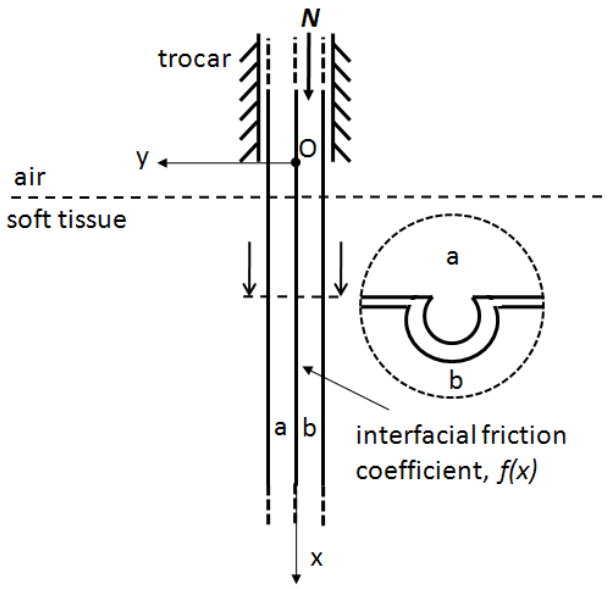


Figure 5.1: Schematic of the simplified model

tuting the simplified probe. In this model, variation of the friction coefficient along the interface is considered. In fact, lack of lubrication may occur along the interface between the moving parts, which may result in the interlocking mechanism failing. Two different failure scenarios are investigated and are illustrated in Figure 5.2.

The first, shown in Figure 5.2a, assumes that the interfacial friction coefficient is high enough to prevent the relative movement between the parts, which have a total length of L. In this scenario, the interlocking mechanism does not fail and, consequently, the equivalent mechanical model is such that the point of the moving segment, b, at $x{=}L$ is left free to rotate but not to translate. According to this scenario, the flexible probe undergoes a deformation (buckling) which forces the probe itself to deviate from the desired trajectory. However, the interlocking mechanism does not fail because an increment of the interfacial friction coefficient with respect to the value required to guarantee relative movement between the mating parts also increases the force needed to disengage the interlocking mechanism itself.

In the second scenario, illustrated in Figure 5.2b, the friction coefficient results in the absence of relative movement between the two segments at $x{=}L$ only. The equivalent mechanical model of the system is thus similar to the one devised in the first scenario, but results in the failure of the interlocking mechanism itself, rather than the buckling of the probe as a whole.

The first condition is trivial, as it can be treated with Euler's formulation for buckling in elastic structures [Timoshenko and Gere, 1961]. Conversely, the second situation includes large deformations and, eventually, failure of the interlocking mechanism.

In order to investigate this failure scenario and identify the interlocking mecha-

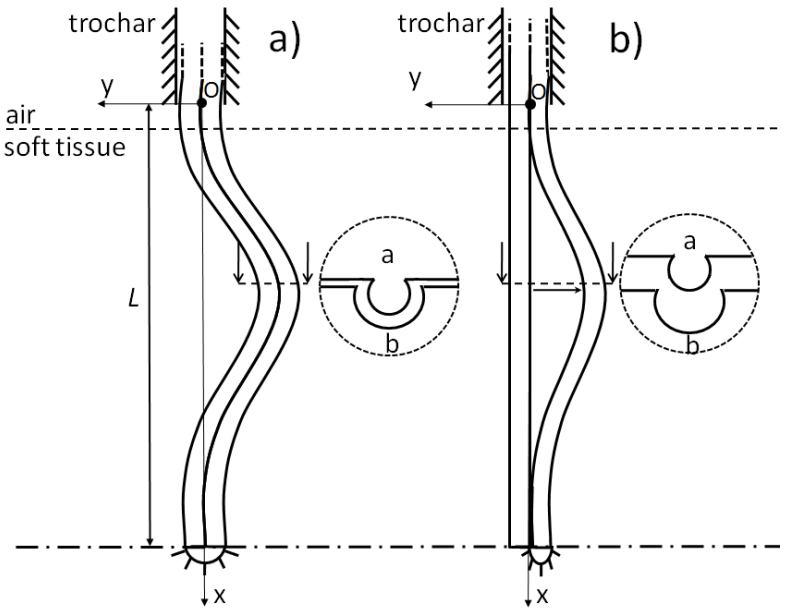


Figure 5.2: Local instabilities that the probe may experience

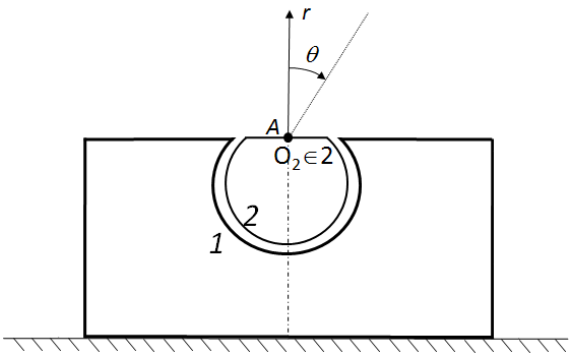


Figure 5.3: Diagrammatic of the numerical model devised for the FE simulations

nism less prone to fail, a systematic analysis of the interlocking mechanism is deemed necessary. For this reason, a 2D numerical model of the interlocking mechanism is proposed, which is shown in Figure 5.3.

The model consists of a block, *1*, where a rail is used to contain and drive the element indicated with *2*. A polar coordinate system, r-ϑ, is located along the axis of symmetry of the system and centred at A, with A being the rest position of element *2*. The point O_2, coincident with the origin of the reference system when no forces are applied, is rigidly attached to body *2* and its position is tracked within the polar reference system. Moreover, all points located at the top surface of body *2* are also rigidly connected to O_2, so that the body can be driven by imposing displacement and/or rotation to O_2 directly.

The ultimate scope for the development of the 2D model shown in Figure 5.3 is the optimisation of the cross-section of the interlocking mechanism. The model,

which provides the foundations for a systematic analysis of the interlocking mechanism, is fully defined when all of the following parameters are considered and defined:

- interlock section geometries
- material properties
- boundary conditions
- interfacial friction conditions between mating surfaces
- loading scenarios

The loading scenarios are simulated by imposing prescribed combinations of displacement and rotation to body *2* via O_2, until failure of the interlocking mechanism occurs. Failure is here intended as irreversible separation between the two probe segments.

The main output of the model is the maximum force that can be sustained by the interlocking mechanism before the two segments come apart. In addition, each simulation provides information regarding the deformation of the interlocking mechanism when the conditions for separation between the moving parts are reached. The maximum extraction force sustainable provides an estimation of the stiffness of the interlocking mechanism and it will serve as the basis for the cross-sectional optimisation of the probe prototype.

5.2.2 Model definition and assessment

Starting from considerations and observations about the real probe prototype and its working conditions, as described in the previous chapter, a more specific 2D interlock model is proposed for cross-sectional optimisation. To this end, some of the parameters mentioned in the previous section will be considered as "variable inputs" to the optimisation procedure, while others will be set for all simulations.

Figure 5.4a shows the simplified cross-section of a four-part-probe. Figure 5.4b shows the geometry of the simplified FE model. In order to limit the number of parameters defining univocally the **interlock geometry**, while allowing a broad sweep of possible geometries to be analyzed, a simple interlock geometry, fully identifiable by four parameters *N*, *R1*, *R2* and *W,* is chosen. This simplified interlock geometry was also selected based upon the design of previous probe prototypes, as described in Appendix A. Only the external half of the interlock geometry is modelled as qualitative observations on the probe prototype demonstrated that failure (i.e. disengagement) starts from this part of the interlocking mechanism. The internal half is indeed constrained by the other three probe segments and thus less prone to failure.

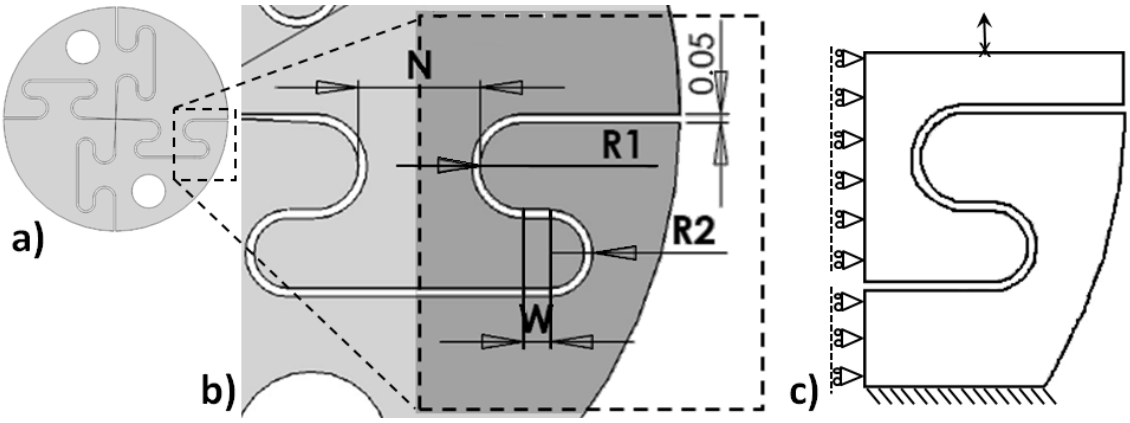


Figure 5.4: a) Simplified probe cross-section. b) The part of the cross-section which constitutes the FE model of the interlocking mechanism (dotted square). The geometrical parameters used to define the cross-section are *N*, *R1*, *R2* and *W*; the clearance between the segments is 0.05 mm. c) Diagrammatic of the numerical model devised for the FE simulations.

The parameter combinations corresponding to interlock geometries which do not interfere with the probe side walls (Equation 5.1) or with functional channels (Equation 5.2) constitute the space where the optimum search is performed (see Figure 5.5 for maximum limits). All values are referred to a probe which is 3 mm in radius, with a working channel 0.9 mm in diameter and a clearance between the segments of 0.05 mm. These values were chosen taking into account the dimensions of the alpha prototype and manufacturing tolerances introduced by the RP technology used in experiments. However, while in numerical models for geometrical optimisation absolute values of geometrical dimensions are not important, relative dimensions between the various features are.

Equation 5.1 limits the sum of all the parameters along the horizontal direction in order to avoid the rail getting too close to the side walls (i.e. not less than 0.1 mm), thus weakening the material layer at the right-hand edge. In addition to Equation 5.1, Equation 5.2 limits the sum of *R1* and *R2* along the vertical direction in order to avoid the interlock getting too close to the working channel (i.e. not less than 0.22 mm), reducing the space between the interlocking rail and the channel, and thus weakening the material surrounding the working channel itself (see also Figure 5.5).

$$N + 2 \cdot R1 + 2 \cdot R2 + 2 \cdot W \leq 2.50 \tag{5.1}$$

$$2 \cdot R1 + 2 \cdot R2 \leq 1.50 \tag{5.2}$$

A plane strain condition is assumed, as the axial length of the segment (200 mm)

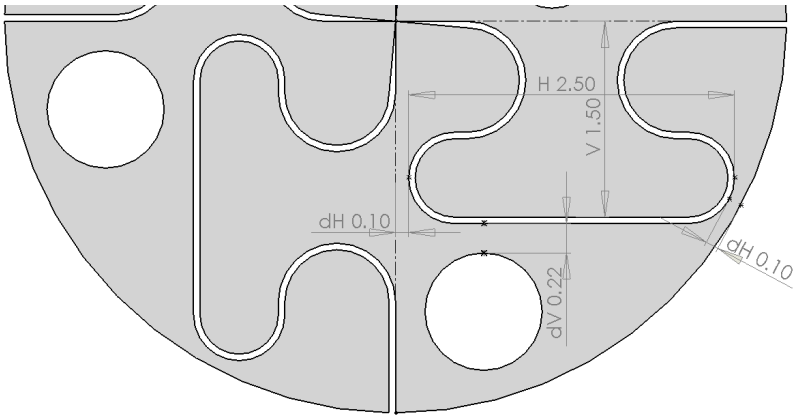


Figure 5.5: Horizontal and vertical limits for possible parameter combinations. Upper limit from Equation 5.1: H=2.50 mm; minimum horizontal distance from sidewalls dH=0.10 mm. Upper limit from Equation 5.2: V=1.50 mm; minimum distance from working channel dV=0.22 mm.

is very large compared to the desired cross-section dimension ($\phi = 6$ mm).

The choice of modelling only the most critical half of the interlocking mechanism (Figure 5.4b, dotted square) leads to the identification of a specific **loading scenario** in which the male part of the interlocking mechanism is pulled out vertically from the female part. Different combinations of displacement and rotation would represent either less critical conditions (i.e. male and female parts engaging more firmly) or impossible conditions (i.e. male part displacing towards the centre of the probe). Therefore, the vertical force required to extract the male part from the corresponding female is chosen as the objective function to be optimised. For larger extraction forces, the interlocking mechanism stiffness would increase, preventing/delaying irreversible failure.

Boundary conditions are detailed in Figure 5.4c, and defined as follows: the bottom of the female part is fixed (Encastré) and the left side of both female and male parts can only slide vertically. The constrained vertical movement is due to the fact that only the right-hand part of the cross-section is considered for the optimisation. Finally, the top of the male part is displaced vertically and the corresponding vertical reaction force is measured.

Regarding **material** choice, it was noticed that linear elastic material models, within the typical average strains calculated in the simulations, are also representative of the hyperelastic material models generally used for rubber-like materials. The extraction force profile is virtually not affected by the material model chosen. Therefore, a linear elastic material model is used, with parameters chosen in the range of almost-incompressible, soft, rubber-like materials: Young's modulus = 2 MPa and Poisson's ratio = 0.475.

Friction behavior at the male/female contact is also considered. As shown in

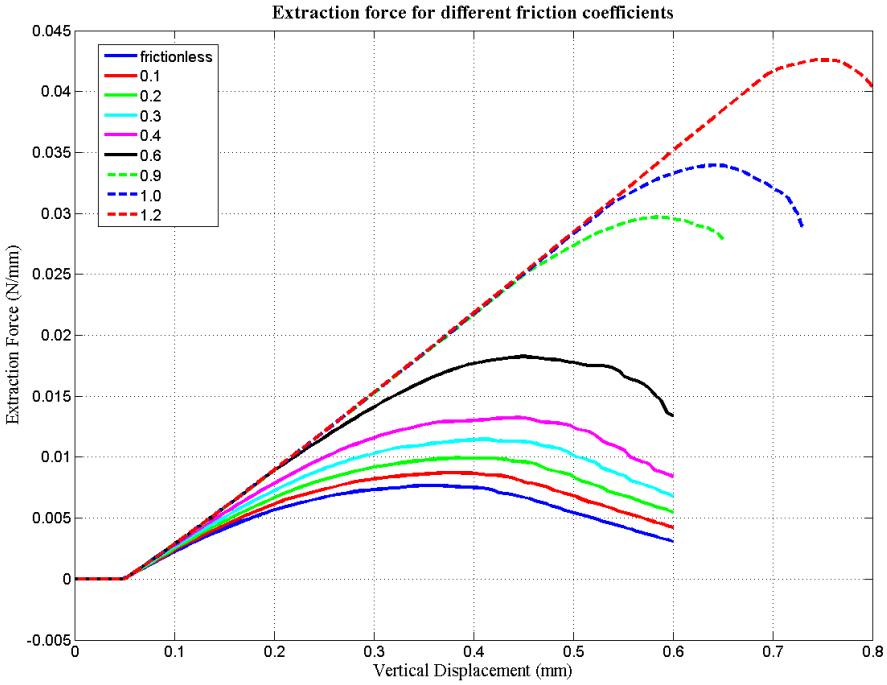


Figure 5.6: Extraction force versus vertical displacement profiles for simulations with different friction coefficients between contact surfaces (from 0 to 1.2, typical of polymer-polymer contact). The geometrical parameters of the model used for this simulation are: N=0.7, $R1$=0.3, $R2$=0.25, W=0.2 mm.

Figure 5.6, for friction coefficients up to 0.6, the maximum vertical reaction force increases linearly with the friction coefficient itself. For friction coefficients larger than 0.6, a sticking behavior predominates and the male and female segments move together as a whole, resulting in a constant interlock stiffness up to the irreversible failure and this is independent of the friction coefficients. Therefore, a frictionless contact behavior is applied to the FE model, as this also represents the weakest scenario.

5.2.3 Cross-section optimisation procedure

The optimisation problem consists of identifying, within all the possible combinations of different values for the geometrical parameters, the combination which provides the maximum extraction force. To guarantee sufficient resolution, the number of possible parameter combinations and the computational time required for each simulation make the problem unmanageable using combinatorial methods. Therefore, an optimisation procedure consisting of a statistical sampling method followed by a probabilistic heuristic method is applied (Figure 5.7).

Initially, the Latin Hypercube Sampling (LHS) [McKay et al., 2000] method is used to identify 30 parameter combinations which homogeneously cover the parameter space with a constant marginal distribution, in order to take into account

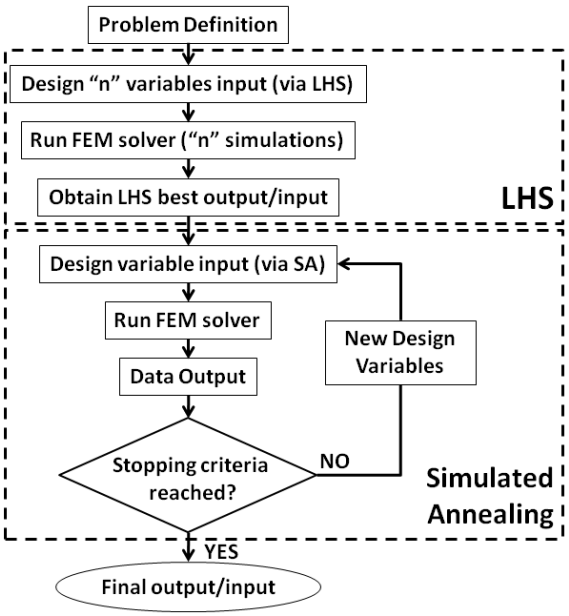


Figure 5.7: Optimum search procedure. A Latin hypercube Sampling algorithm is followed by a Simulated Annealing algorithm. *N*, *R1*, *R2*, *W* are considered as inputs, extraction force as the output.

the maximum possible information available with a limited number of combinations [Hilmann et al., 2005]. The best LHS solution, which has a good probability of being close to the optimum, is then used as the input for the ensuing phase. Here, a heuristic global optimisation method, simulated annealing (SA), searches the optimum, according to user-defined stopping criteria, such as function tolerance and maximum number of iterations [Kim and Hong, 2007]. At each step, the algorithm replaces the current solution with a random nearby solution chosen with a probability that depends on the corresponding objective function value and on a time-varying global parameter.

Latin Hypercube Sampling

The LHS method ensures that the range of each input variable is simultaneously partitioned into n equally probable intervals (or "levels"), where n is also the number of parameter combinations considered. As such, using the LHS method to identify 30 equally distributed parameter combinations means that each parameter range is divided into 30 levels. However, apart from describing the equations defining the "possible" (i.e. existing) combinations, nothing has been said about the range of values for each parameter.

The choice of the parameter ranges resulted in a compromise between the need to explore a wide parameter space (i.e. large ranges) and limitations due to the imple-

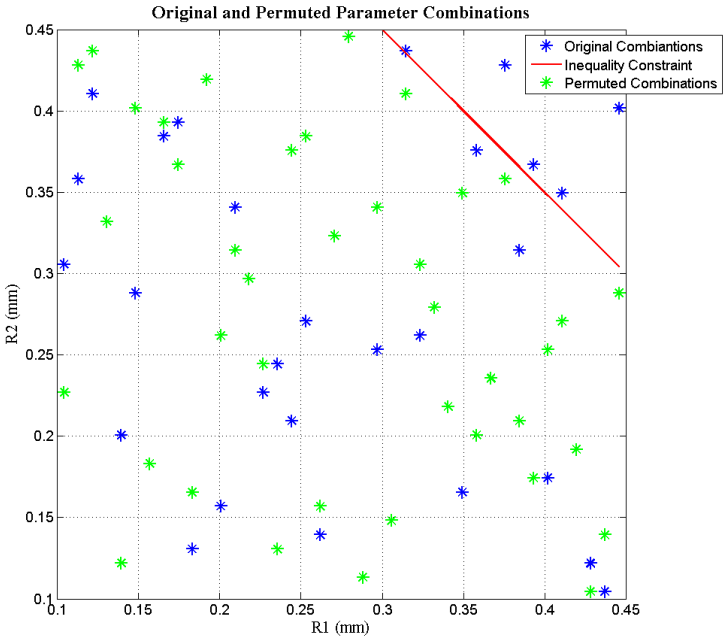


Figure 5.8: Example of CLHS algorithm for a two-parameter space (variables *R1* and *R2*, range 0.1-0.45). In blue the starting LHS combinations, in green the permuted LHS combinations, the red line represents the inequality constraint $R1 + R2 \leq 0.75$.

mentation of the LHS method, which, in the presence of large ranges, may suggest parameter combinations lying outside the "possible" combination space defined by Equations 5.1 and 5.2.

Petelet et al. [2009] proposed an algorithm, the constrained LHS (CLHS), to build a latin hypercube sample which takes into account inequality constraints between the sampled variables. The CLHS algorithm is based on the fact that permuting two values of a variable in a LHS does not break the LHS structure of the sample [Iman and Conover, 1982].

The CLHS algorithm, implemented in MATLAB by the author, was used in this study to scan the initial latin hypercube sample to find the combinations of values that violate the constraints (i.e. Equations 5.1 and 5.2) and then it executes permutations between the values of randomly chosen variables till all new combinations are found, which satisfy the constraints. However, the severity of the inequality constraint affects the distribution of the samples in the parameter space (without substantially affecting the single parameter marginal distribution) because the CLHS algorithm tends to accumulate all permuted combinations near the inequality constraint itself (see Figure 5.8, green permuted parameter combinations).

Since the inequality constraints are defined from geometrical considerations (see Figures 5.1 and 5.2) and are therefore fixed, in order to ensure that the four-parameter "forbidden" volume (the top left section beyond the constraint line in

	N (mm)	**R1** (mm)	**R2** (mm)	**W** (mm)
Min	0.3	0.1	0.1	0.05
Max	1.1	0.45	0.45	0.3

Table 5.1: Maximum and minimum values of the geometrical parameters

the two-parameter example of Figure 5.8) was no more than 20% of the overall four-parameter space, as suggested by Petelet et al. [2009], the parameter ranges presented in Table 5.1 were selected.

Simulated Annealing

Within the 30 parameter combinations provided by the CLHS algorithm, the combination which defines the interlocking geometry with the maximum extraction force is chosen as the input for the ensuing phase, consisting of the implementation of a heuristic global optimisation method.

From the 30 LHS simulation results, any relationship between parameter values and extraction force could not be identified, confirming that all the parameters are simultaneously non-linearly affecting the outcome of the simulations. In addition, considering, for example, the first five best LHS solutions, these are characterised by parameter values which are spread over up to 60% of the original parameter range (the range of the parameter N for the 5 best solutions is 52.5% of the original, 60% for *R1*, 27.5% for *R2*, 47.5% for *W*); this may possibly suggest that the solution to the problem may present many local optima.

With respect to these preliminary considerations, SA was chosen as the optimisation algorithm because it is well suited for solving highly non-linear problems where the global optimum is hidden among many local optima [Kim and Hong, 2007, Kolahan et al., 2007].

The SA algorithm takes its name from the annealing process which takes place in metals. By heating a solid state metal to a high temperature and then cooling it down very slowly according to a specific schedule, the atoms of the material will place themselves in a pattern that corresponds to the minimum global energy of a perfect crystal.

Starting from an initial state (or parameter combination), at each step, the algorithm replaces the current state s with a random nearby state s' chosen with a probability that depends on the objective function values of s and s' and on a time-varying global parameter generally called "temperature", T. Because of this last parameter T, the system can potentially move to a new state s', which is worse than the current one s and this prevents the algorithm getting stuck in a local minimum. The temperature T is gradually reduced as the algorithm proceeds (annealing sched-

	N (mm)	**R1** (mm)	**R2** (mm)	**W** (mm)
Min	0.3	0.1	0.1	0.05
Max	0.5	0.3	0.3	0.2
Initial	0.35	0.148125	0.244375	0.146875

Table 5.2: Maximum and minimum values of the geometrical parameters for the SA algorithm, and initial parameter combination (best LHS solution)

ule), ensuring that at the beginning the parameter space is broadly explored and then the algorithm moves "downhill" according to gradient descent (when $T = 0$). "Re-annealing" can also be scheduled, which forces other "high temperature injections" before execution is terminated. The iterative algorithm is stopped according to user-defined stopping criteria, such as function tolerance, maximum number of iterations and number of stall iterations (i.e. the maximum number of iterations during which the current state s is not modified).

The SA algorithm looks for the optimum within a parameter space defined taking into considerations the results from the LHS simulation results (see Table 5.2). All the possible parameter combinations in Table 5.2 satisfy the physical geometrical constraints expressed in Equations 5.1 and 5.2.

A MATLAB toolbox (Matlab, [The-MathWorks-Inc, 2010]) was used to run the SA algorithm. The initial parameter combination and the parameter space (value of the range for each parameter) are shown in Table 5.2. Stopping criteria are defined as follows: function tolerance= 10^{-4}, maximum number of iterations = 600, stall iterations = 180. These values are based on preliminary tests to optimise algorithm convergence. The objective function consists of a MATLAB function where the four geometrical parameters are the inputs and the corresponding extraction force is the output. The MATLAB function consists of:

1. generation of a Python script able to launch the FE simulation with the current geometrical parameters in Abaqus

2. post-processing of the output file of an FE simulation in Abaqus, where the "maximum extraction force" is extracted, recorded, then inserted into the running SA optimisation algorithm.

5.2.4 Experimental validation of the optimum geometry

Experimental validation of the interlock geometry identified as the optimum was performed by assessing the model's capability of reproducing the experimental extraction force profile. Extraction tests under lubricated (silicone grease) and dry

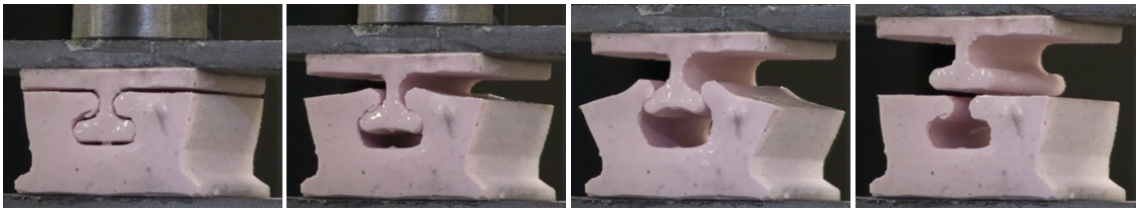


Figure 5.9: Experimental test of the interlocking mechanism. The male and female samples are firmly glued to steel plates. The top plate, attached to a 100 N load cell (2525-807 Series Drop-through), is moved vertically at a constant speed (0.5 mm/s).

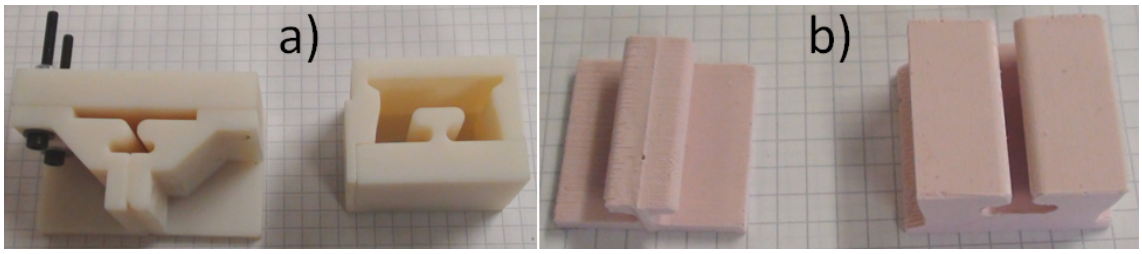


Figure 5.10: a) RP molds for the male (left) and female (right) samples; b) the silicone-rubber samples extracted from the molds (paper grid dimensions of 5x5 mm).

conditions were performed with a Testing Instron machine (Dual Column Model 5565, [Instron, 2010]) (Figure 5.9). Extraction is performed at two, very low, constant speeds (0.1 mm/s and 0.5 mm/s) in order to approach a quasi-static process and identify whether possible velocity-dependent behavior remains.

The samples, designed starting from the optimum interlock geometry (Figure 5.11) were created using a silicone rubber composite (Moldsil, Notcutt Ltd.). Silicone rubber was selected because, as opposed to the flexible materials available with RP methods (e.g. Tango Black), its manufacturing method does not introduce any anisotropy in the material itself and it is easy to mold. Silicone rubber, in its liquid form, was mixed with the catalyst and then poured into molds manufactured in rigid plastic (using RP). After a curing period of 24 hours, the molded pieces were carefully removed from the mold (see Figure 5.10). The rubber-like interlock has external dimensions of 35x30x20 mm; this choice is dictated by sample manufacturing and testing requirements. The base of the female sample is extended on the lateral sides to increase the bottom surface area glued to the fixed plate. This prevents any relative motion between the female sample and the fixed plate during the extraction tests.

In order to improve the reliability of comparisons between simulated and experimental results, the following modifications of the FE model were performed:

- a modified cross-section was obtained by adding the lateral extensions onto

the female part (as seen in Figure 5.10).

- the plane-strain assumption was removed because manufacturing and testing limitations did not allow a sample where the width to length ratio satisfies the plane-strain assumption to be produced.
- a 3D model with dimensions of the actual sample was built.
- a Mooney-Rivlin, hyperelastic, material model was applied, with parameters obtained from tensile and shear tests of the silicone rubber used in the experiment.

With regard to the last point, the choice of a suitable material model and the identification of the right values for the model parameters are of paramount importance to ensure that numerical simulations can be properly compared and validated through physical experiments. The linear elastic model used for the 2D cross-sectional optimisation procedure could introduce undesired approximations and therefore a more accurate material model for the silicone rubber was chosen.

Tensile tests and shear tests were deemed necessary to identify the tensile stress-strain and the shear stress-strain behaviour of the material used. The tests were performed according to the British Standard "*Physical testing of rubber. Guide to the selection and use of methods of test for rubber*" (BS 903-1:1995), particularly "*BS 903-5: Physical testing of rubber - Part 5: Guide to the application of rubber testing to finite element analysis*" and "*BS903-A14: Physical testing of rubber: Method for determination of modulus in shear or adhesion to rigid plates - Quadruple shear method*".

Silicone rubbers at large strains are accurately modelled with hyperelastic models [Korochkina et al., 2008]. An evaluation function feature available in the Abaqus software was used to determine which hyperelastic model (e.g., Ogden model, Mooney-Rivlin model, Yeoh model) fitted better the tensile and shear stress-strain data. The software then provided the parameter values for the model chosen. A Mooney-Rivlin model was selected as the most suitable and the corresponding model parameters identified were used for validation.

5.3 Results and discussion

Figure 5.11 shows the interlock geometry that maximises the extraction force according to the described optimisation procedure; corresponding geometrical parameters are listed in Table 5.3. The extraction force profile for this geometry is shown in Figure 5.13, blue line. A 2D FE model of the interlocking mechanism of

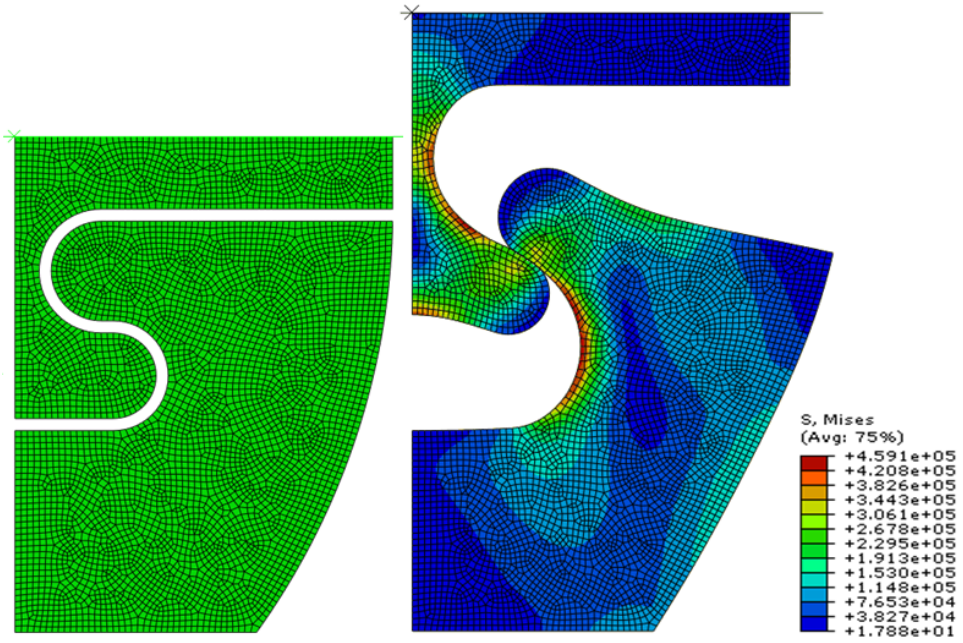


Figure 5.11: Undeformed and deformed cross-sectional optimal geometry

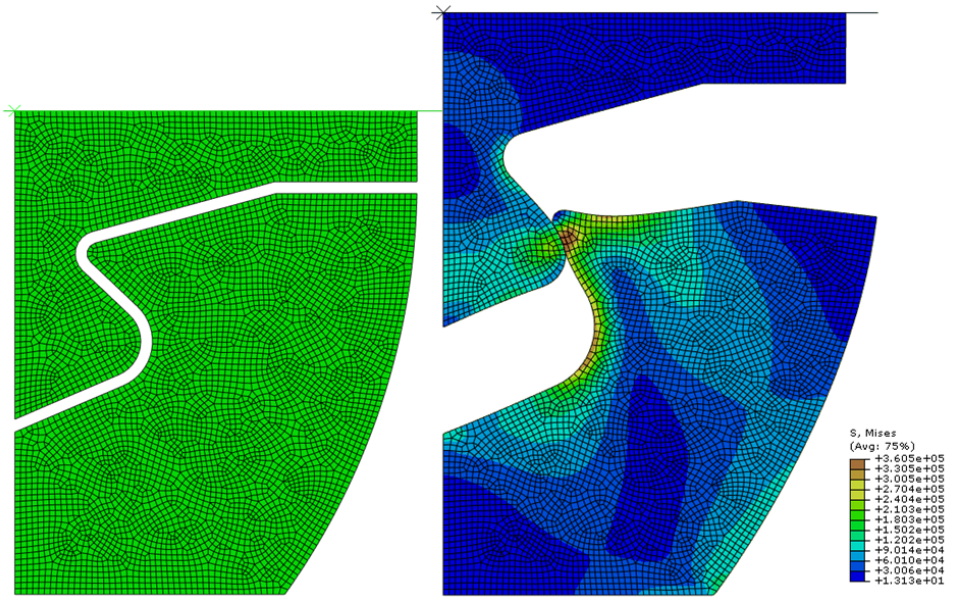


Figure 5.12: Undeformed and deformed cross-sectional geometry of the alpha prototype

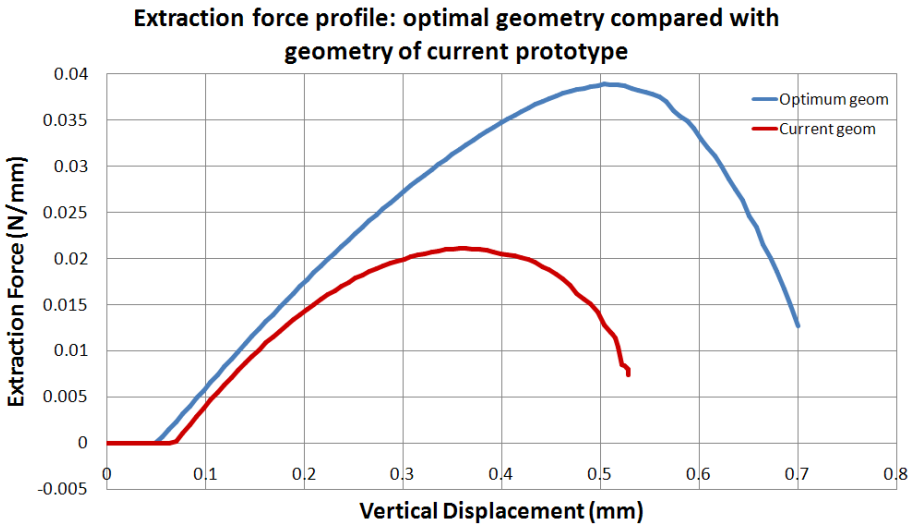


Figure 5.13: Vertical extraction force profile versus vertical displacement for the optimal interlock geometry and the interlock geometry of the alpha probe prototype as obtained from the 2D simulations (force expressed per unit length due to plane strain assumption).

N (mm)	**R1** (mm)	**R2** (mm)	**W** (mm)	**Optimum geometry Extraction Force** (N/mm)	**Current geometry Extraction Force** (N/mm)
0.3	0.206	0.227	0.051	0.039	0.021

Table 5.3: Geometrical parameters of the optimum solution, peak extraction force values of optimum and current geometry.

the current alpha probe prototype, consistent with all the assumptions made for the 2D models used in the optimisation, was built (see Figure 5.12). The corresponding extraction force profile was calculated and is shown in Figure 5.13, red line. It is evident that the maximum extraction force corresponding to the model of the optimum interlock geometry is almost double that obtained from the model of the current interlock geometry (see Table 5.3). This optimisation study has also shown that the main geometrical feature affecting the interlock extraction force is the minimum lateral thickness of the female part, which is a combination of all four parameters. For larger thicknesses, the extraction force increases.

The accuracy of the results from the simulation of the 3D FE model of the optimum interlock was validated through experiments. The extraction force profile of the 3D numerical model, characterised by a hyperelastic material and frictionless contacts, is compared, in Figure 5.14, with the extraction force profile of an experimental test. The results show that different extraction speeds do not significantly affect the extraction forces: the difference in extraction force, for lubricated and dry

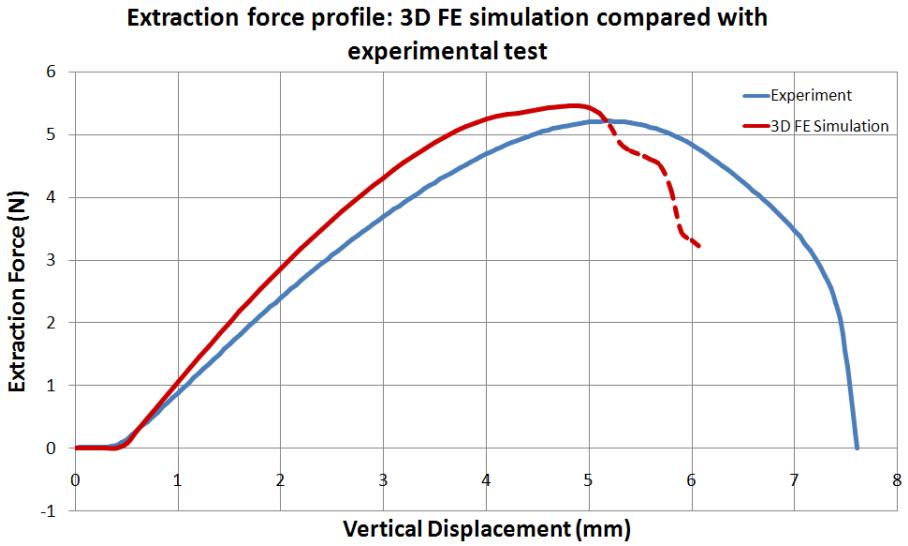


Figure 5.14: Vertical extraction force profile versus vertical displacement of the 3D FE simulation and of an experimental test. The dotted line represents possible quality deterioration of numerical results due to computational limitations.

Peak Force - Mean (N)	**Peak Force - STD** (N)	**Peak Force from Simulation** (N)	**Difference Experiments/Simulation**
5.2	0.019	5.46	4.87%

Table 5.4: Mean and standard deviation of peak extraction force from experiments; peak force from FE simulation and corresponding percent difference.

conditions at extraction speeds of 0.1 mm/s and 0.5 mm/s were 8% and 3.1%, respectively. Therefore, a constant speed of 0.5 mm/s was chosen. In order to replicate as closely as possible the frictionless contact condition selected for the numerical models, abundant silicone grease was spread at the interface between female and male samples. Lubrication also reduced the effect of more complex material interactions, which occur when high friction is involved (e.g. complete sticking between contact surfaces, unstable slip and stick behaviour).

According to Table 5.4, the FE simulation produced a peak extraction force value consistent with the experimental results to within 4.87%. The experimental peak extraction force was evaluated by averaging the results of 5 extraction tests (speed = 0.5 mm/s, lubricated conditions). In addition, extraction force-displacement profiles of the 3D FE model (Figure 5.14), and recordings of deformation during physical experiments (Figure 5.9) further validated the 3D FE model.

Though results from experimental tests clearly appear to be in line with results from the FE simulation, it should be noted that minor residual discrepancies - such as a larger interlock stiffness in the FE simulation - remain between the two extraction force profiles. These may be due to manufacturing imperfections in the

silicone sample and to frictional contact conditions during experiments.

5.4 Conclusions

An optimisation procedure to identify the geometry which provides the strongest interlocking mechanism for the flexible multi-part probe described in Chapter 4 was developed and applied. As a result, a new cross-sectional geometry has been identified, which considerably improves resistance to failure of the interlocking mechanism. From the identified optimal planar interlock geometry, a 3D FE model was developed. A silicone-rubber sample replicating the 3D FE interlock model was manufactured and used for the experimental validation of the 3D FE model itself. Results from the 3D FE simulation were shown to be consistent with those obtained in experiments.

This study was clearly an important part in the provision of a novel miniature steerable probe. The optimal geometry, identified through the optimisation procedure described here, suggests a need for modifications to the design of the current alpha probe prototype (section 4.4.2) with the aim of developing a new version able to sustain more critical working conditions while reducing actuation constraints (e.g. axial push).

In Chapter 7, a novel probe prototype designed taking into account the results from the optimisation procedure will be described and corresponding steerability tests will be presented.

In addition, the FE interlock model developed and described in this chapter forms the starting point for the definition of analytical approaches to probe behaviour and failure study, which will be presented and discussed in Chapter 6. These analytical approaches build on the cross-sectional interlocking stiffness, as obtained numerically from the 2D model presented in this chapter, with the aim of correlating actuation loads, probe cross-sectional geometries and failure situations.

Several simplifications have been introduced in the definition of the numerical 2D model of the interlocking mechanism used for the optimisation procedure, which should be addressed in future works (Chapter 8). The interlock geometry used for the optimisation procedure is, to a certain extent, self similar; the four parameters can vary, providing different geometries, but with some strong invariants, such as the parallelism and the perpendicular angle between the main lines. It would be possible to define a new geometry which is able to explore more diversified interlock shapes and possibly suggest even stronger interlocking mechanisms, for example by adding angular parameters between the main interlock geometrical lines.

Assumptions made with regard to the material model used (linear elastic) and the frictional properties defined (frictionless contact) should be explored, and their

effect on the optimisation outcome considered. A more complex material model representing the mechanical properties of the flexible probe prototypes used should be introduced and an experimental characterisation of frictional properties should be carried out in order to provide the model with more realistic frictional parameters. The model also took into account only one half (the weakest) of the interlock cross-section; however, the optimisation outcome could possibly differ if the full cross-section was modelled, where each segment is constrained by two other segments and presents two interlocking mechanisms.

Chapter 6

Towards the development of a 3D model

This chapter describes the preliminary approach towards the development of a 3D model of the flexible probe, with a focus on how the interlocking mechanism affects probe segment irreversible separation when the segment is driven by an axial push. While limited in scope, this study forms the basis for the extension of an initial simplified analytical and numerical approach to probe behaviour modelling towards the understanding and modelling of all the complex interactions which occur during the actuation of a multi-part flexible and steerable probe. Starting from the buckling analysis of a beam resting on non-linear elastic foundations, a method to formulate a link between probe failure conditions (i.e. probe segment buckling) and actuation strategies is proposed and discussed.

6.1 Introduction

Irreversible segment separation is identified, in Chapter 4, as the most serious failure. In Chapter 5, a procedure for the optimisation of the interlock geometry is performed, and a new, stronger interlock geometry is identified, which reduces the risk of segment separation. However, the strategy adopted to actuate each segment, which can be considered as the ultimate cause of failure, was not considered. The failing scenario illustrated in Figure 5.2b represents a case of irreversible segment separation which is triggered by the actuation of a single segment and it is determined by operative conditions (e.g. lack of local lubrication).

The aim of this chapter is to correlate the previous study on the flexible probe cross-section to the probe behavior along the axial length. This will help to formulate a link between failure conditions and actuation strategies, which in turn will form the basis for future research on an analytical model of probe behaviour that truly

reflects the complex interaction between all of the flexible probe steering aspects.

Specifically, the hypothesis underlying this part of the study is that the critical actuation load (N in Figure 5.1) which causes the interlock to fail (and thus the segments to separate), is affected by the cross-sectional interlocking stiffness, as defined and numerically calculated in the previous chapter: the greater the interlock stiffness, the greater the actuation load before failure is triggered.

This chapter describes a simple analytical and numerical approach for the formulation of the link between the interlocking mechanism and the critical load required to disengage a probe segment (Section 6.2). According to the proposed approach, an interlocked segment is firstly described as a beam resting on non-linear elastic foundations (Sections 6.2.1 and 6.2.2), buckling analysis of such constrained beam (i.e. segment disengagement) is proposed and a finite difference method is applied to calculate the critical buckling load corresponding to the maximum axial actuation load applicable before buckling (Sections 6.2.3 and 6.2.4). Preliminary results of this approach are then discussed (Section 6.3), followed by conclusions and future works (Section 6.4).

6.2 Materials and methods

This section describes the steps taken towards the formulation of the link between the interlocking mechanism and the critical load required to disengage a probe segment. When necessary, intermediate results of preliminary models or algorithm validations are also discussed.

6.2.1 Beam resting on elastic foundations

The scenario in Figure 5.2b can be simplified and treated with the theory of buckling of a beam on elastic foundations. This approach enables the formulation of a relationship between interlock stiffness, actuation load and failure (i.e. buckling). The conceptual model for an elastic foundation (*Winkler foundation*) is an infinite set of parallel springs with equal rigidity and with no shear coupling between them (see Figure 6.1). The action of the equally spaced springs on the buckled beam can be replaced by the action of a continuous elastic medium. The reaction of the medium at any cross-section of the beam is proportional to the deflection at that section, and the displacement at each point affects the foundation reaction at others [Brush and Almroth, 1975, Timoshenko and Gere, 1961].

In the current problem definition, the elastic foundations represent the action of the interlocking mechanism on a single probe segment. The rigidity of the elastic medium can indeed be associated with the interlock stiffness of a probe cross-section,

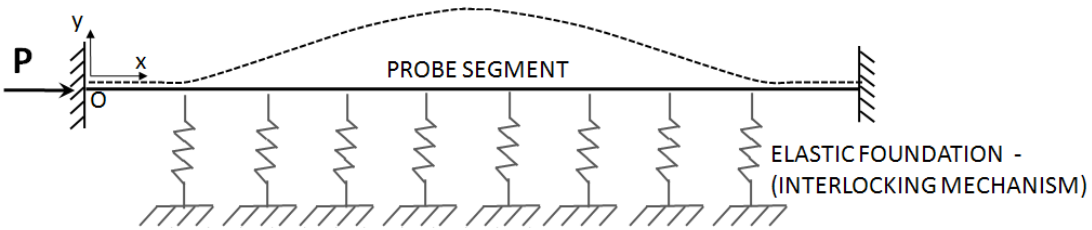


Figure 6.1: Schematic of the model devised for the analysis of probe axial behaviour under a load P, which is resting on elastic foundations (which represents the cross-sectional interlock stiffness).

or, to be more precise, to the "extraction force versus vertical displacement" profile as shown in Figure 5.13. Indeed, the single probe segment is represented as a beam, and the interlocking mechanism is represented as a set of springs acting orthogonally to the beam itself.

The differential equation of the axis of a beam subjected to an axial compressive force P and to a distributed lateral load of intensity q, which varies with the distance x along the beam, can be expressed in the following form (equations are reported here for clarity from Brush and Almroth [1975] and Timoshenko and Gere [1961]):

$$EI\frac{d^4y(x)}{dx^4} + P\frac{d^2y(x)}{dx^2} = q(x) \tag{6.1}$$

where EI is the flexural rigidity of the beam in the plane of bending (E = elastic modulus, I = second moment of area).

When considering Euler's formula for determining critical loads in a buckled beam not subjected to lateral loads, the following differential equation is used:

$$EI\frac{d^4y(x)}{dx^4} + P\frac{d^2y(x)}{dx^2} = 0 \tag{6.2}$$

The general solution of this differential equation is in the form:

$$y = A\sin(kx) + B\cos(kx) + Cx + D \tag{6.3}$$

where $k^2 = \frac{P}{EI}$.

As an example, in the case of a beam with hinged ends (simply supported ends), where the boundary conditions are defined as follows,

$$y(0) = y''(0) = 0, \quad y(l) = y''(l) = 0 \tag{6.4}$$

the critical load P_{cr} for which particular solutions to Equation 6.2 exist is:

$$P_{cr} = \left(\frac{n\pi}{l}\right)^2 EI \tag{6.5}$$

where l is the beam length and $n = 1, 2, 3 \ldots$.

The deflection shape of the beam is then given by:

$$y = A \sin(\frac{n\pi x}{l}) \tag{6.6}$$

where A represents the undetermined amplitude of the deflection.

When considering a beam resting on elastic foundations, the term q representing lateral loads in Equation 6.1 is substituted with a term representing the foundation reaction q_f:

$$EI\frac{d^4y(x)}{dx^4} + P\frac{d^2y(x)}{dx^2} = q_f \tag{6.7}$$

q_f is the force intensity between the beam and the foundations and it is defined as follows [Brush and Almroth, 1975]:

$$q_f = -k_f y(x) \tag{6.8}$$

where k_f is the foundation modulus and y is the lateral beam displacement.

k_f is defined as the ratio beetween the spring constant of the individual support and the distance between the supports [Timoshenko and Gere, 1961].

In the example of a beam with hinged ends (boundary conditions described by Equation 6.4) the critical load is:

$$P_{cr} = \left(\frac{n\pi}{l}\right)^2 EI + \left(\frac{l}{n\pi}\right)^2 k_f \tag{6.9}$$

and the deflection shape of the beam is still described by Equation 6.6. If the elastic foundations are removed (i.e. $k_f = 0$), the critical load as calculated in Equation 6.9 corresponds to the Euler critical buckling load (Equation 6.5).

For the definition of the foundation modulus k_f in the case of "beam on elastic foundations" ($k_f = 0$ in the Euler's beam), the force-displacement profile shown in Figure 5.13 is considered. Because of the plane strain assumption, the extraction force in Figure 5.13 is expressed per axial unit length (N/mm) and it represents the force required to extract vertically one unit length of half of the male cross-section from the corresponding half female cross-section. Figure 6.2 shows the force-displacement profiles for both the optimum interlock geometry and the current geometry (interlock cross-section of the alpha prototype), multiplied by a factor of 2 in order to take into account the fact that only half of the interlock cross-section was modelled. The foundation modulus k_f is then calculated by considering the average interlock stiffness (dotted lines in Figure 6.2); the coefficient of the average interlock stiffness is the foundation modulus itself.

It should be noted that the situation herein described represents a single probe

segment interlocked to a second segment and therefore it is only a preliminary approximation of the more realistic situation where 4 segments are interlocked together.

Both the solutions of Euler's buckling and buckling on elastic foundations are periodic with n. Different deflection configurations are assumed for different values of n, and corresponding critical loads P_{cr} can be identified in correspondence of each possible configuration. However, in a real buckling situation, where an increasing axial load is applied, the physical configuration which is most likely to be assumed is the one characterised by the minimum critical load.

As an example, a comparison between the critical load for a beam buckling with and without elastic foundation is shown in Table 6.1. The critical loads shown in Table 6.1 are calculated for a beam consistent with the dimensions and material properties of a probe segment. The beam is 200 mm long (l), characterised by a filled quarter circle cross-section with radius r of 3 mm (second moment of area $I = \frac{\pi r^4}{16}$) and the Young's modulus E of the constituent material is 2 Mpa. The foundation modulus k_f is extrapolated from the interlock stiffness of the optimal cross-sectional geometry (second row) and from the interlock stiffness of the geometry of the alpha prototype (third row).

As expected, the critical buckling load of an unsupported beam, as thin and long as a probe segment, and characterised by a soft material (Young's modulus $E = 2$ Mpa) is virtually unable to hold any axial load ($P_{cr} = 0.0079$ N). However, the critical load P_{cr} values in Table 6.1 demonstrate how the interlock stiffness, herein approximated with linear elastic foundation, plays a major role in increasing the critical buckling load ($P_{cr} = 3.9565$ N for the optimal cross-sectional geometry). Correspondingly, as shown in Figure 6.3, the shape of the deflection associated with the configuration of minimum critical load is significantly different if the elastic foundation support is provided. In case of a beam resting on elastic foundations, the more the beam deflects, the more the elastic foundations resist to the deflection and a sinusoidal "multi-peak" deflection configuration is assumed. This configuration is significantly different from the case of Euler's buckling, where only one peak is present.

6.2.2 Non-linear elastic foundation modulus

Equation 6.7 describes the behaviour of a beam resting on elastic foundations characterised by a constant foundation modulus k_f and subject to an axial load P. Thanks to Equation 6.9, it is possible to calculate the critical load which triggers buckling in the beam. However, as clear from Figure 6.2, a linear interpolation of the interlock stiffness (average interlock stiffness) is a simple approximation of the actual interlocking mechanism reaction and consequently the critical buckling loads

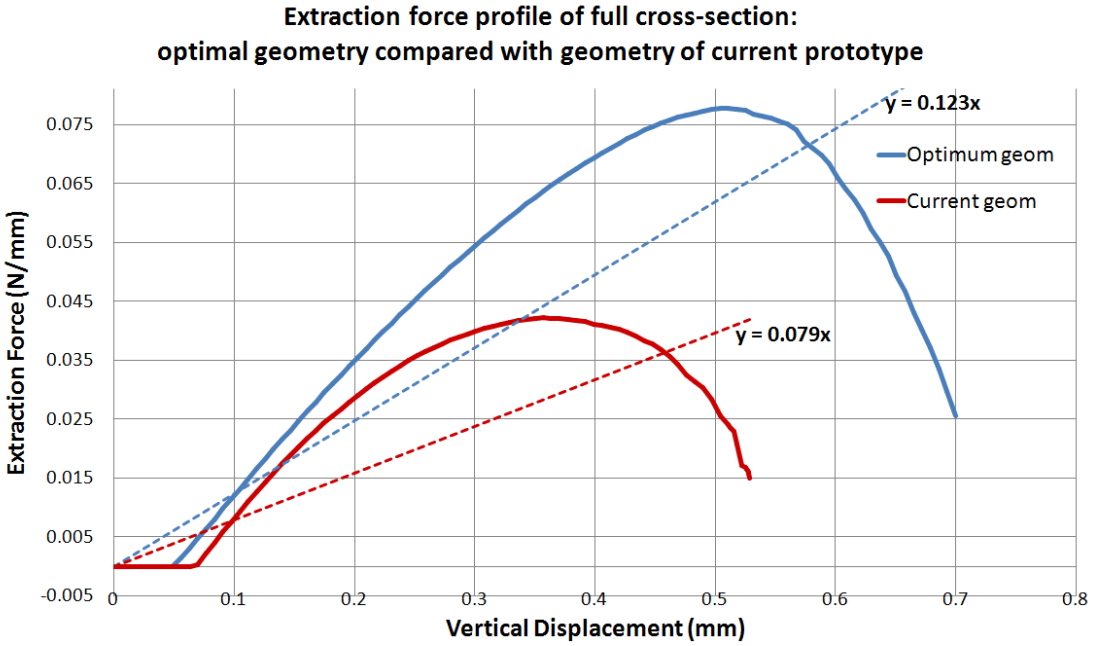


Figure 6.2: Linear interpolation of the average interlock stiffness of the optimal geometry ("Optimum geom") and the geometry of the alpha prototype ("Current geom"), for the full cross-section (extraction force values are double those in Figure 5.13). The intercept is set to 0-0. The coefficient of the linear interpolation represents the foundation modulus k_f.

	l (mm)	r (mm)	E (MPa)	$\mathbf{k_f}$ (N/mm^2)	**min** n	$\mathbf{P_{cr}}$ (N)	y (mm)
Euler's beam	200	3	2	-	1	0.0079	$A\sin(\frac{\pi}{200}x)$
Beam on elastic foundation (optimal geometry)	200	3	2	0.123	16	3.9565	$A\sin(\frac{16\pi}{200}x)$
Beam on elastic foundation (geometry of alpha prototype)	200	3	2	0.079	14	3.1718	$A\sin(\frac{14\pi}{200}x)$

Table 6.1: Beam buckling: effect of elastic foundation (beam with hinged ends)

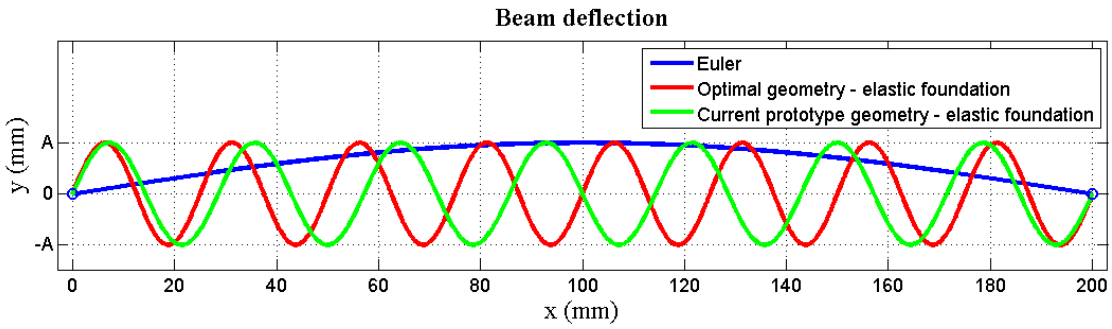


Figure 6.3: Beam deflection for the three scenarios envisioned in Table 6.1. Hinged ends are assumed as boundary conditions.

shown in Table 6.1 cannot be considered representative of a more realistic scenario. Therefore, non-linear elastic foundations are introduced [Yankelevsky et al., 1988].

Equation 6.10 describes the behaviour of a beam resting on elastic foundations and subject to an axial load P, where the elastic foundations are represented by a non-linear function of y, $f_{nl}(y)$, which is a more accurate approximation of the interlock stiffness as calculated from the cross-sectional 2D model (Section 5.3):

$$EI\frac{d^4y(x)}{dx^4} + P\frac{d^2y(x)}{dx^2} = -f_{nl}(y(x)) \tag{6.10}$$

where $f_{nl}(y(x))$ is described by the following system of equations:

$$\begin{cases} y(x) = -0.05, \ [f_{nl}(y(x)) = -\infty] & y \leq -0.05 \\ f_{nl}(y(x)) = 0, & -0.05 < y \leq 0.05 \\ f_{nl}(y(x)) = -1.849y(x)^4 + 1.766y(x)^3 + & \\ \quad -0.750y(x)^2 + 0.353y(x) - 0.017, & 0.05 < y \leq 0.734 \\ f_{nl}(y(x)) = 0, & y > 0.734 \end{cases} \tag{6.11}$$

The non-linear elastic foundation function $f_{nl}(y(x))$ is shown in Figure 6.4. The four equations of the system 6.11 cover all possible configurations of the interlocking mechanism.

1. For $y \leq -0.05$, the male part is in contact with the female part at the bottom, and it cannot compenetrate further.

2. For$-0.05 < y \leq 0.05$, the male part is within the ± 0.05 mm clearance, and it is not in contact with the female part; the segment behaves as a beam subjected to Euler's buckling.

3. For $0.05 < y \leq 0.734$, the male part is engaging and being deformed at the contact with the female part; in this range, the foundation function is increas-

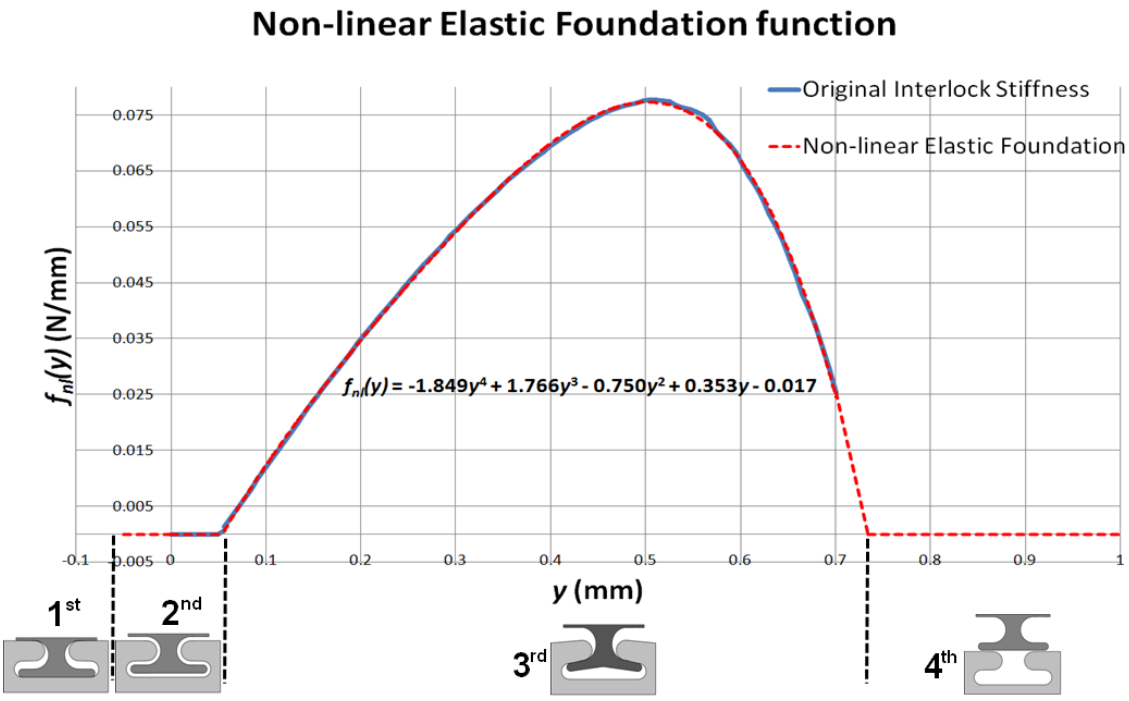


Figure 6.4: Non-linear elastic foundation function $f_{nl}(y(x))$ (red dotted line). Interlock stiffness, as calculated from the 2D cross-sectional model (blue line). Diagrammatics of the 4 interlock configurations in correspondence of the main sections of the non-linear elastic foundation function are shown at the bottom. The original interlock stiffness when male and female parts are in contact is approximated with a 4^{th}order polynomial.

ing till a maximum point, after which it drops down to zero. The non-linear elastic foundation function within this range is defined as the 4^{th}order polynomial which approximates the original interlock stiffness profile. A 4^{th}order polynomial is the smallest order with a regression error $R^2 > 0.995$.

4. For $y > 0.734$, the male part is completely disengaged from the female part and the segment behaves as a beam subjected to Euler's buckling.

6.2.3 Boundary value problem solved with a relaxation method

Because of the non-linear term $f_{nl}(y(x))$, equation 6.10 cannot be easily solved mathematically, therefore a numerical method is deemed necessary.

The deflection equation of a beam constrained at both ends is an example of a two-point boundary-value problem. Finite difference methods can be used to obtain numerical solutions to boundary value problems and the solution can be found through iterative methods (e.g. relaxation method, shooting method), as described next.

Equation 6.10 will be solved over the interval $[0, l]$, representing the beam length,

where the boundary conditions are specified at the end points of this interval. A finite difference representation of equation 6.10 is proposed. The interval $[0, l]$, representing the beam length, is split into N equal parts, each of width $\triangle x = \frac{l}{N}$. The points (or nodes) defining the N parts into which the beam is split are called *interior nodes* (see Figure 6.5). The *interior nodes* are defined as:

$$x_i = x_0 + i\triangle x, \;\; i = 1,\, 2,\, ...,\, N \tag{6.12}$$

where $x_0 = 0$ and $x_N = l$.

In addition, in order to apply the boundary conditions at the endpoints, fictitious *exterior nodes* are required:

$x_{-1} = x_0 - \triangle x \quad x_{N+1} = x_N + \triangle x$

$x_{-2} = x_{-1} - \triangle x \quad x_{N+2} = x_{N+1} + \triangle x$

Figure 6.5 shows the beam, divided into equally spaced segments, and corresponding interior and exterior nodes.

Then, a finite difference approximation for each of the derivatives that appear in Equation 6.10 is defined using central difference [Hamming, 1986]:

$$\frac{d^2y(x)}{dx^2} \approx \frac{y_{i+1} - 2y_i + y_{i-1}}{\triangle x^2} \tag{6.13}$$

$$\frac{d^4y(x)}{dx^4} \approx \frac{y_{i+2} - 4y_{i+1} + 6y_i - 4y_{i-1} + y_{i-2}}{\triangle x^4}$$

Equation 6.10 can be rewritten as follows:

$$EI\frac{y_{i+2} - 4y_{i+1} + 6y_i - 4y_{i-1} + y_{i-2}}{\triangle x^4} + P\frac{y_{i+1} - 2y_i + y_{i-1}}{\triangle x^2} = -f_{nl}(y_i) \tag{6.14}$$

where $f_{nl}(y_i)$ is described by the following system of equations:

$$\begin{cases} y_i = -0.05, [f_{nl}(y_i) = -\infty] & y_i \leq -0.05 \\ f_{nl}(y_i) = 0, & -0.05 < y_i \leq 0.05 \\ f_{nl}(y_i)) = -1.849y_i^4 + 1.766y_i^3 - 0.750y_i^2 + 0.353y_i - 0.017, & 0.05 < y_i \leq 0.734 \\ f_{nl}(y_i) = 0, & y_i > 0.734 \end{cases} \tag{6.15}$$

and the boundary conditions for a beam with hinged or fixed ends can be rewritten solving the derivatives in Equation 6.13 according to the original boundary condi-

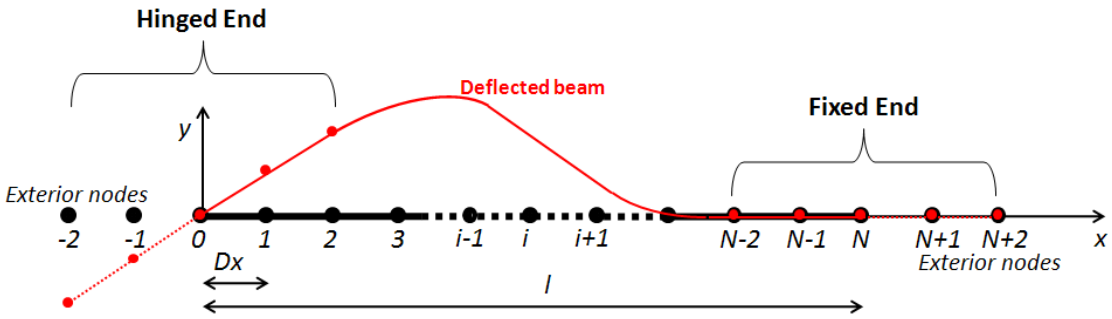


Figure 6.5: Interior and exterior nodes of a beam of length l, used for the central finite difference scheme. A deflected beam is shown in red as an example, to illustrate how two different boundary conditions (hinged end to the left, fixed end to the right) are implemented in the finite difference scheme (see Table 6.2).

Hinged Ends		**Fixed Ends**	
$x = 0$	$x = l$	$x = 0$	$x = l$
$y_1 = 0$	$y_N = 0$	$y_1 = 0$	$y_N = 0$
$y_{-1} = y_1$	$y_{N-1} = y_{N+1}$	$y_{-1} = y_1 = 0$	$y_{N-1} = y_{N+1} = 0$
$y_{-2} = y_2$	$y_{N-2} = y_{N+2}$	$y_{-2} = y_2 = 0$	$y_{N-2} = y_{N+2} = 0$

Table 6.2: Finite difference boundary conditions for a beam with hinged or fixed ends

tions (see Table 6.2).

Now, the *relaxation* method states that a solution to Equation 6.14 can be found by generating a sequence of guesses ${}^{(k)}y_i$ that starts with an arbitrary configuration ${}^{(0)}y_i$ and that converges to the solution ${}^{(\infty)}y_i$ of the system represented by Equation 6.14 and boundary conditions expressed in Table 6.2. One way to generate such a sequence is to imagine that, instead of solving Equation 6.10, the following time-dependent equation is being solved:

$$\frac{dy(x;t)}{dt} = EI\frac{d^4y(x;t)}{dx^4} + P\frac{d^2y(x;t)}{dx^2} + f_{nl}(y(x;t)) \tag{6.16}$$

If enough steps are taken, the initial arbitrary configuration $y(x;0)$ will relax to a time-independent configuration $y(x;\infty)$ that satisfies $EI\frac{d^4y(x;\infty)}{dx^4} + P\frac{d^2y(x;\infty)}{dx^2} + f_{nl}(y(x;\infty)) = 0$, which is the original Equation 6.10 to be solved. A more detailed explanation will follow.

Equation 6.16 can be represented in its finite difference form by adding a fictitious discrete time parameter t to Equation 6.14:

$$\frac{y_i^{t+1} - y_i^t}{\triangle t} = EI\frac{y_{i+2}^t - 4y_{i+1}^t + 6y_i^t - 4y_{i-1}^t + y_{i-2}^t}{\triangle x^4} + P\frac{y_{i+1}^t - 2y_i^t + y_{i-1}^t}{\triangle x^2} + f_{nl}(y_i^t) \tag{6.17}$$

The right hand side of Equation 6.17 is:

$$RHS_i^t = EI\frac{y_{i+2}^t - 4y_{i+1}^t + 6y_i^t - 4y_{i-1}^t + y_{i-2}^t}{\triangle x^4} + P\frac{y_{i+1}^t - 2y_i^t + y_{i-1}^t}{\triangle x^2} + f_{nl}(y_i^t) \quad (6.18)$$

So, Equation 6.16 becomes:

$$y_i^{t+1} = y_i^t + \triangle t RHS_i^t \quad (6.19)$$

where y_i^t is the approximate solution of $y(x)$ obtained at the t_{th} relaxation step and y_i^{t+1} is the updated guess for the next relaxation step. This iterative method, starting from an initial guess (or configuration), is applied to produce successive guesses y_i^t for different values of fictitious time t, until the residual RHS_i^t is considered small enough (i.e. the solution has converged). In other words, if a solution exists, $y_i^{t+1} \approx y_i^t$ for $t \to \infty$ and therefore $RHS_i^t \approx 0$, which is an approximated solution to Equation 6.16.

6.2.4 Numerical algorithm for the identification of the critical buckling load

The previous section has described a numerical method to solve the two-point boundary value problem of a beam resting on non-linear elastic foundations, which deflects under a constant axial load P. However, the aim of this study is to identify the critical load P_{cr} which triggers buckling under those conditions.

According to the definition of critical buckling load, if a beam is subjected to an axial load $P < P_{cr}$ and a lateral perturbation is applied to the beam, the beam will return to the resting (straight) position when the perturbation is removed. However, if an axial load $P > P_{cr}$ is acting on the beam, and a lateral perturbation is applied, the beam will fail under the axial load when the perturbation is removed.

This consideration is at the basis of the algorithm devised for the identification of the critical buckling load, via a dichotomic search through numerical solutions of the two-point boundary-value problem previously illustrated.

The algorithm can be described as follows:

1. A range of axial loads $[P_{min}, P_{max}]$, wide enough to include the possible critical buckling load, is selected.

2. An axial load of value $P = \frac{P_{max}+P_{min}}{2}$ is assigned (dichotomic search).

3. An initial guess (or beam deflection configuration) is assigned to y_i^0 with $i =$ 1, 2, ..., N. A gaussian function ($y_i = A\exp\frac{\frac{1}{2}(x_i-\frac{1}{2}l)^2}{\sigma^2}$ where $A = 0.01$, $l =$

200, $\sigma = 10$) is chosen as the initial perturbation. The amplitude and shape of the initial perturbation are chosen in such a way not to affect the results of the simulations.

4. RHS_i^0 is calculated for $i = 1, 2, ..., N$, according to Equation 6.18 and to corresponding boundary conditions as in Table 6.2.

5. y_i^1 is updated as follows: $y_i^1 = y_i^0 + \triangle t RHS_i^0$.

6. Steps 4 and 5 are reiterated with increasing t until the residual error ($res = \sum_{i=1}^{N} \sqrt{(y_i^{t+1} - y_i^t)^2}$) is either smaller than an arbitrary "convergence limit" (i.e. $res < 10^{-9}$) or it keeps increasing, becoming bigger than an arbitrary "divergence limit" (i.e. $res > 10^3$).

7. If the solution converges (i.e. $res < 10^{-9}$), the current axial load P is below the critical buckling load, and P is assigned to P_{min} ($P = P_{min}$).

8. If the solution diverges (i.e. $res > 10^3$), the current axial load P is beyond the critical buckling load, and P is assigned to P_{max} ($P = P_{max}$).

9. The algorithm is reiterated from step 2 until the difference between P_{max} and P_{min} is considered small enough for the approximation of the critical buckling load (i.e. $P_{max} - P_{min} < 10^{-4}$).

The solutions of Euler's buckling and buckling on elastic foundations are periodic with n, and different deflection configurations are assumed for different values of n, therefore corresponding critical loads P_{cr} can be identified for each possible configuration. However, the algorithm herein presented will find the sole solution of the configuration corresponding to the minimal critical load (e.g. $n = 1$ in Euler's buckling). This can be explained by the fact that the algorithm "relaxes" the solution from an initial perturbation configuration which was chosen to be very small. The results of the algorithm should not be affected by the magnitude of the initial perturbation, unless the initial perturbation corresponds to a configuration which is already beyond the configuration corresponding to the case of minimum critical buckling load. Only in this case the solution could potentially relax on a final configuration, which is not the one characterised by the minimum buckling load.

The numerical algorithm herein described was implemented using the programming language C++ in the Microsoft Visual Studio development environment (Microsoft Visual Studio 2008, Microsoft Corporation).

Algorithm Validation

The algorithm was firstly validated against the theoretical results known from the theory on Euler's beam buckling and buckling of a beam resting on linear elastic

	$\mathbf{k_f}$ (N/mm^2)	**Boundary Conditions**	**Theoretical $\mathbf{P_{cr}}$ (N)**	**Calculated $\mathbf{P_{cr}}$ (N)**
Euler's beam	–	Hinged ends	0.0079	0.0080
		Fixed ends	0.0314	0.0314
Beam on elastic foundations (optimal geometry)	0.123	Hinged ends	3.9565	3.9564
Beam on elastic foundations (geometry of alpha prototype)	0.079	Hinged ends	3.1718	3.1715

Table 6.3: Theoretical critical buckling load compared to the critical buckling load as obtained from the proposed algorithm.

foundations. The results are reported in the Table 6.3; the beam geometrical and mechanical properties are the same as the ones illustrated in Section 6.2.1.

Results from Table 6.3 show that the dichotomic search of the critical buckling load produced values highly consistent with the theoretical ones; the minimal discrepancies are simply due to rounding approximations.

A further validation of the results produced by the algorithm can be obtained by considering the deflection of the beam, as calculated by the algorithm, in correspondence of the critical buckling load (see Figure 6.6).

Comparing the beam deflection profiles of Figure 6.3 and Figure 6.6, it is evident that the theoretical deflections, as calculated from Equation 6.6, are consistent with the ones obtained from the algorithm. Particularly, in the case of a beam resting on linear elastic foundations (bottom graphs of Figure 6.6), the number of peaks of the deflection profile is the same as the number of peaks as calculated theoretically (red and green deflection profiles in Figure 6.3). This confirms that the algorithm correctly identifies a critical buckling load, which corresponds to the deflection configuration characterised by the minimum critical buckling load (i.e. in Equations 6.6 and 6.9, $n = 1$ for Euler's buckling, $n = 14$ for a beam resting on elastic foundations of modulus $k_f = 0.079$, $n = 16$ for a beam resting on elastic foundations of modulus $k_f = 0.123$). It should be noted that the amplitude values of the deflection vary within the four different results shown in Figure 6.6 according to how close the rounded axial load P used in the algorithm is to the theoretical critical load.

6.3 Results and Discussion

Table 6.4 reports on the critical buckling load for a beam resting on non-linear elastic foundations as obtained from the algorithm presented previously, for two different boundary conditions, hinged and fixed endpoints. The algorithm is run

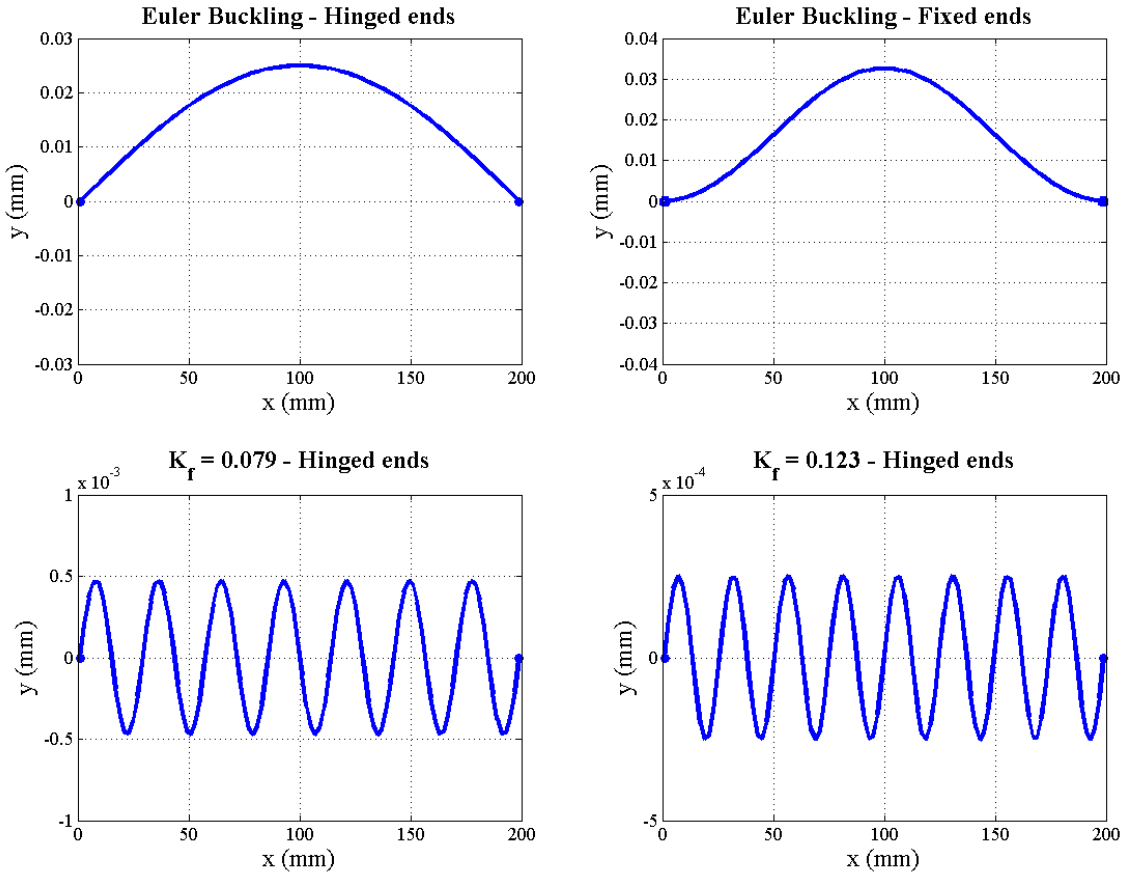


Figure 6.6: Beam deflection in four different cases. *Top-left:* Euler's buckling of a hinged beam; *top-right:* Euler's buckling of a fixed beam; *bottom-left:* buckling of a beam on linear elastic foundations characterised by a $k_f = 0.079$ (corresponding to the linearised interlock stiffness of the cross-sectional geometry of the alpha prototype); *bottom-right:* buckling of a beam on linear elastic foundations characterised by a $k_f = 0.123$ (corresponding to the linearised interlock stiffness of the optimal cross-sectional geometry).

Boundary Conditions	**Alpha Interlock Geometry P_{cr}** (N)	**Optimal Interlock Geometry P_{cr}** (N)	**Improvement**
Hinged ends	5.1861	7.2150	35%
Fixed ends	5.9275	7.2150	22%

Table 6.4: Critical buckling load for a beam resting on non-linear foundations, as derived from the stiffness of the alpha prototype interlock geometry and from the stiffness of the optimised interlock geometry.

with non-linear elastic foundations derived from the interlock stiffness of both the optimal geometry (Equation 6.10) and the geometry of the alpha prototype. Figure 6.7 shows the beam deflection in correspondence of the calculated critical buckling load for the two cases (optimal geometry and geometry of the alpha prototype) and for both hinged and fixed ends.

According to the results herein presented, a beam (i.e. one probe segment) 200 mm long (l), characterised by a filled quarter circle cross-section with radius r of 3 mm and a Young's modulus E of the constituent material equal to 2 Mpa, which is interlocked through the dovetail mechanism shown in Figure 5.11, will buckle under an axial load of about 7.2 N. The results in Table 6.4 demonstrate that the boundary conditions at the end points of the beam do not affect the critical buckling load (the effect of the non-linear foundations is "masking" the effect of the boundary conditions). The same beam, but with non-linear foundations derived from the interlock stiffness of the alpha prototype, presents a significantly smaller critical buckling load (5.18 N in hinged end and 5.91 N in fixed end conditions). Therefore, the critical axial load which triggers segment separation is more than 20% higher when the optimal interlock geometry is employed, as compared to the interlock geometry of the alpha prototype.

The results shown in Figure 6.7 were obtained from simulations run with axial loads very close to the calculated critical buckling load, but slightly smaller (for loads equal to the critical load, the solution would diverge). Because of the definition of the non-linear elastic foundations ($f_{nl}(y(x))$ in Equations 6.11), the beam cannot deflect negatively below -0.05 mm (see Figure 6.7, red lines), but it can only deflect upwards. The deflection peaks tend to exceed the second "interlock configuration" (Figure 6.4) and to fall into the third "interlock configuration", where the non-linear elastic foundations are acting. Greater axial loads would cause the deflection peaks to reach the fourth "interlock configuration", where the interlock stiffness becomes void, and therefore the failure scenario envisioned in Figure 5.2b would be reached.

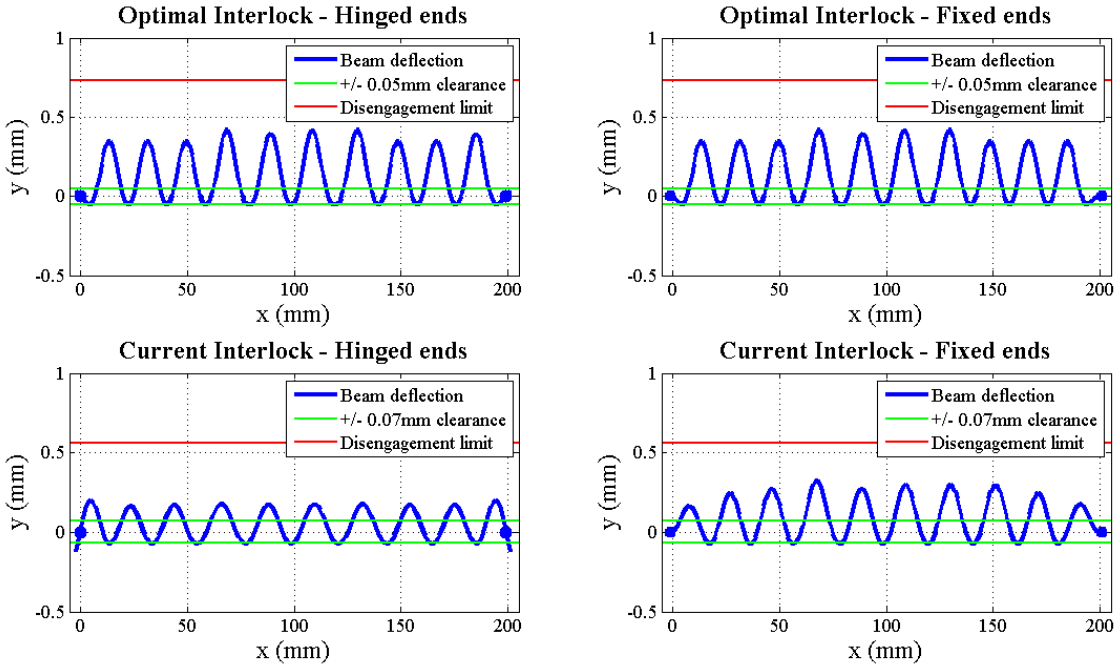


Figure 6.7: Beam deflection in correspondence of the critical buckling load for the optimal interlock geometry (top) and the geometry of the alpha prototype (bottom). Both hinged and fixed end conditions are illustrated. The green lines represent the interlock clearance (second "interlock configuration" in Figure 6.4): ± 0.05 mm for the optimal interlock and ± 0.073 mm for the interlock of the alpha prototype. The red line represents the interlock disengagement limit.

6.4 Conclusions

A method for extending the study on the flexible probe 2D cross-section to the third (longitudinal) dimension was proposed. The cross-sectional interlocking stiffness obtained numerically from a 2D model of the interlocking mechanism was introduced into the mathematical equation defining beam (i.e. probe segment) deflection and buckling under axial load. A finite difference relaxation method was applied to solve numerically the resulting non-linear beam equation and a dichotomic search was performed to identify the critical buckling load at which the beam buckles.

Although limited in accuracy, because of the evident simplifications, a link between failure conditions (i.e. buckling) and actuation strategies can be formulated. According to the results obtained, if one probe segment, interlocked to a stationary second probe segment, is pushed by an actuation force larger than 7.2 N, the driven probe segment will tend to buckle and to disengage from the interlocking mechanism. This buckling load is more than 20% larger than the critical buckling load for a probe segment featured with the interlock geometry of the alpha prototype (described in Section 4.4.2). This further confirms the need for modifications to the cross-sectional design of the alpha probe prototype, as suggested already in Chapter 5.

Future developments will regard the extension of the method herein presented to a scenario where one probe segment is interlocked to two others (see Figure 5.1a) and the extension to a scenario where the probe segment is resting in a bent configuration, rather than in a straight one, because this may constitute a weaker condition for failure. In addition, an experimental validation of the results will be required.

With regard to longer-term future research, this study forms the basis for the development of more complex analytical and numerical models of the probe behaviour towards a 3D model which takes into account the interaction between the probe's segments and resulting deformations during the insertion strategy, and which could be possibly coupled with information obtained from models of probe-tissue interaction. A better and complete understanding of the probe behaviour will definitely be beneficial for the provision of more specific functional and design specifications for next-stage prototypes, and it will constitute the basis for the development of kinematics models necessary to predict the probe behaviour and therefore optimise the actuation strategy and control of the probe.

Chapter 7

New Probe Prototype and System Integration

This chapter presents the design of a new flexible probe prototype, the cross-sectional geometry of which was modified having taken into account the results from the optimisation procedure described in Chapter 5. Results about the steerability performance of the new prototype in a compliant medium are then discussed. Finally this chapter concludes with a description of the integration of the flexible probe prototype within a neurosurgical robotic suite (EU FP7 ROBOCAST).

Part of the work presented in this chapter has been published in a conference publication [Ko et al., 2010a].

7.1 Introduction

In Chapter 4, a prototype of a biologically inspired flexible and steerable probe was presented, which was used to demonstrate the feasibility of multiple curvilinear trajectories in a compliant medium. In Chapter 5, a methodology for the optimisation of the probe design was introduced, with the aim of reducing irreversible probe segment separation, and an optimised cross-sectional geometry for the interlocking mechanism was proposed.

Based on the probe prototype design and operation detailed in Chapter 4, and on the results of the cross-sectional optimisation presented in Chapter 5, the development of a new probe prototype is described here. The new prototype, or beta prototype, characterised by an optimised interlock cross-section, has a smaller diameter (10 mm) and it is slightly longer (226 mm) than the alpha prototype (12 mm in diameter and 200 mm in length). In addition, a new feature is introduced, which has the potential to improve the steerability capabilities of the flexible probe, as described in the next section.

The beta prototype is tested using the same experimental setup described in Section 4.4.3, with the aim of demonstrating improved performances with respect to the alpha prototype. Steerability in a compliant medium along curvilinear trajectories with different radii is assessed and, to this end, the "direct push" strategy is compared to the "reciprocal motion" strategy. However, some technical problems are encountered, which limit the possibility of an in depth analysis of the probe's performance; these problems are described and will be addressed in future research (Chapter 8). With regard to the work presented in this section, the author was solely not responsible for the development of the actuation system and of its graphical user interface, as already mentioned in Chapter 4.

This chapter ends with the description of the integration of the flexible probe prototype within a neurosurgical robotic suite (EU FP7 ROBOCAST, [Robocast-Project, 2010]). Although the aim of the research presented in this thesis is to demonstrate the feasibility of flexible probe steering in a compliant medium, parallel work was also carried out to ensure that, where possible, specifications for the integration of the flexible probe system (flexible probe prototype and actuator system) within a neurosurgical robotic suite were addressed. An overview of these efforts is also included in this chapter (Section 7.4) and in Appendix D. With regard to the work presented in this section, the author's main focus was centered solely on the aspects related to the design of the mechanical interfaces between the ROBOCAST system components.

7.2 Materials and methods

This section describes the beta probe prototype design and manufacturing, with a focus on the main differences compared to the alpha prototype described in Chapter 4. Furthermore, "direct push" and "reciprocal motion" insertion strategies are compared and the experimental protocol applied to test probe performance is explained.

7.2.1 Beta prototype design

The beta probe was designed to be manufactured with the RP technique already described in Section 4.4.2. Figure 7.1a shows a 3D view of the interlocked segments composing the probe. The beta prototype was built with the same materials used for the previous (alpha) prototype, described in Section 4.4.2. The back of each probe segment is rigid, the middle body is flexible and the tip of the two leading segments is more rigid than the body.

Although the beta prototype looks very similar to the previous one, the following modifications are introduced:

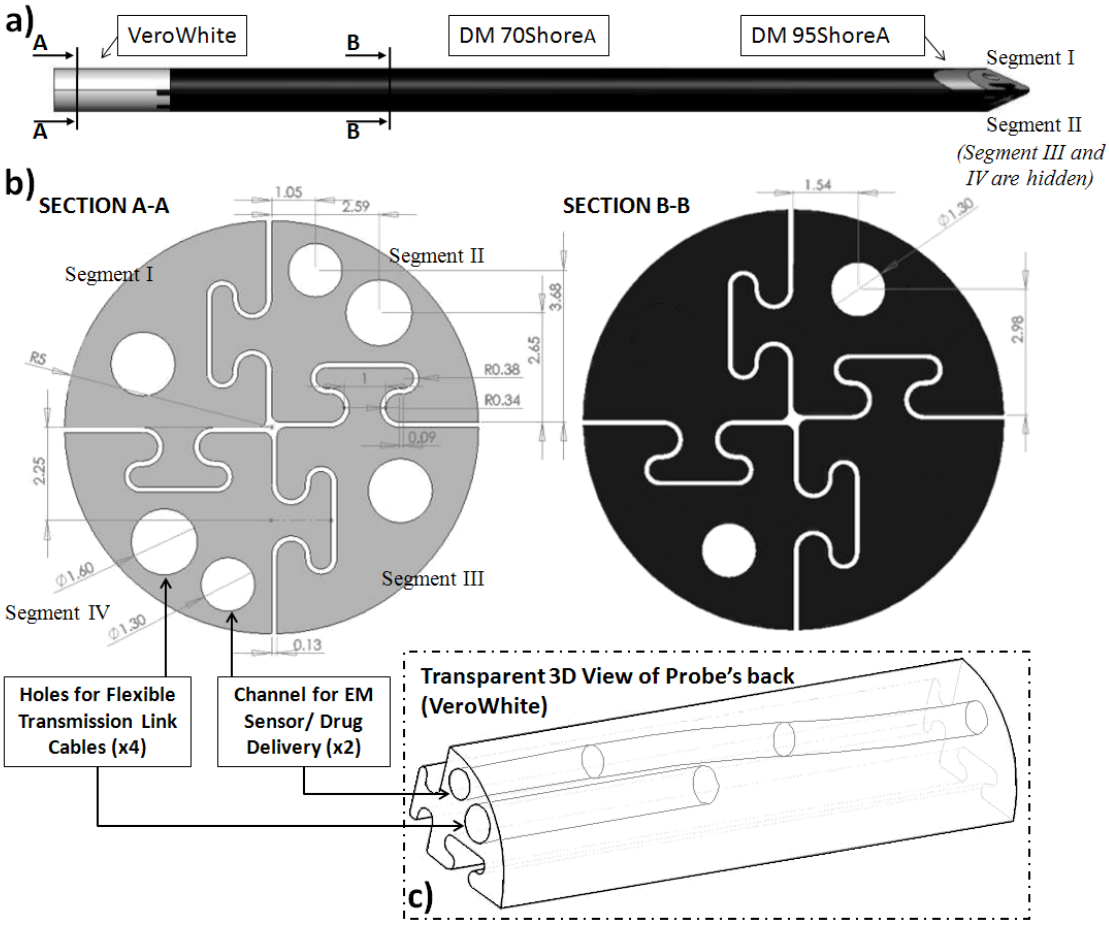


Figure 7.1: Beta probe prototype. a) 3D view with material labels. b) Cross-section at sections AA and BB, with relevant quotes (in mm). c) Transparent 3D view of the probe's back: note the bent shape of the channel for the EM sensor (or Drug Delivery).

- *New interlock design:* based on the results of the geometrical optimisation of the interlocking mechanism presented in Chapter 5, a new interlock is designed (Figure 7.1b). The geometrical parameters defining shape and dimensions of the interlock obtained from the geometrical optimisation are imported directly into the CAD drawing of the prototype cross-section. However, because of manufacturing limitations, two modifications with respect to the optimal interlock geometry identified in Chapter 5 are introduced: the geometry is scaled up by a factor of $\frac{5}{3}$ (from a 3 mm radius to a 5 mm probe radius) and the clearance between the segments, which however is not an optimisation parameter in the interlocking mechanism model, is fixed to 0.13 mm. These modifications do not affect the relationships between the original geometrical model parameters.

- *Reduced dimensions:* due to the new interlock design, a new release of the EM tracking sensor, which is smaller than the previous one (Aurora 5DOF Catheter, Type 1, 1.1mm external diameter, Northern Digital inc.) and a reduced clearance between the segments from 0.15 to 0.13 mm, it was possible to reduce the probe external diameter from 12 mm to 10 mm. This reduction, coupled with a small increase of the probe length (from 200 mm to 226 mm), makes the new probe more flexible and possibly more steerable.

- *Pre-bent shape of leading segments:* given the extensive manufacturing capabilities of RP techniques, the leading segments are designed in such a way that, in their resting position, the leading segment tips have a natural inward preload, as shown in Figure 7.2. This feature is believed to improve the capabilities of the "programmable bevel tip"; smaller offsets will be required to obtain the same radii of curvature. The effect of the tissue resistive forces acting onto the bevel tip when a segment is pushed forward with respect to the other three was already explained in Section 4.5. However, when the leading pre-bent segment projects outwards from the other three segments, it is also forced to bend, because of the pre-bent shape, depending on the amount of offset. This is believed to increase the effect of the steering offset on the bevel-tip reorientation. It should be noted that the radius of curvature of the pre-bent shape (45 mm, Figure 7.2), and its length (70 mm), were arbitrarly selected as a compromise between contrasting requirements: on one side, the need for a very bent shape which would increase the steering capabilities, and therefore achieve tighter curvatures, and on the other, the risk that a very bent shape could cause excessive segment deformations when forced in a straight position.

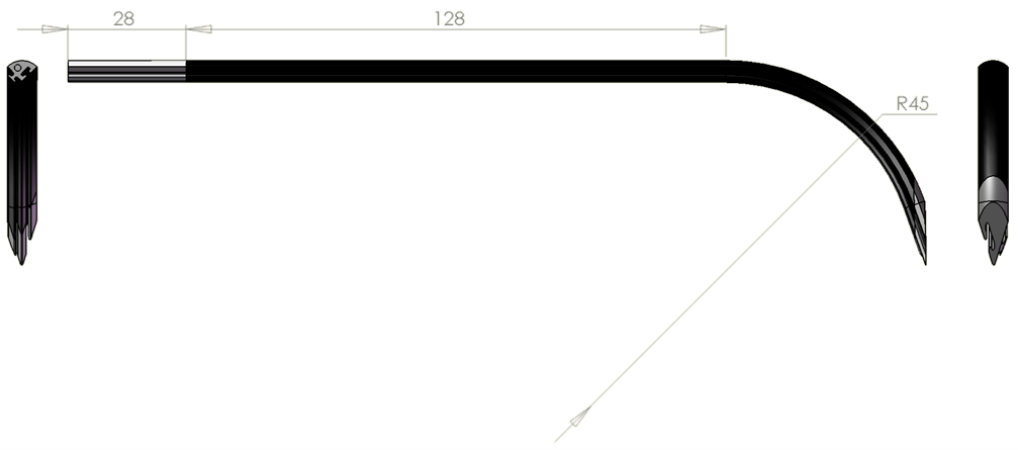


Figure 7.2: Pre-bent probe segment: projected views.

7.2.2 Beta prototype manufacturing

The new flexible probe prototype is shown in Figure 7.3. Figure 7.3a shows the four segments. Figure 7.3b shows the probe in its "initial" position, when all segments are interlocked and aligned. Because of the interlocking mechanism between the segments, the pre-bent segments are kept in a straight position. Figure 7.3c shows the probe when one of the two pre-bent segments projects forward. Because of its natural preload, the segment tends to bend: the larger the offset, the more marked the curvature.

7.2.3 Experimental setup and protocol

The experimental setup used to test the steering capabilities of the new prototype, when a "direct push" or a "reciprocal motion" insertion strategy are applied, is the same as the one described in Section 4.4.3, which is shown in Figure 4.5. The only difference is that the original trocar (12.5 mm internal diameter) is replaced with a smaller trocar fitting the new probe (10.5 mm internal diameter).

Regarding the experimental protocol, "direct push" and "reciprocal motion" protocols are performed as follows:

1. *Direct Push*: the probe was inserted 10 mm inside the gelatine, with all probe segments aligned; the speed parameter was set to 2 mm/s. The four segments were then actuated together, but, until the desired offset was reached, the speed of segment III (leading segment) was set to 15 mm/s. Once the offset was reached, all probe segments were pushed together inside the gelatine at a speed of 2 mm/s, down to a depth of at least 100 mm. The following offsets were imposed: +10, +12, +15 mm and -10, -12, -15 mm (the offset sign relates to the steering direction: segment I is associated to a negative offset, segment III to a positive one, see Figure 7.1).

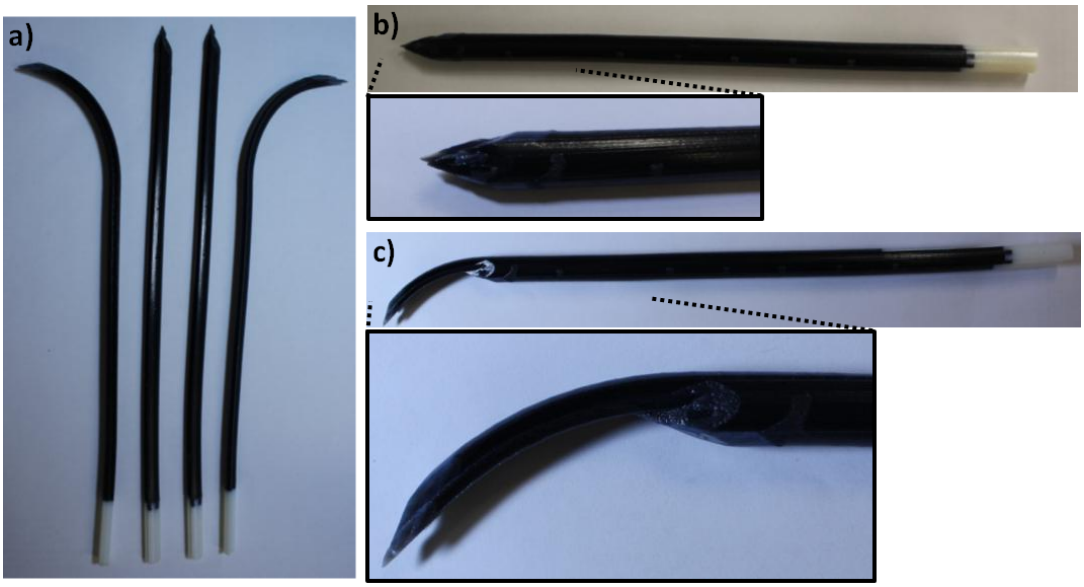


Figure 7.3: New RP flexible probe prototype. a) Four segments, two of which are pre-bent and have a more rigid tip. b) Segment assembly, all segments are aligned and the probe is straight; tip's probe in the inset, where the more rigid tip of one of the segments is visible. c) Segment assembly, one of the pre-bent segments is projected forward to show its tendency to bend.

2. *Reciprocal Motion*: the probe was inserted 10 mm inside the gelatine with all probe segments aligned; the amplitude of the stroke used to reciprocally push each probe segment was set to 10 mm. All segments were then reciprocally actuated with an average speed of 10 mm/s (peak speed of 20 mm/s and overall probe motion of 2.5 mm/s, see Appendix C), but, until the desired offset was reached, the stroke amplitude of the leading segment was increased by a predefined amount, bigger than the intended amplitude of 10 mm. At the same, time the amplitude of the other segments was reduced by the same amount. Once the offset was reached, the cycle of segment strokes was repeated constantly until the whole probe was pushed inside the gelatine down to a depth of at least 100 mm. The following offsets were imposed: +5, +7, +9 mm and -5, -7, -10 mm (the offset sign relates to the steering direction: segment I is associated to a negative offset, segment III to a positive one, as before).

All the parameters used for these experiments resulted from preliminary tests. Further details on the probe's behaviour will be given in the next section. It is worth mentioning at this point that the higher speeds and greater offsets applied in these experimental protocols with respect to the protocols described in Chapter 4 are justified by the fact that, at lower speed and smaller offsets, the offset imposed at the probe's base was absorbed by the probe's deformation (axial compression of the offset segment, coupled with axial extension of the other segments) and was thus not transmitted up to the probe's tip. This also explains why offsets between

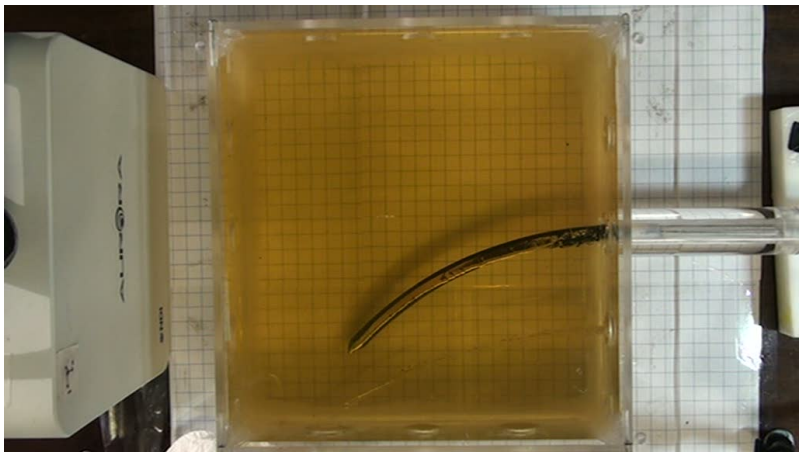


Figure 7.4: Flexible probe trajectory achieved through a "direct push" insertion strategy, with an offset of 10 mm

±10 mm are not considered in "direct push" experiments and, similarly, offsets between ±5 mm are omitted from the "reciprocal motion" experiments.

On a further note, the difference in the overall velocity of insertion after the leading segment offset is established (2 mm/s for "direct push" and 2.5 mm/s for "reciprocal motion") is expected not to affect the probe curving path, as demonstrated by Webster et al. [2005].

After each test, the plane of best fit of the trajectory data measured by the EM tracking system is identified through a "principal component analysis" function available in MATLAB, as already described in Section 4.5.1. The coefficients of the first two principal components define vectors that form a basis for the plane of best fit (i.e. the regression plane which minimises the perpendicular distances from the data to the plane). The third component is orthogonal to the first two and it defines the normal vector of the plane, which is the error term in the regression. The original 3D data points are then projected onto the plane of best fit and then fitted to a circle to find the average radius of curvature for each trajectory. Curvature values (i.e. the inverse of the radii of curvature) for each offset are computed and the off-plane regression is considered.

7.3 Results and discussion

Figure 7.4 shows a typical example of probe insertion into gelatine ("direct push", 10 mm offset).

All the flexible probe tip trajectories, projected onto the plane of best fit, are shown in Figures 7.5 and 7.6 (zoomed view). The original data is represented by the thick lines; the circles fitting each trajectory are also plotted on the same graphs.

Table 7.1 shows the curvature and steering radius values calculated for the tra-

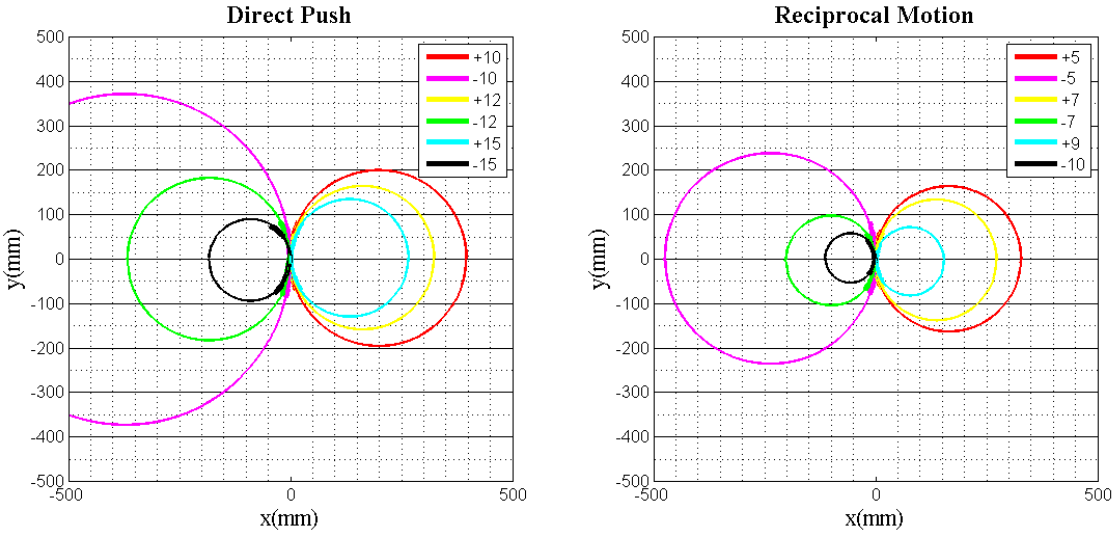


Figure 7.5: "Direct push" and "reciprocal motion" trajectories (thick lines) projected onto the best-fit plane and corresponding circles of best fit. Note that each trajectory is plotted with respect to its central position, thus the x-y axes do not correspond to the original EM reference system.

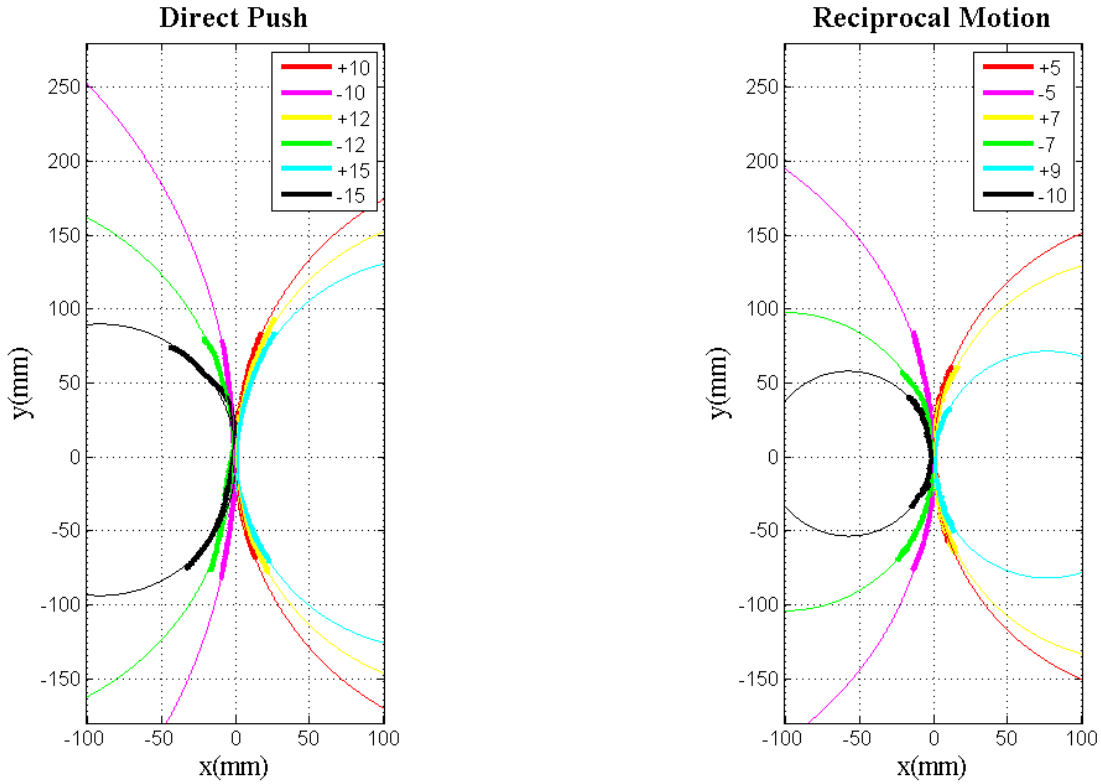


Figure 7.6: "Direct push" and "reciprocal motion" trajectories (thick lines) projected onto the best-fit plane and corresponding circles of best fit, zoomed view

Direct Push			**Reciprocal Motion**		
Offset (mm)	**Curvature** $\times 10^3$ (mm^{-1})	**Steering Radius** (mm)	**Offset** (mm)	**Curvature** $\times 10^3$ (mm^{-1})	**Steering Radius** (mm)
-15	-10.9	-91.85	-10	-17.9	-55.75
-12	-2.5	-182.61	-7	-9.9	-100.86
-10	-2.7	-372.21	-5	-4.2	-236.99
+10	5.1	197.77	+5	6.1	163.45
+12	6.2	161.3	+7	7.4	135.87
+15	7.6	132.2	+9	13	76.69

Table 7.1: Steering Offset vs. Curvature and Steering Radius

jectory of each experiment.

Figures 7.5 and 7.6 and the results presented in Table 7.1 confirm that there is a relationship between the offset and the degree of curvature achieved in gelatine by the flexible probe, as demonstrated already in Section 4.5.2. A linear interpolation of the curvature as a function of the offset is provided in Figure 7.7, both for the "direct push" and the "reciprocal motion" experiments.

As expected, the beta prototype, if compared to the prototype described in Section 4.4.2, shows better steerability performances when "direct push" experiments are compared. Smaller offsets are required to achieve curvatures similar to those obtained with the alpha prototype (smaller radii of curvature). The coefficient of the linear "Offset-Curvature function" of the beta prototype is indeed $5.27 \cdot 10^{-4}\,mm^{-2}$, almost 3 times larger than the same coefficient calculated for the alpha prototype ($1.96 \cdot 10^{-4}\,mm^{-2}$). This is believed to be justified by the reduced probe dimensions and by the increased "programmable bevel tip" re-orientability provided by the pre-bent shape of the leading segments.

The steerability performance is improved further when a "reciprocal motion" insertion strategy is applied. The coefficient of the linear "Offset-Curvature function" in "reciprocal motion" experiments is $14.2 \cdot 10^{-4}\,mm^{-2}$, about 3 times larger than in the case of "direct push" ($5.21 \cdot 10^{-4}\,mm^{-2}$).

However, through observations of the experiments, it was also noticed that the beta flexible probe tends to axially deform quite substantially. As briefly explained in Section 7.2.3, when one segment is pushed forward (to generate the steering offset in the "direct push" strategy or at each stroke in the "reciprocal motion" strategy), the segment is compressed axially because of the high friction between the other segments. For the same reason, the stationary segments are "pulled" by the frictional forces of the moving segment and tend to extend slightly. This effect was observed to be related to the relative speed between the segments: with higher velocities, the

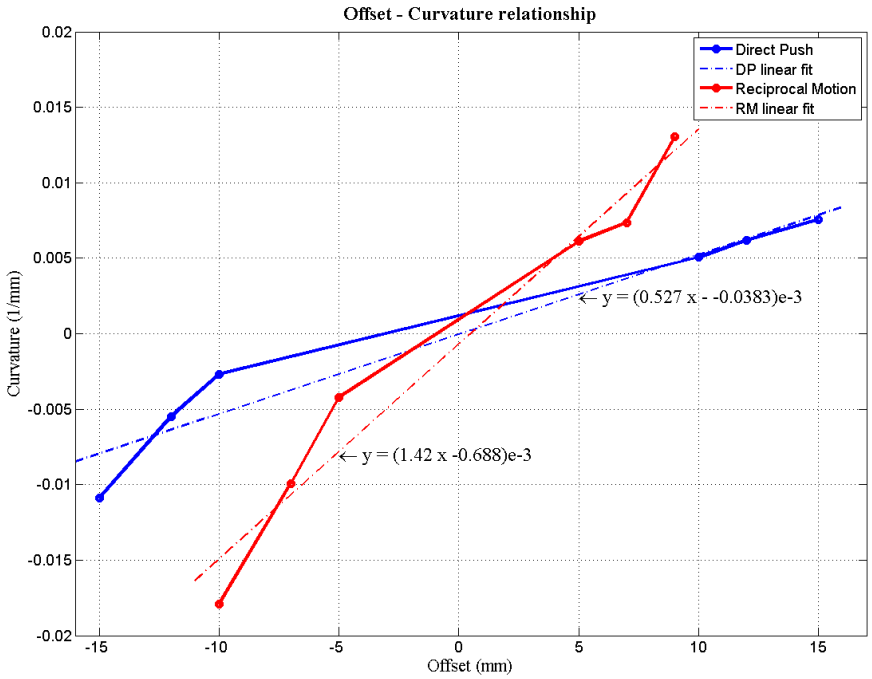


Figure 7.7: Relationship between offset and curvature for "direct push" and "reciprocal motion" experiments. A linear fit for the two sets of experiments is also identified.

effect was partially reduced, but still very evident. The relative high velocities at which one of the segments is slid with respect to the others (10 mm/s to 20 mm/s peak), is required to overcome the high static friction which exists between rubber materials. Therefore, an offset imposed at the base of the leading segment results in an offset at the tip which is smaller and this depends on many variables (probe stiffness, friction between the segments, lubrication regime and relative displacement and velocity of the moving segment), which were not considered or quantified in this study.

The reason for the better steering capability of "reciprocal motion", compared to "direct push" is thus not clear. It is possibly related to the way the offset at the base is transmitted to the tip. The higher stroke speed (peak of 20 mm/s in "reciprocal motion" as compared to the speed of 15 mm/s required to create the steering offset in "direct push") can partially justify this behaviour. Another possibility may explain this difference to be due to the fact that the segments are always in relative motion with respect to each other. At each segment stroke, part of the deformation accumulated by the segments which were previously pushed forward is released and, therefore, the offset imposed at the base can "travel" more easily towards the tip after a full stroke cycle.

Figure 7.8 shows the mean and standard deviation of the off-plane errors of the

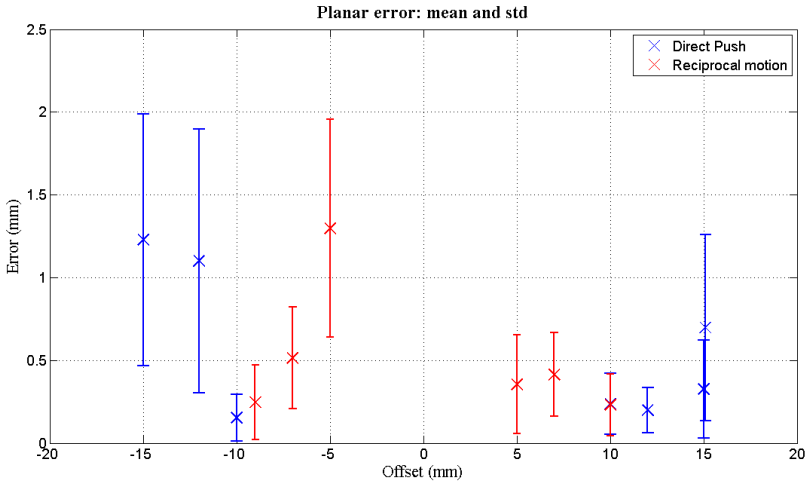


Figure 7.8: Mean off-plane absolute error and error standard deviation for "direct push" (blue) and "reciprocal motion" experiments (red).

trajectory as a function of the offset, for each experiment. The probe was initially manually aligned along the horizontal plane, therefore initial misalignments are eliminated by finding the best-fit plane and by considering the curvature projected onto the plane of best fit. The off-plane error can thus be considered to be an indicator of the amount of probe torsion during the insertion process. A torsion of the tip during insertion can be caused by the frictional forces between the segments and by the fact that the tip of each segment is not completely flat and symmetric. The interlocking hollow rail creates a material weakness at the bevel tip (see Figure 7.2, right view), which causes the tip itself to tend to bend slightly off-plane. However, with regard to the off-plane errors, it was not possible to identify any significant difference between "direct push" and "reciprocal motion" strategies. To confirm this, a two-sample t-test on the mean errors of "direct push" and "reciprocal motion" experiments provided a p-value of 0.7752 ($p>0.05$). Therefore, the sequence of "reciprocal motion" does not seem to affect the extent of the off-plane error with respect to a "direct push" strategy. In addition, it is not possible to clearly identify any significant difference depending on the steering offset imposed and therefore on the curvature achieved.

The only difference in probe's behaviour between the "direct push" and the "reciprocal motion" strategies can be identified by considering the profile of the off-plane error during the insertion into gelatine. As an example, Figure 7.9 shows the off-plane error for the "direct push" +12 mm offset and the "reciprocal motion" +5 mm offset experiments respectively. These two experiments were selected because they provide similar curvatures (see Table 7.1).

A "reciprocal motion" insertion shows oscillations around the best-fit plane (corresponding to error = 0 in Figure 7.9), due to the cyclical actuation strategy. It is believed that, when each segment is pushed with respect to the others, because

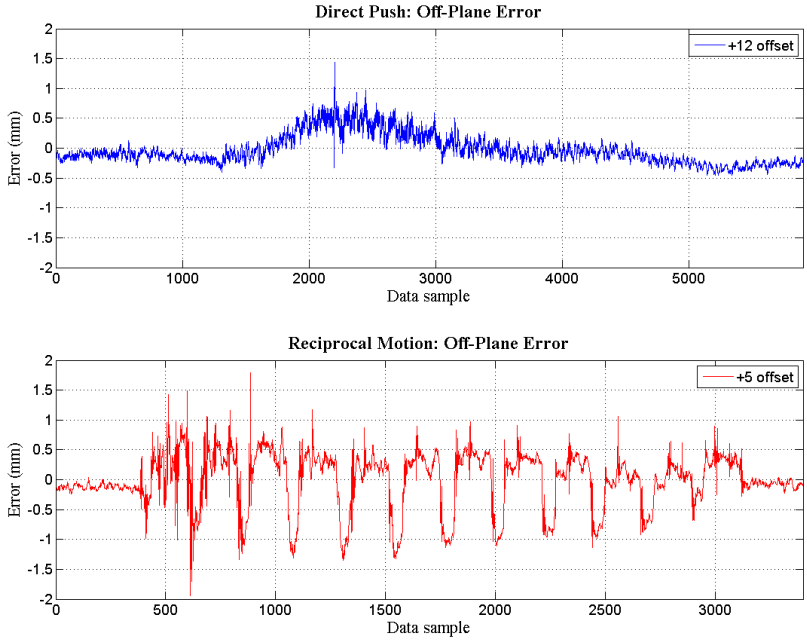


Figure 7.9: Examples of off-plane error for a "direct push" (+12 mm steering offset) experiment (top) and for a "reciprocal motion" (+5 mm steering offset) experiment (bottom). Note that, in this case, the "reciprocal motion" experiment was shorter than the "direct push" experiment.

of the frictional force between the sliding segments, the probe's tip tends to tilt accordingly. Note that the high frequency noise of the measured data is intrinsic to position measurements taken with an EM tracking system and that the off-plane error is within the noise floor of the Aurora EM measurement system used in the experiments (position accuracy of 0.9 mm, [Norhter-Digital-Inc., 2010a]).

As a further point of note, it is necessary to mention here that, although the new probe prototype shows improved steerability performances thanks to the reduction in cross-sectional dimensions and the introduction of the pre-bent shape of the leading segments, it is also weaker and more prone to fracture than the previous probe prototype. Particularly, the pre-bent leading segments easily broke at the interface between the rigid back and the flexible body (see Figure 7.1a), where material stresses are higher due to the segment deformations already described, which are caused by the frictional forces between the segments. For this reason, it was not possible to perform further experiments with the current prototype.

7.4 ROBOCAST: flexible probe system integration

The flexible and steerable probe presented in this thesis was also developed in the context of the EU FP7 ROBOCAST (ROBOt and sensors integration for Computer

Assisted Surgery and Therapy) project [Robocast-Project, 2010]. The aim of this european project is to realise a robotic system to assist surgeons performing brain surgery through a very small hole in the patient's skull. This aim is addressed by integrating existing and novel medical technologies in the fields of medical robotics, augmented reality and surgical planning into a next-generation neurosurgical suite.

This section provides a broad description on how the flexible probe system was designed to meet the specifications for its integration within the overall robotic system, with the aim of demonstrating the potential real clinical impact of the flexible probe. The surgical application considered here, even though not intended to be compliant with medical directives for clinical use, is "multiple targeting of therapy agents to tumours" (i.e. liquid delivery).

Given the author's main focus in this respect centered on the aspects related to the design of the flexible probe system, and the design of the mechanical interfaces between system components, these will be the only aspects addressed in this section. Further details on the ROBOCAST architecture and specifications are provided in Appendix D.

Following is a description of the ROBOCAST system, as available at the project website "www.robocast.eu" (accessed in June 2010):

"A modular system, allowing the simulation of small footprint, will be developed with 2 robots and one active biomimetic probe, able to cooperate among themselves in a biomimetic sensory-motor integrated framework. A gross positioning 6-axis revolute robot will support a miniature parallel robot holding the probe to be introduced through a "keyhole" opening into the skull of the patient. Optical trackers (tracking the end effector and the patient), an imaging endoscope camera, and electromagnetic position and force sensors (on the probe) will extend robot perception by providing the control system with position and force feedback from the operating tools, and with visual information of the surgical field. Path planning outside and inside the body will be autonomously proposed by the control system by processing of preoperative diagnostic information. The path inside the brain will be planned on the basis of a "risk atlas" reproducing a fuzzy representation of a brain atlas, relating structures to a "level of danger". Construction of the atlas will rely on cognitive learning, where the system will be able to provide the surgeon with explanations for any suggested action."

Figure 7.10 shows a view of the integrated components of the ROBOCAST system. The gross positioning robot (GP) holds the fine positioning robot (FP), which holds the flexible probe trocar (rigidly attached to the FP robot). The flexible probe actuator box, which measures 300x90x70 mm and weights 2.9 Kg, is mounted onto axis-4 of the GP robot. A flexible transmission link transmits the actuation from the actuator box to the flexible probe sitting in the trocar. The trocar can assume

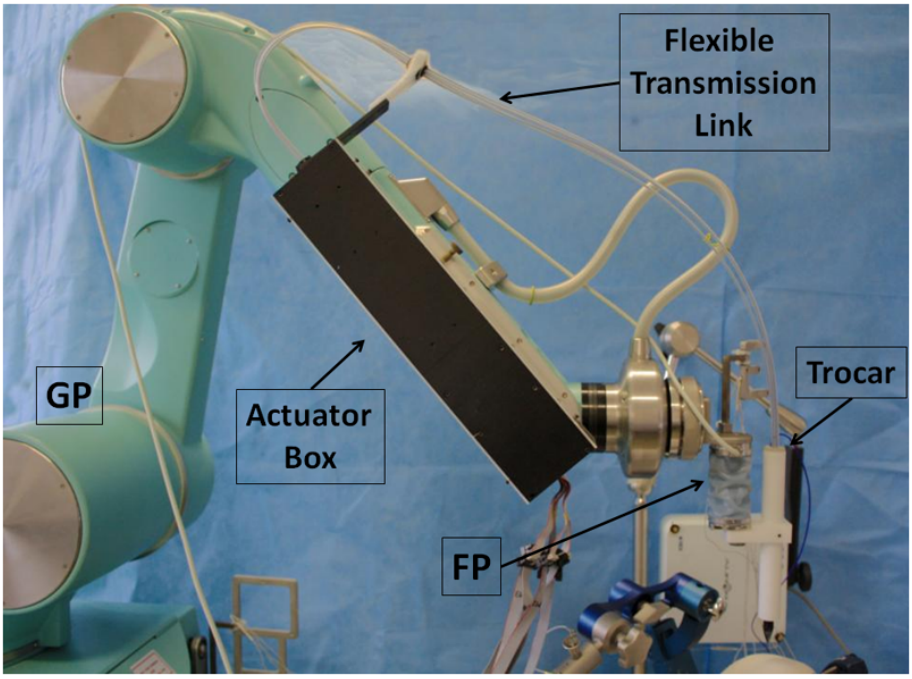


Figure 7.10: ROBOCAST system view. The GP robot is holding the FP robot, which is holding the trocar where the flexible probe is inserted. The actuator box, which is sitting on GP Axis-4, transmits the actuation via the "Flexible Transmission Link" to the flexible probe.

different positions and orientations in order to provide the optimum alignment with the insertion trajectory at the keyhole entry point in the skull and the flexible transmission link can connect the actuators and the flexible probe regardless of the trocar position and orientation.

The flexible transmission link is composed of four teflon (PTFE) tubes (3 mm OD, 2 mm inner diameter (ID) and 1 m length, Figure 7.12c), which house four mechanical cables. Each cable connects one probe segment to the corresponding moving nut in the actuator box, as described in Section 4.4.2. The inner cables (described in Section 4.4.2) can assume any shape according to the relative position of the GP robot holding the actuator box and the FP robot holding the trocar (see Figure 7.10 and Figure 7.12). The use of teflon for the cable housing guarantees a very low friction sliding between the nitinol wires and inner surfaces of the housing.

The trocar (25 mm OD, 12.5 mm ID and 210 mm length), shown in Figures 7.12a and 7.12b, is rigidly connected to the FP. This trocar was originally designed to house the aplha probe prototype (Section 4.4.2), but minor modifications were made to fit the beta prototype (internal diameter reduction to 10.5 mm). The position of the flexible probe in the trocar is uniquely determined by the keyed feature in the "trocar cap" (see Figure 7.12a). The teflon tubes are rigidly connected to the trocar cap, while the inner cables of the transmission link are attached to the rigid parts of the probe segments. The trocar cap is also provided with two holes, one for the

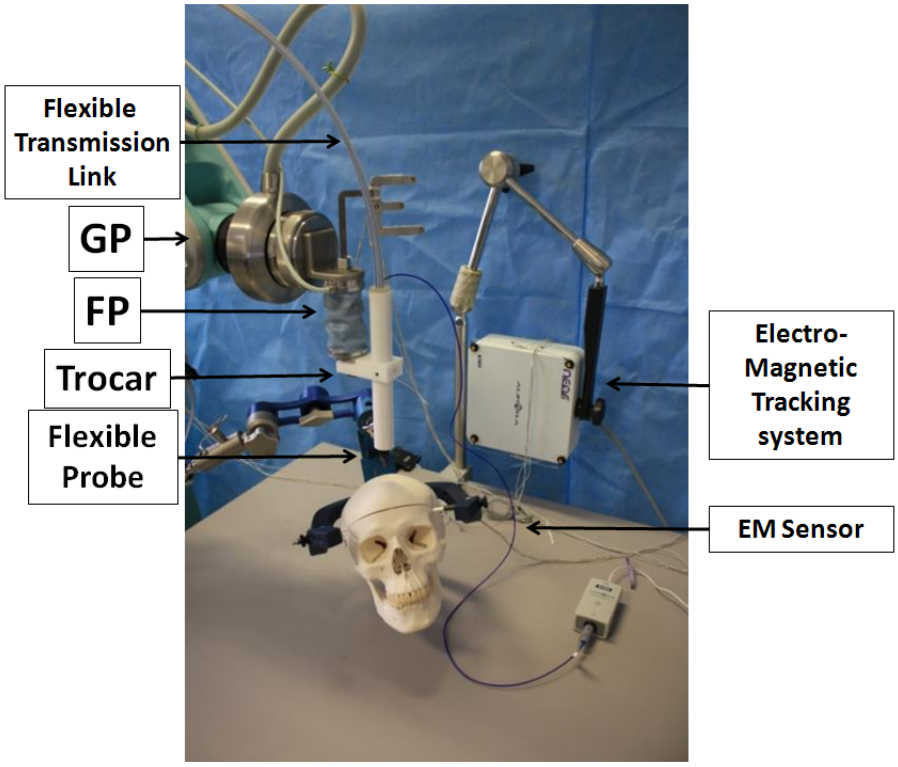


Figure 7.11: ROBOCAST system, zoomed view. The EM tracking system is used to provide position and orientation (5DOF) of the EM sensor inserted at the tip of the flexible probe

EM sensor and the other for a catheter for liquid delivery. A possible system for liquid injection and extraction was devised and it is shown in Figure 7.13. The liquid delivery system is composed of a syringe connected to the segment channel via a micro-catheter (0.8 mm OD). In the complete ROBOCAST system setup, an optical tracking measurement system (Optotrack Certus, [Norhter-Digital-Inc., 2010b]) is employed to monitor the position of the GP and the FP robots and, in the case of the flexible probe, the position of the trocar. Four optical markers were thus fixed onto the trocar in order to identify the initial position of the flexible probe (Figure 7.12b).

The mechanical interface between the actuator box and the GP axis-4 side plate is shown in Figure 7.14. The insert, rigidly attached to the actuator box, is inserted in the groove, also rigidly attached to the GP robot. Fixation is performed manually with the 'Handy Knob'. A corner of the insert, partially cut, prevents possible dislocation of the insert inside the groove. The interface between the trocar and the lower plate of the FP robot is shown in Figure 7.12. A screw is used to fix the trocar to the FP lower-plate. In addition, two pins in the FP lower-plate, with corresponding holes in the trocar holder, ensure a rigid assembly between the two.

Although a detailed description of all the specifications for the integration of the flexible probe is beyond the scope of this thesis, not being a research activity under

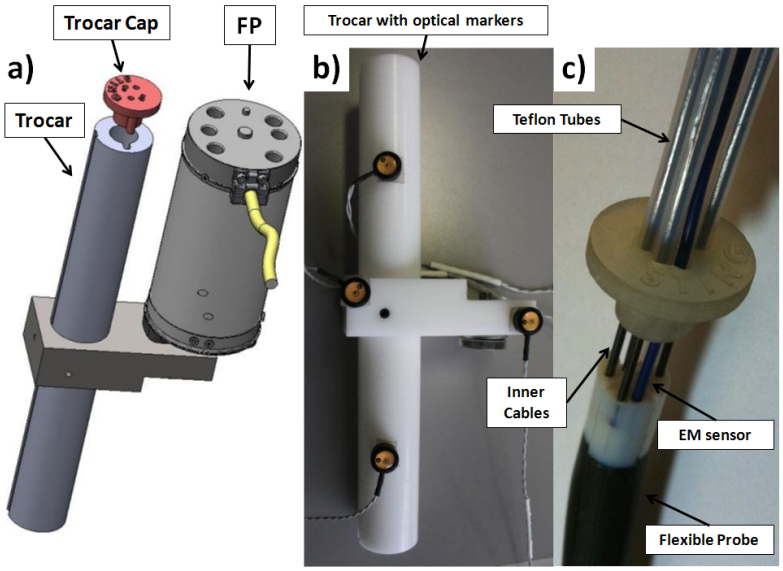


Figure 7.12: a) FP robot and trocar assembly. b) Trocar with 4 optical markers. c) Detail of the trocar cap, the teflon tubes, the inner cables and the EM sensor.

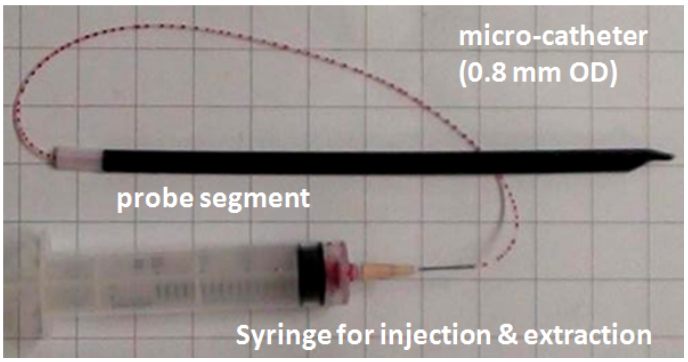


Figure 7.13: Flexible probe segment provided with a liquid delivery system.

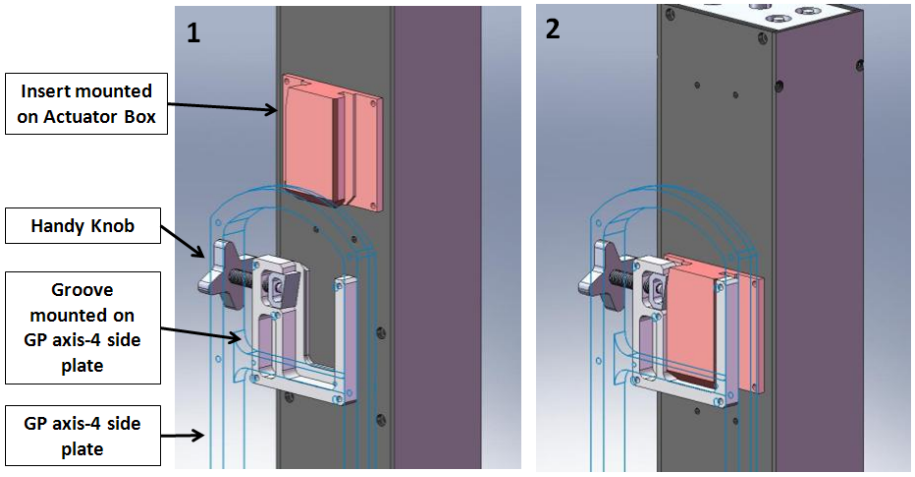


Figure 7.14: Interface between actuator box and GP axis-4 side plate. 1) Interface dismounted. 2) Interface mounted.

complete responsibility of the author, a summary of the key outcomes related to the experiments performed with the beta prototype within the context of ROBOCAST are included in Appendix D.

7.5 Conclusions

This chapter presented a new flexible probe prototype (beta prototype), designed on the basis of the prototype developed as a concept demonstrator for flexible probe steering and described in Chapter 4 (alpha prototype). Modifications to the alpha prototype were introduced on the basis of the results from the cross-sectional optimisation procedure described in Chapter 5. The main improvements to the prototype design are:

- a novel interlocking mechanism geometry, characterised by a larger interlock stiffness (less prone to irreversible segment separation)
- smaller probe cross-section dimensions and increased probe length (with a consequent increase in probe flexibility)
- pre-bent shape of leading segments, with increased probe steering capabilities

It was demonstrated that the beta probe prototype has improved steering capabilities with respect to the alpha prototype, due to its smaller cross-section and to the pre-bent shape of the leading segments: smaller radii of curvature are obtained with smaller base offsets of the leading segment. A "reciprocal motion" insertion strategy also demonstrated to be more effective with regard to steerability, for the prototype described in this chapter.

The off-plane error of each trajectory was considered as an indicator of probe torsion during insertion, which causes the probe to deviate from the plane of curvature. However, it was not possible to establish any significant difference between "reciprocal motion" and "direct push" strategies, or any significant effect of torsion caused by the amount of curvature.

However, although the new flexible probe has demonstrated improved steering capabilities, it also showed that there are many technical problems which currently limit the performance and the use of the beta prototype. Particularly, the development of this prototype has reached the boundaries of what is possible with RP methods with regard to the resistance to tear of the flexible materials available and with regard to the resolution of the manufacturing technique itself. Medical-grade silicone extrusion methods were also preliminary explored (refer to Appendix B), to produce a smaller and more durable probe prototype, but many manufacturing

challenges still need to be addressed. Additional suggestions for future research on this topic will be addressed in Chapter 8.

This chapter concludes with the description of the integration of the flexible probe prototype into a robotic system aimed at assisting neurosurgeons in performing key-hole neurosurgery, within the context of the european EU FP7 ROBOCAST project. The flexible probe was designed and developed to meet the specifications required for the integration of the beta prototype into a potential clinical system. Some of the salient features of the integration process are described, while details of the validation process are included in Appendix D. The flexible probe system, both hardware and software, was integrated within the complete robotic system, meeting most of the objectives required by the ROBOCAST project, demonstrating that the flexible probe system can be applied to a clinical setting and potentially inserted into the workflow of a complete keyhole neurosurgical operation, from the pre-operative planning to the actual surgery.

Chapter 8

Conclusions and Future Work

This chapter concludes with an overview of the research presented in this thesis on the topic of flexible probe steering for percutaneous intervention. A summary of the salient contributions of this research is presented, and suggestions for future research on several aspects regarding flexible probe steering are proposed.

8.1 Overview

The aim of the research presented in this thesis was *to prove the viability of a novel biologically-inspired, probe steering mechanism - as demonstrated by a fully functional prototype, capable of curvilinear motion on a plane, within a compliant medium of brain-like tissue consistency.* The journey towards the fulfillment of this aim began in *Chapter 2*. Here, the understanding of the medical motivations behind the need for novel instruments to expand the potential of percutaneous interventions was established. It was described how percutaneous interventions, with a focus on brain interventions for tumour diagnosis and treatment, could benefit from the development of novel, active, "smart instrumentation" that would enable surgeons to target lesions deep within the brain, both safely and accurately, by allowing them to chose a desired curvilinear trajectory between an entry point and a soft tissue target. An overview of the latest research on the topic of flexible needle steering for percutaneous intervention was then presented. Three different needle steering approaches are currently proposed by other research groups: steering via a bevel tip needle, steering by relying upon tissue resistance (needle bending) and steering via curved, nested concentric tubes. However, all these approaches present drawbacks which narrow the benefits for potential clinical application. They show, for example, limitations in the dimensions of the instruments, limitations in the range of curvilinear trajectories available and problems due to excessive tissue tearing. In the attempt to address these limitations, a novel approach to needle steering is suggested by Nature, through the example of ovipositing wasps. This unique approach to needle

steering is the focus of this thesis. A detailed overview of the biological inspiration was presented in Chapter 2, with the aim of understanding how ovipositing wasps use their long, thin and flexible ovipositor to lay eggs in different substrates. The ovipositor is composed of interlocked segments and drives itself inside the target tissue thanks to a reciprocal insertion of the segments, coupled with a toothed outer surface. This insertion strategy prevents the ovipositor from buckling, even when a substrate as hard as the bark of a tree is traversed. In addition, by relying solely upon the interaction between the ovipositor segments (no "active components" are embedded at the tip), the ovipositor tip can be reoriented in order to reach desired target locations.

On the basis of the biological example, *Chapter 3* proposed a preliminary study which aimed to replicate the penetration strategy as employed by ovipositing wasps. This was done with the aim of demonstrating that a multi-part probe, composed of interlocked segments with anisotropic surface texture, could penetrate soft tissue thanks to a strategy based on the reciprocal actuation of the probe segments. Anisotropic surface microtexturing of rigid probes was shown to facilitate probe insertion into porcine brain tissue while limiting the probe's migration inside the tissue. Soft tissue surface traversal of toothed samples was then achieved by exerting a "zero net force" on the sample assembly. A method for the characterisation of the tracks left by the toothed samples traveling onto the tissue surface was proposed and used to conclude that the reciprocal motion of a segmented probe provided with anisotropic textured outer walls could be potentially implemented to penetrate a specific tissue (i.e. fibrous tissue, such as muscle) with virtually no net axial push on the probe assembly from the back. Because of the absence of a net forward force acting on the probe assembly, it was claimed that a biologically-inspired penetration strategy could possibly offer the benefit of a greatly reduced risk of buckling and no theoretical limit on the probe's length. Chapter 3 concluded by outlining practical limitations inherent to this insertion mechanism: the need for a cumbersome very low friction bearing, and the restricted range of soft materials for which such an insertion strategy is viable (since the cutting force, which is material specific, was found to be the single most important factor affecting the ability of the probe to penetrate the substrate).

On the basis of these considerations, a simplified concept demonstrator was proposed in *Chapter 4*, which demonstrated that a flexible multi-part probe composed of interlocked segments can achieve curvilinear trajectories in a compliant medium. Three hypotheses were identified and proved through suitable experiments with a flexible probe prototype. These hypotheses and corresponding findings can be summarised as follows:

- *The probe can steer in a compliant medium along curvilinear trajectories with*

different radii. Thanks to the concept of a "programmable bevel tip", the flexible probe was steered along different curvilinear trajectories, where the probe tip orientation was found to be a function of the offset imposed at the base of one of its segments. A linear relationship between offset and curvature (inverse of radius) was identified.

- *The probe can steer in a compliant medium along curvilinear trajectories with reduced risk of buckling.* Thanks to a "reciprocal motion" insertion strategy, where the probe segments are actuated one at a time rather than the probe being pushed as a whole, the effect of buckling of the flexible probe was significantly reduced.

- *The probe can steer in a compliant medium along multiple curve trajectories.* By coupling the effect of the "programmable bevel tip" with a "reciprocal motion" insertion strategy of the probe segments, the flexible probe was steered along a double curve trajectory.

Chapter 4 concluded with an analysis of problems and failures observed during the experiments: probe buckling, probe twisting, probe segment compression and segment irreversible separation. Within all of these, the irreversible separation of the segments was defined as the most critical. It was therefore addressed in the following chapters through mathematical and numerical modelling.

Chapter 5 proposed an optimisation procedure of the design of the interlocking mechanism between probe segments, aimed at reducing the risk of irreversible separation. A numerical model was developed for the optimisation of the interlock geometry, and a probabilistic heuristic method was used to identify the geometry which shows the greatest stiffness. The accuracy of the optimum interlock model was then validated through experiments. In *Chapter 6,* a mathematical model, solved using a numerical method, was then proposed to calculate the critical axial load which triggers segment separation as a function of interlock stiffness. It was demonstrated that the optimised interlock geometry has a stiffness which is double that of the interlock geometry of the prototype described in Chapter 4 (i.e. alpha prototype). As a result, the critical axial load triggering segment separation was found to be more than 20% higher in a probe segment featuring the optimised interlock geometry. The aim of this study was to lay the foundations for a 3D parametric analysis of the flexible probe behaviour, the outcome of which will help to elucidate operative conditions, understand the reasons behind how the probe is able to steer and suggest improvements for enhancing the performance of future embodiments of the probe.

Finally, the new interlock design obtained from the optimisation procedure described in Chapter 5 and the early results summarised in Chapter 4, were employed

to produce a further prototype of the flexible probe system, details of which are presented in *Chapter 7*. Three main improvements were introduced: a new cross-sectional interlock geometry, reduced dimensions and pre-bent shape steering segments, which were used to increase the steering range of thee "programmable bevel tip". The new prototype was then tested in a compliant medium. The new prototype showed increased steering capabilities with respect to the previous prototype, particularly when a "reciprocal motion" insertion strategy was applied. However, the results presented in this chapter also highlighted the limitations of the manufacturing technique employed to date - Rapid Prototyping - and of the flexible materials used to produce the probe. Chapter 7 also reported on the work carried out on the integration of a fully functional flexible probe system, consisting of a probe prototype and actuation system, into a next-generation robotic system designed to assist neurosurgeons when performing keyhole neurosurgical interventions. The performance of the integrated system, carried out within the context of the EU FP7 ROBOCAST Project, was validated through laboratory trials, results of which are summarised in Appendix D.

8.2 Summary of salient contributions

The research herein presented has resulted in the following specific contributions:

- Analysis of the biological example of ovipositing wasps to solve the engineering problem of flexible needle steering in a compliant medium.
- Introduction of a novel "microtexturing" approach to the treatment of probe surfaces, which can be used to modify the contact behaviour at the probe-tissue interface.
- Development of new methods for the characterisation of surface interactions within compliant mediums.
- **Successful implementation of a novel biomimetic probe which (a) can steer along variable planar trajectories, where the steering radius can be controlled, and (b) with reduced risk of buckling.** This specific work has resulted in a patent on "steerable probes" [Rodriguez y Baena et al., 2009].
- Use of analytical methods for geometrical modelling and optimisation to improve the design of the biomimetic probe prototype.
- Implementation and integration of a fully functional 10 mm OD robotic probe within a neurosurgical suite, the performance of which was validated through

laboratory trials.

- Built the foundations of a multi-purpose technology platform in the area of percutaneous robotic surgery, which will fuel future research on this topic.

8.3 Clinical contributions

The research presented in this thesis was aimed at addressing current drawbacks of clinical procedures for soft tissue surgery, with a particular focus on minimally invasive brain surgery. Although future work is deemed necessary on mainly all aspects of the flexible probe development (see Section 8.4, but particularly probe miniaturisation and biocomaptibility), the results herein presented could be implemented clinically, as long as the outer diameter of the probe can be further reduced and a fruitful collaboration with clinical partners is estabilished.

8.4 Future work

The research presented in this thesis represents the very first attempt to identify and demonstrate the feasibility of a novel bio-inspired method for achieving curvilinear trajectories in a compliant medium. Although much work has been done to successfully demonstrate the viability of the novel concept, more research, both fundamental and applied, is still necessary.

Four main future research streams can be identified which will be discussed separately: medical mechatronics, computational modelling, medical image computing and histological analysis.

8.4.1 Computational modelling

Advanced modelling is necessary to deepen our understanding of the reasons underlying probe function in many diverse areas:

- A kinematic model of the flexible probe is suggested in order to fully understand how the probe's approach angle can be controlled by varying the steering offset. This work would start from a study of existing models for continuous robots (infinite degree-of-freedom robots characterised by flexible backbones [Webster, 2007]).

- Building on the foundations of the modelling approach presented in Chapter 6, a more realistic numerical model of the probe is required in order to understand how the probe segments interact with each other and under which

operating conditions the probe fails (i.e. probe buckling or twisting, probe segment separation and deformation). This model, corroborated by experiments, should provide useful insights on how to optimise and miniaturise the probe design and on the desired characteristics of the most suitable material.

- A model of the probe-tissue interaction, also corroborated by experimental tests, could explain the complex interactions between a compliant steerable probe and the surrounding tissue (tissue deformation, tissue cracking). This information would be used to identify the probe's geometrical parameters and material properties - vital to improving probe steerability - depending on the tissue to be penetrated (i.e. gelatine, liver, brain). This work is currently being addressed by the author's research group, and preliminary results are described in Oldfield et al. [2011].

8.4.2 Medical mechatronics

With regard to the aspects more relevant to mechatronics, though linked to the ones listed in Section 8.4.1, future research should be centred upon:

- Exploration of new manufacturing techniques, in order to overcome the current limitations of Rapid Prototyping.
- Identification of new, suitable, biocompatible flexible materials (an early attempt to develop a medical grade silicone multi-part probe prototype is discussed in Appendix B).
- Extension of probe steering from a planar curvilinear trajectory to a full 3D trajectory.
- Investigation of closed-loop control strategies for the biomimetic probe which will produce accurate tracking of curvilinear trajectories. This work is currently being addressed by the author's research group, and preliminary results are described in Ko et al. [2010b].
- Design and manufacture of a new actuation system that will be able to operate in proximity of an MRI scanner. This would couple the potential benefits of a remotely actuated flexible probe with the advantages of exploiting intra-operative images for better closed-loop control.

8.4.3 Medical image computing

Further research should be conducted on designing and implementing software for pre-operative image processing and trajectory planning. In the context of path

planning for steerable probes, a preliminary risk-based trajectory planning algorithm for a 2D brain atlas is described by the author [Frasson et al., 2010a] and can constitute the starting point for future works. Novel path planning algorithms, including risk assessment and probe motion constraints, should indeed be explored and integrated with the low-level control system of the flexible probe, with the aim to produce real-time trajectory updates to correct for tracking inaccuracies and soft tissue deformation during probe insertion.

8.4.4 Histological analysis

Further research should aim to measure the extent of tissue disruption, damage and tear which occurs at the probe-tissue interface. This could be addressed initially by studying the flexible probe track in biological target tissues through *in-vitro* experiments. It should be ultimately addressed by performing histological analysis on animal tissue samples of brain or liver in *ex-vivo* or *in-vivo* trials.

8.5 Conclusions

To conclude, the viability of a novel biologically-inspired probe steering mechanism for robotic percutaneous interventions is demonstrated and the foundations of a multi-purpose technology platform to fuel future research in the area of flexible probe steering are built. The results presented in this thesis have substantially advanced the state of the art, while also bringing the concept of needle steering for surgical applications one step closer to live patient trials.

Bibliography

3DSystems-Inc. - official website - available at: http://www.3dsystems.com/ - accessed: 06 july 2010, 2009.

R. Acharya, A. Bhutani, H. Saxena, and V. S. Madan. Complete migration of ventriculoperitoneal shunt into the ventricle. *Neurological Sciences*, 23(2):75–77, 2002.

R. Alterovitz, K. Goldberg, and A. M. Okamura. Planning for steerable bevel-tip needle insertion through 2d soft tissue with obstacles. *Ieee International Conference on Robotics and Automation*, 2:1640–1645, 2005.

D. K. Binder, G. M. Rau, and P. A. Starr. Risk factors for hemorrhage during microelectrode-guided deep brain stimulator impalnatation for movement disorders, 2005.

J. Blakeley. Drug delivery to brain tumors. *Current Neurology and Neuroscience Reports*, 8(3):235–241, 2008.

P. Blomstedt and M. I. Hariz. Hardware-related complications of deep brain stimulation: a ten year experience. *Acta Neurochirurgica*, 147(10):1061–1064, 2005.

Brainlab-Gmbh. - official website - available at: http://www.brainlab.com/ - accessed: 16 november 2010, 2010.

D.O. Brush and B.O. Almroth. *Buckling of bars, plates, and shells*. McGraw-Hill, 1975.

E. Clif Burdette, D. Caleb Rucker, Punit Prakash, Chris J. Diederich, Jordon M. Croom, Clyde Clarke, Philipp Stolka, Titania Juang, Emad M. Boctor, and Robert J. Webster Iii. The acusitt ultrasonic ablator: the first steerable needle with an integrated interventional tool. In *Medical Imaging 2010: Ultrasonic Imaging, Tomography, and Therapy*, volume 7629, pages 76290V–10, San Diego, California, USA, 2010. SPIE.

R. G. Craig and F. A. Peyton. Physical properties of elastic duplicating materials. *J. Dent. Res.*, 39(2):391–404, 1960.

S. P. DiMaio and S. E. Salcudean. Needle insertion modeling for the interactive simulation of percutaneous procedures. *Proceedings of the 5th International Conference on Medical Image Computing and Computer-Assisted Intervention-Part II*, pages 253–260, 2002.

S. P. DiMaio and S. E. Salcudean. Interactive simulation of needle insertion models. *Biomedical Engineering, IEEE Transactions on*, 52(7):1167–1179, 2005a.

S. P. DiMaio and S. E. Salcudean. Needle steering and motion planning in soft tissues. *Ieee Transactions on Biomedical Engineering Bme*, 52:965–974, 2005b.

V. Duindam, R. Alterovitz, S. Sastry, and K. Goldberg. Screw-based motion planning for bevel-tip flexible needles in 3d environments with obstacles. In *Robotics and Automation, 2008. ICRA 2008. IEEE International Conference on*, pages 2483–2488, 2008.

P. E. Dupont, J. Lock, B. Itkowitz, and E. Butler. Design and control of concentric-tube robots. *Robotics, IEEE Transactions on*, 26(2):209–225, 2010.

J. A. Engh, G. Podnar, S. Y. Khoo, and C. N. Riviere. Flexible needle steering system for percutaneous access to deep zones of the brain. In *Bioengineering Conference, 2006. Proceedings of the IEEE 32nd Annual Northeast*, pages 103–104, 2006a.

J.A. Engh, G. Podnar, D. Kondziolka, and C.N. Riviere. Toward effective needle steering in brain tissue. *Proceedings of the 28th IEEE EMBS Annual International Conference New York City, USA, Aug 30-Sept 3, 2006*, 2006b.

EUROFLEX-GmbH. - official website - available at: http://www.euroflex-gmbh.de/ - accessed: 06 july 2010, 2010.

L. Frasson, T. Parittotokkaporn, B. L. Davies, and F. Rodriguez y Baena. Early developments of a novel smart actuator inspired by nature. In *15th International Conference on Mechatronics and Machine Vision in Practice*, pages 163–168, 2008a.

L. Frasson, T. Parittotokkaporn, A. Schneider, B. L. Davies, J. F. V. Vincent, S. E. Huq, P. Degenaar, and F. M. Rodriguez y Baena. Biologically inspired microtexturing: Investigation into the surface topography of next-generation neurosurgical probes. In *Engineering in Medicine and Biology Society, 2008. EMBS 2008. 30th Annual International Conference of the IEEE*, pages 5611–5614, 2008b.

L. Frasson, S. Reina, B. L. Davies, and F. M. Rodriguez y Baena. Design optimization of a biologically inspired multi-part probe for soft tissue surgery. In O. Dossel Schlegel and W C., editors, *11th International Congress of the IUPESM, Medical Physics and Biomedical Engineering*, volume IFMBE Proceedings 25/ VI, pages 307–310, Munich, Germany, 2009. Springer.

L. Frasson, S.Y. Ko, A. Turner, T. Parittotokkaporn, J. F. Vincent, and F. Rodriguez y Baena. Sting: a soft-tissue intervention and neurosurgical guide to access deep brain lesions through curved trajectories. *Proceedings of the Institution of Mechanical Engineers. Part H, Journal of engineering in medicine*, 224(6):775–788, 2010a.

L. Frasson, J. Neubert, S. Reina, M. Oldfield, B. L. Davies, and F. M. Rodriguez y Baena. Development and validation of a numerical model for cross-section optimization of a multi-part probe for soft tissue intervention. In *Engineering in Medicine and Biology Society, 2010. EMBS 2010. 32th Annual International Conference of the IEEE*, pages 3202–3205, 2010b.

L. Frasson, T. Parittotokkaporn, B. L. Davies, and F. Rodriguez y Baena. Early developments of a novel smart actuator inspired by nature. *Int. J. Intelligent Systems Technologies and Applications*, 8(1-4):409–422, 2010c.

J. Furusho, H. Kobayashi, T. Kikuchi, T. Yamamoto, H. Tanaka, M. Terayama, and M. Monden. Development of cmtd (curved multi-tubed device) -system iii and its application to the needle-insertion for liver. In *Engineering in Medicine and Biology Society, 2008. EMBS 2008. 30th Annual International Conference of the IEEE*, pages 2508–2513, 2008.

Y. Gao, A. Ellery, M. Jaddou, and J. Vincent. Deployable wood wasp drill for planetary subsurface sampling. *IEEE 2006*, 2005.

D. Gerling, D. L. J. Quicke, and T. Orion. Oviposition mechanisms in the whitefly parasitoids encarsia transvena and eretmocerus mundus. *Biocontrol*, 43:289–297, 1998.

D. Glozman and M. Shoham. Flexible needle steering and optimal trajectory planning for percutaneous therapies. *Lecture Notes in Computer Science*, (3217): 137–144, 2004.

D. Glozman and M. Shoham. Image-guided robotic flexible needle steering. *Ieee Transactions on Robotics*, 23:459–467, 2007.

C. Guerin. Recent advances in brain tumor therapy: Local intracerebral drug delivery by polymers. *Investigational New Drugs*, 22(1):27–37, 2004.

W. A. Hall. The safety and efficacy of stereotactic biopsy for intracranial lesions, 1998.

R.W. Hamming. *Numerical Methods for Scientists and Engineers - second Edition.* McGraw-Hill, 1986.

G. Hilmann, M. Paas, and V. Schindler. Automatic geometry based fe model generation for optimization and robust design for passive safety of passenger vehicles. *PAMM - Proceedings in Applied Mathematics and Mechanics*, 5(1):7–10, 2005.

J. T. Hing, A. D. Brooks, and J. P. Desai. A biplanar fluoroscopic approach for the measurement, modeling, and simulation of needle and soft-tissue interaction. *Medical Image Analysis*, 11(1):62–78, 2007.

R. L. Iman and W. J. Conover. A distribution-free approach to inducing rank correlation among input variables, 1982.

Instron. - official website - available at: http://www.instron.co.uk/ - accessed: 05 august 2010, 2010.

K.D. Jamani, E. Harrington, and H.J. Wilson. Rigidity of elastomeric impression materials. *J. Oral Rehabil.*, 16:241–248, 1989.

X. Jijie, V. Duindam, R. Alterovitz, and K. Goldberg. Motion planning for steerable needles in 3d environments with obstacles using rapidly-exploring random trees and backchaining. In *Automation Science and Engineering, 2008. CASE 2008. IEEE International Conference on*, pages 41–46, 2008.

H. Kataoka, T. Washio, M. Audette, and K. Mizuhara. A model for relations between needle deflection, force, and thickness on needle penetration. *Lecture Notes in Computer Science*, (2208):966–974, 2001.

H. Kataoka, T. Washio, K. Chinzei, K. Mizuhara, C. Simone, and A. M. Okamura. Measurement of the tip and friction force acting on a needle during penetration. *Lecture Notes in Computer Science*, (2488):216–223, 2002.

H. K. Kim and S. K. Hong. Fem-based optimum design of multi-stage deep drawing process of molybdenum sheet. *Journal of Materials Processing Technology*, 184 (1-3):354–362, 2007.

S.Y. Ko, L. Frasson, B. L. Davies, and F. M. Rodriguez y Baena. Software & hardware integration of a biomimetic flexible probe within the robocast neurosurgical robotic suite. In *The Hamlyn Symposium on Medical Robotics*, pages 5–6, London, 2010a.

S.Y. Ko, L. Frasson, and F. M. Rodriguez y Baena. Closed-loop planar motion control of a steerable probe with a programmable bevel inspired by nature. *Submitted to IEEE Transactions on Robotics (T-RO)*, (1552-3098), 2010b.

F. Kolahan, H. Abolbashari, and S. Mohitzadeh. Simulated annealing application for structural optimization. *Proceedings of World Academy of Science, Engineering and Technology*, 35(November 2007):326–329, 2007.

T. V. Korochkina, E. H. Jewell, T. C. Claypole, and D. T. Gethin. Experimental and numerical investigation into nonlinear deformation of silicone rubber pads during ink transfer process. *Polymer Testing*, 27(6):778–791, 2008.

D. F. Louw, T. Fielding, P. B. McBeth, D. Gregoris, P. Newhook, and G. R. Sutherland. Surgical robotics: A review and neurosurgical prototype development. *Neurosurgery*, 54(3):525–537, 2004.

L. A. Lyons, R Webster, and R. Alterovitz. Planning active cannula configurations through tubular anatomy. In *IEEE International Conference on Robotics and Automation*, Anchorage, Alaska, USA, 2010.

A. Majewicz, T. R. Wedlick, K. B. Reed, and A. M. Okamura. Evaluation of robotic needle steering in ex vivo tissue. In *Robotics and Automation, 2010. ICRA 2010. IEEE International Conference on*, pages 2068–2073, 2010.

M. D. McKay, R. J. Beckman, and W. J. Conover. A comparison of three methods for selecting values of input variables in the analysis of output from a computer code. *Technometrics*, 42(1):55–61, 2000.

C. Menon, J. F. V. Vincent, N. Lan, L. Bilhaut, A. Ellery, Y. Gao, D. Zangani, S. Carosio, C. Manning, and M. Jaddou. Caneus2006-11022 bio-inspired microdrills for future planetary exploration. In M. Pimprikar and M. Dastoor, editors, *CANEUS 2006 MNT for aerospace applications*, pages 117–128, Toulouse, France, 2006. New York N.Y.:.

K. Miller and K. Chinzei. Constitutive modelling of brain tissue: experiment and theory. *Journal of Biomechanics*, 30(11/12):1115–1121, 1997.

D. Minhas, J.A. Engh, M.M. Fenske, and C. Riviere. Modeling of needle steering via duty-cycled spinning. In *Proceedings of the 29th Annual International Conference of the IEEE Engineering in Medicine and Biology Society, August*, 2007.

D. Minhas, J. A. Engh, and C. N. Riviere. Testing of neurosurgical needle steering via duty-cycled spinning in brain tissue in vitro. In *Engineering in Medicine*

and Biology Society, 2009. EMBC 2009. Annual International Conference of the IEEE, pages 258–261, 2009.

S. Misra, K. B. Reed, A. S. Douglas, K. T. Ramesh, and A. M. Okamura. Needle-tissue interaction forces for bevel-tip steerable needles. In *Biomedical Robotics and Biomechatronics, 2008. BioRob 2008. 2nd IEEE RAS & EMBS International Conference on*, pages 224–231, 2008.

S. Misra, K. B. Reed, B.W. Schafer, K.T. Ramesh, and A.M. Okamura. Observations and models for needle-tissue interactions. In *IEEE International Conference on Robotics and Automation*, pages 2687–2692, Kobe International Conference Center, 2009.

N. Nathoo, M. C. Cavusoglu, M. A. Vogelbaum, and G. H. Barnett. In touch with robotics: Neurosurgery for the future. *Neurosurgery*, 56:421–433, 2005.

National-Instruments-Inc. - official website - available at: http://www.ni.com/ - accessed: 17 november 2010, 2010.

NeuroArm. - official website - available at: http://www.neuroarm.org/ - accessed: 04 august 2010, 2010.

NeuroMate. - official website - available at: http://www..renishaw.com/ - accessed: 20 september 2010, 2010.

Norhter-Digital-Inc. - official website - aurora electromagnetic measurement system - available at: http://www.ndigital.com/medical/aurora.php - accessed: 09 august 2010, 2010a.

Norhter-Digital-Inc. - official website - optotrak certus motion capture system - available at: http://www.ndigital.com/lifesciences/certus-motioncapturesystem.php - accessed: 12 november 2010, 2010b.

Objet-Geometries-Ltd. - official website - available at: http://www.objet.com/ - accessed: 06 july 2010, 2010a.

Objet-Geometries-Ltd. - official website - digital materials - available at: http://www.objet.com/pages/digital_materials_/dm9840_dm9895/ - accessed: 06 july 2010, 2010b.

S. Okazawa, R. Ebrahimi, J. Chuang, S. E. Salcudean, and R. Rohling. Hand-held steerable needle device. *Ieee Asme Transactions on Mechatronics*, 10:285–296, 2005.

M.J. Oldfield, D. Dini, G. Giordano, and F. M. Rodriguez y Baena. Detailed finite element modelling of deep needle insertions into a soft tissue phantom using a cohesive approach. *Submitted to Computer Methods in Biomechanics and Biomedical Engineering*, 2011.

S. Pandya, J. W. Motkoski, C. Serrano-Almeida, A. D. Greer, I. Latour, and G. R. Sutherland. Advancing neurosurgery with image-guided robotics, 2009.

T. Parittotokkaporn, L. Frasson, A. Schneider, S. E. Huq, B. L. Davies, P. Degenaar, J. Biesenack, and F. M. Rodriguez y Baena. Soft tissue traversal with zero net force: Feasibility study of a biologically inspired design based on reciprocal motion. In *Robotics and Biomimetics, 2008. ROBIO 2008. IEEE International Conference on*, pages 80–85, 2009.

T. Parittotokkaporn, L. Frasson, A. Schneider, B. L. Davies, P. Degenaar, and F. M. Rodriguez y Baena. Insertion experiments of a biologically inspired microtextured and multi-part probe based on reciprocal motion. In *Engineering in Medicine and Biology Society, 2010. EMBS 2010. 32th Annual International Conference of the IEEE*, pages 3190–3193, 2010.

T. Z. Pavan, A. A. Carneiro, E. L. Madsen, G.R. Frank, and T.G. Hall. Exploring the nonlinear elastic behavior of phantoms materials for elastography. In *IEEE International Ultrasonics Symposium Proceedings*, pages 463–466, 2009.

A. Perneczky. *Keyhole concept in neurosurgery: with endoscope-assisted microsurgery and case studies*. 1999.

M. Petelet, B. Iooss, O. Asserin, and A. Loredo. Latin hypercube sampling with inequality constraints, 2009. arXiv [http://arXiv.org/oai2] (United States) ER.

J. W. Powell. *The Design of Aerostatic Bearings*. 1970.

D. L. J. Quicke. Ovipositor mechanics of the braconine wasp genus zaglyptogastra and the ichneumonid genus pristomerus. *Journal of Natural History*, 25:971–977, 1991.

D. L. J. Quicke and M. G. Fitton. Ovipositor steering mechanisms in parasitic wasps of the families gasteruptiidae and aulacidae (hymenoptera). *Proceedings- Royal Society of London B*, page 99, 1995.

D. L. J. Quicke, M. G. Fitton, J. R. Tunstead, and S. N. Ingram. Ovipositor structure and relationships within the hymenoptera, with special reference to the ichneumonoidea. *Journal of Natural History*, 28(3):635, 1994.

D. L. J. Quicke, M. G. Fitton, and J. Harris. Ovipositor steering mechanisms in braconid wasps. *Journal of Hymenoptera Research*, 4:194– 203, 1995.

D. L. J. Quicke, A. Le Ralec, and L. Vilhelmsen. Ovipositor structure and function in the parasitic hymenoptera with an exploration of new hypotheses. *Lecture Notes*, 1999.

R. Raghavan, M. L. Brady, M. I. RodrÃ-guez Ponce, A. Hartlep, C. Pedain, and J. H. Sampson. Convection-enhanced delivery of therapeutics for brain disease, and its optimization. *Neurosurgical focus*, 20(3):E12, 2006.

M. H. Rahman, M. G. Fitton, and D. L. J. Quicke. Ovipositor internal microsculpture in the braconidae (insecta, hymenoptera). *Zoologica Scripta*, 27(4):319–332, 1998.

Reda-SPA. - official website - available at: http://www.grupporeda.com/ - accessed: 16 november 2010, 2006.

K. B. Reed, V. Kallem, R. Alterovitz, K. Goldbergxz, A. M. Okamura, and N. J. Cowan. Integrated planning and image-guided control for planar needle steering. In *Biomedical Robotics and Biomechatronics, 2008. BioRob 2008. 2nd IEEE RAS & EMBS International Conference on*, pages 819–824, 2008a.

K. B. Reed, A. M. Okamura, and N. J. Cowan. Compensating for torsion windup in steerable needles. In *Biomedical Robotics and Biomechatronics, 2008. BioRob 2008. 2nd IEEE RAS & EMBS International Conference on*, pages 936–941, 2008b.

R. C. Ritter, E. G. Quate, G. T. Gillies, M. S. Grady, M. A. Howard, and W. C. Broaddus. Measurement of friction on straight catheters in in vitro brain and phantom material. *Ieee Transactions on Biomedical Engineering Bme*, 45(4): 476–485, 1998.

Robocast-Project. - official website - available at: http://www.robocast.eu/ - accessed: 12 november 2010, 2010.

F. M. Rodriguez y Baena, L. Frasson, and J. F. Vincent. Steerable probes, Patent filed on 30 November 2009, Application Number 0920938.8 2009.

E. Samur, M. Sedef, C. Basdogan, L. Avtan, and O. Duzgun. A robotic indenter for minimally invasive characterization of soft tissues. *International Congress Series*, 1281:713–718, 2005.

H. Schiffbauer. *Neuronavigation in Brain Tumor Surgery Clinical beta-phase of the Oulu Neuronavigator System.* PhD thesis, University of MÃ¼nster, 1999.

A. Schneider, L. Frasson, T. Parittotokkaporn, F. M. Rodriguez y Baena, B. L. Davies, and S. E. Huq. Microfabrication of components for a novel biomimetic neurological endoscope. In S. Dimov and W. Menz, editors, *4M Multi-Material Micro Manufacture; 4th Int. Conf., 9-11 Sept. 2008*, Cardiff, UK, 2008a.

A. Schneider, L. Frasson, T. Parittotokkaporn, F. M. Rodriguez y Baena, B. L. Davies, and S. E. Huq. Biomimetic microtexturing for neurosurgical probe surfaces to influence tribological characteristics during tissue penetration. In *Micro & Nano Engineering 2008; 34th Internaltional Conference, 15 -18 September*, Athens - Greece, 2008b.

A. Schneider, L. Frasson, T. Parittotokkaporn, F. M. Rodriguez y Baena, B. L. Davies, and S. E. Huq. Biomimetic microtexturing for neurosurgical probe surfaces to influence tribological characteristics during tissue penetration. *Microelectronic Engineering*, 86(4-6):1515–1517, 2009.

P. Sears and P. Dupont. A steerable needle technology using curved concentric tubes. In *Intelligent Robots and Systems, 2006 IEEE/RSJ International Conference on*, pages 2850–2856, 2006.

M. Shoham, M. Burman, E. Zehavi, L. Joskowicz, E. Batkilin, and Y. Kunicher. Bone-mounted miniature robot for surgical procedures: Concept and clinical applications. *Ieee Transactions on Robotics and Automation*, 19(5):893–901, 2003.

C. Simone and A. M. Okamura. Modeling of needle insertion forces for robot-assisted percutaneous therapy. *Ieee International Conference on Robotics and Automation*, 2:2085–2091, 2002.

Simulia-Corp. - official website - available at: http://www.simulia.com/ - accessed: 17 november 2010, 2010.

D. Stoianovici, J. A. Cadeddu, R. D. Demaree, and S. A. Basile. A novel mechanical transmission applied to percutaneous renal access. In G. Rizzoni, editor, *American Society of Mechanical Engineers: Dynamic Systems and Control Division*, pages 401–406, Dallas; TX, 1997. Asme.

TAO-CORBA. - official website of tao corba - available at http://www.cs.wustl.edu/~schmidt/tao.html - accessed: 12 november 2010, 2010.

M. Terayama, J. Furusho, and M. Monden. Curved multi-tube device for path-error correction in a needle-insertion system, 2007.

The-MathWorks-Inc. - matlab official website - available at: http://www.mathworks.com/ - accessed: 10 november 2010, 2010.

S.P. Timoshenko and J.M. Gere. *Theory of Elastic Stability, 2ed.* McGraw-Hill, 1961.

J. C. Van Lenteren, N. Isidoro, and F. Bin. Functional anatomy of the ovipositor clip in the parasitoid leptopilina heterotoma (thompson) (hymenpotera: Eucoilidae), a structure to grip escaping host larvae. *Int. J. Insect Morphol. & Embryol.*, 27(3):263–268, 1998.

L Varkey. *Quantifying the Diffusivity of Dye in the agar gel model of brain.* PhD thesis, 2006.

T. R. K. Varma and P. Eldridge. Use of the neuromate stereotactic robot in a frameless mode for functional neurosurgery. 2(2):107–113, 2006.

L. Vilhelmsen, N. Isidoro, R. Romani, H. H. Basibuyuk, and D. L. Quicke. Host location and oviposition in a basal group of parasitic wasps: the subgenual organ, ovipositor apparatus and associated structures in the orussidae (hymenoptera, insecta). *Zoomorphology*, 121(2):63–84, 2001.

J. F. V. Vincent and M. J. King. The mechanism of drilling by wood wasp ovipositors. *Biomimetics*, 3(4):187–201, 1995.

R Webster. *Design and Mechanics of Continuum Robots for Surgery.* PhD thesis, John Hopkins University, 2007.

R. J. Webster, J. Memisevic, and A. M. Okamura. Design considerations for robotic needle steering. In *Robotics and automation; 2005 IEEE international conference on robotics and automation*, pages 3588–3594, Barcelona, Spain, 2005. Washington D.C.

R. J. Webster, J. S. Kim, N. J. Cowan, G. S. Chirikjian, and A. M. Okamura. Nonholonomic modeling of needle steering. *International Journal of Robotics Research*, 25:509–526, 2006.

R. J. Webster, J. Swensen, J. Romano, and N. J. Cowan. Closed-form differential kinematics for concentric-tube continuum robots with application to visual servoing. In *Experimental Robotics*, pages 485–494. 2009. 10.1007/978-3-642-00196-3_56.

T. R. Wedlick and A. M. Okamura. Characterization of pre-curved needles for steering in tissue. In *Engineering in Medicine and Biology Society, 2009. EMBC 2009. Annual International Conference of the IEEE*, pages 1200–1203, 2009.

S. L.-Y. Woo, M. A. Ritter, D. Amiel, T. M. Sanders, M. A. Gomez, S. C. Kuei, S. R. Garfin, and W. H. Akeson. The biomechanical and biochemical properties of swine tendons-long term effects of exercise on the digital extensors. *Connect. Tissue Res*, 7:177–183, 1980.

N.A. Wood, K. Shahrour, C.O. Ost, and C. Riviere. Needle steering system using duty-cycled rotation for percutaneous kidney access. In *Engineering in Medicine and Biology Society, 2010. EMBS 2010. 32th Annual International Conference of the IEEE*, pages 5432–5435, 2010.

D. Z. Yankelevsky, M. A. Adin, and M. Eisenberger. Beams on nonlinear winkler foundation with gaps. *Computers and Geotechnics*, 6(1):1–11, 1988.

M. Zimmermann, R. Krishnan, A. Raabe, and V. Selfert. Robot-assisted navigated endoscopic ventriculostomy: implementation of a new technology and first clinical results. *Acta Neurochirurgica*, 146(7):697–704, 2004.

Appendix A: Flexible Probe Design Process

This appendix describes the most salient steps taken towards the development of the alpha flexible probe prototype system described in Chapter 4. A preliminary actuation RIG, based on a friction drive mechanism to actuate a very first rigid multi-part probe prototype is firstly described and discussed. Few relevant flexible probe prototypes are then shown, in order to justify the main decisions underlying the choice for the design of the alpha prototype discussed in Chapter 4.

Friction drive mechanism and rigid four-part probe

The very first rig, which will be described shortly, was developed for two main reasons:

- exploring the feasibility of RP techniques for manufacturing a multi-part probe, where two or more segments are interlocked together and can slide reciprocally
- proposing a suitable actuation strategy which could possibly be applied to a flexible probe prototype

A first prototype of the multi-part probe was manufactured in RP by 3D Systems [3DSystems-Inc., 2009] and a rig for the servo-assisted actuation of the probe was developed. In order to explore the RP manufacturing technique resolution, a rigid prototype was designed first, instead of a flexible one, since manufacturing was easy and inexpensive.

The cross-section and a picture of the first prototype are shown in Figure A.1. The probe is composed of 4 interlocked segments, it is 12 mm in diameter and 110 mm long. The clearance between the segments is 0.2 mm.

Concerning the design of a testing rig for the probe, one of the most significant problems underlying flexible needle insertion into soft tissue is buckling of the part of the needle which is outside the tissue. Two main approaches have been developed to avoid needle buckling outside the tissue, and they both try to reduce the unsupported

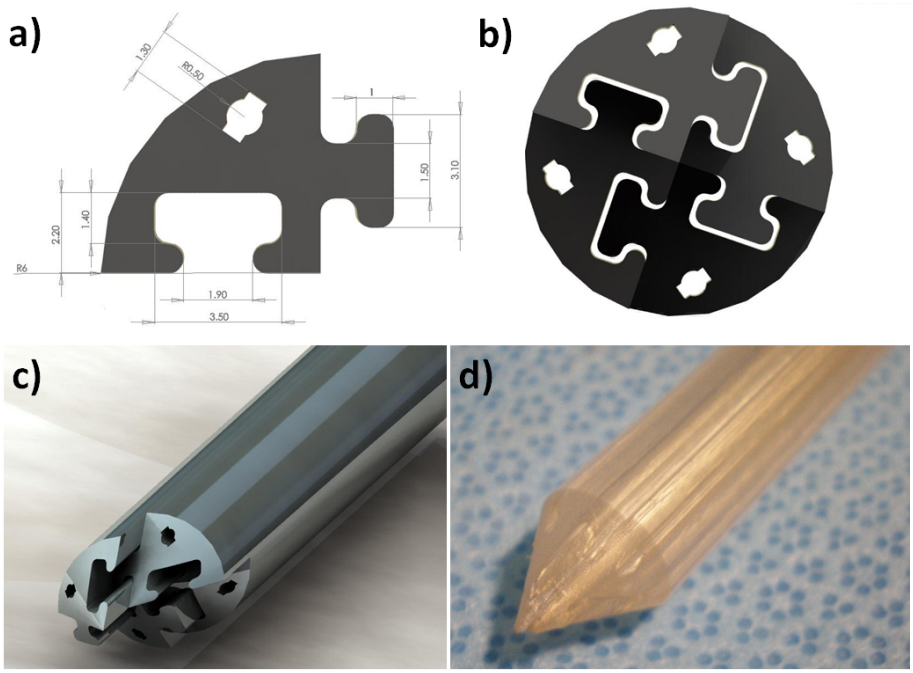


Figure A.1: First rigid probe prototype (material used: "Accura 60", [3DSystems-Inc., 2009]). a) single segment cross section; b) 4-part probe cross-section, the clearance between segments is 0.2 mm; c) assembly of non-aligned probe segments; c) picture of the prototype

needle length between the point where force is transmitted to the needle (bottom or shaft of the needle) and the entry point in the target tissue. Webster et al. [2005], in order to drive a flexible needle (see Section 2.2), compared two different actuation approaches. Inspired by the PAKY system [Stoianovici et al., 1997], Webster et al. developed a friction drive mechanism, where the needle's core is grasped by two opposing rubber wheels in correspondence of the entry point in the tissue (Figure 2.4a). A second approach was to use a telescoping support sheath enclosing the needle, which was compressed as the needle was advanced in the tissue (Figure 2.4c). Considering the requirement of driving the four segments of the probe independently, with the advantage of having a direct control over the forces exerted on each segment by adjusting the lateral forces used to "grasp" the probe's segments, a friction drive mechanism was proposed, developed and tested.

The friction drive mechanism is shown in Figure A.2. It is composed of four stepper motors (Hybrid stepper motor 440-458, RS), the shafts of which are equipped with 4 custom-made rubber wheels (RTV silicone rubber, Moldsil, W.P. Notcutt LTD), each one pressing against a corresponding probe segment. The amount of lateral force applied to grasp each probe segment by the corresponding motor can be manually adjusted by a lead-screw mechanism. A Labview [National-Instruments-Inc., 2010] graphical user interface is used to drive the motors, through four 4-Phase Unipolar Stepper Motor Drive Boards (217-3611, RS).

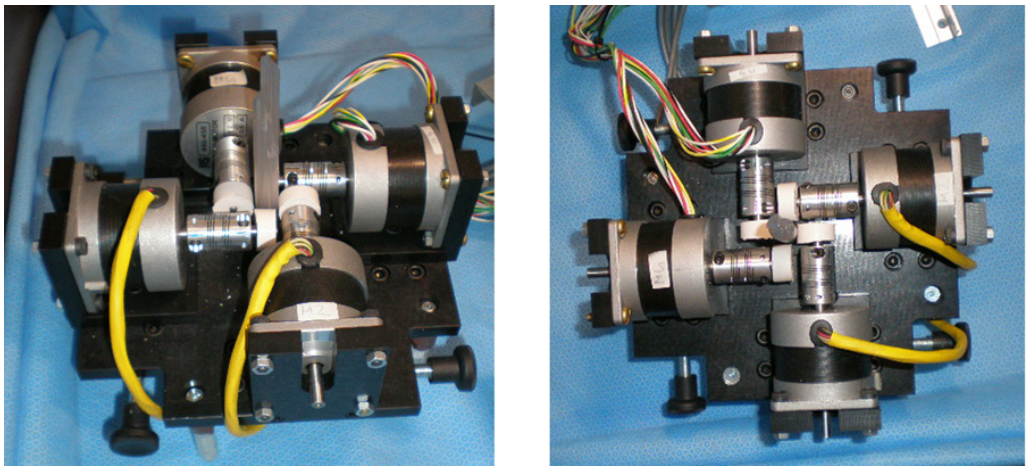


Figure A.2: Pictures of the actuation RIG: the multi-part probe is held by the four rubber wheels, each pressed against the core of one segment. 4 lead-screws (see black handles) are used to independently adjust the later forces pressing against the probe segments.

Very simple feasibility tests were run in order to roughly characterise probe behaviour during actuation; a 6-axis load cell (Nano25, 500N) and a manual dial tension gauge (range 100 gf, required for measurements of very small forces) were used to measure approximately the forces generated at the tip of the probe by the actuation system. Three main tests were run:

- *Direct Push*: the motors were actuated all together and the four parts (or segments) of the probe were pushed downwards. Because no reciprocal motion was required between the segments, it was possible to clamp tightly the probe with the four rubber wheels. A maximum force of **5 N** (500 gf) was measured at the tip of the probe, before the rubber wheels slid on the probe core.

- *Reciprocal motion*: the motors were actuated sequentially, each for a time period which could be defined by the user. The force measured at the tip of the moving segment was about **0.2 N** (20 gf). Increasing the perpendicular force by clamping tightly the segments with the rubber wheels implied a displacement of the rails of the interlocking mechanism inside the corresponding grooves, which caused a wedging between the parts. This affected the distribution of the pressure applied to the contact areas, thus modifying the minimum tangential force required to slide reciprocally each segment.

- *Two-part motion*: the motors were actuated in close pairs, with two stationary and two moving segments at any one time. The maximum force measured at the tip of the two segments of the probe pushed downwards was about **1 N** (100 gf). Although in this configuration the pairs of probe segments face each

other along the sliding surface and the rails do not wedge in the grooves, an excessive increase in the perpendicular force (i.e. clamping too tightly the parts of the probe with the rubber wheels) prevented the segments from moving. As a result, the rubber wheels slid onto the probe surface.

These tests, although limited to a rigid probe prototype, demonstrated that the segments composing the probe could easily slide one with respect to the other, confirming that the probe cross-section shown in Figure A.1b is indeed valid. However, the friction at the surface in contact between the interlocking parts of the segments, dependent on the probe material but also on the interlock design, is definitely a feature which needs to be carefully considered, because it can impact the performance of the probe to cause failure.

Regarding the actuation mechanism, these simple tests demonstrated that, in the proposed setup (i.e. a friction drive mechanism for actuating a multi-part probe), too many variables can affect the actuation performance. The clamping force required to drive the probe's segments affects not only the frictional forces between the driving wheels (rubber wheels) and the probe surface, but also the frictional forces between the probe's segments, and this behaviour is also dependent on the geometry and design of the probe and the properties of the material it is made of.

In conclusion of this study, a friction drive mechanism seems to introduce major inconveniences, therefore a standard "push from the back" actuation strategy is chosen, which is described in the main body of the thesis (Chapter 4). Buckling of a flexible probe outside the target tissue was addressed with the use of an external trocar constraining the probe's body, as described in Chapter 4.

Development of flexible probe prototypes

Additional prototypes were designed and manufactured using RP methods. The only available flexible (rubber-like) material for RP, at the time of the first flexible prototype manufacturing (2008) was provided by Objet Geometries Ltd. [Objet-Geometries-Ltd., 2010a] and it was called TangoBlack (tensile strength of 2 MPa; hardness of 61 Shore Scale A; elongation at break of 48%, please note that the TangoBlack material developed by Objet in 2008 differs from the TangoBlack material currently - 2010 - developed by the same company).

Few "design and development" iterations where required to obtain a flexible 4-part probe prototype which could be tested in a compliant medium (gelatine), with the aim to achieve curvilinear insertion trajectories.

A very detailed description of the different designs is out of the scope of this thesis, thus only relevant information about the designing process will be provided.

Because the first two prototypes were designed in parallel with the study on the

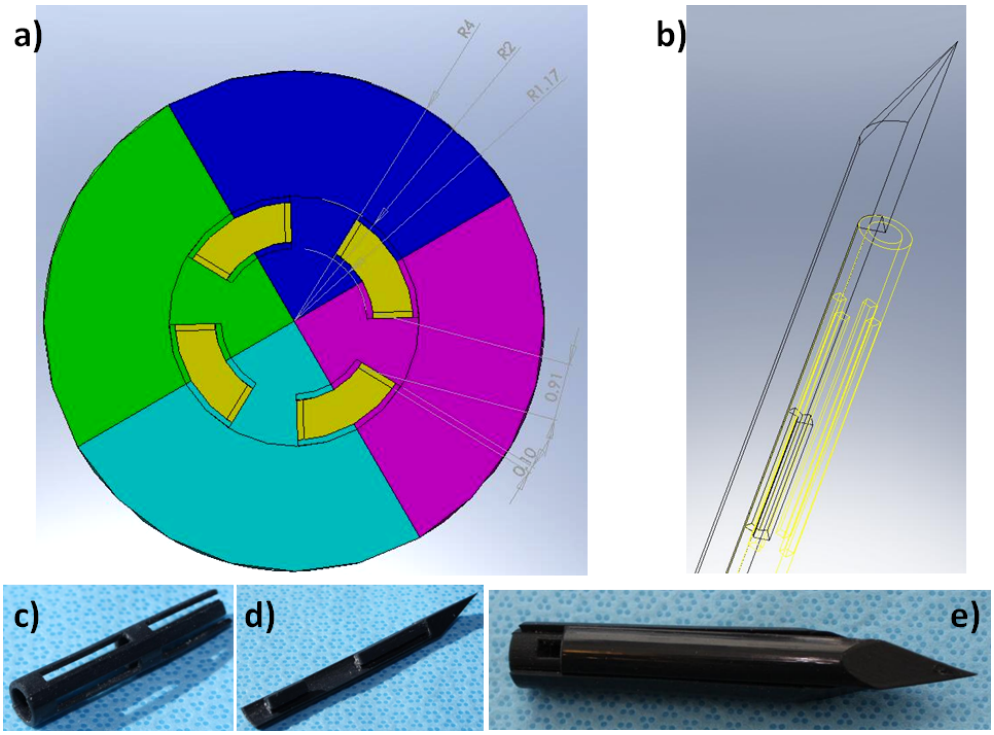


Figure A.3: First flexible probe prototype. a) Cross-section with relevant measurements (in mm). b) Sketch of the inner tube (yellow) used to interlocked the segments (black). c) RP inner tube. d) RP single segment. e) RP assembled probe (please note that the probe is 80 mm long and 12 mm in OD).

friction drive mechanism described in the previous section, one of the specifications was to produce a prototype with a central radial symmetry, in order to avoid wedging of the interlocking mechanism if the probe segments (see Figure A.1) were not clamped homogeneously.

The very first flexible prototype is shown in Figure A.3. It consists of one inner tube to which four lateral segments are interlocked and free to slide for a limited distance with respect to the tube. The main disadvantages of this design are that the travel distance of each segment is quite limited, the interlocking mechanism does not run up to the tip of the probe, leaving the segments free to separate at the tip, and the inner tube is quite weak and subject to deformations which can easily cause segment disengagement.

A new prototype was developed in a second iteration and it is shown in Figure A.4. A cross-shape inner core interlocks four segments with central radial symmetry. This prototype showed good interlocking strength in terms of both segment engagement and segment sliding capability, even though the small clearance gap between the moving parts (0.1 mm) was found to be excessively tight. On a negative note, the presence of the inner core stiffened the whole design, reducing overall probe flexibility. Though reduced, the problem of the probe tips separating from each other

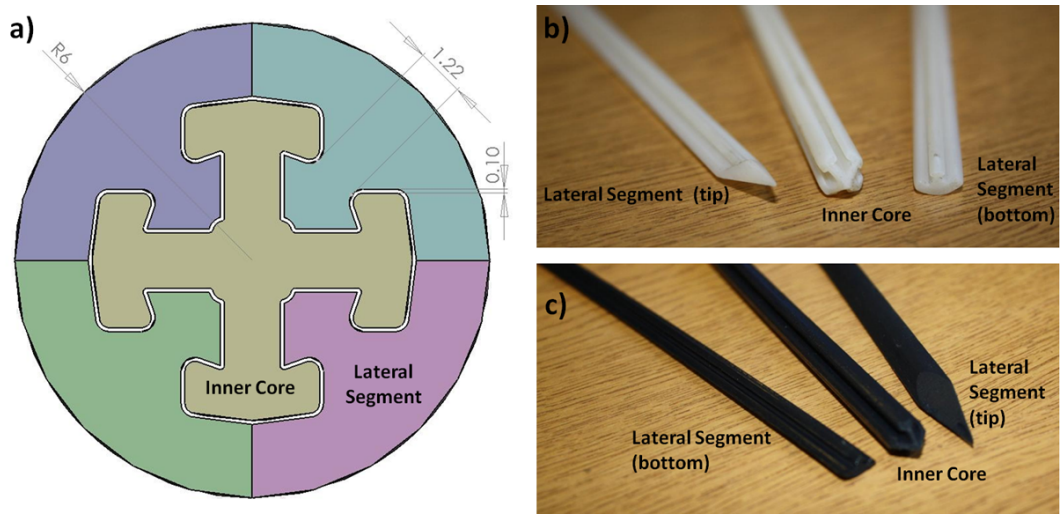


Figure A.4: a) Cross-section of an intermediate prototype, characterised by a central inner core, with circular symmetry and a clearance gap of 0.1 mm; b) Picture of rigid RP sample; c) Picture of flexible RP sample (TangoBlack). This prototype, even though overall unsatisfactory, demonstrated that an arrow-shape interlock between the lateral segments and the inner core was indeed effective, and therefore maintained in following prototypes. However, the 0.1 mm clearance was found to be too tight for the flexible prototype.

because of the lack of an interlocking mechanism at the very tip of the probe still existed.

Other designs were considered and analysed, but evidence suggested that the original design (Figure A.1) of a four-part probe where all segments are interlocked together from the bottom to the tip could be the most suitable. Furthermore, the decision of actuating the probe by "pushing the segments from the back" posed less strict constraints about the need for central radial symmetry.

The cross-section and a picture of the precursor of the alpha probe prototype is shown in Figure A.5. The probe is 12 mm in diameter and 200 mm long. This prototype differs from the alpha prototype described in Section 4.4.2 only in terms of material properties, because the multi-material RP machine (described in Section 4.4.1) was not yet available at the time when this prototype was manufactured (2008).

The shape and the position of the interlocking mechanism and the clearance distribution between the segments of the alpha prototype were designed based on the experienced gained during previous attempts. For example, the interlocking mechanism is offset towards the centre of the probe, rather than being at the centre of the segment, to ensure improved interlock stiffness. The clearance gap between the segments was increased from 0.1 mm (see Figure A.4) to 0.15 mm. The "arrow shape"

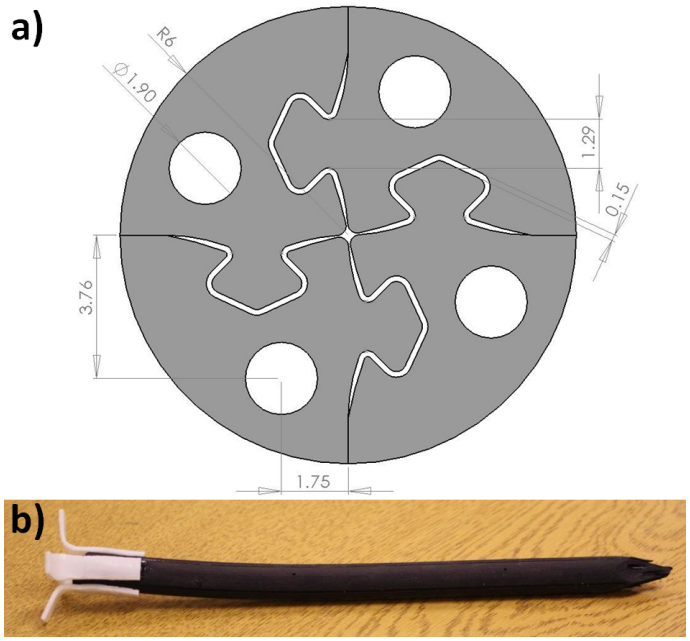


Figure A.5: Precursor of the alpha flexible probe prototype. a) Cross-section with relevant measurements (in mm); b) Picture of the flexible probe (the white handles, glued to the probe surface, were used for manual probe insertion into gelatine).

of the interlock derives from the previous prototype with central radial symmetry (see Figure A.4), which was discarded because of the presence of an inner core stiffening the whole design, but which showed a good interlocking mechanism in terms of both segment engagement and segment sliding capabilities.

The high elasticity and flexibility of the Tango Black material proved to be satisfactory: one probe segment manually inserted into brain-like gelatine was made to follow a curved trajectory, as shown in Figure A.6.



Figure A.6: Single probe segment inserted into gelatine. The high flexibility of the material is confirmed by the small radius of curvature assumed by the segment.

Appendix B: Medical-Grade Silicone Extrusion

Given the fixed cross-sectional profile of the flexible probe segments, polymer extrusion was another manufacturing method explored. An early trial of extrusion was carried out between 2008 and 2009, when the new multi-material RP technique described in Section 4.4.2 was not yet available. The extrusion of the flexible probe segments was outsourced to Reda s.p.a [Reda-SPA, 2006].

Extrusion was chosen for two main reasons: the possibility of reducing the outer diameter of the flexible probe to 6 mm and the possibility of using a material with medical grade properties.

Two kinds of medical-grade silicone compounds were identified as the most suitable for manufacturing:

- AXILMED-64/T (Shore A hardness of 63, tensile strength of 8 MPa, Elongation 450%)
- AXIL-76/T MD (Shore A hardness of 75, tensile strength of 7.5 MPa, Elongation 300%)

The cross-section of the probe prototype was designed in collaboration with Reda s.p.a, which took into account both the manufacturing resolution of the die used to extrude the material (cross-section in Figure B.1a) and the shrinking of the material when cooled to room temperature (Figure B.1b). The final assembled probe cross-section is shown in Figure B.1c.

Figure B.2a shows 4 silicone probe segments, each provided with a rigid coupling at the back, and a custom made trocar. Both rigid couplings and the trocar were manufactured in RP. Each rigid coupling was glued to a probe segment on one side and to a transmission cable (compare Section 4.4.2) on the other side (see Figure B.2b for an assembled silicone probe with rigid couplings and transmission cables). The trocar was manufactured in such a way to house the rigid couplings, but leaving them free to slide within (Figure B.2c and inset). The actuation system used to test the silicone probe is shown in Figure B.2d, which is the same system described in Section 4.4.2). The segment tips were manually cut in a bevel-tip shape.

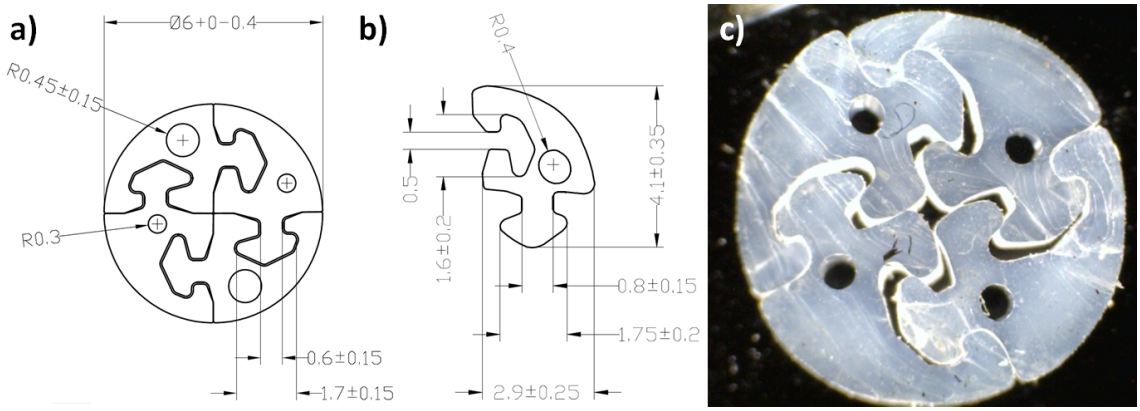


Figure B.1: a) Proposed 4-segment cross-section with relevant dimensions in mm. b)Real segment cross-section with relevant dimensions in mm. This design takes into account material shrinking which happens after extrusion; the central channel, for example, it is not circular but elliptical. c) Picture of the cross-section of an assembled probe.

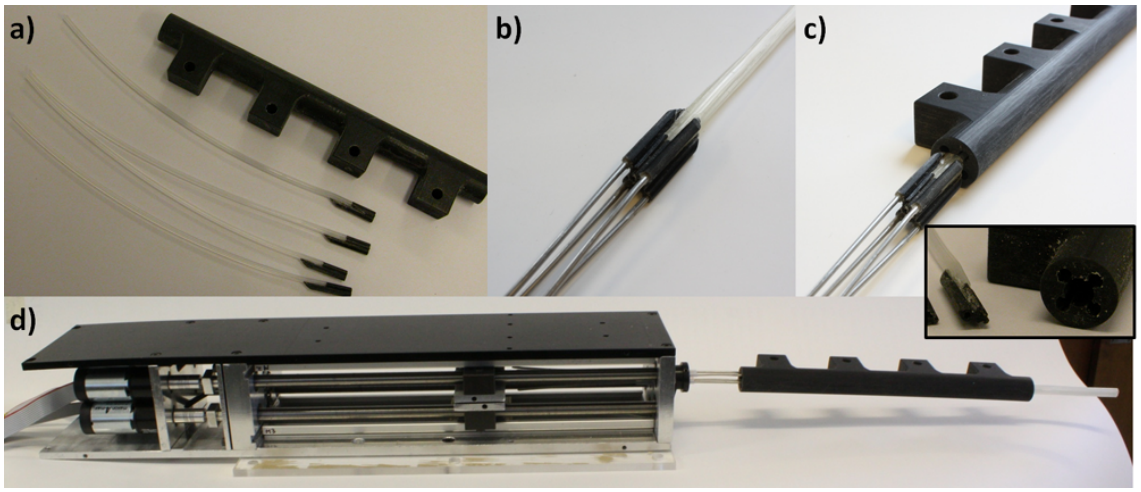


Figure B.2: a) Silicone probe segments with rigid coupling and custom made trocar. b) Assembled silicone probe segments. Each segment is connected to a transmission cable. c) Silicone probe assembly partially inserted into the trocar. Inset: trocar cross-section to house the rigid couplings. d) Actuation system for silicone probe prototype.

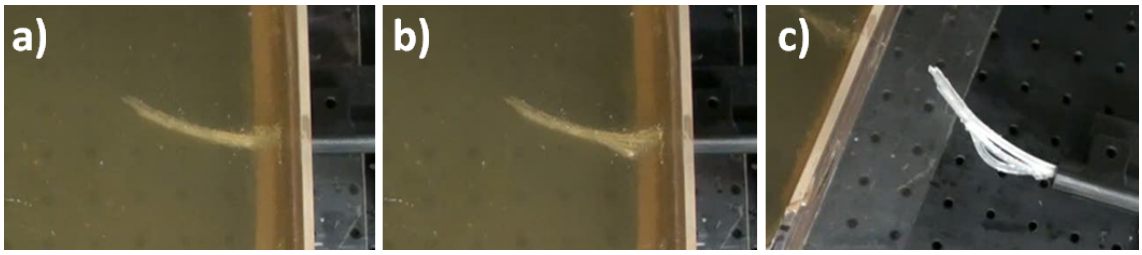


Figure B.3: a) Silicone probe curvilinear shape achieved in gelatine. b) Silicone probe segment irreversible separation during insertion process. c) Picture of the failed probe.

Very preliminary tests were performed and recorded with a video camera. The experimental setup used is shown in Figure 4.5; the electro magnetic (EM) tracking system (see Chapter 4) was not used for the preliminary tests. The probe was lubricated with a special silicone-compatible grease lubricant because silicone tends to absorb standard lubricants and therefore it tends to swell.

Although it was possible to demonstrate curvilinear trajectories qualitatively (Figure B.3a), the probe prototype segments separated too easily (Figures B.3b and c) and therefore insertion tests were interrupted prematurely.

A possible reason for segment separation is the high friction between the probe segments. This problem was encountered and described in Sections 4.8 and 7.3 already. However, it was much more marked in these tests, probably because of the silicone material properties and the design of the interlocking mechanism. Differently from what happens with RP, with extrusion there is not a 1:1 correspondence between original CAD drawings and final prototype, and the contact pressures at the various interfaces between the segments are difficult to predict and control.

Despite all of the limitations encountered, future research is suggested on exploring extrusion methods for manufacturing medical-grade silicone probe prototypes. Extrusion is indeed already used for the manufacture of medical catheters, which means that both the manufacturing technique and the materials used are suited for medical applications. Furthermore, investment in manufacturing tools could result in probe miniaturisation. Medical-grade silicone is not the only medical material available in extrusion processes. Another extrudable, interesting, material is teflon (PTFE), which is also characterised by very low friction properties, even though it is generally stiffer.

Appendix C: Reciprocal Motion

The "reciprocal motion" insertion strategy is inspired by the ovipositing wasp behaviour and it is introduced to minimise the risk of probe buckling inside soft tissue. Each probe segment moves sequentially, so at a specific instant only one probe segment moves and the other three are stationary with respect to the surrounding tissue. This is believed to improve the stability of the probe insertion process, because at each instant, three probe segments are providing a stationary rail for the fourth moving one.

In order to explain the "reciprocal motion" insertion strategy applied to move and steer the four-part probe along a planar trajectory, a simplified description regarding the actuation of only the "active" segments (Segment I and Segment III in Figures 4.2 and 4.3) will first be provided. The two active segments are defined as the segments which are used to turn "left" or "right" on the steering plane. Only one probe segment is pushed at a time and the leading segment is defined as the active segment which is protruded forward with respect to the others (i.e. the segment which defines the bending direction).

Three main parameters are used to define the "reciprocal motion" strategy which are illustrated in Figure C.1:

- Steering Offset O: it represents the desired displacement difference between the leading segment and the following segments. In Section 4.5, the radius of curvature was shown to be a function of this parameter.

- Stroke Amplitude A: it represents the average displacement amplitude imposed at each probe segment when the probe is moving on a straight line. If the probe is curving, the actual stroke amplitude depends also on the steering offset and it is different for the leading segment and the other segments.

- Maximum Stroke Velocity V: it represents the maximum speed of each probe segment during the stroke, and it is constant throughout all the experiment. Each probe segments at each stroke is accelerated constantly until the maximum stroke velocity is reached and then decelerated constantly to a stationary state, as shown in Figure C.1.

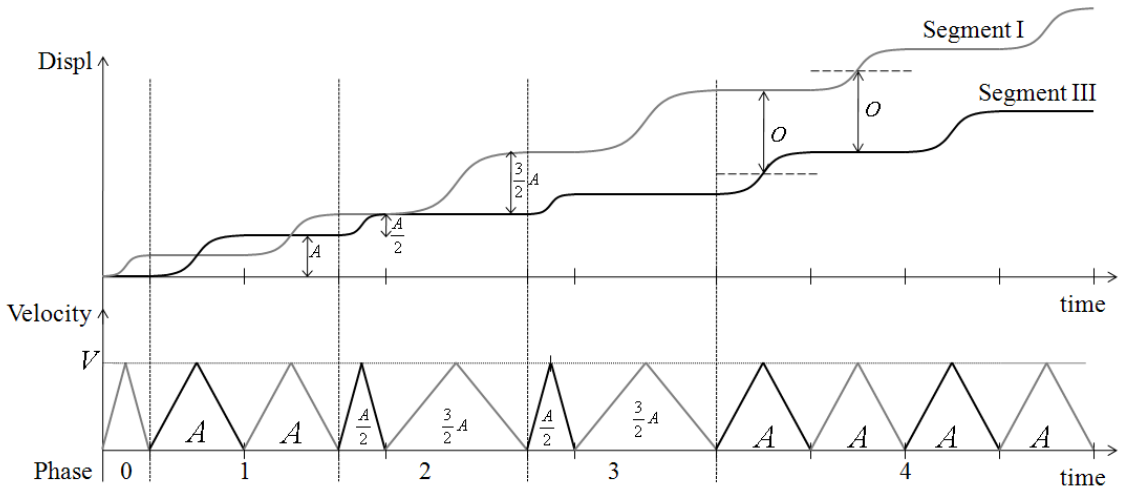


Figure C.1: "Reciprocal motion" actuation strategy for a simplified two-part probe. The grey line corresponds to the displacement of Segment I (top graph) and its Velocity profile (bottom graph). The black line corresponds to Segment III. V is the maximum stroke velocity, A the stroke amplitude and O the desired steering offset.

Considering the motion of an ideal two-part probe, with Segment I defining the curvature (active leading segment), Figure C.1 shows different phases of the insertion strategy:

- *Phase 0, initialisation.* Segment I moves half of the stroke amplitude. From this instant, the "reciprocal motion" actuation starts.

- *Phase 1, straight motion.* The two segments take the lead in turn, being pushed by a stroke amplitude (A), and therefore the overall probe motion is straight.

- *Phase 2, increasing steering offset.* The leading segment (Segment I) moves more (stroke amplitude = $\frac{3}{2}A$) than the other segment (stroke amplitude = $\frac{A}{2}$). This phase lasts until the temporary steering offset reaches the desired steering offset (O). If the steering offset is bigger than half of the stroke amplitude ($O \geq \frac{A}{2}$), more than one "reciprocal motion" cycle will be required to reach the steering offset. If the steering offset is smaller than half of the stroke amplitude ($O < \frac{A}{2}$), the leading segment will move only for the amount of displacement required to reach the desired steering offset.

- *Phase 3, steering offset reached.* At the end of phase 3, the desired steering offset is reached (O is calculated as shown in Figure C.1).

- *Phase 4, steering offset maintained.* During phase 4 the steering offset is maintained and the probe segments are actuated with a constant stroke amplitude (stroke amplitude A). If the steering offset is not modified, for example if the

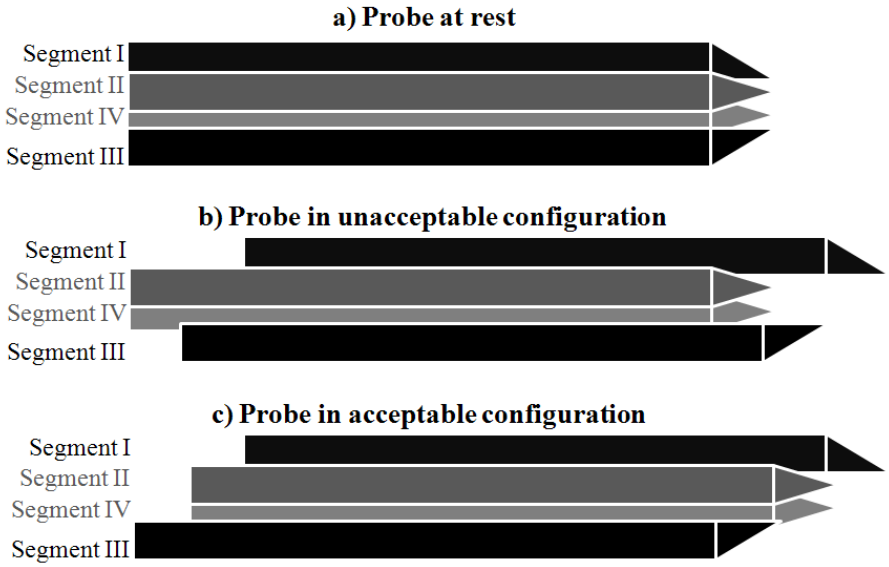


Figure C.2: Three possible probe configurations. a) Probe at rest. b) Probe in unacceptable configuration; Segment I and III are both separately protruding further than any other segment. c) Probe in acceptable configuration.

radius of curvature or the direction of concavity do not need to be changed, the probe will keep curving according to the desired steering offset.

Regarding the actuation of the two passive segments (Segment II and IV in Figures 4.2 and 4.3), these are both actuated in between the two active segments strokes (Segment I and III), with the same maximum stroke velocity V. The rationale for the actuation of the two passive segments is that, at any instant, they have to prevent the active segments from being in a configuration where they both are protruded further than the two passive segments (see Figure C.2 for different examples). This could indeed results in a configuration where the active segments are not connected to each other through any rail provided by the passive segments.

Therefore, just before each active segment is actuated, the passive segments move in such a way that they always align with the position that will be assumed by the most lagging active segment at the next step, within the "reciprocal motion" cycle, as shown in Figure C.3. According to this rule, it may happen that, during a certain "reciprocal motion" cycle, the passive segments do not move at all (black arrows in Figure C.3).

It should also be noted that, during a standard (straight motion) reciprocal motion cycle, each segment covers a displacement corresponding to the stroke amplitude A. This also corresponds to an overall probe advancement of A. According to Figure C.3, the time required to complete a full "reciprocal motion" cycle is:

$$t = 2t_l + 4t_f = 2\left(\frac{2A}{V}\right) + 4\left(\frac{A}{V}\right) = \frac{8A}{V}$$

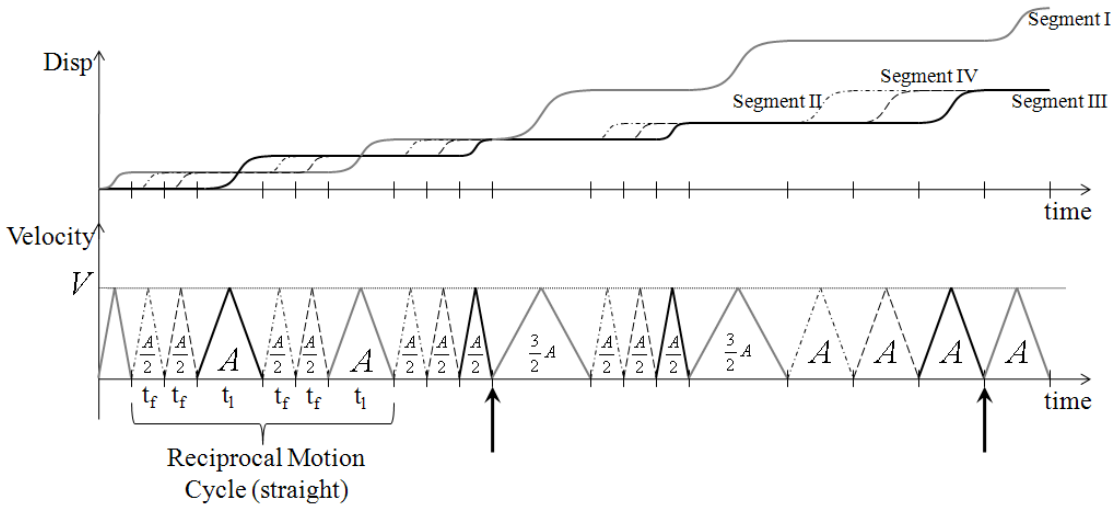


Figure C.3: "Reciprocal motion" actuation strategy for a four-part probe. The grey line corresponds to the displacement of Segment I (top graph) and its Velocity profile (bottom graph). The black line, the dot-dashed line and the dashed line correspond to Segment III, II and IV respectively. Black arrows point at instants when passive segments do not need to be actuated.

where t_l is the time required by a leading segment to complete its stroke; it can be calculated from $A = \frac{1}{2}t_l V$ (displacement as the integral of the velocity profile with respect to time, i.e. the area of the black or grey triangles in Figure C.3).

Similarly, t_f is the time required by a passive segment (follower) to complete its stroke; it can be calculated from $\frac{A}{2} = \frac{1}{2}t_f V$.

Therefore the overall probe velocity $V_{overall}$ is:

$$V_{overall} = \frac{A}{t} = \frac{A}{8A/V} = \frac{V}{8}$$

The overall probe velocity is one eighth of the maximum stroke velocity. Considering that the velocity profile is triangular (which approximate the real experimental velocity profile), the average velocity of each segment at each stroke can be considered to be half of the maximum stroke velocity. As an example, a maximum stroke velocity of 8 mm/s corresponds to an average stroke velocity of 4 mm/s and to an overall probe velocity of 1 mm/s.

Appendix D: The ROBOCAST Project

This appendix provides an overview of the ROBOCAST project and its outcome with regard to the specifications for the flexible probe design, development and integration.

System Overview

The EU FP7 ROBOCAST (ROBOt and sensors integration for Computer Assisted Surgery and Therapy) project [Robocast-Project, 2010] aimed to develop a system for robot assisted MI neurosurgery based on the integration of information and communication technologies (ICT), scientific methods and technologies for surgical application, such as MI burr-hole tumour biopsy, multiple targeting for localised tumour therapy, tissue sampling, liquid micro-dialysis, multiple cyst drainage and electrode placement for DBS. In the ROBOCAST project, a 6-axis serial gross positioning robot (Prosurgics Ltd., UK) is used to support a miniature parallel robot (MAZOR Ltd., Israel) holding a biomimetic flexible and steerable probe (Imperial College, UK) to be introduced through a keyhole opening in the skull of the patient; path planning inside and outside the body is autonomously proposed by the control system by processing preoperative diagnostic information (Politecnico di Milano, Italy), while an electromagnetic position sensor, embedded at the tip of the flexible probe, provides a closed-loop control system with the current position of the probe tip inside the brain (a ROBOCAST system overview is shown in Figure D.1). All robot sub-systems are directed by a high-level controller (University of Karlsrue, Germany), which is responsible for the correct and safe operation of all modules (overall system motion planning, collision avoidance, faults monitoring, etc.), to be accessed through a Common Object Request Broker Architecture (CORBA) interface [TAO-CORBA, 2010]. While a small entry hole in the skull minimises brain-shift (which results from the escape of cerebrospinal fluid from the incision in the dura), within the ROBOCAST consortium the use of intra-operative ultrasound technology was planned to enable the real-time monitoring of any brain-shifted features (Uni-

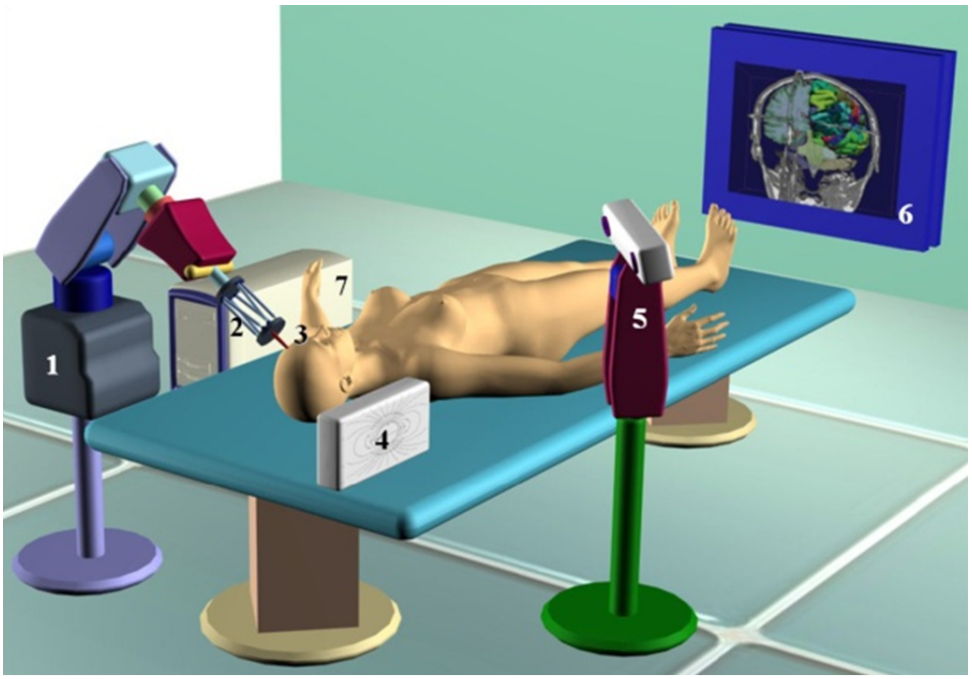


Figure D.1: ROBOCAST System at a glance. A 6-axis serial gross positioning robot (1) is used to support a miniature parallel robot (2) holding the biomimetic steerable probe (3) to be introduced through a keyhole opening in the skull of the patient; an electromagnetic tracking system (4) is used to control position and orientation of the steerable probe tip, while an optical tracking system (5) monitors robot and patient positions; operative images are visualised on a screen (6) and a central station (7) is in charge of the supervision of the system [Robocast-Project, 2010].

versity of Munich, Germany). In the context of ROBOCAST, Imperial College's probe enables MI instrumentation, exemplified by a localised and multiple-targeting drug delivery system, to accurately reach the target through curved paths within the brain, following minimum risk trajectories provided by a brain risk atlas, minimizing tissue damage and avoiding buckling, thus resulting in better targeting and reduced morbidity.

The block diagram in Figure D.2 shows the architecture of the system: preoperative diagnostic images (MRI images showing the location of the deep brain target), together with the physical constraints imposed by the flexible probe (minimum radius of curvature) are processed by the "high level controller", which supplies the "path of minimum risk" for a specific intervention based on digital brain segmentation, a risk grading of brain areas and a suitable path planning algorithm; on the basis of this minimum risk trajectory, the "low level controller" generates the motion signals required to actuate the flexible probe. An electromagnetic position sensor, embedded at the tip of the flexible probe, provides the position feedback to control probe motion, which in turn enables path following.

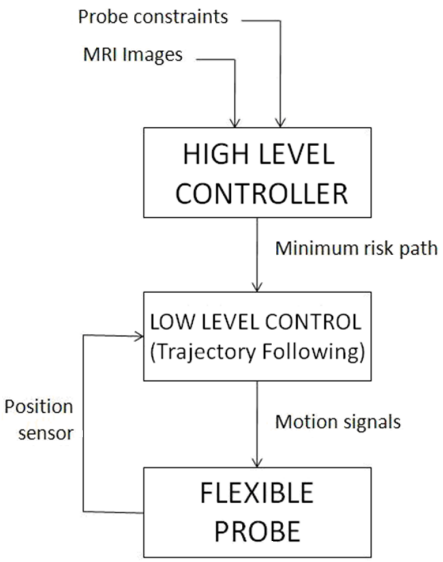


Figure D.2: Block diagram of the system architecture. The high level controller takes into consideration pre-operative images (e.g. MRI, CT) and probe constraints (e.g. maximum radius of curvature) to define a minimum risk path inside the brain, which will then be used by the low level controller to generate appropriate motion signals to drive the probe towards the target. A position sensor (e.g. electromagnetic tracker) will provide tip position feedback.

System Software Architecture

Figure D.3 shows the overall configuration of the software. The flexible probe is physically connected to the actuation box. Four motors in the actuation box are physically wired to the input/output modules of the controller (CompactRio 9002, [National-Instruments-Inc., 2010]). The Labview-based, low-level controller is embedded in this real-time controller module. This low-level controller is responsible for tracking the curved path and controlling the motors and it is connected to the Interpreter via TCI/IP communication. The main objective of the interpreter is to connect the Labview-based low-level controller and the CORBA-based high-level controller. The high-level controller connects the low-level controller of the flexible probe and the sensor manager through the CORBA interface. The sensor manager is physically wired to the Aurora EM tracking system. The EM tracking system localises the tip of the flexible probe by measuring the position of the EM sensor embedded in the tip of the flexible probe. Most of the feedback controls are performed in the Labview-based low-level controller. For the feedback information, the sensor manager measures the tip position and this is delivered via the high-level controller and the interpreter to the low-level controller. All user commands are gathered in the high-level controller and delivered to the low-level controller. The high-level controller is in charge of many functions including the graphical user interface, safety checking of the whole system and integration of many sub-systems.

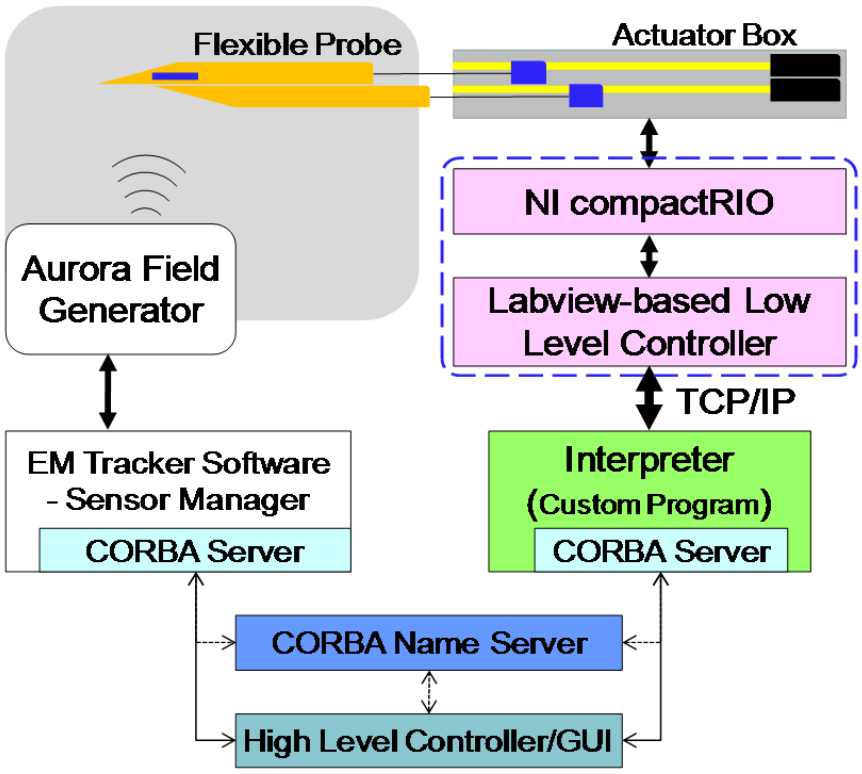


Figure D.3: Overall software configuration for feedback control

However, in order to perform the feedback control, a simplified console-based user interface was implemented.

Original Specifications and Deviations from Specifications

Table D.1 presents a summary of the original requirements for the design, development and integration of the flexible probe system within ROBOCAST. While a detailed description of all tests done to ensure that all of the flexible probe original specifications were met is out of scope of this thesis and can be found in the ROBOCAST final deliverable documents [Robocast-Project, 2010], deviations from the original specifications are described and justified.

Most of the technical specifications for the flexible probe have been met. Reasons for those elements of the specification which have not been met are outlined in the following sections.

Probe Size

The main shortcomings of the current prototype pertain to limitations in the manufacturing process used to implement the current prototype (rapid prototyping techniques, [Objet-Geometries-Ltd., 2010a]). Specifically, both the overall diame-

Original Specifications	Deviations
Micro-dispensing system for delivery and extraction of liquid from probe tip	No
Probe capable of planar curvilinear motion within brain-like material	No
Maximum "degree of curvature" better than 30 degrees	No
Minimum degree of curvature 0 degree (i.e. straight line motion)	No
Ability to curve once and twice	No
Hardware e-stop to halt motion in the event of an emergency	No
Calibrated tip position via EM sensor in tip	No
Maximum insertion force 10N (physical limit to ensure safety)	No
Biocompatible material	No
Targeting accuracy: 1mm	yes (˜1.61mm)
Outer diameter of 8mm or less	yes (10mm)
Probe length of 300mm	yes (226mm)
Ability to curve three times	yes

Table D.1: Original Specifications and Deviations

ter (10mm) and length (226mm) of the current prototype exceed those agreed in the specification. The original aim was to produce medical grade silicone extrusions to fulfill these requirements, but results to date have brought to surface a number of manufacturing difficulties (e.g. elastic deformation of each probe segment during motion), for which further research is required (see Chapters 4, 7 and Appendix B).

Due to limitations in probe size (specifically probe "diameter to length" ratio), a trajectory demonstrating **three curves** was also not possible.

Probe Targeting Accuracy

The targeting accuracy is obtained from the trajectory following performance of the alpha probe prototype (Chapter 4), when both single and double bend planar trajectories are performed in gelatine. The overall targeting accuracy falls below that required (1mm). Indeed, the prototype has been found to produce a targeting accuracy of approximately 0.68mm $\pm$ 1.45mm, with a root mean square (RMS) value of 1.61mm [Ko et al., 2010b].

Although the overall targeting accuracy needs to be obtained in experimental setups including all subsystems such as the Gross Positioner and the Fine Positioner, the sole targeting accuracy of the flexible probe is reported here, when the probe is controlled by the low-level close-loop feedback controller described in Ko et al. [2010b]. Since the current controller is designed to follow the curvilinear trajectory in a plane, the off-plane error is currently not controllable and it is mainly dependent on

the accuracy of placement of the probe (tip and length) on the chosen plane and on any torsional errors during insertion. These have not been considered, as the error values measured are those projected onto the desired plane, but such limitations will need to be addressed before a potential clinical application of the probe can be considered.